2020-2021

Cornell NanoScale Facility (CNF)

Research Accomplishments

intentionally blank page

250 Duffield Hall • 343 Campus Road • Ithaca NY 14853-2700
Phone: 607.255.2329 • Fax: 607.255.8601 •
Email: information@cnf.cornell.edu • Website: www.cnf.cornell.edu

Cornell NanoScale Facility 2020-2021 Research Accomplishments

CNF Lester B. Knight Director:
Christopher Kemper Ober

CNF Director of Operations:
Ronald Olson

Cornell NanoScale Facility (CNF) is a member of the National Nanotechnology Coordinated Infrastructure *(www.nnci.net)* and is supported by the National Science Foundation under Grant No. NNCI-2025233, the New York State Office of Science, Technology and Academic Research, Cornell University, Industry, and our Users.

**The 2020-2021 CNF Research Accomplishments are also available on the web:
http://cnf.cornell.edu/publications/research_accomplishments**

Table of Contents

2021 CNF Interns in June

Materials, 54-75

2021 CNF Interns in the CNF Cleanroom

Mechanical Devices, 76-91

Optics & Opto-Electronics, 92-111

Physics & Nano-Structure Physics, 112-139

Process & Characterization, 140-147

CNF Youth Outreach; At-Home Science Experiments

- CNF's Youth Outreach Program Coordinator, Tom Pennell has developed several at home science experiments for youth to explore the growing field of nanotechnology.
- These experiments will be accompanied by a three part virtual presentation at Cornell University's upcoming 4H Career Explorations event (June 2021).
- Students will have a live tour of the CNF cleanroom, live demonstrations and an introduction into interesting areas of nanoscale research.
- Researchers from the facility will also be available to discuss how they got into the field of nanoscale research with attendees.
- CNF will also be distributing these at home experiments to other schools and youth groups in the surrounding area.

Directors' Welcome

The Cornell NanoScale Science & Technology Facility presents the 2020-2021 CNF Research Accomplishments!

We are honored to showcase excellence in research demonstrated by users and research groups utilizing the plethora of resources offered at the CNF. We thank the users for their contributions to this publication. This collection of work demonstrates the wide range of emerging science and technology fields that utilize nanotechnology tools to achieve diverse state-of-the-art results. In addition to the 73 featured research reports, a section on CNF-research-related patents, presentations, and publications (close to 360 in 2020) is included.

National Nanotechnology Coordinated Infrastructure

NNCI and NNCI Awards

The CNF is delighted to continue its membership in the National Nanotechnology Coordinated Infrastructure (NNCI) with support provided by the National Science Foundation (NSF) and the NYSTAR/ESD Matching Grant Program from New York State. This support is essential to CNF and its position at the forefront of nanofabrication. Earlier this year the CNF submitted the year 6 annual report and participated in a successful, virtual, reverse site visit as part of the cooperative agreement with the NNCI.

Congratulations are extended to Michael Skvarla and Phil Infante who were honored with national awards from the NNCI. Annually, the NNCI acknowledges the efforts of NNCI staff who provide exceptional service and support to network users in the categories of Technical Staff, Education and Outreach, and User Support. This year Mike was awarded the NNCI Staff Award in the User Support category and Phil was granted the NNCI Staff Award for Technical Staff. Phil and Mike will receive a plaque and acknowledgement at the NNCI Annual Conference as well as travel support to attend the conference. The 2021 NNCI Annual Conference, hosted by Northwestern University (SHyNE), will be held Monday, November 1st through Wednesday, November 3rd. The exceptional staff at the CNF have been consistently recognized with NNCI Outstanding Staff Member Awards. Past award recipients include Chris Alpha-Technical Staff (2018), and Tom Pennell-Education and Outreach (2020).

New User Fees Waived for the Remainder of 2021

In June the CNF fully reopened, allowing out of state users back into the facility. With this announcement we introduced an incentive benefiting new grad students and new external users looking to utilize the CNF — new user orientation fees have been eliminated for the remainder of the year.

If you or someone in your research group would like to become a new CNF user, please visit the Getting Started section of the CNF website to initiate the process Additionally, if you know of someone who may be interested in becoming a new CNF user, please feel free to share this announcement. (https://cnf.cornell.edu/howto)

New Partnerships

Cornell Visualization and Imaging Partnership (CVIP)

CNF and the Cornell Institute of Biotechnology (Biotech) partnered to further advance Cornell's excellence in life science characterization and imaging capabilities. CNF users now have access to a broad range of 3-D characterization tools including a variety of confocal microscopes, super-resolution microscopes, and micro/nano-x-ray-CT scanning. The mission of this partnership is to foster and enhance the convergence of research fields while unifying new approaches and ideas to inspire innovation and discovery. CNF cleanroom and Biotech users are now able to mutually access resources in both centers.

Cornell Multiscale 3D Fabrication Partnership (CM3FP)

CNF has also partnered with the Rapid Prototyping Lab in the Mechanical Engineering department to provide access to additional multiscale, 3D printing resources. The objective is to provide a broader range of technologies to users. These expanded resources will leverage existing expertise, instrumentation/tools, and administrative support to impact research involving life sciences, heterointegration, and nano/micro-scale technology. CNF and RPL staff will serve as a gateway to new 3D printers, provide consultation, software services, design help, billing, and user support.

Please contact the user program managers (userprogram@cnf.cornell.edu) and/or visit the CNF websites below for additional information on utilizing these resources.

https://www.cnf.cornell.edu/howto/cvip
https://www.cnf.cornell.edu/howto/cm3fp

New Equipment

The CNF continues to upgrade its capabilities in order to remain at the forefront of nanotechnology. We thank you for your patience and continued support as it has been a major effort by the CNF staff to catch up on installation of these tools while dealing with supply chain issues, and other COVID-imposed obstacles. The following equipment has been acquired over the past year and either is installed or being installed.

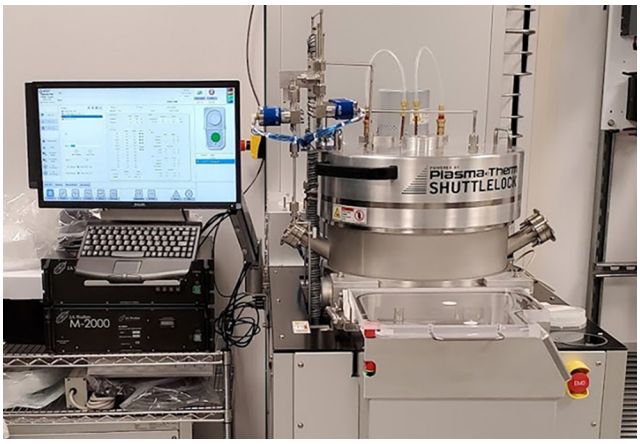

Plasma-Therm ALE (installed, developing the technology)

CNF was able to obtain an advanced ALE instrument from Plasma-Therm. CNF and Plasma-Therm have partnered to develop processes and instrumentation for Atomic Layer Etching (ALE). ALE is an etching technology analogous to Atomic Layer Deposition (ALD) whereby atomically thin layers are added (in the case of ALD) or subtracted (in the case of ALE), by alternating self-limiting chemical reactions, allowing ultra-precise processing, one atomic layer at a time. The system is equipped with a Woollam M2000 in-situ spectroscopic ellipsometer and Langmuir probe. We look forward to developing and sharing new processes on this tool with the CNF and NNCI user communities.

AJA Sputtering Deposition System #3 (Installed, ready for use)

CNF installed an AJA Orion 5 system that supplements CNF's other two AJA Orion 8 RF and DC sputtering systems. The tool will have a host of standard materials available and will allow sputtering of materials like Gold that would not otherwise be permitted in the sputter tools. The Orion 5 tool currently has three 2-inch guns installed but has room for five guns total and has two DC power supplies to allow for co-sputtering. Please reach out to staff for information on criteria for new target additions to the sputter tools.

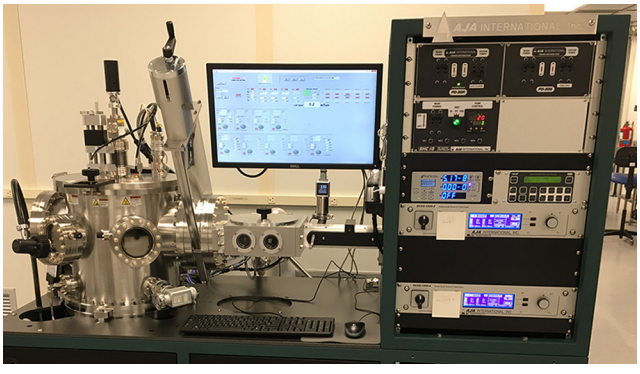

Veeco Savannah Atomic Layer Deposition System (ALD) (installed, ready for qualification)

This system joins CNF's other two ALD systems, the Oxford FlexAL and the Arradiance GemStar; The Savannah will be dedicated to the deposition of metal films, in particular Aluminum, Platinum, Palladium, and Ruthenium. It is equipped with an ozone generator to assist in lower temperature deposition and to broaden the spectrum of available precursors.

Plasma-Therm HDPCVD (installed, SiO_2 and Si_3N_4 process qualified)

CNF has obtained a high-density plasma chemical vapor deposition system (HPCVD or ICP-PECVD). This system is capable of depositing high density SiO_2, Si_3N_4, a-SiC, and doped a-Si films at low temperatures, ranging from 80°C to 175°C. These materials will be exceptionally smooth, dense, and conformal; perfect for applications where ALD or PECVD may not be ideal due to rate or temperature limitations. This new system has replaced the GSI PECVD system and further supports efforts in 2D materials and heterointegration, as well as photonics, biotech, MEMS, and CMOS projects.

Angstrom UHV Load-locked Evaporator (just arrived at the end of August)

This custom tool from Angstrom Engineering includes in situ ion beam cleaning, GLAD (Glancing Angle Deposition) with rotation, and sample heating. With a load lock and an ultrahigh vacuum system this tool can deposit high purity metal films required for many CNF applications.

Bruker Dektak XT (installed, being qualified)

In order to increase the reliability and capability of our profilometry suite, the CNF has added a Bruker Dektak XT stylus profilometer with 4Å repeatability. We have sample stages to accommodate wafer pieces, as well as full size wafers up to 200 mm. The software gives us motorized stage translation and rotation in addition to sequencing for up to 200 sites. The tool is loaded with a 2 μm radius of curvature diamond-tipped stylus. The Vision64 software can also use the tool measurements to create a 3D map of the scanned surface.


Kareena Dash


Niaa Jenkins-Johnston

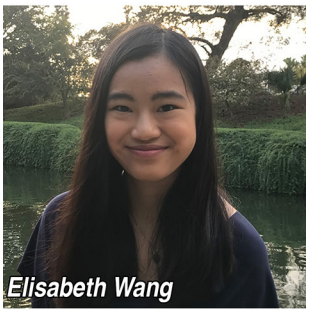
Elisabeth Wang


Zhangqi Zheng


Micah Chen


Francesca Bard

CNF REU Interns

Since 1991, we have hosted the Cornell NanoScale Science & Technology Facility Research Experiences for Undergraduates (CNF REU) Program.

After canceling the hands-on event last year due to COVID restrictions, we were pleased to welcome six interns from the Cornell College of Engineering undergraduate community this year. Four students participated as CNF REU interns — Kareena Dash (see page 56), Niaa Jenkins-Johnston (page 2), Elisabeth Wang (page 4), and Zhangqi Zheng (page 112). In addition, Micah Chen from the Cornell Center for Transportation, Environment, and Community Health's (CTECH) REU Program and Francesca Bard (page 54), a summer undergraduate student and CNF user, were "adopted" in order for them to benefit from our logistical support over the summer.

These six students worked diligently for ten weeks on their specific research projects focusing on topics that included biological applications, materials characterization, nanophysics, and evaluation of transportation sustainability. There were multiple opportunities to garner presentation skills by offering progress updates and concluding the program with the submission of a final report. Many of the participants will continue with their respective research groups into the fall semester.

The 2021 CNF REU Program reports, photo album, and final presentation videos will soon be available online at https://cnf.cornell.edu/education/reu/2021

We plan to conduct a nation-wide search for our 2022 CNF REU interns in November. Keep an eye on https://cnf.cornell.edu/education/reu for information regarding next year's application process.

TCN and Outreach

The CNF's Technology and Characterization at the Nanoscale (TCN) short course is offered twice each year. It continues to provide an excellent opportunity for the scientific community to learn about the field of nanofabrication from in-house experts. The TCN is open to participants from academia, industry and government, and includes lectures, demonstrations and activities in the cleanroom. Due to COVID we were pleased to offer this course virtually, which resulted in us reaching a broader audience with increased attendance. With this in mind, going forward, the CNF will be offering the January TCN course virtually and the June TCN course in person. The technical staff are also working to develop new educational modules based on developing technologies. Please reach out to Tom Pennell, our Youth Outreach Program Coordinator, if you are interested in having a specific device type featured in the instruction.

CNF's youth outreach program continues to partner with 4H and recently hosted students from across NY State for Cornell's annual Career Explorations event. Tom Pennell, created five new at home nanoscience experiments based on photolithography, materials science, and nanorobotics. He has packaged nearly 300 of them with the required materials to be distributed to any youth groups interested in learning more about our field. (See page iv for more....)

The youth outreach program will also be taking part in a national 4H summit in September, teaching students about nanotechnology and how it relates to space exploration.

Staffing News

Welcome

A warm welcome is extended to new User Program Assistant, Stacy Clementson who came to us from the Praxis Center for Venture Development at Cornell. Stacy will focus 75% of her time assisting with new User onboarding for the CNF and 25% of her time supporting Praxis.

Comments, feedback, and suggestions about CNF are always welcome. Feel free to use our online User Comment Form at https://www.cnfusers.cornell.edu/user_feedback

In Person Again

With the lifting of restrictions in June, almost all the CNF staff came back to work in the office full time, in person. We celebrated in the most typical CNF staff kind of way — we gathered with a BBQ party. A good time was had by all!

While we are back in the office for the most part, it's a good idea to call ahead if you want to meet with someone in particular, to make sure they are in fact "in person" that day.

THANK YOU to the CNF COMMUNITY!

Thank you to all CNF users for their continued patience and understanding during these unprecedented times. It is imperative we remain diligent in our efforts as a community to support ongoing safety protocols in order to help safeguard the progress we have made. We will continue to monitor the course of the pandemic and provide updates when warranted and directed by the University and Tompkins County Health Department.

Christopher Ober
Lester B. Knight Director, CNF
director@cnf.cornell.edu

Claudia Fischbach-Teschl
CNF Associate Director
cf99@cornell.edu

Ron Olson
CNF Director of Operations
olson@cnf.cornell.edu

CNF in the NEWS

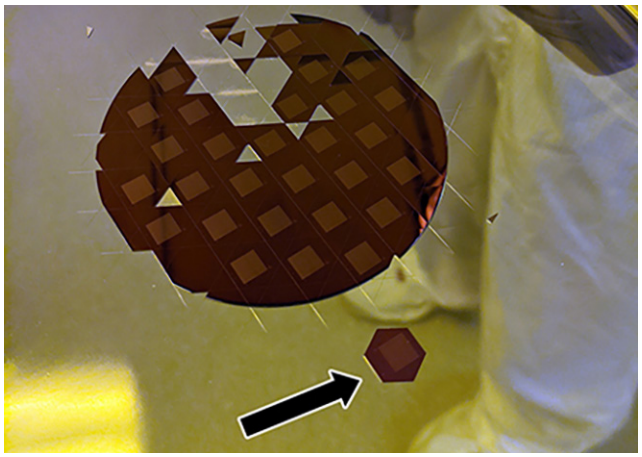

More than 27,000 Civil Air Patrol Names Headed to the Moon

The US Air Force Auxiliary Civil Air Patrol (CAP) partnered with the CNF to etch more than 27,000 CAP member names, 270 Air Force Association (AFA) StellarXplorers names, an 80th anniversary CAP logo, and messages from CAP and AFA leadership onto a microchip the size of a postage stamp. This microchip, carrying 27,285 names, messages, and images, is set to be carried to the Moon later this year aboard Astrobotic's Peregrine lunar lander.

"Among these names are more than 4,000 CAP high school cadets," says Lt. Paul Douglas, Burke Composite Squadron's Aerospace Education officer. "My personal hope is that our young cadets will stand in their back yards, look up at the Moon, and dream big. They'll know if they can make it to the Moon, they can do anything."

The CNF technical staff worked with CAP to design the chip, starting with a computer-aided design (CAD) through using their photolithography, etching, and dicing tools to lay down an 80-nanometer thin film of silicon nitride on a standard silicon wafer. Details of the process — from start to finished chip, 0.5" across the hexagon, flat edge to flat edge — can be found in the Image Gallery online. https://cnf.cornell.edu/node/325

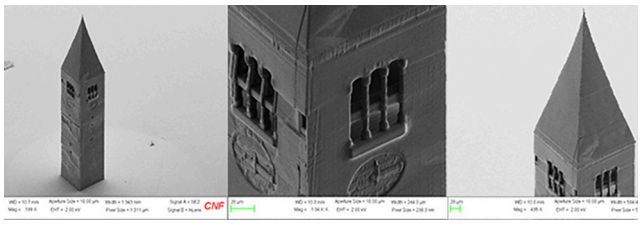

The CNF's Nano-Sized McGraw Tower

Once again the Cornell NanoScale Facility (CNF) makes a molehill out of a mountain — or in this case, the smallest rendition of Cornell's iconic McGraw Clock tower.

Twenty-four years ago, physics professor Harold Craighead and then-doctoral student Dustin Carr, Ph.D. '00, created the world's smallest guitar using cutting-edge technology in what was then the Cornell Nanofabrication Facility. They're at it again at the center – now known as the Cornell NanoScale Science and Technology Facility (CNF), in Duffield Hall. A team led by staff photolithographer Ed Camacho has created the world's smallest rendition of Cornell's iconic McGraw Tower – complete with its 161 interior steps, two sets of stairs and 21 bells.

"This is possibly the world's smallest bell tower," said Camacho, whose achievement of epic proportions was accomplished using one of CNF's newest tools: the NanoScribe GT2 Laser Lithography System, a two-photon polymerization volumetric 3D printer.

https://www.14850.com/051119827-mcgraw-tower-model/

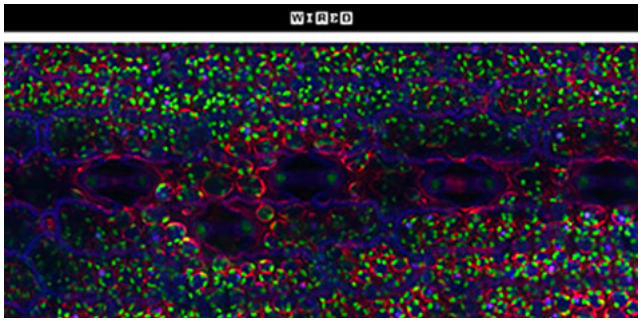

Which Crops Can Survive Drought? Nanosensors May Offer Clues.

Abraham Stroock's technique can be used to track how water flows through plants, which could be key to breeding more resilient crops in an increasingly hot, dry climate. (This work was performed in part at the CNF)

https://www.wired.com/story/which-crops-can-survive-drought-nanosensors-may-offer-clues/

A Selection of 2020 Cornell NanoScale Facility Research-Related Patents, Presentations, and Publications

"A discrete interface in matrix stiffness creates an oscillatory pattern of endothelial monolayer disruption"; J.A. VanderBurgh, A.V. Potharazu, S.C. Schwager, C.A. Reinhart-King; J. of Cell Science 2020 133: jcs244533 doi: 10.1242/jcs.244533.

"A Highly Selective, Tunable High-Pass X-Ray Filter System and the Method of Fabrication"; D.Agyeman-Budu, A.Woll; 8827-02-US, United States, US from PRV, Filed, 8/3/20, 16/983,887.

"A minimally disruptive method for measuring water potential in-planta using hydrogel nanoreporters"; Jain, P.; Liu, W.; Zhu, S.; Melkonian, J.; Pauli, D.; Riha, S.; Gore, M.; Stroock, A.; bioRxiv, Posted May 30, 2020, doi: https://doi.org/10.1101/2020.05.29.122507.

"A Multiplexed Diagnostice Assay for Iron and Vitamin A Deficiency and Methods of Use Thereof"; D.Erickson, Z.Lu, S.Mehta; 7107-03-US Filed, US from PCT, 5/13/20, 16/763,707.

"A tissue engineering approach to metastatic colon cancer"; Sarvestani, SK, RK Dehaan, PG Miller, S Bose, X Shen, ML Shuler, and EH Huang; iScience 23:101719, Nov.20, 2020.

"a-axis YBa2Cu3O7-x/PrBa2Cu3O7-x/YBa2Cu3O7-x trilayers with subnanometer rms roughness"; Y. Eren Suyolcu, J.Sun, B.Goodge, J.Park, J.Schubert, L.Kourkoutis, D.Schlom; arXiv:2010.12624 [cond-mat.supr-con] [Submitted 23 Oct 2020].

"Absence of spin current generation in Ti/FeCoB bilayers with strong interfacial spin-orbit coupling"; L.Zhu, R.A. Buhrman; arXiv preprint arXiv:2010.13137, 2020 - arxiv.org.

"Acoustic Sensing Systems, Devices and Methods"; M.Abdelmejeed, J.Kuo, A.Lal; 7683-05-EP, Europe, EPC - European Patent Convention, Filed, 9/1/20, 19747141.

"Acoustically Driving the Single-Quantum Spin Transition of Diamond Nitrogen-Vacancy Centers"; Chen, H. Y.; Bhave, S. A.; Fuchs, G. D.; Physical Review Applied, 13, 5, 54068.

"Acoustically-driven Quantum Spin Sensor"; H.Chen, G.Fuchs; 9329-01-US, United States, Filed, MPR 1/24/20, 62/965,533; 9329, Invention, Filed by Cornell.

"Adsorption-controlled growth of Ga2O3 by suboxide molecular-beam epitaxy"; P.Vogt, F.Hensling, K.Azizie, C.Chang, D.Turner, J.Park, J.McCandless, H.Paik, B.Bocklund, G.Hoffman, O.Bierwagen, D.Jena, H.Xing, S.Mou, D.Muller, S.Shang, Z.Liu, and D.Schlom; arXiv:2011.00084 [Oct 2020].

"All-Epitaxial Bulk Acoustic Wave Resonators"; J.Miller, J.Wright, H.Xing, D.Jena; physica status solidi (a), 217, 7, 1900786.

"An array microhabitat device with dual gradients revealed synergistic roles of nitrogen and phosphorous in the growth of microalgae"; Liu, F.; Yazdani, M.; Ahner, B.; Wu, M.; Lab on a Chip, 20, 4, 798-805.

"An automated controlled release device for livestock management"; D.Erickson, J.Giordano, Ma.Masello, Y.Ren; 9391-01-US, United States, Filed, MPP, 4/27/20, 63/016,235.

"An organotypic in vitro model of matured blood vessels"; J.Lee, E.Lee; bioRxiv, Posted August 04, 2020. doi: https://doi.org/10.1101/2020.08.03.234807.

"An unexplored MBE growth mode reveals new properties of superconducting NbN"; Wright, J.; Chang, C.; Waters, D.; Lüpke, F.; Raymond, L.; Koscica, R.; Khalsa, G.; Feenstra, R.; Muller, D.; Xing, H.G.; arXiv:2008.09596 [cond-mat.mtrl-sci] [Submitted on 21 Aug 2020 (v1), last revised 24 Dec 2020 (this version, v3)] DOI: 10.1103/PhysRevMaterials.5.024802.

"Antifouling urinary catheters with shape-memory topographic patterns"; D.Ren, H.Gu; US Patent App. 16/674,199, 2020.

"Applying uniaxial strain to graphene devices fabricated on flexible substrates"; Oh, J.; Schaefer, B.; Sunko, V.; Watanabe, K.; Taniguchi, T.; Hicks, C.; Mackenzie, A.P.; Nowack, K.; Bulletin of the American Physical Society, 65.

"Area-selective atomic layer deposition enabled by competitive adsorption"; Suh, T., Y.Yang, H.Sohn, R.DiStasio Jr., and J.Engstrom; Journal of Vacuum Science & Technology A 38, 062411 (2020) [Editor's Pick in JVST A].

"Athermal lithium niobate microresonator"; Ling, Jingwei; He, Yang; Luo, Rui; Li, Mingxiao; Liang, Hanxiao; Lin, Qiang; Optics Express, 28, 15, 21682-21691.

"Atomic Layer Deposition for Mechanical, Magnetic, and Robotic Systems"; Dorsey, K.; Ph.D. Thesis, Cornell University, 2020. 28025674.

"Automated microfluidic Oocyte Denudation Module"; A.Abbaspourrad, A.Mokhtare, G.Palermo; 9534-01-US, United States, Filed, MPR - Manuscript Provisional, 7/6/20, 63/048,531; 9534, Invention, Filed by Cornell.

"Automated, Ultra-Fast Laser-Drilling of Nanometer Scale Pores and Nanopore Arrays in Aqueous Solutions"; Gilboa, T.; Zvuloni, E.; Zrehen, A.; Squires, A.; Meller, A.; Advanced Functional Materials, 30, 18, 1900642.

"Bidirectional Self-Folding with Atomic Layer Deposition Nanofilms for Microscale Origami"; Bircan, B.; Miskin, M. Z.; Lang, R. J.; Cao, M. C.; Dorsey, K. J.; Salim, M. G.; Wang, W.; Muller, D. A.; McEuen, P. L.; Cohen, I.; Nano Letters, 2020, 20(7), 4850-4856.

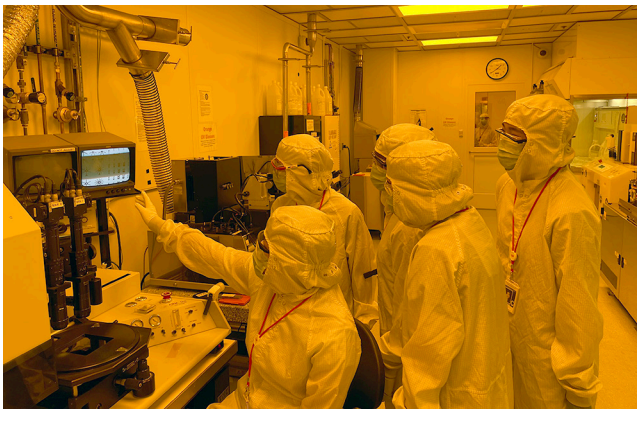

"Biological Small-Molecule Assays Using Gradient-based Microfluidics"; A.Abbaspourrad, M.Azizi; 9495-01-US, United States, MPR, Filed, 12/23/20, 63/130,172.

"Block Copolymer Self-Assembly-Directed and Transient Laser Heating-Enabled Nanostructures toward Phononic and Photonic Quantum Materials"; F.Yu, Q.Zhang, R.P.Thedford, A.Singer, D.M. Smilgies, M.O. Thompson, and U.B. Wiesner; ACS Nano 2020, 14, 9, 11273-11282; Publication Date:August 11, 2020; https://doi.org/10.1021/acsnano.0c03150.

"Blood-immersed Bearing System for a Blood Pump"; J.Antaki; 9293, Invention, Filed - Ownership Determination - TBD.

"Body-on-a-Chip Microscale models for Drug Development"; Shuler, M.L.; SelectBio 2D to 3D Culture and organoids. Boston, MA March 23-25. (virtual talk).

"Body-on-a-Chip: Conception to Practical Applications"; Shuler, M.L.; EUROoCS Conf. 2020. Held virtually (originally scheduled for Uppsala Sweden), July 8-9.

"Body-on-a-Chip: Human Microscale Models for Drug Development"; Shuler, M.L.; Select Bio Organ-on-a-Chip 2020. San Diego, CA September 28-30. (virtual talk).

"Bottom Tunnel Junction Blue Light-emitting Field-effect Transistors"; S.Bharadwaj, A.Hickman, D.Jena, K.Lee, K.Nomoto, V.Protasenko, L.van Deurzen, H.G.Xing; 9544, Invention, Filed by Cornell 2020; APL 117, 031107 (2020); https://doi.org/10.1063/5.0009430.

"Breakdown of the Small-Polaron Hopping Model in Higher-Order Spinels"; A.Bhargava, R.Eppstein, J.Sun, M.Smeaton, H.Paik, L.Kourkoutis, D.Schlom, M.Toroker, R.Robinson; Advanced Materials Volume 32, Issue 49; December 10, 2020; https://doi.org/10.1002/adma.202004490.

"Broadband Ultrahigh-Resolution chip-scale Scanning Soliton Dual-Comb Spectroscopy"; Lin, T.; Dutt, A.; Joshi, C.; Phare, C.; Okawachi, Y.; Gaeta, A.; Lipson, M.; arXiv preprint arXiv:2001.00869.

"Characterization of AlScN on CMOS"; Y. Liu, J. Kuo, B. Davaji, V. Gund, J. Sharma, N. Singh and A. Lal; IEEE International Frequency Control Symposium (IFCS), 2020.

"Characterization of Metal Effect on Solidly Mounted AlScN on CMOS"; Y.Liu; J.Kuo; A.Lal; J.Sharma; N.Singh; 2020 IEEE International Ultrasonics Symposium (IUS), 7-11 Sept. 2020, DOI: 10.1109/IUS46767.2020.9251681.

"Characterization of topologically protected charge-parity qubits"; Y.Liu, K.Dodge, M.Senatore, B.Cole, J.Ku, S.Zhu, A.Shearrow, A.Klots, L.Faoro, L.Ioffe, R.McDermott, B.Plourde; Applied Superconductivity Conference, Nov. 2020 Invited poster.

"Chemical-Genetic Interrogation of Nuclear Size Control Reveals Cancer-Specific Effects on Cell Migration and Invasion"; Rizzotto, A.; Tollis, S.; Pham, N.; Wildenhain, J.; Zuleger, N.; Keys, J.; Batrakou, D.; Culley, J.; Zheng, S.; Lammerding, J.; bioRxiv, Posted January 11, 2020, doi: https://doi.org/10.1101/2020.01.10.902148.

"Chip-scale blue light phased array"; M.Shin, A.Mohanty, K.Watson, G.Bhatt, C.Phare, S.Miller, M.Zadka, B.Lee, X.Ji, I.Datta, and M.Lipson; Optics Letters 45 (7), 1934-1937 (2020).

"Chirp-sensitive Response of Nonlinear Semiconductor Metasurfaces"; G. Sartorello, M. R. Shcherbakov, Z. Fan, R. M. Schwartz, D. Woodbury, H. M. Milchberg and G. Shvets; Metamaterials 2020, the 14th International Congress on Artificial Materials for Novel Wave Phenomena, 29 February 2020.

"Circuits and Devices Based on Enhanced Spin Hall Effect for Efficient Spin Transfer Torque"; R.Buhrman, M.Nguyen, C.Pai, D.Ralph; 6764-08-US, United States, Issued, 6/25/18, 16/017,565, 11/24/20, 10,847,197.

"Collaborative RFID Reader Using Code Divisional Multiple Access and Methods for Same"; X.Hui, E.Kan; 8145-03-US, US from PCT Filed, 11/16/20, 17/055,974; 8145-04-EP, EPC Filed, 11/30/20, 19084527; 8145-05-CA FOR Filed, 11/12/20, 3100324.

"Compact Actuators and Related Robotic Devices"; I.Cohen, P.McEuen, M.Miskin; 9343-01-US MPR 3/5/20, 62/986,512.

"Compact Actuators, Electrically Programmable Microscale Surface Oxide Memory Actuators and Related Robotic Devices"; I.Cohen, Q.Liu, P.McEuen, M.Miskin; 9343-02-US, United States, MPR, Converted, 10/2/20, 63/087,056; 9343-03-US, United States, MPR, Converted, 12/21/20, 63/128,778.

"Competitive adsorption as a route to area selective deposition"; Suh, T., Y.Yang, P.Zhao, K.Lao, H.Ko, J.Wong, R.DiStasio, and J.Engstrom; ACS Appl. Mater. Interfaces 12, 9989-9999 (2020).

"Computation Devices and Artificial Neurons Based on Nanoelectromechanical Systems"; S.Ardanuc, J.Hoople, J.Kuo, A.Lal; 5966-05-US DIV, Filed, 12/7/20, 17/114,040; 5966-04-US Issued, 5/8/14, 15/880,261, 12/8/20, 10,860,916.

"Confined cancer cell migration causes DNA damage by increasing replication stress"; Shah P, Cheng S, Lammerding J.; BMES Annual Meeting. (Oct. 14-17, 2020).

"Contraction of the rear cortex drives nuclear translocation in 3D migration"; Keys J, Isermann P, Lammerding J.; Biomedical Engineering Society (BMES) Annual Meeting. (Oct. 2020).

"Controlling spin current polarization through non-collinear antiferromagnetism"; T.Nan, C.Quintela, J.Irwin, G.Gurung, D.Shao, J.Gibbons, N.Campbell, K.Song, S.Choi, L.Guo, R.Johnson, P.Manuel, R.Chopdekar, I.Hallsteinsen, T.Tybell, P.Ryan, J.Kim, Y.Choi, P.Radaelli, D.Ralph, E.Tsymbal, M. Rzchowski, and C.Eom; Nature Comm 11, 4671 (2020). https://doi.org/10.1038/s41467-020-17999-4.

"Correlation induced emergent charge order in metallic vanadium dioxide"; Singh, C.; Piper, L.; Paik, H.; Schlom, D.; Lee, W.; arXiv preprint arXiv:2005.02957.

"Coupling a Superconducting Qubit to a Left-Handed Metamaterial Resonator"; S.Indrajeet, H.Wang, M.Hutchings, B.Taketani, F.Wilhelm, M.LaHaye, and B.Plourde; Physical Review App 14, 064033 10 Dec 2020.

"Cryogenic Control of Coherent Quantum Systems"; B.Plourde; Applied Superconductivity Conference, Nov 2020; Invited talk.

"Cryogenic Memory Architecture Integrating Spin Hall Effect based Magnetic Memory and Superconductive Cryotron Devices"; M.Nguyen, G.Ribeill, M.Gustafsson, S.Shi, S.Aradhya, A.Wagner, L.Ranzani, L.Zhu, R.Baghdadi, B.Butters, E.Toomey, M.Colangelo, P.Truitt, A.Jafari-Salim, D.McAllister, D.Yohannes, S.Cheng, R.Lazarus, O.Mukhanov, K.Berggren, R.Buhrman, G.Rowlands and T.Ohki; Scientific Reports, 10, 248 (2020).

"Cryogenic methods for biological small-angle x-ray scattering"; D.Moreau; 2020 American Crystallographic Conference (virtual), Session 2.1.4: Frontiers in SAS.

"Custom silicon technologies for high detection efficiency SPAD arrays"; A.Gulinatti, F.Ceccarelli, G.Acconcia, M.Ghioni, I.Rech; The International SPAD Sensor Workshop 2020 (ISSW2020), June 8-10 2020, Edinburgh, Scotland (UK), Invited presentation, June 8th 2020; https://issw.ed.ac.uk/scrolling_nav/index.html.

"Custom silicon technology for SPAD-arrays with red-enhanced sensitivity and low timing jitter"; A.Gulinatti, F.Ceccarelli, M.Ghioni, I.Rech; arXiv:2009.06728 [physics.ins-det], DOI: 10.1364/OE.413821 [Submitted on 14 Sep 2020].

"CVD thick Nb film and cavity coating"; Z. Sun, M. Ge, H. Katrina, M. Liepe, J. Maniscalco, T. Oseroff, R. D. Porter; V. Arrieta, S. McNeal; TESLA Technology Collaboration, Geneva, Switzerland, February 2020.

"Cytokine profiling of extracellular vesicles isolated from plasma in myalgic encephalomyelitis/chronic fatigue syndrome: a pilot study"; Giloteaux L, O'Neal A, Castro-Marrero J, Levine SM, Hanson MR; Journal of Translational Medicine. 2020 Oct 12;18(1):387. doi: 10.1186/s12967-020-02560-0. PMID: 33046133; PMCID: PMC7552484.

"Czochralski growth and characterization of perovskite-type (La,Nd)(Lu,Sc)O3 single crystals with a pseudocubic lattice parameter of about 4.09 Å"; Guguschev, C.; Klimm, D.; Brützam, M.; Gesing, T. M.; Gogolin, M.; Paik, H.; Markurt, T.; Kok, D. J.; Kwasniewski, A.; Jendritzki, U.; Journal of Crystal Growth, Volume 536, 15 April 2020, 125526.

"Defect accommodation in off-stoichiometric (SrTiO3) nSrO Ruddlesden-Popper superlattices studied with positron annihilation spectroscopy"; N.Dawley, B.Goodge, W.Egger, M.Barone, L.Kourkoutis, D.Keeble, and D.Schlom; APL 117, 062901 (2020); https://doi.org/10.1063/5.0011136.

"Degradation Mechanisms of GaN-Based Vertical Devices: A Review"; Meneghini, M.; Fabris, E.; Ruzzarin, M.; De Santi, C.; Nomoto, K.; Hu, Z.; Li, W.; Gao, X.; Jena, D.; Xing, H.G.; physica status solidi (a), 217, 7, 1900750.

"Demonstration of chip-based coupled degenerate optical parametric oscillators for realizing a nanophotonic spin-glass"; Y. Okawachi, M. Yu, J. K. Jang, X. Ji, Y. Zhao, B. Y. Kim, M. Lipson, and A. L. Gaeta; Nature Comm. 11, 4119 (2020).

"Depth Field Imaging Apparatus, Methods, and Applications"; S.Jayasuriya, A.Molnar, S.Sivaramakrishnan; 6955-09-US, United States, Filed, CON, 2/21/20, 16/797,251; 6955-03-US, United States, Issued, 8/30/17, 15/554,550, 3/31/20, 10/605,916.

"Depth Field Imaging Apparatus, Methods, and Applications"; S.Jayasuriya, A.Molnar, S.Sivaramakrishnan; 6955-06-JP, Japan, Issued, 9/15/17, 2017-548977, 6/23/20, 6722194.

"Design principles for achieving record-low surface roughness of stoichiometric Nb3Sn superconductors via electrochemical deposition"; Z. Sun, R. D. Porter, K. D. Dobson, K. Howard, T. Oseroff, M. Ge, N. Sitaraman, M. Kelly, X. Deng, A. Connolly, M. O. Thompson, J. Sethna, T. Arias, and M. U. Liepe; Center of Bright Beam Annual Meeting, Zoom, June 2020.

"Design, Fabrication, Characterization and Modeling of CMOS-Compatible PtSe2 MOSFETs"; Xiong, K.; Lehigh University Ph.D. Thesis, 2020.

"Detection of some amino acids with modulation-doped and surface-nanoengineered GaAs Schottky P-I-N diodes"; T.Alkhidir, M.Abi Jaoude, D.Gater, C.Alpha, and A.Isakovic; Journal of Vacuum Science and Technology B 38, 054002 (2020); https://doi.org/10.1116/6.0000186.

"Development of a Pull-In Free Electrostatic MEMS Microphone"; M Ozdogan; State University of New York at Binghamton, Ph.D. Thesis, 2020. 27993391.

"Development of isoporous microslit silicon nitride membranes for sterile filtration applications"; Wright, E.; Miller, J.J.; Csordas, M.; Gosselin, A.; Carter, J.; McGrath, J.; Latulippe, D.; Roussie, J.; Biotechnology and Bioengineering, 117, 3, 879-885.

"Devices and Methods for Data Communications and Sensing"; H.An, M.Daniel, X.Liu, R.Shepherd; 9470-01-US, United States, Filed, EPR - Enhanced Provisional, 6/15/20, 63/039,413.

"Devices for Terahertz Signal Generation and Transmitter"; E.Afshari, R.Han; 6475-03-US, United States, Issued, 8/21/17, 15/552,339, 3/10/20, 10,587,223.

"Differential Monocyte Actuation in a Three-Organ Functional Innate Immune System-on-a-Chip"; T. Sasserath, J. W. Rumsey, C. W. McAleer, L. R. Bridges, C. J. Long, D. Elbrecht, F. Schuler, A. Roth, C. Bertinetti-LaPatki, M. L. Shuler, J. J. Hickman; Advanced Science 7,2000323, DOI: 10.1002/advs.202000323.

"Direct comparison of optical and electron microscopy methods for structural characterization of extracellular vesicles"; Noble, J.; Roberts, L.; Vidavsky, N.; Chiou, A.; Fischbach, C.; Paszek, M.; Estroff, L.; Kourkoutis, L.; Journal of Structural Biology, Volume 210, Issue 1, 1 April 2020, 107474.

"Disjoining Pressure of Water in Nanochannels"; A.Zou, S.Poudel, and S.Maroo; arXiv:2010.09928 [Sub. 19 Oct 2020].

"Distributed-feedback blue laser diode utilizing a tunnel junction grown by plasma-assisted molecular beam epitaxy"; Muziol, G.; Hajdel, M.; Turski, H.; Nomoto, K.; Siekacz, M.; Nowakowski-Szkudlarek, K.; Żak, M.; Jena, D.; Xing, H. G.; Perlin, P.; Optics Express Vol. 28, Issue 23, pp. 35321-35329 (2020), https://doi.org/10.1364/OE.405994.

"Down Regulation of SIRT2 Reduced ASS Induced NSCLC Apoptosis Through the Release of Autophagy Components via Exosomes"; L.Wang, P.Xu, X.Xie, F.Hu, L.Jiang, R.Hu, F.Ding, H.Xiao and H.Zhang; Frontiers in Cell Dev. Biol., 03 December 2020 | https://doi.org/10.3389/fcell.2020.601953.

"Droplet Evaporation on Porous Nanochannels for High Heat Flux Dissipation"; S.Poudel, A.Zou, and S.Maroo; ACS Appl. Mater. Interfaces 2021, 13, 1, 1853-1860, December 28, 2020, https://doi.org/10.1021/acsami.0c17625.

"Droplet-Coupled Wicking in Nanochannels with Micropores"; S.Poudel, A.Zou, S.Maroo; 73rd Annual Meeting of the APS Division of Fluid Dynamics 2020, Nov 22, 24, 2020; Session U08: Microscale Flows: Interfaces and Wetting.

"e-Synch: an automated controlled release device for livestock management"; D.Erickson, J.Giordano, M.Masello, Y.Ren; 9391, Invention, Filed by Cornell.

"Effect of flagellar beating pattern on sperm rheotaxis and boundary-dependent navigation"; Zaferani, M.; Javi, F.; Mokhtare, A.; Abbaspourrad, A.; bioRxiv, Posted January 21, 2020, doi: https://doi.org/10.1101/2020.01.20.913145.

"Effects of Surface Topography on Bacterial Biofilm Formation"; Lee, S.; Syracuse University, Ph.D. Thesis, 2020. 28088082.

"Efficient high-pass filtering with practical, high-yield x-ray transmission mirror optics"; DN Agyeman-Budu, JD Brock, AR Woll; Powder Diffraction, Published online by Cambridge University Press: 29 April 2020.

"Egg-Like Multi-Volume Microchamber-based Microfluidic (EL-MVM2) platform for Bacterial Antimicrobial Susceptibility Testing"; A.Abbaspourrad, M.Azizi; 9528-01-US, United States, MPR - Manuscript Provisional, Filed, 12/23/20, 63/130,161.

"Electrical and Thermal Transport through Silver Nanowires and Their Contacts: Effects of Elastic Stiffening"; Y.Zhao, M.Fitzgerald, Y.Tao, Z.Pan, G.Sauti, D.Xu, Y.Xu, and D.Li; Nano Letters, 2020, 20, 10, 7389-7396. DOI: 10.1021/acs.nanolett.0c02014.

"Electrically Programmable Micro-Scale Shape Memory Devices"; Q.Liu, W.Wang, M.Reynolds, M.Miskin, M.Cao, D.Muller, P.McEuen, I.Cohen; APS March Mtg 2020, 65, 1; X22.00010: Robophysics IV and Animal Behavior; March 2020.

"Electro-Ultrasonic Devices for Nerve Stimulation and Treatment"; A.Lal; 7004-02-US, United States, Issued, 3/16/16, 15/072,232, 8/11/20, 10,371,124.

"Electrochemical deposition for generating Nb3Sn films with low surface roughness and stoichiometry"; Z.Sun, R.Porter, Z.Baraissov, K.Dobson, N.Sitaraman, M.Kelly, K.Howard, T.Oseroff, M.Ge, X.Deng, A.Hire, A.Connolly, M.Thompson, R.Hennig, J.Sethna, D.Muller, T.Arias, M.Liepe; Int'l Workshop on Nb3Sn SRF Science, Technology, & Apps, Nov 2020.

"Electronic nematicity in Sr2RuO4"; Wu, J.; Nair, H.; Bollinger, A.; He, X.; Robinson, I.; Schreiber, N.; Shen, K.; Schlom, D.; Božović, I.; PNAS, 117, 20, 10654-10659.

"Electronically Coupled 2D Polymer/MoS2 Heterostructures"; H.B. Balch, A.M. Evans, R.R. Dasari, H. Li, R. Li, S. Thomas, D. Wang, R.P. Bisbey, K. Slicker, I. Castano, S. Xun, L. Jiang, C. Zhu, N. Gianneschi, D.C. Ralph, J.-L. Brédas, S.R. Marder, W.R. Dichtel, and Feng Wang; Journal of the American Chemical Society, 142, 50, 21131-21139; December 7, 2020; https://doi.org/10.1021/jacs.0c10151.

"Electronically integrated, mass-manufactured, microscopic robots"; M.Miskin, A.Cortese, K.Dorsey, E.Esposito, M.Reynolds, Q.Liu, M.Cao, D.Muller, P.McEuen and I.Cohen; Nature, volume 584, pages 557-561 (Published: 26 August 2020).

"Electroplating of Sn Film on Nb Substrate for Generating Nb3Sn Thin Films and Post Laser Annealing"; Sun, Z.; Liepe, M.; Oseroff, T.; Porter, R. D.; Arias, T.; Sitaraman, N.; Connolly, A.; Scholtz, J.; Thompson, M.; 19th Int. Conf. on RF Superconductivity SRF2019, Germany, JACoW Pub, ISBN: 978-3-95450-211-0 doi:10.18429/JACoW-SRF2019-MOP014.

"Electropolymerization onto Flexible Substrates for Electronic Applications"; H.Abruna, S.Conte, K.Hernandez-Burgos, W.Li, D.Ralph, N.Ritzert, G.Rodriguez-Calero, C.Tan; 6272-03-US, United States, Issued, 9/30/16, 15/301,085, 3/17/20, 10,591,435.

"Embryonic Stem Cell-Derived Extracellular Vesicles Maintain ESC Stemness by Activating FAK"; Y.Hur, S.Feng, K.Wilson, R.Cerione, M.Antonyak; Developmental Cell, 56, 3, 8 February 2021, 277-291.e6, https://doi.org/10.1016/j.devcel.2020.11.017.

"Energy Harvesting Using Raindrops Through Solar Panels: A Review"; Shetty, S.; Kishore, V.; Pinto, S.; Bommegowda, K.; Advances in Communication, Signal Processing, VLSI, and Embedded Systems, Springer, 289-298.

"Energy-Efficient Ultrafast SOT-MRAMs Based on Low-Resistivity Spin Hall Metal Au0.25Pt0.75"; Zhu, L.; Zhu, L.; Shi, S.; Ralph, D.; Buhrman, R.; Adv Electronic Mats, 6, 2, 1901131.

"Engineering spin and orbital states in diamond using a mechanical resonator"; G.D.Fuchs; Quantum Huddle Seminar, Harvard University, 8/3/2020; Virtual Photonics for Quantum 2, RIT, 6/23/2020; Princeton GIA Diamond Symposium 1/24/2020.

"Enhanced injection efficiency and light output in bottom tunnel-junction light-emitting diodes"; S.Bharadwaj, J.Miller, K.Lee, J.Lederman, M.Siekacz, H.G.Xing, D.Jena, C.Skierbiszewski, and H.Turski; Optics Express Vol. 28, Issue 4, pp. 4489-4500 (2020), https://doi.org/10.1364/OE.384021.

"Enhanced nonlinear light generation in oligomers of silicon nanoparticles under vector beam illumination"; Kroychuk, M.; Shorokhov, A.; Yagudin, D.; Shilkin, D.; Smirnova, D.; Volkovskaya, I.; Shcherbakov, M.; Shvets, G.; Fedyanin, A.; Nano Letters, 20, 5, 3471-3477.

"Enhancement-mode ion-based transistor as a comprehensive interface and real-time processing unit for in vivo electrophysiology"; Cea, C.; Spyropoulos, G.; Jastrzebska-Perfect, P.; Ferrero, J.; Gelinas, J.; Khodagholy, D.; Nature Materials, 19, 6, 679-686.

"Enthalpy and entropy of oxygen electroadsorption on RuO2 (110) in alkaline media"; Hu, B.; Kuo, D.; Paik, H.; Schlom, D.; Suntivich, J.; The Journal of Chemical Physics, 152, 9, 94704.

"Epitaxial stabilization of rutile germanium oxide thin film by molecular beam epitaxy"; S. Chae, H. Paik, N. M. Vu, E. Kioupakis, and J. T. Heron; Applied Physics Letters 117, 072105 (2020); https://doi.org/10.1063/5.0018031 (editors pick).

"Evaporation Dynamics in Buried Nanochannels with Micropores"; Poudel, S.; Zou, A.; Maroo, S.; Langmuir 2020, 36, 27, 7801-7807, https://doi.org/10.1021/acs.langmuir.0c00777.

"Exchange magnetostriction in two-dimensional antiferromagnets"; S. Jiang, H. Xie, J. Shan, and K.F. Mak; Nature Materials, volume 19, pages 1295-1299 (2020).

"Experimental and Numerical Investigation of Evaporation Dynamics in Nanochannels With Micropores"; S.Poudel, A.Zou, S.Maroo; ASME 2020 Summer Heat Transfer Conference, 13th 15th July 2020, Orlando, FL.

"Experimental and numerical local heat transfer study on micro pin fin with tip clearance"; Ha.Tabkhi, A.Nayebzadeh, Y.Peles; Applied Thermal Engineering, Volume 179, October 2020, 115756, https://doi.org/10.1016/j.applthermaleng.2020.115756.

"Experimental demonstration of broadband solar absorption beyond the lambertian limit in certain thin silicon photonic crystals"; M.Hsieh, A.Kaiser, S.Bhattacharya, S.John, and S.Lin; Scientific Reports 10 11857 (2020).

"Expitaxial Semiconductor/Superconductor Heterostructures"; B.Downey, D.Jena, D.Katzer, G.Khalsa, D.Meyer, N.Nepal, J.Wright, H.G.Xing, R.Yan; 8152-03-US, United States, US from PCT, Filed, 9/4/20, 16/978,415.

"Exploring the intrinsic limit of the charge-carrier-induced increase of the Curie temperature of Lu-and La-doped EuO thin films"; R.Held, T.Mairoser, A.Melville, J. Mundy, M.Holtz, D.Hodash, Z.Wang, J.Heron, S.Dacek, B.Holländer, D.Muller, and D.Schlom; Phys. Rev. Mats 4, 104412 - 20 October 2020.

"Externally driven nonlinear time-variant metasurfaces"; V.Zubyuk, P.Shafirin, M.Shcherbakov, G.Shvets, A.A. Fedyanin; arXiv:2012.06604 [physics.optics] [Submitted on 11 Dec 2020].

"Extracellular vesicles in plasma before and after exercise"; Giloteaux L; 2020 Myalgic Encephalomyelitis/Chronic Fatigue Syndrome All-Centers Research Consortium Meeting October 6-7 2020. Ithaca, NY.

"Fabrication of Injectable Micro-Scale Opto-Electronically Transduced Electrodes (MOTEs) for Physiological Monitoring"; S.Lee; A.J.Cortese; A.Mok; C.Wu; T.Wang; J.U.Park; C.Smart; S.Ghajari; D.Khilwani; S.Sadeghi; Y.Ji; J.H.Goldberg; C.Xu; P.L.McEuen; A.C.Molnar; Journal of Microelectromechanical Systems, vol. 29, no. 5, pp. 720-726, Oct. 2020, doi: 10.1109/JMEMS.2020.2999496.

"Fiber Optical Parametric Chirped-Pulse Amplification (FOPCPA)"; W.Fu, F.Wise; 7948-02-US, United States, Issued, 4/1/19, 16/372,226, 12/22/20, 10,873,172.

"Fibrotic Cell-ECM Interactions Regulate Breast Cancer Stem-Like Behavior via Altering Cell Metabolism"; A Shimpi, M Tan, E Moore, M Paszek, C Fischbach; Physical Science of Oncology Network (PSON) Annual Investigator Meeting. Poster Presentation: Virtual 23-25 September 2020; Biomedical Engineering Society (BMES) Annual Meeting. Oral Presentation: Virtual 14-17 October 2020.

"Fighting Broken Symmetry with Doping: Toward Polar Resonant Tunneling Diodes with Symmetric Characteristics"; Encomendero, J.; Protasenko, V.; Rana, F.; Jena, D.; Xing, H.G.; Physical Review Applied, 13, 3, 34048.

"Fingerprints of the Strong Interaction between Monolayer MoS2 and Gold"; Velicky, M.; Rodriguez, A.; Bousa, M.; Krayev, A.; Vondracek, M.; Honolka, J.; Ahmadi, M.; Donnelly, G.; Huang, F.; Abruna, H.; arXiv preprint arXiv:2004.07133.

"Flow boiling in microchannel with synthetic jet in cross-flow"; Sourtiji, E.; Peles, Y.; International Journal of Heat and Mass Transfer, 147, 119023.

"Frequency-Domain Quantum Interference with Correlated Photons from an Integrated Microresonator"; C. Joshi, A. Farsi, A. Dutt, B. Y. Kim, X. Ji, Y. Zhao, A. M. Bishop, M. Lipson, and A. L. Gaeta; Phys. Rev. Lett. 124 (14), 143601 (2020); CLEO, OSA Technical Digest (2020), paper FTu4C.6.

"Fully transparent field-effect transistor with high drain current and on-off ratio"; Park, J.; Paik, H.; Nomoto, K.; Lee, K.; Park, B.; Grisafe, B.; Wang, L.; Salahuddin, S.; Datta, S.; Kim, Y.; APL Materials, 8, 1, 11110.

"Gallium nitride tunneling field-effect transistors exploiting polarization fields"; Chaney, A.; Turski, H.; Nomoto, K.; Hu, Z.; Encomendero, J.; Rouvimov, S.; Orlova, T.; Fay, P.; Seabaugh, A.; Xing, H.G.; Applied Physics Letters, 116, 7, 73502.

"GaN HEMTs on Si With Regrown Contacts and Cutoff/Maximum Oscillation Frequencies of 250/204 GHz"; L.Li, K.Nomoto, M.Pan, W.Li, A.Hickman, J.Miller, K.Lee, Z.Hu, S.Bader, S.Lee, J.Hwang, D.Jena, and H.G.Xing; IEEE Electron Device Letters, Vol. 41, No. 5, May 2020.

"GaN Power Electronics and Associated Fundamental Limits"; H.G.Xing, W.Li, K.Nomoto, and D.Jena; ECS Meeting Abstracts, Volume MA2020-02, G03: SiGe, Ge, and Related Compounds: Materials, Processing, and Devices (Invited).

"Generative Critique in Interdisciplinary Collaborations: From Critique in and of the Neurosciences to Socio-Technical Integration Research as a Practice of Critique in R (R) I"; Smolka, M. (References the work of Ana Viseu, CNF Staff); NanoEthics volume 14, pages 1-19 (2020).

"GHz-THz Ultrasonics and Optics for Neurotechnology Devices, Methods and Applications"; A.Lal, A.Singh, C.Xu; 8282-03-US, United States, US from PCT, Filed, 11/24/20, 17/058,237.

"Giant Enhancement of Spin-Orbit Torque by Interface Scattering from Ultra-thin Insertion Layers"; R.Buhrman, L.Zhu; 8546-02-US, United States, Filed, US from PRV, 3/16/20, 16/820, 496.

"Graphene-based membrane and method of preparation thereof"; S.Garaj, S.Hong; US Patent App. 16/854,176, 2020-09-03 Publication of US20200276543A1.

"Guiding Principles for Trench Schottky Barrier Diodes Based on Ultrawide Bandgap Semiconductors: A Case Study in Ga2O3"; W. Li, K. Nomoto, Z. Hu, D. Jena and H. G. Xing; IEEE Transactions on Electron Devices, vol. 67, no. 10, pp. 3938-3947, Oct. 2020, doi: 10.1109/TED.2020.3003292.

"Heat Transfer Characterization of Supercritical Carbon Dioxide in Microchannel"; Asadzadehmehdialghadami, M.; University of Central Florida Electronic Theses and Dissertations 2020, 170, https://stars.library.ucf.edu/etd2020/170.

"HI-Light: A Glass-Waveguide-Based"Shell-and-Tube" Photothermal Reactor Platform for Converting CO2 to Fuels"; X.Cao, Y.Kaminer, T.Hong, P.Schein, T.Liu, T.Hanrath, D.Erickson; iScience, Vol 23, 12, 101856, December 18, 2020, https://www.cell.com/iscience/fulltext/S2589-0042(20)31053-1.

"High harmonic optomechanical oscillations in the lithium niobate photonic crystal nanocavity"; H.Jiang, X.Yan, H. Liang, R.Luo, X.Chen, Y.Chen, and Q.Lin; Applied Physics Letters 117, 081102 (2020); https://doi.org/10.1063/5.0016334.

"High Sensitivity Magnet-Tipped Cantilevers and Micrometer-Scale Coplanar Waveguides to Enable Nanoscale Magnetic Resonance Imaging"; P.Nasr; Cornell University, Ph.D. Thesis, 2020. 13806681.

"High-Harmonic Synchronization of Optomechanical Oscillators"; C.Rodrigues, C.Kersul, M.Lipson, T.Alegre, and G.Wiederhecker; CLEO, OSA Technical Digest, paper JW2B.27. https://www.osapublishing.org/abstract.cfm?URI=CLEO_AT-2020-JW2B.27.

"How a raindrop gets shattered on biological surfaces"; Kim, S.; Wu, Z.; Esmaili, E.; Dombroskie, J.; Jung, S.; Proc of the National Academy of Sciences, June 23, 2020, V117, 25, 13901-13907; https://PNAS.altmetric.com/details/83683010/news.

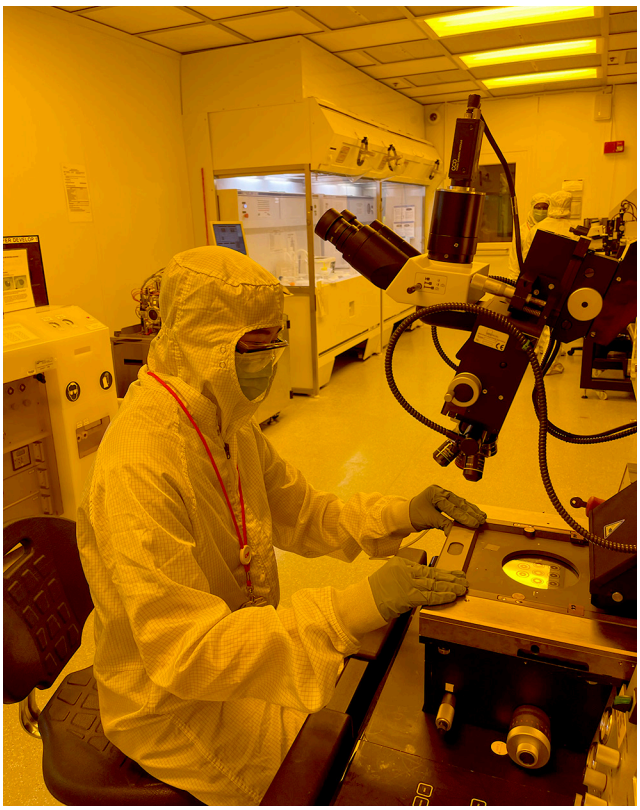

"HP-Bio: High Pressure BioSAXS for Deep Life and Extreme Biophysics"; R.Gillilan; American Crystallographic Association Session 2.1.4 Fronteirs in SAS - Aug 3/2020. (online).

"Hybrid PZT Lateral Bimorphs and 3D-Printed Spring-Mass Resonators for Battery-Less RF Transmission and Vibration Identification"; V.Pinrod; S.Gupta; S.Nadig; A.Ruyack; B.Davaji; A.Lal; IEEE Internet of Things Journal, vol. 8, no. 6, pp. 5009-5022, 15 March15, 2021, doi: 10.1109/JIOT.2020.3036872.

"Impact of Residual Carbon on Avalanche Voltage and Stability of Polarization-Induced Vertical GaN pn Junction"; E.Fabris, C. De Santi, A.Caria, K.Mukherjee, K.Nomoto, Z.Hu, W.Li, X.Gao, H.Marchand, D.Jena, ; IEEE Transactions on Electron Devices, 67, 10, 3978-3982, Oct 2020, doi: 10.1109/TED.2020.2993192.

"Implantation and extraction of penetrating electrode arrays in minipig retinas"; Chen, J.; Poulaki, V.; Kim, S.; Eldred, W.; Kane, S.; Gingerich, M.; Shire, D.; Jensen, R.; DeWalt, G.; Kaplan, H.; Translational Vision Science & Technology April 2020, Vol.9, 19. doi:https://doi.org/10.1167/tvst.9.5.19.

"In situ Sensing of Water Potential"; M.Gore, P.Jain, D.Pauli, A.Stroock, O.Vincent; 7532-03-US, United States, Filed, US from PCT, 1/28/20, 16/634,665.

"In vitro modeling of solid tumor interactions with perfused blood vessels"; T.Kwak, E.Lee; Scientific Reports 10, 20142 (2020). https://doi.org/10.1038/s41598-020-77180-1; bioRxiv, Posted August 03, 2020, doi: https://doi.org/10.1101/2020.08.03.234633.

"Incoherent Cooper pairing and pseudogap behavior in single-layer FeSe/SrTiO3"; B.Faeth, S.Yang, J.Kawasaki, J.Nelson, P.Mishra, L.Chen, D.Schlom, K.Shen; arXiv:2010.11984 [cond-mat.supr-con] [Submitted on 22 Oct 2020].

"Infrared spectroscopy of live cells from a flowing solution using electrically-biased plasmonic metasurfaces"; Kelp, G.; Li, J.; Lu, J.; DiNapoli, N.; Delgado, R.; Liu, C.; Fan, D.; Dutta-Gupta, S.; Shvets, G.; Lab on a Chip, Issue 12, 2020.

"Insulated nanoelectrode-nanopore devices and related methods"; M.Drndic, K.Healy, V.Ray, L.Willis, N.Peterman, J.Bartel; US Patent US10876157B2, 2020-12-29 Application granted.

"Integrated Circuits Based Biosensors"; V.Gund, A.Lal; 6595-04-EP, Issued, 8/29/16, 15739947.8, 9/9/20, 3100024; 6595-05-DE, Issued, 8/29/16, 6.02015E+11, 9/9/20, 3100024; 6595-06-GB, Issued, 8/29/16, EP15739947.8, 9/9/20, 3100024.

"Integrated electronics on the aluminum nitride platform"; R.Chaudhuri, A.Hickman, J.Hwang, D.Jena, H.G.Xing; 9692-01-US, United States, MPR, Filed, 12/19/20, 63/128,044; 9692, Filed by Cornell, 11/19/20, Invention.

"Integrated near-field thermo-photovoltaics for heat recycling"; Bhatt, G.; Zhao, B.; Roberts, S.; Datta, I.; Mohanty, A.; Lin, T.; Hartmann, J.; St-Gelais, R.; Fan, S.; Lipson, M.; Nature communications, 11, 1, 1-7.

"Interfacial Dzyaloshinskii-Moriya interaction and spin-orbit torque in Au1-xPtx/Co bilayers with varying interfacial spin-orbit coupling"; L.Zhu, X.Ma, X.Li, R.Buhrman; arXiv:2007.09817 [cond-mat.mtrl-sci] [v1] Sun, 19 Jul 2020 23:28:04 UTC.

"Investigation of Thin Film Evaporation in Nanochannels Sample Using Surface Heating"; S.Poudel, A.Zou, S.Maroo; American Society of Mechanical Engineers 2020 Summer Heat Transfer Conference July 2020, Orlando, FL.

"Iron and nitrogen-doped double gyroid mesoporous carbons for oxygen reduction in acidic environments"; F.Matsuoka, K.Fritz, P.Beaucage, F.Yu, J.Suntivich, and U.Wiesner; J. of Physics: Energy, Volume 3, Number 1; Published 12 November 2020.

"Kinetics of all-dry free radical polymerization under nano-confinement"; Cheng Y., Khlyustova A., Chen P., Yang R.; Macromolecules, V53, 24, Dec 2020. https://doi.org/10.1021/acs.macromol.0c01534 — COVER.

"Lamin B2 follows lamin A/C-mediated nuclear mechanics and cancer cell invasion efficacy"; M.Vortmeyer-Krause, M.te Lindert, J.te Riet, V.te Boekhorst, R.Marke, R.Perera, P.Isermann, T.van Oorschot, M.Zwerger, F.Yang, M.Svoreň, A.Madzvamuse, J.Lammerding, P.Friedl, K.Wolf; bioRxiv, doi: https://doi.org/10.1101/2020.04.07.028969.

"Large-Scale Fabrication of Submicrometer-Gate-Length MOSFETs With a Trilayer PtSe2 Channel Grown by Molecular Beam Epitaxy"; Xiong, K.; Hilse, M.; Li, L.; Göritz, A.; Lisker, M.; Wietstruck, M.; Kaynak, M.; Engel-Herbert, R.; Madjar, A.; Hwang, J.; IEEE Trans on Electron Devices, 67, 3, 796-801.

"Large-scale optical phased array using a low-power multi-pass silicon photonic platform"; S. A. Miller, Y. C. Chang, C. T. Phare, M. C. Shin, M. Zadka, S. P. Roberts, B. Stern, X. Ji, A. Mohanty, O. A. J. Gordillo, U. Dave, M. Lipson; Optica 7 (1), 3-6 (2020).

"Light Field Image Sensor, Method and Applications"; P.Gill, A.Molnar, A.Wang; 4895-06-EP, Europe, Issued, 4/25/13, 11837049.3, 6/17/20, 2633277; 4895-08-BE, Belgium, Issued, 10/27/11, EP11837049.3, 6/17/20, EP2633277; 4895-09-FR, France, Issued, 10/27/11, EP11837049.3, 6/17/20, EP2633277; 4895-10-DE, Germany, Issued, 10/27/11, EP11837049.3, 6/17/20, EP2633277; 4895-11-GB, United Kingdom, Issued, 10/27/11, EP11837049.3, 6/17/20, EP2633277.

"Light-emitting diodes with AlN polarization-induced buried tunnel junctions: A second look"; K.Lee, S.Bharadwaj, Y.Shao, L.van Deurzen, V.Protasenko, D.Muller, H.G.Xing, and D.Jena; APL 117, 061104 (2020); https://doi.org/10.1063/5.0015097.

"Lithium Niobate Optomechanical Disk Resonators"; R.Wang; S.Bhave; 2020 Joint Conference of the IEEE IFCS-ISAF, Keystone, CO, USA, 2020, pp. 1-4, doi: 10.1109/IFCS-ISAF41089.2020.9264025.

"Lithium niobate photonic-crystal electro-optic modulator"; Li, M.; Ling, J.; He, Y.; Javid, U.; Xue, S.; Lin, Q.; arXiv preprint arXiv:2003.03259.

"Lithium niobate photonic-crystal electro-optic modulator"; M.Li, J.Ling, Y.He, U.Javid, S.Xue and Q.Lin; Nature Communications volume 11, Article number: 4123 (2020) https://doi.org/10.1038/s41467-020-17950-7.

"Local magnetic measurements of few-layer superconducting MoS2"; Jarjour, A.; Schaefer, B.; Ferguson, G.; Lee, M.; Nowack, K.; Bulletin of the American Physical Society, APS March Meeting 2020, Vol.65, 1, March 2-6, 2020; Denver, CO.

"Local Photothermal Control of Phase Transitions for On-Demand Room-Temperature Rewritable Magnetic Patterning"; Mei, A.; Gray, I.; Tang, Y.; Schubert, J.; Werder, D.; Bartell, J.; Ralph, D.; Fuchs, G.; Schlom, D.; Adv.Mats, 32, 22, 2001080.

"Low-loss composite photonic platform based on 2D semiconductor monolayers"; Datta, I.; Chae, S.; Bhatt, G.; Tadayon, M.; Li, B.; Yu, Y.; Park, C.; Park, J.; Cao, L.; Basov, D.; Nature Photonics, 14, 4, 256-262.

"Lymphoidal chemokine CCL19 promoted the heterogeneity of the breast tumor cell motility within a 3D microenvironment revealed by a Lévy distribution analysis"; B.Kim, P.Hannanta-anan, A.Ryd, M.Swartz, M.Wu, Integrative Biology, 12, 1, 12-20.

"Magnetic devices including iron-rhodium films providing bi-stable magnetic order at room temperature, magnetic memory systems including the same and related methods of operation"; A.Mei, G.Fuchs, I.Gray; US patent 2020-12-10 Publication of US20200388750A1, application #16896787 (2020).

"Magnetic Etch-a-Sketch using the 1st-order phase transition in FeRh"; Gray, I.; Mei, A.; Tang, Y.; Schubert, J.; Werder, D.; Bartell, J.; Ralph, D.; Fuchs, G.; Schlom, D.; Bulletin of the APS, V.65, N.1; Abstract: G41.00005 Session G41: Magnetic Characterization and Imaging; March 2-6, 2020.

"Magnetic field detection limits for ultraclean graphene Hall sensors"; B.Schaefer, L.Wang, A.Jarjour, K.Watanabe, T.Taniguchi, P.McEuen and K.Nowack; Nature Communications volume 11, Article number: 4163 (2020), https://www.nature.com/articles/s41467-020-18007-5.

"Magnetically driven active topography for long-term biofilm control"; Gu, H.; Lee, S.; Carnicelli, J.; Zhang, T.; Ren, D.; Nature Communications volume 11, Article number: 2211 (2020), https://doi.org/10.1038/s41467-020-16055-5.

"Magneto-thermal microscopy of spin-torque switching and uncompensated moments in antiferromagnetic materials"; G.D.Fuchs; Online Spintronics Seminar Series, 4/7/2020.

"Making EuO multiferroic by epitaxial strain engineering"; V.Goian, R.Held, E.Bousquet, Y.Yuan, A.Melville, H.Zhou, V.Gopalan, P.Ghosez, N.Spaldin, D.Schlom, and S.Kamba; Communications Materials V1, Article number: 74 (2020), https://doi.org/10.1038/s43246-020-00075-1.

"Manipulation of the van der Waals Magnet Cr2Ge2Te6 by Spin-Orbit Torques"; V. Gupta, T.M. Cham, G.M. Stiehl, A. Bose, J. A. Mittelstaedt, K.F. Kang, S. Jiang, K.F. Mak, J. Shan, R. A. Buhrman, and D. C. Ralph; Nano Letters 20, 7482-7488 (2020).

"Materials and methods enabling two-dimensional junctions on three-dimensional particles"; P.Chen, X.Mao; 9684, Filed by Cornell, 11/13/20, Invention.

"Materials Combining Asymmetric Pore Structures with Well-Defined Mesoporosity for Energy Storage and Conversion"; S.Hesse, K.Fritz, P.Beaucage, R.P.Thedford, F.Yu, F.DiSalvo, J.Suntivich, and U.Wiesner; ACS Nano 2020, 14, 12, 16897-16906, Nov 25, 2020, https://doi.org/10.1021/acsnano.0c05903.

"Mechanical Stress Promotes Disassembly of the Antibiotic Efflux Complex MacAB-TolC"; C.Harper, W.Zhang, P.Chen, and C.Hernandez; Biophysical Society Annual Meeting, San Diego, California, February 17, 2020.

"Metabolic requirements for cell migration in confined 3D environments"; Bell ES, Isermann P, Courtney O, Garvey K, Gopalan T, Zuela-Sopilniak N, Zaragoza Rodrigues N, Zipfel WR, Lammerding J.; American Society for Cell Biology (ASCB) and European Molecular Biology Organization (EMBO) Cell Bio Virtual Meeting (Dec. 14-16, 2020).

"Metamaterial-Boosted Quantum Electromechanical Transducer for Microwave-Optical Interfacing"; M.LaHaye, and B.Plourde; US Patent Application 16/898,843, 2020.

"Metasurface-enhanced infrared spectroscopy for continuously monitoring the effect of cholesterol depletion in live cells"; Huang, S.; Delgado, R.; Shvets, G.; Biomedical Vibrational Spectroscopy 2020: Adv in Research and Industry, Int'l Society for Optics and Photonics, 11236, 112360P; SPIE proceedings, 11236, 112360P 7 pp. (2020), DOI: 10.1117/12.2547141.

"Method and Device for Evaluation of Local Tissue's Biological or biomechanical Character"; J.Butcher, R.Gould; 4443-04-US, United States, CON - Continuation, Filed, 11/2/20, 17/086,621.

"Method for removing re-sputtered material from patterned sidewalls"; D.Lishan, K.Dorsey, V.Genova; Application #: 62949653, October 28, 2020 / non-provisional patent application.

"Methods and Systems for Near-Field Coherent Sensing"; X.Hui, E.Kan; 7785-06-EP, Europe, Filed, EPC, 1/13/20, 18818131.7; 7785-07-CN, China, Filed, FOR - Foreign, 2/16/20, 2.02E+11.

"Micro-fabrication of components for a high-density sub-retinal visual prosthesis"; D.Shire, M.Gingerich, P.Wong, M.Skvarla, S.Cogan, J.Chen, W.Wang, and J.Rizzo; Micromachines 2020, 11(10), 944; https://doi.org/10.3390/mi11100944.

"Microfluidic Device for Analysis of Sperm Motility, and Methods of Use"; A.Abbaspourrad, M.Azizi, M. Yaghoobi; 9698-01-US, United States, MPR, Filed, 12/23/20, 63/130,142.

"Microresonator Based Discrete- and Continuous-Variable Quantum Sources on Silicon-Nitride"; Y. Zhao, Y. Okawachi, B. Y. Kim, C. Joshi, J. K. Jang, A. Farsi, X. Ji, M. Lipson, and A. L. Gaeta; OSA Quantum 2.0 Conference, M. Raymer, C. Monroe, and R. Holzwarth, eds., OSA Technical Digest (Optical Society of America, 2020), paper QM4B.3.

"Microscale Combustion for High Density Soft Actuation"; C.Aubin, R.Heisser, R.Shepherd; 8847-02-US, United States, US from PRV, Filed, 8/19/20, 16/997,929.

"Microscopic sensors using optical wireless integrated circuits"; A.J. Cortese, C.L. Smart, T. Wang, M.F. Reynolds, S.L. Norris, Y. Ji, S. Lee, A. Mok, C. Wu, F. Xia, N.I. Ellis, A.C. Molnar, C. Xu, and P.L. McEuen; Proceedings of the National Academy of Sciences April 28, 2020 117 (17) 9173-9179; first published April 17, 2020 https://doi.org/10.1073/PNAS.1919677117.

"MINI - A high throughput, portable diagnostic system and LAMP Assay for SARS-CoV-2"; J.Boza, D.Erickson, D.McCloskey; 9581-01-US, United States, MPR - Manuscript Provisional, Filed, 10/6/20, 63/088,116; 9581, Filed by Cornell, 8/13/20, Invention.

"Miniature MEMS: Novel Key Components Toward Terahertz Reconfigurability"; Demir, K.; Unlu, M.; Journal of Microelectromechanical Systems, vol. 29, no. 4, pp. 455-467, Aug. 2020, doi: 10.1109/JMEMS.2020.2992491.

"Mixed Metal Oxide Compounds and Electrocatalytic Compositions, Devices and Processes using the Same"; H.Abruna, F.DiSalvo, M.Murphy, R.Van Dover, R.Wakabayashi; 7413-03-US, United States, Issued, 11/19/18, 16/303,010, 12/29/20, 108,795,539.

"Mixed-conducting particulate composites for soft electronics"; Jastrzebska-Perfect, P.; Spyropoulos, G.; Cea, C.; Zhao, Z.; Rauhala, O.; Viswanathan, A.; Sheth, S.; Gelinas, J.; Khodagholy, D.; Science Advances, 24 Apr 2020, Vol. 6, no. 17, eaaz6767, DOI: 10.1126/sciadv.aaz6767.

"Modeling and Characterization of a Pull-in Free MEMS Microphone"; Ozdogan, M.; Towfighian, S.; Miles, R.; IEEE Sensors Journal, 20, 12, 6314-6323.

"Molecular Beam Epitaxy Growth of Large-Area GaN/AlN 2D Hole Gas Heterostructures"; Chaudhuri, R.; Bader, S.; Chen, Z.; Muller, D.; Xing, H.G.; Jena, D.; physica status solidi (b), 257, 4, 1900567, Wiley Online Library.

"Monolithically p-down nitride laser diodes and LEDs obtained by MBE using buried tunnel junction design"; Turski, H.; Bharadwaj, S.; Siekacz, M.; Muziol, G.; Chlipala, M.; Zak, M.; Hajdel, M.; Nowakowski-Szkudlarek, K.; Stanczyk, S.; Xing, H.G.; Gallium Nitride Materials and Devices XV, International Society for Optics and Photonics, 11280, 1128010.

"Mott gap collapse in lightly hole-doped Sr2-xKxIrO4"; Nelson, J. N.; Parzyck, C. T.; Faeth, B. D.; Kawasaki, J. K.; Schlom, D. G.; Shen, K. M.; Nature Communications 11, 2597 (2020). https://doi.org/10.1038/s41467-020-16425-z.

"Multiferroic behavior confined by symmetry in EuTiO3 films"; Ryan, P. J.; Sterbinsky, G. E.; Choi, Y.; Woicik, J. C.; Zhu, Leyi; Jiang, J. S.; Lee, J. H.; Schlom, D. G.; Birol, T.; Brown, S. D.; arXiv preprint arXiv:2002.01996.

"Multiferroic behavior in EuTiO3 films constrained by symmetry"; Ryan, P. J.; Sterbinsky, G. E.; Choi, Y.; Woicik, J. C.; Zhu, Leyi; Jiang, J. S.; Lee, J.-H.; Schlom, D. G.; Birol, T.; Brown, S. D.; Physical Review B, 101, 18, 180409.

"Multiferroic LuFeO3 on GaN by molecular-beam epitaxy"; Casamento, J.; Holtz, M.; Paik, H.; Dang, P.; Steinhardt, R.; Xing, H.; Schlom, D.; Jena, D.; APL, 116, 10, 102901.

"Multiorgan microfluidic platform with breathable lung chamber for inhalation or intravenous drug screening and development"; Miller, P.; Chen, C.; Wang, Y.; Gao, E.; Shuler, M.; Biotechnology and Bioengineering, 117, 2, 486-497.

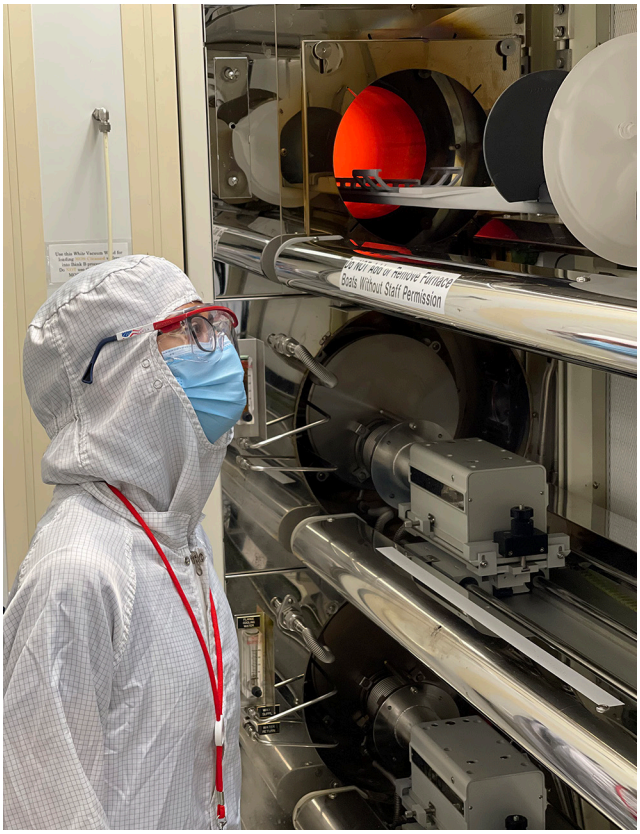

"Mutant lamins cause nuclear envelope rupture and DNA damage in skeletal muscle cells"; Earle, A.; Kirby, T.; Fedorchak, G.; Isermann, P.; Patel, J.; Iruvanti, S.; Moore, S.; Bonne, G.; Wallrath, L.; Lammerding, J.; Nature Materials, 19, 4, 464-473.

"N-polar GaN/AlN resonant tunneling diodes"; Cho, Y.; Encomendero, J.; Ho, S.; Xing, H.G.; Jena, D.; Applied Physics Letters 117, 143501 (2020); https://doi.org/10.1063/5.0022143.

"Nano within nano: Kinetics of vapor-phase free radical polymerization of nanolayers under nano-confinement"; Cheng Y., Khlyustova A., Chen P., Yang R.; 2020 Virtual AIChE Annual Meeting, November 16-20, 2020; https://www.aiche.org/conferences/aiche-annual-meeting/2020.

"Nanooze and Teaching Middle School STEM"; C.Batt; nanoHUB, https://nanohub.org/resources/34549.

"NanothermoMechanical AND and OR Logic Gates"; Hamed, A.; Ndao, S.; Scientific Reports, 10, 1, 1-8, DOI https://doi.org/10.1038/s41598-020-59181-2.

"Near-degenerate quadrature-squeezed vacuum generation on a silicon-nitride chip"; Y. Zhao, Y. Okawachi, J. K. Jang, X. Ji, M. Lipson, and A.Gaeta; Phys. Rev. Lett. 124 (19), 193601 (2020).

"Near-ideal reverse leakage current and practical maximum electric field in β-Ga2O3 Schottky barrier diodes"; Li, W.; Saraswat, D.; Long, Y.; Nomoto, K.; Jena, D.; Xing, H.G.; Applied Physics Letters, 116, 19, 192101.

"Negative Extinction and Broadband Light-matter Interactions in High-Q Time-variant Metasurfaces"; M.Shcherbakov, R.Lemasters, J.Song, P.Shafirin, T.Lian, H.Harutyunyan, and G.Shvets; CLEO OSA Technical Digest (2020), paper FTh4Q.1 https://doi.org/10.1364/CLEO_QELS.2020.FTh4Q.1.

"Net negative contributions of free electrons to the thermal conductivity of NbSe3 nanowires"; Z.Pan, L.Yang, Y.Tao, Y.Zhu, Y.Xu, Z.Mao and D.Li; Physical Chemistry 2020, 22, 21131-21138. DOI: 10.1039/d0cp03484c.

"New Approach Methodologies (NAMs) for Human-Relevant Biokinetics Predictions: Meeting the Paradigm Shift in Toxicology Towards an Animal-Free Chemical Risk Assessment"; A.Punt, H.Bouwmeester, B.Blaauboer, S.Coecke, B.Hakkert, D.Hendriks, P.Jennings, N.Kramer, S.Neuhoff, R.Masereeuw, A.Paini, A.Peijnenburg, M.Rooseboom, M.Shuler, I.Sorrell, B.Spee, M.Strikwold, A.van der Meer, M.van der Zande, M.Vinken, H.Yang, P.Bos, and M.Heringa; ALTEX 37 607-622, 2020; DOI 10.14573/altex2003242.

"Non-Linear Displacement Mechanisms of Thermally Actuated MEMS Chevron"; Hamed, A.; Ndao, S.; Journal of Microelectromechanical Systems, 29, 2, 255-259.

"Nuclear deformation causes DNA damage by increasing replication stress"; Shah, P.; Cheng, S.; Hobson, C.; Colville, M.; Paszek, M.; Superfine, R.; Lammerding, J.; bioRxiv, Posted June 13, 2020, doi: https://doi.org/10.1101/2020.06.12.148890.

"Obesity-associated Adipose Stromal Cells Promote Invasion of Premalignant Breast Cancer Cells"; L. Ling, J. Mulligan, Y. Ouyang, S. Adie, C. Fischbach; Physics of collective cell migration. Princeton, NJ, Jan 15-19, 2020; PS-ON Annual Investigators Meeting, Virtual meeting. Sept 21-23.

"Observation and nonlinear optical probing of flat band states in high-Q dielectric metasurfaces"; K.Okhlopkov, I.Antropov, A.Nazarenko, M.Shcherbakov, V.Bessonov, A.Rubtsov, G.Shvets, and A.Fedyanin; CLEO: Science and Innovations 2020, Washington, DC, May 2020; ISBN: 978-1-943580-76-7l Joint Poster Session 3 (JTu2D).

"Observation of Strong Bulk Damping-Like Spin-Orbit Torque in Chemically Disordered Ferromagnetic Single Layers"; L Zhu, X Zhang, D Muller, D Ralph; Adv Functional Mats for Organoids and Tissues, Special Issue, V 30, 48, 11/25/20; 2005201.

"On-Chip Squeezed-State Generation via Dual-Pumped Four-Wave Mixing"; Y. Zhao, Y. Okawachi, J. K. Jang, X. Ji, M. Lipson, and A. L. Gaeta; CLEO, OSA Technical Digest (Optical Society of America, 2020), paper FTu3C.2.

"On-Chip Synchronization of Kerr Frequency Combs"; J. K. Jang, X. Ji, C. Joshi, Y. Okawachi, M. Lipson, and A. L. Gaeta; CLEO, OSA Technical Digest (Optical Society of America, 2020), paper FTh3J.3.

"Onset and critical radius of heterogeneous bubble nucleation"; Gupta, M.; Zou, A.; Maroo, S.; APL, 116, 10, 103704.

"Operando Control of Skyrmion Density in a Lorentz Transmission Electron Microscope with Current Pulses"; Park, A.; Chen, Z.; Zhang, X.; Zhu, L.; Muller, D.; Fuchs, G.; Journal of Applied Physics 128, 233902 (2020); https://doi.org/10.1063/5.0020373.

"Optical beam steering by using tunable, narrow-linewidth butt-coupled hybrid lasers in a silicon nitride photonics platform"; Zhu, Y.; Zeng, S.; Zhu, L.; Photonics Research, 8, 3, 375-380.

"Optical Identification of Materials Transformations in Oxide TF"; D.Sutherland, A.Connolly, M.Amsler, M.Chang, K.Gann, V. Gupta, S.Ament, D.Guevarra, J.Gregoire, C.Gomes, R.van Dover, and M.Thompson; ACS Combinatorial Science, 22, 12, 887-894, Oct 2020, https://doi.org/10.1021/acscombsci.0c00172.

"Optical properties of metasurfaces infiltrated with liquid crystals"; A.Lininger, A.Zhu, J.Park, G.Palermo, S.Chatterjee, J.Boyd, F.Capasso, and G.Strangi; PNAS, August 25, 2020, 117 (34) 20390-20396; first published August 10, 2020; https://doi.org/10.1073/PNAS.2006336117.

"Optomechanical sensing in the nonlinear saturation limit"; Javid, U.; Rogers, S.; Graf, A.; Lin, Q.; arXiv preprint arXiv:2007.04279.

"Organ-on-a-chip systems: translating concept into practice"; Shuler, M.; Lab on a Chip, 2020, 20, 3072-3073 DOI: 10.1039/D0LC90083D (Editorial).

"Origin of Strong Two-Magnon Scattering in Heavy-Metal/Ferromagnet/Oxide Heterostructures"; Zhu, L.; Zhu, L.; Ralph, D. C.; Buhrman, R. A.; Physical Review Applied, 13, 3, 34038.

"Overcoming the Trade-Off Between Loss and Dispersion in Microresonators"; M. C. Zanarella, X. Ji, A. Mohanty, U. D. Dave, A. L. Gaeta, M. Lipson; CLEO OSA Technical Digest (2020), paper STh1J.1.

"Oxygen Incorporation in the Molecular Beam Epitaxy Growth of ScxGa1- xN and ScxAl1- xN"; Casamento, J.; Xing, H.G.; Jena, D.; physica status solidi (b), 257, 4, 1900612.

"Paper-Based Semi-Quantitative Antimicrobial Susceptibility Testing"; D.Erickson, R.Wang; 9575-01-US, United States, MPR - Manuscript Provisional, Filed, 9/15/20, 63/078,377; 9575, Filed by Cornell, 8/5/20, Invention.

"Path-Dependent Supercooling of the 3He Superfluid A-B transition"; D.Lotnyk, A.Eyal, N.Zhelev, A.Sebastian, A.Chavez, E.Smith, J.Saunders, E.Mueller, J.Parpia; arXiv:2012.14044 [cond-mat.supr-con] [Submitted 28 Dec 2020, revised 7 Jan 21.

"Pattern-forming Method and Radiation-sensitive Composition"; E.Giannelis, V.Kosma, C.Ober, K.Sakai; 8416-03-JP, Japan, FOR - Foreign, Filed, 12/16/20, 2020-53879.

"Perfect soliton crystals on demand"; Y He, J Ling, M Li, Q Lin; CLEO: Science and Innovations 2020, Washington, DC, 10-15 May 2020, ISBN: 978-1-943580-76-7; Laser & Photonics Reviews, 2020, 14, 8, https://doi.org/10.1002/lpor.201900339.

"Performance scaling of a 10-GHz solid-state laser enabling self-referenced CEO frequency detection without amplification"; L. M. Krüger, A. S. Mayer, Y. Okawachi, X. Ji, A. Klenner, A. R. Johnson, C. Langrock, M. M. Fejer, M. Lipson, A. L Gaeta, V. J. Wittwer, T. Südmeyer, C. R. Phillips and U. Keller; Optics Express 28, 12755-12770 (2020).

"Photoinitiated Transformation of Nanocrystal Superlattice Polymorphs Assembled at a Fluid Interface"; Y.Gao, J.Huang, D.Balazs, Y.Xu, T.Hanrath; Adv Materials Interfaces, V7, 21, Nov 5, 2020, 2001064, https://doi.org/10.1002/admi.202001064.

"Photonic Ising Spin-Glass via Chip-Based Degenerate Kerr Oscillators"; Y. Okawachi, M. Yu, J. K. Jang, X. Ji, Y. Zhao, M. Lipson, and A. L. Gaeta; CLEO, OSA Technical Digest (Optical Society of America, 2020), paper SM3L.2.

"Planar Lens for GHz Fourier Ultrasonics"; J Hwang, B Davaji, J Kuo, A Lal; 2020 IEEE International Ultrasonics Symposium (IUS), 7-11 Sept. 2020, DOI: 10.1109/IUS46767.2020.9251614.

"Platinum based surface electrochemical actuators"; I.Cohen, P.McEuen, M.Miskin; 9343, Invention, Filed by Cornell.

"Polymeric Sorbent Sheets Coupled to Direct Analysis in Real Time Mass Spectrometry for Trace-Level Volatile Analysis—A Multi-Vineyard Evaluation Study"; Bee-DiGregorio, M.Y.; Feng, H.; Pan, B.S.; Dokoozlian, N.K.; Sacks, G.L.; Foods, 9, 4, 409.

"Porous cage-derived nanomaterial inks for direct and internal three-dimensional printing"; T.Aubert, J.Huang, K.Ma, T.Hanrath, and U.Wiesner; Nature Comm V11, 4695 (2020).

"Preschool classroom environment, task engagement, and academic performance: the role of anxious solitude"; M.Reynolds Weber; University of Rochester Ph.D. Thesis 2020.

"Programmable Ultrasonic Field Driven Microfluidics"; J.Kuo, A.Lal, A.Ravi, A.Ruyack; 9170-02-US, United States, US from PRV, Filed, 10/7/20, 17/065,459.

"Progressive Sperm Separation Using Parallelized, High-Throughput, Microchamber-based Microfluidics"; M.Yaghoobi, M.Azizi, A.Mokhtare, A.Abbaspourrad; bioRxiv, Posted August 04, 2020, doi: https://doi.org/10.1101/2020.07.31.231373.

"Prospects for Wide Bandgap and Ultrawide Bandgap CMOS Devices"; S.Bader, H.Lee, R.Chaudhuri, S.Huang, A.Hickman, A.Molnar, H.G.Xing, D.Jena, H.Then, N.Chowdhury, T.Palacios; IEEE (67, 10, Oct. 2020), DOI: 10.1109/TED.2020.3010471.

"Pumpless, unidirectional microphysiological system for testing metabolism-dependent chemotherapeutic toxicity"; LaValley DJ, Miller PG, Shuler ML; Biotechnology Progress. 2020 Dec:e3105. DOI: 10.1002/btpr.3105.

"Quantitative Scanning Microwave Microscopy of Few-layer Platinum Diselenide"; X. Wang, K. Xiong, L. Li, J. C. M. Hwang, X. Jin, G. Fabi, M. Farina, O. Hartwig, M. Prechtl, G. S. Düsberg, A. Göritz, M. Wietstruck, M. Kaynak; European Microwave Conf. (EuMC), Utrecht, Netherlands, Jan. 2021, Proceedings pp. 987-990, DOI: 10.23919/EuMC48046.2021.9338192.

"Quantum Acoustic Control of Diamond Nitrogen-Vacancy Centers"; Chen, H.; Cornell University, Ph.D. Thesis, 2020. 27838358.

"Quantum Artificial Intelligence: Leveraging Microscopic Transport Phenomena for Beyond Von Neumann Computing"; Singh, C.N.; SUNY at Binghamton, Ph.D. Thesis, 2020. 28002984.

"Rapid multilayer microfabrication for modeling organotropic metastasis in breast cancer"; TJ Kwak, E Lee; Biofabrication, Volume 13, Number 1, 2020 IOP Publishing Ltd.

"Realization of Epitaxial Thin Films of the Topological Crystalline Insulator Sr3SnO"; Y.Ma, A.Edgeton, H.Paik, B.Faeth, C.Parzyck, B.Pamuk, S.Shang, Z.Liu, K.Shen, D.Schlom, C.Eom; Advanced Materials, Volume 32, Issue 34, August 27, 2020, https://doi.org/10.1002/adma.202000809.

"Recirculating Unidirectional Perfusion Flow Devices & Methods of Use Thereof"; M Shuler, Y Wang; Cornell Research Foundation US Patent 2020/0070165 A1, 3/5/20.

"Reconfigurable nanophotonic silicon probes for sub-millisecond deep-brain optical stimulation"; A.Mohanty, Q.Li, M.Tadayon, S.Roberts, G.Bhatt, E.Shim, X.Ji, J.Cardenas, S.Miller, A.Kepecs, M.Lipson; Nature Biomedical Engineering, 4, 2, 223-231.

"Resonantly-Driven Drop Contact-Line Mobility Measurement"; Paul Steen (deceased), Yi (James) Xia; 7616-02-US, United States, Issued, 7/18/18, 16/039,265, 9/8/20, 10,768,085.

"Robust Hybrid III-V/Si3N4 Laser with kHz-Linewidth and GHz-Pulling Range"; A. Gil-Molina, O. Westreich, Y. Antman, X. Ji, A. L. Gaeta, M. Lipson; CLEO, OSA Technical Digest (Optical Society of America, 2020), paper STu3M.4.

"Robust Miniature Pure-Phase Modulators at λ = 488 nm"; H. Huang, G. Liang, A. Mohanty, X. Ji, M.C. Shin, M. Lipson, N. Yu; Conference on Lasers and Electro-Optics (CLEO), OSA Technical Digest (Optical Society of America, 2020), paper STh1J.4 (2020 Conference Paper, Columbia University)

"Role of Dirac nodal lines and strain on the high spin Hall conductivity of epitaxial IrO2 thin films"; A.Bose, J.Nelson, X.Zhang, R.Jain, D.Schlom, D.Ralph, D.Muller, K.Shen, R.Buhrman; arXiv:2006.04365 [cond-mat.mes-hall].

"Sample Cell Arrays and Hardware for High-throughput Cryosaxs"; R.Thorne; 7906-04-US, United States, Filed, US from PCT, 2/4/20, 16/636,378.

"Scalable Terahertz Phased Array and Method"; E.Afshari, Y.Tousi; 6519-04-US, United States, Filed, CON, 6/8/20, 16/896,202; 6519-03-US, United States, Issued, 8/5/16, 15/117,060, 6/9/20, 10,680,553.

"Self-Referenced CEO Frequency Detection of a 10-GHz Laser Enabled by Highly Efficient Nonlinear Waveguides"; L.Kruager, A.Mayer, Y.Okawachi, X.Ji, A.Klenner, A.Johnson, C.Langrock, M.Fejer, M.Lipson, A.Gaeta, V.Wittwer, T.Suadmeyer, C.Phillips, and U.Keller; Laser Congress 2020 (ASSL, LAC), P. Schunemann, et al., eds., OSA Technical Digest 2020, AF1A.5.

"Separated transport relaxation scales and interband scattering in SrRuO3, CaRuO3, and Sr2RuO4 thin films"; Youcheng Wang, H. P. Nair, N. J. Schreiber, J. P. Ruf, Bing Cheng, D. G. Schlom, K. M. Shen, N. P. Armitage; arXiv:2012.12800 [cond-mat.str-el] [Submitted on 23 Dec 2020].

"Shear Wave Methods, Systems and Gyroscope"; B.Davaji, A.Lal, V.Pinrod; 8383-03-US, United States, US from PRV, Filed, 10/5/20, 17/063,179.

"Silica-PMMA hairy nanoparticles prepared via phase transfer-assisted aqueous miniemulsion atom transfer radical polymerization"; D.Wu, F.Käfer, N.Diaco, C.Ober; Journal of Polymer Science, Volume 58, Issue 17, September 1, 2020, Pages 2310-2316, https://doi.org/10.1002/pol.20200382.

"Silicon carbide zipper photonic crystal optomechanical cavities"; Lu, X.; Lee, J.; Lin, Q.; APL, 116, 22, 221104.

"Simultaneous implementation of antireflection and antitransmission through multipolar interference in plasmonic metasurfaces and applications in optical absorbers and broadband polarizers"; Zhang, J.; Wei, R.; Guo, C.; Nanophotonics, 9, 15, 4529-4538, 2020. https://doi.org/10.1515/nanoph-2020-0325.

"Simultaneous Structural and Electronic Transitions in Epitaxial VO2/TiO2 (001)"; Paez, G.; Singh, C.; Wahila, M.; Tirpak, K.; Quackenbush, N.; Sallis, S.; Paik, H.; Liang, Y.; Schlom, D.; Lee, T.; Physical Review Letters, 124, 19, 196402.

"Slaving a Highly Multi-Mode Laser to an On-Chip Single Mode Microresonator"; Y. Antman, O. Westreich, A. Gil-Molina, X. Ji, A. L. Gaeta, M. Lipson; CLEO, OSA Technical Digest, 2020, paper STh3O.4.

"Soft Actuator and Methods of Fabrication"; B.MacMurray, R.Shepherd, H.Zhao; 6577-03-US, United States, Issued, 10/10/16, 15/303,044, 9/8/20, 10,767,024.

"Solar-Concentration Solarization Apparatus, Methods, and Applications"; S.Ardanuc, A.Lal; 6053-03-US, United States, Issued, 3/5/15, 14/426,242, 9/8/20, 10,768,398.

"Solution-processable thermally crosslinked organic radical polymer battery cathodes"; S.Wang, A.Park, P.Flouda, A.Easley, F.Li, T.Ma, G.Fuchs, and J.Lutkenhaus; ChemSusChem, 13, 9, 2371, https://doi.org/10.1002/cssc.201903554 (2020).

"Sonic Testing Method, Apparatus and Applications"; C.Batten, A.Lal; 7685-03-US, Filed, US from PCT, 1/16/20, 16/631,590.

"Spectral and spatial isolation of single WSe2 quantum emitters using hexagonal boron nitride wrinkles"; R.Daveau, T.Vandekerckhove, A.Mukherjee, Z.Wang, J.Shan, K.Mak, A.Vamivakas, and G.Fuchs; APL Photonics 5, 096105 (2020); arXiv preprint arXiv:2005.07013.

"Sperm Rheotaxis Sensor: Motility-Based Fertility Diagnosis with Microfluidics"; A.Abbaspourrad, M.Azizi, M.Yaghoobi; 9698, Filed - Attorney Instructed to File, 11/24/20, Invention.

"Spinwave detection by nitrogen-vacancy centers in diamond as a function of probe-sample separation"; C. M. Pursor, V. P. Bhallamundi, F. Guo, M. R. Page, Q. Guo, G. D. Fuchs, and P. C. Hammel; Appl. Phys. Lett. 116, 202401 (2020).

"Sputtered AlN Lateral Bimorph: Process Integration Challenges and Opportunities"; B.Davaji; M.Abdelmajeed; A.Lal; T.Pennell; V.Genova; 2020 Joint Conference of the IEEE IFCS-ISAF; DOI: 10.1109/IFCS-ISAF41089.2020.9234864; 19-23 July 2020.

"Strain and Charge Doping Fingerprints of the Strong Interaction between Monolayer MoS2 and Gold"; Velickỳ, M.; Rodriguez, A.; Bouša, M.; Krayev, A.; Vondráček, M.; Honolka, J.; Ahmadi, M.; Donnelly, G.; Huang, F.; Abruña, H.; Journal of Physical Chemistry Letters, 11, 15, 6112-6118, July 7, 2020, https://doi.org/10.1021/acs.jpclett.0c01287.

"Strain relaxation induced transverse resistivity anomalies in SrRuO3 thin films"; L.Miao, N.Schreiber, H.Nair, J.Ruf, Y.Lee, M.Fu, B.Tsang, B.Goodge, S.Jiang, J.Shan, K.Mak, L.Kourkoutis, D.Schlom, and K.Shen; Physical Review B 102, 064406 (2020).

"Strain-stabilized superconductivity"; Ruf, J.; Paik, H.; Schreiber, N.; Nair, H.; Miao, L.; Kawasaki, J.; Nelson, J.; Faeth, B.; Lee, Y.; Goodge, B.; arXiv preprint arXiv:2005.06543.

"Stretchable distributed fiber-optic sensors"; H.Bai, S.Li, J.Barreiros, Y.Tu, C.Pollock, R.Shepherd; Science, 13 Nov 2020: 370, 6518, pp. 848-852, DOI: 10.1126/science.aba5504.

"Stretchable Lightguide Sensors and Uses Thereof"; J.Barreiros Flores, A.Pratt, R.Shepherd, P.Xu; 9337-01-US, United States, EPR - Enhanced Provisional, Filed, 8/11/20, 63/064,339.

"Strong, Temperature-Dependent Spin-Orbit Torques in Heavy Fermion YbAl3"; Reynolds, N.; Chatterjee, S.; Stiehl, G.; Mittelstaedt, J.; Karimeddiny, S.; Buser, A.; Schlom, D.; Shen, K.; Ralph, D.; arXiv preprint arXiv:2004.03678.

"Structural and piezoelectric properties of ultra-thin ScxAl1-xN films grown on GaN by molecular beam epitaxy"; J.Casamento, C.Chang, Y.Shao, J.Wright, D.Muller, H.G.Xing, and D.Jena; APL 117, 112101 (2020); https://doi.org/10.1063/5.0013943.

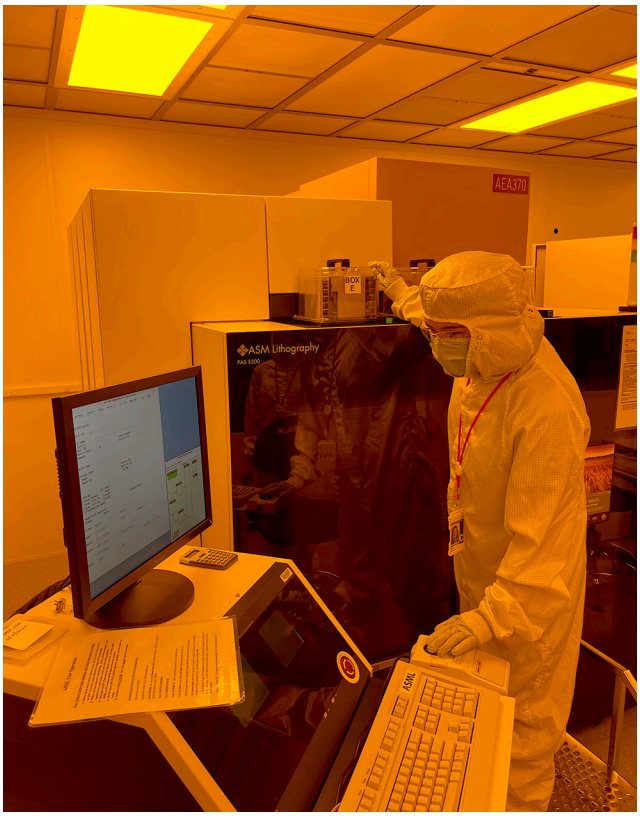

"Sub-THz momentum drag and violation of Matthiessen's rule in an ultraclean ferromagnetic SrRuO3 metallic thin film"; Wang, Y.; Bosse, G.; Nair, H.; Schreiber, N.; Ruf, J.; Cheng, B.; Adamo, C.; Shai, D.; Lubashevsky, Y.; Schlom, D.; arXiv preprint arXiv:2003.12024.

"Subcooled Flow Boiling of Carbon Dioxide Near the Critical Point Inside a Microchannel"; A.Parahovnik, M.Asadzadeh, S.Vasu, and Y.Peles; Physical Review Applied 14, 054050 - Published 19 November 2020.

"Suboxide Molecular-Beam Epitaxy and Related Structures"; K.Azizie, B.Bocklund, F.Hensling, Z.Liu, D.Schlom, S.Shang, P.Vogt; 9573-01-US, UTM - Utility, Filed, 10/21/20, 17/076,011.

"Subterahertz Momentum Drag and Violation of Matthiessen's Rule in an Ultraclean Ferromagnetic SrRuO3 Metallic Thin Film"; Y.Wang, G.Bossé, H.Nair, N.Schreiber, J.Ruf, B.Cheng, C.Adamo, D.Shai, Y.Lubashevsky, D.Schlom, K.Shen, and N.Armitage; Physical Review Letters 125, 217401, 16 Nov 2020.

"Supercapillary Architecture-Activated Two-Phase Boundary Layer Structures for Highly Stable and Efficient Flow Boiling Heat Transfer"; Li, W.; Wang, Z.; Yang, F.; Alam, T.; Jiang, M.; Qu, X.; Kong, F.; Khan, A.; Liu, M.; Alwazzan, M.; Yan, T.; Li, C.; Advanced Materials, 32, 2, 1905117.

"Surface electrochemical actuators for micron-scale fluid pumping and autonomous swimming"; M.Reynolds, A.Cortese, Q.Liu, W.Wang, M.Cao, D.Muller, M.Miskin, I.Cohen, P.McEuen; APS March Meeting 2020, 65, 1; Abstract: W22.00009, Session W22: Robophysics III; March 2-6, 2020.

"Surface Functionalization with Femtosecond Lasers and Application"; C.Guo (Invited); 2020 SPIE Optics + Photonics; iCANX Talks - global Science Livestream with a live audience of ~ 350K (Invited) (July 24, 2020).

"Synergistic effects of nitrogen and phosphorous on the growth of algal cells reveled by a microfluidic platform"; Liu, F.; Yazdani, M.; Wagner, N.; Ahner, B.; Wu, M.; APS Bulletin, APS March Meeting 2020, 65, 1, March 2-6, 2020; Denver, Colorado.

"System and Devices for Monitoring Cell-Containing Materials and Methods"; L.Bonassar, J.Matthews; 9131-02-US, United States, US from PRV, Filed, 9/30/20, 17/039,234.

"Systems and methods to redistribute field of view in spectroscopy"; M.Gazes, N. Pervez, I.Kymissis; U.S. Patent Application No. 63/088,278, Filed: October 6, 2020.

"Tabletop Imaging of Antiferromagnetism with Magneto-Thermal Microscopy"; Gray, I.; Cornell University Ph.D. Thesis, 2020. 28030846.

"Tailoring PEDOT properties for applications in bioelectronics"; Donahue, M.; Sanchez-Sanchez, A.; Inal, S.; Qu, J.; Owens, R.; Mecerreyes, D.; Malliaras, G.; Martin, D.; Materials Science and Engineering: R: Reports, V 140, April 2020, 100546.

"Targeted chemical pressure yields tuneable millimetre-wave dielectric"; Dawley, N.; Marksz, E.; Hagerstrom, A.; Olsen, G.; Holtz, M.; Goian, V.; Kadlec, C.; Zhang, J.; Lu, X.; Drisko, J.; Nature Materials, 19, 2, 176-181, 2020.

"Temperature dependence RF Characteristics of Al2O3-passivated WSe2 RF MOSFETs"; K.Xiong, X.Zhang, L.Li, F.Zhang, B.Davis, A.Madjar, A.Göritz, M.Wietstruck, N.Strandwitz, M.Kaynak, M.Terrones, J.Redwing, and J.Hwang; IEEE Electron Device Lett., vol. 41, no. 7, pp. 1134-1137, Jul. 2020, DOI: 10.1109/LED.2020.2999906.

"The architecture of co-culture spheroids regulates tumor invasion within a 3D extracellular matrix"; Huang, Y.; Shiau, C.; Wu, C.; Segall, J.; Wu, M.; Biophysical Reviews and Letters, 15, 3, 131-141 (2020), https://doi.org/10.1142/S1793048020500034.

"The Breakdown of Mott Physics at VO2 Surfaces"; M.Wahila, N.Quackenbush, J.Sadowski, J.Krisponeit, J.Ingo Flege, R.Tran, S.Ong, C.Schlueter, T.Lee, M.Holtz, D.Muller, H.Paik, D.Schlom, W.Lee, L. Piper; arXiv:2012.05306 [12.9.2020].

"The Design of the CCAT-prime Epoch of Reionization Spectrometer Instrument"; Cothard, N.; Choi, S.; Duell, C.; Herter, T.; Hubmayr, J.; McMahon, J.; Niemack, M.; Nikola, T.; Sierra, C.; Stacey, G.; J of Low Temperature Physics (2020) 199:898-907, https://doi.org/10.1007/s10909-019-02297-1.

"The Design, Fabrication, and Testing of Low-Power Mems Relays"; Pancoast, L.; Cornell University Ph.D. Thesis, 2020 https://doi.org/10.7298/vy3k-za06.

"The Intricate Love Affairs between MoS2 and Metallic Substrates"; M.Velický, G.Donnelly, W.Hendren, W.DeBenedetti, M.Hines, K.Novoselov, H.Abruña, F.Huang, O.Frank; Advanced Materials Volume 7, Issue 23; December 3, 2020; 2001324; https://doi.org/10.1002/admi.202001324.

"The surface stress of biomedical silicones is a stimulant of cellular response"; Cheng, Z.; Shurer, C.; Schmidt, S.; Gupta, V.; Chuang, G.; Su, J.; Watkins, A..; Shetty, A.; Spector, J.; Hui, C.; Science advances, 6, 15, eaay0076.

"Theoretical Investigation of Boundary Layer Behavior and Heat Transfer of Supercritical Carbon Dioxide in a Microchannel"; U.Manda; A.Parahovnik; Y.Peles; 2020 19th IEEE ITherm, Orlando, FL, 888-892, doi: 10.1109/ITherm45881.2020.9190408.

"Thermal Management using Buried Nanochannels"; S.Poudel, A.Zou, S.Maroo; APS-2020 researchgate.net.

"Thermal transport of helium-3 in a strongly confining channel"; D.Lotnyk, A.Eyal, N.Zhelev, T.Abhilash, E.Smith, M.Terilli, J.Wilson, E.Mueller, D.Einzel, J.Saunders, and J.Parpia; Nature Communications, 11, 4843 (2020).

"Thermionic emission or tunneling? The universal transition electric field for ideal Schottky reverse leakage current: A case study in β-Ga2O3"; W.Li, K.Nomoto, D.Jena, and H.G.Xing; APL 117, 222104 (2020); https://doi.org/10.1063/5.0029348.

"Thermo-optic Dielectric Metasurfaces for Polarization State Synthesizers and Active Lensing"; Bosch, M., Shcherbakov, M., Fan, Z., Huang, S., and Shvets, G.; CLEO: QELS_Fundamental Science. OSA, May 2020, Washington, DC.

"Thin Film Iridium Electrodes for Hexagonal Ferroelectrics"; M.Holtz, D.Schlom, R.Steinhardt; 9189-02-US, United States, US from PRV, Filed, 10/21/20, 17/076,131.

"Time-dependent metasurfaces for tunable broadband harmonics generation"; V. Zubyuk, P. Shafirin, A. Shorokhov, A. Musorin, T. Dolgova, G. Shvets, M. Shcherbakov, A. Fedyanin; 2020 14th International Congress on Artificial Materials for Novel Wave Phenomena (Metamaterials), NY, NY, USA, 2020, pp. 257-260, doi: 10.1109/Metamaterials49557.2020.9285142.

"Transmit-Receive Delay Element, Apparatus, Method and Applications"; M.Abdelmejeed, J.Kuo, A.Lal; 7369-03-US, United States, Issued, 9/17/18, 16/085,699, 9/8/20, 10,771,043.

"Transverse and Longitudinal Spin-Torque Ferromagnetic Resonance for Improved Measurements of Spin-Orbit Torques"; Karimeddiny, S.; Mittelstaedt, J.; Buhrman, R.; Ralph, D.; arXiv preprint arXiv:2007.02850; Phys. Rev. Applied 14, Iss. 2, 024024 - Published 11 August 2020.

"Trapping and Detrapping Mechanisms in β-GaO Vertical FinFETs Investigated by Electro-Optical Measurements"; Fabris, E.; De Santi, C.; Caria, A.; Li, W.; Nomoto, K.; Hu, Z.; Jena, D.; Xing, H.G.; Meneghesso, G.; Zanoni, E.; IEEE Transactions on Electron Devices, vol. 67, no. 10, pp. 3954-3959, Oct. 2020, doi: 10.1109/TED.2020.3013242.

"Tumor spheroids under perfusion within a 3D microfluidic platform reveal critical roles of cell-cell adhesion in tumor invasion"; Huang, Y.; Ma, Y.; Wu, C.; Shiau, C.; Segall, J.; Wu, M.; Scientific Reports, 10, 1, 1-11, 2020.

"Ultra-Low Threshold Broadband Soliton Frequency Comb Generation"; X.Ji, J.Jang, U.Dave, C.Joshi, M.Zanarella, A.Gaeta, M.Lipson; CLEO, OSA Tech Digest, 2020, SW3J.6.

"Ultrasonic Fourier Transform Analog Computing Apparatus, Method and Applications"; A.Lal; 7368-05-US, United States, US from PCT, Filed, 11/23/20, 17/057,868.

"Unconventional valley-dependent optical selection rules and landau level mixing in bilayer graphene"; L.Ju, L.Wang, X.Li, S.Moon, M.Ozerov, Z.Lu, T.Taniguchi, K.Watanabe, E.Mueller, F.Zhang, D.Smirnov, F.Rana and P.McEuen; Nature Communications, 11, 1, 1-7.

"Universal Conversion Efficiency Scaling with Free-Spectral-Range for Soliton Kerr Combs"; J.Jang, Y. Okawachi, X. Ji, C. Joshi, M. Lipson, and A.Gaeta; CLEO, OSA Technical Digest, 2020, paper JTu2F.32.

"Using Recombinant Outer Membrane Vesicles"; M.Rivera-De Jesus, and D.Putnam; International Symposium on Bio Materials for Drug/Gene Delivery, Salt Lake City, UT, Feb 2020.

"Vertical Gallium Oxide (Ga203) Power FETs"; Z.Hu, D. Jena, W.Li, K.Nomoto, H.G.Xing; 8178-03-US, United States, US from PCT, Filed, 9/27/20, 17,042,153.

"Very High Parallel-Plane Surface Electric Field of 4.3 MV/cm in Ga2O3 Schottky Barrier Diodes with PtOx Contacts"; Saraswat, D.; Li, W.; Nomoto, K.; Jena, D.; Xing, H.G.; 2020 Device Research Conference (DRC), Columbus, OH, USA, 2020, pp. 1-2, doi: 10.1109/DRC50226.2020.9135177.

"Visible nonlinear photonics via high-order-mode dispersion engineering"; Y. Zhao, X. Ji, B. Y. Kim, P. S. Donvalkar, J. K. Jang, C. Joshi, M. Yu, C. Joshi, R. R. Domeneguetti, F. A. S. Barbosa, P. Nussenzveig, Y. Okawachi, M. Lipson, and A. L. Gaeta; Optica Vol. 7, Issue 2, pp. 135-141 (2020), https://doi.org/10.1364/OPTICA.7.000135.

"Visualizing Aroma: Spatially Resolved, High-Throughput, and Automated Detection of Odorants in Grapes Using Ambient Ionization Mass Spectrometry"; DiGregorio, M.; Cornell University Ph.D. Thesis 2020.

"Wafer-scale low-loss lithium niobate photonic integrated circuits"; K.Luke, P.Kharel, C.Reimer, L.He, M.Loncar, and M. Zhang; 2020 IEEE Photonics Conference (IPC), 28 Sept.-1 Oct. 2020, DOI: 10.1109/IPC47351.2020.9252499; Optics Express Vol. 28, Issue 17, pp. 24452-24458 (2020), https://doi.org/10.1364/OE.401959.

"Wicking Nanofence-Activated Boundary Layer to Enhance Two-Phase Transport in Microchannels"; W.Li, F.Yang, X.Qu, and C.Li; Langmuir 2020, 36, 51, 15536-15542, December 14, 2020, https://doi.org/10.1021/acs.langmuir.0c02882.

"Wireless, Optically-Powered Optoelectonics Sensors"; A.Cortese, S.Lee, P.McEuen, A.Molnar; 8107-04-US, United States, US from PCT, Filed, 8/10/20, 16/947,626; 8107-05-EP, European Patent Convention, Filed, 8/25/20, 19751894.7; 8107-06-JP, Japan, Foreign, Filed, 8/12/20, 2020-542832; 8107-07-KR, South Korea, Foreign, Filed, 9/8/20, 10-2020-7025896.

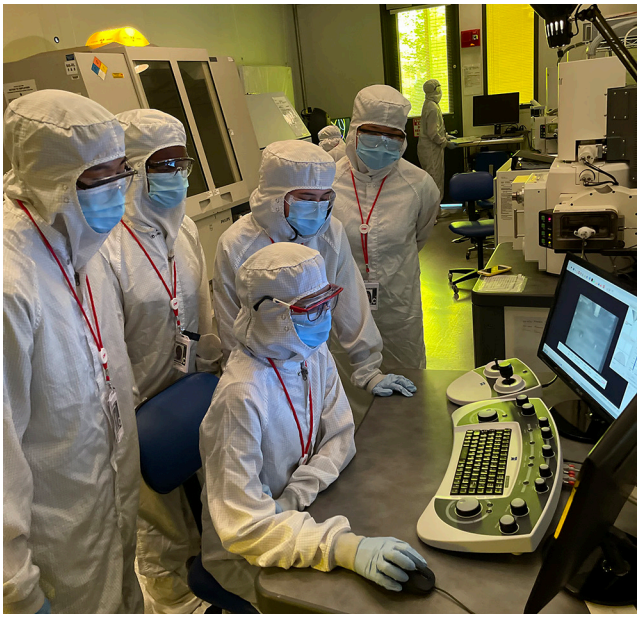

Common Abbreviations & Meanings

μl .. microliter
μm .. micron, micrometer
μN .. micro-Newtons
μs .. microsecond
Ω .. Ohm
< .. is less than
> .. is greater than
~ .. approximately
1D .. one-dimensional
2D .. two-dimensional
2DEG .. two-dimensional electron gas
3D .. three-dimensional
^{3}He .. helium-3
α-Al_2O_3 .. sapphire
a-Si .. amorphous silicon
AC .. alternating current
AFM .. atomic force microscopy/microscope
AFOSR .. Air Force Office of Scientific Research
Ag .. silver
Al .. aluminum
Al_2O_3 .. aluminum oxide
ALD .. atomic layer deposition
AlGaAs .. aluminum gallium arsenide
AlGaN .. aluminum gallium nitride
Ar .. argon
ARC .. anti-reflective coating
ArF .. argon fluoride
As .. arsenic
atm .. standard atmosphere (as a unit of pressure)
Au .. gold
AuNPs .. gold nanoparticles
B .. boron
B. subtilis .. *Bacillus subtilis*
Bi .. bismuth
BOE .. buffered oxide etch
Br .. bromine
C .. carbon
C .. centigrade
C-V .. capacitance-voltage
C_3N_4 .. carbon nitride
$CaCl_2$ .. calcium chloride
$CaCO_3$ .. calcium carbonate
CAD .. computer-aided design
CaF_2 .. calcium fluoride
CCMR .. Cornell Center for Materials Research
Cd .. cadmium
CdS .. cadmium sulfide
CdSe .. cadmium selenide
CDW .. charge-density-wave
Ce .. cerium
CF_4 .. carbon tetrafluoride or tetrafluoromethane
CFD .. computational fluid dynamics
CH_4 .. methane
CHESS .. Cornell High Energy Synchrotron Source
CHF_3 .. trifluoromethane
Cl .. chlorine
Cl_2 .. chlorine gas
Cl_2/SF_6 .. chlorine sulfur hexafluoride
cm .. centimeter
CMOS .. complementary metal oxide semiconductor
CMP .. chemical mechanical polishing
CNF .. Cornell NanoScale Science & Technology Facility
Co .. cobalt
CO_2 .. carbon dioxide
Co_3O_4 .. cobalt oxide
CoFeAl .. cobalt iron aluminum
CoFeB .. cobalt iron boron
CoP .. cobalt porphyrin
CPC .. colloidal photonic crystal
CPD .. contact potential difference
CpG .. cytosine-phosphate-guanine
Cr .. chromium
CRDS .. cavity ring-down spectrometer
cryoSAXS .. cryogenic small angle x-ray scattering
CTE .. coefficients of thermal expansion
CTL .. confinement tuning layer
Cu .. copper
CVD .. cardiovascular disease
CVD .. chemical vapor deposition
CW .. continuous wave
CXRF .. confocal x-ray fluorescence microscopy
DARPA .. Defense Advanced Research Projects Agency
DC .. direct current
DCB .. double cantilever beam
DCE .. 1,2-dichloroethane
DCM .. dichloromethane
DEP .. dielectrophoresis
DFT .. density functional theory
DFT .. discrete Fourier transform
DI .. de-ionized
DMF .. dimethyl formamide
DNA .. deoxyribonucleic acid
DNP .. dynamic nuclear polarization
DOE .. United States Department of Energy
DPPC .. 1,2-dipalmatoyl-sn-glycero-3-phosphocholine
DRAM .. dynamic random access memory
DRIE .. deep reactive ion etch
DSA .. directed self assembly
dsDNA .. double-stranded DNA
DUV .. deep ultraviolet
e-beam .. electron beam lithography
E. coli .. *Escherichia coli*
EBL .. electron-beam lithography
EDS .. energy dispersive spectroscopy
EELS .. electron energy loss spectroscopy
EG .. ethylene glycol

EIS .. .. electrochemical impedance spectroscopy
ELISA .. .. enzyme-linked immunosorbent assays
EO .. .. electro-optic
EOT .. .. equivalent oxide thickness
EPICs .. .. electronic photonic integrated circuits
Er. .. .. erbium
ErAs .. .. erbium arsenide
ESM .. .. effective screening medium
EUV .. .. extreme ultraviolet
ex situ .. .. Latin phrase which translated literally as 'off-site' -- to examine the phenomenon in another setting than where it naturally occurs
ex vivo .. .. Latin for "out of the living" -- that which takes place outside an organism
F .. .. fluorine
FDA .. .. United States Food & Drug Administration
FDMA .. .. fluorinated perfluorodecyl methacrylate
Fe. .. .. iron
Fe_2O_3 . .. . iron oxide
$FeCl_3$.. .. .. iron(III) chloride, aka ferric chloride
FeGe .. .. iron germanium
FEM .. .. finite element method
FET. .. .. field-effect transistor
FFTs .. .. fast Fourier transforms
fg . .. . femto gram
FIB . .. . focused ion beam
FIR . .. . far infrared
fJ.. .. .. femto Joules
FM.. .. .. frequency modulation
FMR .. .. ferromagnetic resonance
FOTS . .. . fluorosilane, tridecafluoro-1,1,2,2-tetrahydrooctyltrichlorosilane
FTIR .. .. Fourier transform infrared spectroscopy
Ga .. .. gallium
Ga_2O_3. .. .. gallium(III) trioxide
GaAs . .. . gallium arsenide
GaAsN.. .. .. .. gallium arsenide nitride
GaInNAs . .. .. gallium indium nitride arsenide
GaN .. .. gallium nitride
GaP. .. .. gallium phosphide
GaSb.. .. .. gallium antimonide
Gd .. .. gadolinium
Ge .. .. germanium
GFET. .. .. graphene field effect transistor
GHz .. .. gigahertz
GI .. .. gastrointestinal
GMR . .. . giant magnetoresistance
GPa. .. .. gigapascal
GPS .. .. global positioning system
h .. .. hours
H.. .. .. hydrogen
H_2O_2 .. .. hydrogen peroxide
HBAR .. .. high-overtone bulk acoustic resonator
hBN .. .. hexagonal boron nitride
HBr. .. .. hydrogen bromide
hcp.. .. .. hexagonal close packing
He .. .. helium
HEMTs . .. . high electron mobility transistors
Hf .. .. hafnium
HF .. .. hydrofluoric acid
HfB_2 .. .. hafnium diboride
HFEs . .. . hydrofluoroethers
HfO_2 .. .. hafnium dioxide
Hg .. .. mercury
high-κ .. .. high dielectric constant
HMDS .. .. hexamethyldisilazane
HRS .. .. high resistance state
HSQ .. .. hydrogen silsesquioxane
HSQ/FOx .. .. negative electron beam resist hydrogen silsesquioxane
Hz .. .. Hertz
I-V .. .. current-voltage
I/O .. .. input/output
IARPA .. .. Intelligence Advanced Research Projects Activity
IC. .. .. integrated circuit
ICP . .. . inductively coupled plasma
ICP-MS .. .. .. inductively coupled plasma mass spectroscopy
ICP-RIE .. .. .. inductively coupled plasma reactive ion etcher
IFVD . .. . impurity free vacancy diffusion
IID .. .. impurity induced disordering
IIEI . .. . ion implant enhanced interdiffusion
In . .. . indium
in situ. .. .. Latin phrase which translated literally as 'in position' -- to examine the phenomenon exactly in place where it occurs
in vitro .. .. Latin for "within glass" -- refers to studies in experimental biology that are conducted using components of an organism that have been isolated from their usual biological context in order to permit a more detailed or more convenient analysis than can be done with whole organisms
in vivo .. .. Latin for "within the living" -- experimentation using a whole, living organism
InAlN .. .. indium aluminum nitride
InAs .. .. indium arsenide
InAs NWs .. .. indium arsenide nanowires
INDEX . .. . Institute for Nanoelectronics Discovery and Exploration
InGaAsN . .. .. indium gallium arsenide nitride
$InGaZnO_4$ .. .. indium gallium zinc oxide
InP .. .. indium phosphide
IPA.. .. .. isopropyl alcohol
IR. .. .. infrared
IrO_2 or IrO_x. .. iridium oxide
ITO . .. . indium tin oxide
JP-8 .. .. Jet Propellant 8
κ .. .. dielectric constant
K.. .. .. Kelvin (a unit of measurement for temperature)
K.. .. .. potassium
KFM .. .. Kelvin force microscopy
kg. .. .. kilogram
kHz . .. . kilohertz
KOH .. .. potassium hydroxide
La .. .. lanthanum
LED .. .. light-emitting diode
LER .. .. line edge roughness
Li . .. . lithium

low-κ . .. . low dielectric constant
LPCVD .. .. .. low pressure chemical vapor deposition
lpm . .. . liter per minute
LRS .. .. low resistance state
Lu .. .. lutetium
LWR .. .. line width roughness
MBE .. .. molecular beam epitaxy
MEMs .. .. microelectromechanical systems
MFMR .. .. microfabricated micro-reactors
MgO .. .. magnesium oxide
MGs .. .. molecular glasses
MHz .. .. megahertz
micron .. .. micrometer, aka μm
min . .. . minutes
ml .. .. milliliter
mm . .. . millimeter
mM . .. . millimolar
Mo .. .. molybdenum
MOCVD .. .. .. metal oxide chemical vapor deposition
MOS .. .. metal oxide semiconductor
MoS_2 .. .. molybdenum disulfide
$MoSe_2$ .. .. molybdenum diselenide
MOSFET . .. .. metal oxide semiconductor field effect transistor
MRAM . .. . magnetic random access memory
MRFM .. .. magnetic resonance force microscopy
MRI .. .. magnetic resonance imaging
ms .. .. millisecond
MSM . .. . metal-semiconductor-metal
mTorr . .. . millitorr
mV .. .. millivolt
MVD . .. . molecular vapor deposition
MΩ . .. . megaohms
N .. .. nitrogen
N_2 .. .. nitrous oxide
nA .. .. nanoAmperes
NaCl .. .. sodium chloride
NASA .. .. National Aeronautics & Space Administration
Nb .. .. niobium
Nb_3Sn .. .. triniobium-tin
NCs .. .. nanocrystals
Nd .. .. neodymium
NEMs .. .. nanoelectromechanical systems
NH_4F . .. . ammonium fluoride
Ni . .. . nickel
NIH .. .. National Institutes of Health
NIR . .. . near-infrared
nL .. .. nanoliter
nm .. .. nanometer
NMP n-methyl-2-pyrrolidone
NNCI . .. . National Nanotechnology Coordinated Infrastructure
NPs . .. . nanoparticles
NPs . .. . nanopores
ns . .. . nanosecond
NSF .. .. National Science Foundation
NV .. .. nitrogen-vacancy
NVM . .. . non-volatile memory
NW FETs . .. .. nanowire field-effect transistors
O .. .. oxygen
O_3 .. .. trioxygen
OFET . .. . organic field effect transistor
OLED .. .. organic light-emitting diode
ONO .. .. oxide/nitride/oxide
ONR-MURI .. Office of Naval Research Multidisciplinary University Research Initiative
OPV .. .. organic photovoltaic cells
OTFT . .. . organic thin-film transistor
Pa . .. . Pascals
PAB .. .. post-apply bake
PaC . .. . Parylene-C
PAG .. .. photoacid generator
Pb .. .. lead
PBG .. .. photonic bandgap
PbS . .. . lead sulfide
PBS .. .. phosphate-buffered saline
PbSe .. .. lead selenide
PC .. .. persistent current
PC .. .. photocurrent
PCN .. .. photonic crystal nanocavity
Pd .. .. palladium
PD .. .. photodetector
PDMS .. .. polydimethylsiloxane
PEB .. .. post-exposure bake
PEC .. .. photoelectrochemical
PECVD .. .. .. plasma enhanced chemical vapor deposition
PEDOT:PSS .. poly(3,4-ethylenedioxythiophene): poly(styrenesulfonate)
PEG .. .. polyethylene glycol
PEI .. .. polyethyleneimine
pFET .. .. p-channel field-effect transistor
PFM .. .. piezo-response force microscopy
PGMA .. .. poly(glycidyl methacrylate)
pH .. .. a measure of the activity of hydrogen ions (H+) in a solution and, therefore, its acidity
Ph.D. . .. . doctorate of philosophy
PhC . .. . photonic crystal
PL .. .. photoluminescence
pL .. .. picoliter
PLD .. .. pulsed laser deposition
PMMA .. .. poly(methyl methacrylate)
poly-Si .. .. polycrystalline silicon
PS .. .. polystyrene
PS-*b*-PMMA polystyrene-*block*-poly(methyl methacrylate)
Pt . .. . platinum
Pt/Ir .. .. platinum/iridium
$PtSe_2$ .. .. platinum diselenide
PV .. .. photovoltaic
PVD .. .. physical vapor deposition
Py .. .. permalloy, $Ni_{81}Fe_{19}$
Q .. .. quality factor
QD .. .. quantum dots
QW . .. . quantum well
RA .. .. resistance-area
REU .. .. Research Experiences for Undergraduates Program
RF .. .. radio frequency

RF MEMS .. .. radio frequency microelectromechanical systems
RIE . .. . reactive ion etch
RMS or rms .. root mean square
RNA .. .. ribonucleic acid
RTA .. .. rapid thermal anneal
RTD .. .. resistance temperature device
RTD .. .. resonant tunneling diodes
Ru .. .. ruthenium
s .. .. seconds
S .. .. sulfur
SAMs .. .. self-assembled monolayers
SAXS .. .. small angle x-ray scattering
Sb .. .. antimony
Sc. .. .. scandium
sccm .. .. standard cubic centimeters per minute
$scCO_2$ .. .. supercritical carbon dioxide
SDS .. .. sodium dodecyl sulfate
Se. .. .. selenium
sec .. .. seconds
SEM .. .. scanning electron microscopy/microscope
SERS . .. . surface enhanced Raman spectroscopy
SF_6 .. .. sulfur hexafluoride
Si . .. . silicon
Si_3N_4 .. .. silicon nitride
SiC.. .. .. silicon carbide
SiH_4 .. .. silane
SiN . .. . silicon nitride
SiO_2 .. .. silicon dioxide, silica
Sn .. .. tin
SnO_2 .. .. tin oxide
$SnSe_2$ . .. . tin selenide or stannous selenide
SOI . .. . silicon-on-insulator
SPR .. .. surface plasmon resonance
SQUID . .. . superconducting quantum interference device
Sr_2RuO_4 .. .. .. strontium ruthenate
SRC .. .. Semiconductor Research Corporation
$SrTiO_3$ .. .. strontium titanate
STEM .. .. scanning transmission electron microscopy/microscope
t-BOC .. .. *tert*-butoxycarbonyl
Ta. .. .. tantalum
Ta_2O_5 . .. . tantalum pentoxide
TaN. .. .. tantalum nitride
TAO_x . .. . tantalum oxide
Te. .. .. tellurium
TEM .. .. transmission electron microscopy/microscope
TFET . .. . tunnel field effect transistor
TFT. .. .. thin-film transistor
Tg .. .. glass transition temperature
THz .. .. terahertz
Ti . .. . titanium
TiN . .. . titanium nitride
TiO_2 .. .. titanium dioxide
TM.. .. .. transverse magnetic
TXM.. .. .. transmission x-ray microscopy
UHV .. .. ultra-high vacuum
USDA .. .. United States Department of Agriculture
UV .. .. ultraviolet
UV-Vis . .. . ultraviolet-visible
V.. .. .. vanadium
V.. .. .. voltage
vdW .. .. van der Waals
VLS .. .. vapor-liquid-solid
VRMs .. .. voltage regulator modules
VSM .. .. vibrating sample magnetometry
W. .. .. tungsten
WDM .. .. wavelength-division multiplexing
WSe_2.. .. .. tungsten diselenide
XeF_2 .. .. xenon difluoride
XPM .. .. cross-phase modulation
XPS .. .. x-ray photoelectron spectroscopy
XRD .. .. x-ray diffraction
XRR .. .. x-ray reflectivity
ZMW. .. .. zero-mode waveguide
Zn .. .. zinc
$ZnCl_2$ . .. . zinc chloride
ZnO .. .. zinc oxide
ZnO:Al . .. . zinc aluminum oxide
ZnS . .. . zinc sulfide or zinc-blende
Zr. .. .. zirconium
ZrO_2 .. .. zirconium dioxide
ZTO .. .. zinc tin oxide

Photography Credits

The cover image is used with permission from Yifeng Hong and Michelle D. Wang. The image is part of their report on "Nanophotonic Standing-Wave Array Trap for Single-Molecule Applications"; CNF Project 1738-08, pages 10-11. The photographs of the 2021 CNF Interns in the Table of Contents and 2020 CNF Research Related PPPs were taken by Ron Olson, CNF Director of Operations. The photographs of the directors on page viii were taken by Cornell University Photography. The remaining photographs were eitehr taken by CNF staff or provided.

The 2020-2021 Cornell NanoScale Facility Research Accomplishments are online in PDF, http://cnf.cornell.edu/publications/research_accomplishments

Cornell NanoScale Science & Technology Facility (CNF)

2020-2021 Research Accomplishments

Investigating Metabolic Regulation of Cancer Stem-Like Cells in the Perivascular Niche

2021 CNF REU Intern: Niaa Jenkins-Johnston

Intern Affiliation: Biomedical Engineering, Cornell University

CNF REU Principal Investigator: Claudia Fischbach, Biomedical Engineering, Cornell University

CNF REU Mentor: Matthew Tan, Biomedical Engineering, Cornell University

Primary Source of Research Funding: 2021 Cornell NanoScale Science & Technology Facility Research Experiences for Undergraduates (CNF REU) Program via National Science Foundation under Grant No. NNCI-2025233

Contact(s): noj4@cornell.edu, cf99@cornell.edu, mlt239@cornell.edu

Primary CNF Tools Used: ABM contact aligner, Heidelberg mask writer - DWL2000, Hamatech 9000

Abstract:

A population of cancer cells known as cancer stem-like cells, or CSCs, promote mortality in breast cancer by driving metastasis and relapse. These cancer cells interact with the extracellular matrix, other cell types, secreted factors and the perivascular niche, the region directly next to blood vessels. One of the major components of the perivascular niche are the endothelial cells, which secrete factors that regulate stemness properties. The perivascular niche also contains a unique metabolic microenvironment, which affects the metabolic behavior of CSCs. In this study, we created a microfluidic device that features a large central reservoir for collagen, four media reservoirs and two channels for seeding breast cancer and endothelial cells. These microfluidic devices can be used to help better understand the tumor microenvironment and determine how targeting the CSC population could help to prevent or treat late stage breast cancer.

Summary of Research:

Introduction. Metastatic breast cancer presents a significant and unmet clinical need. Breast cancer is the leading type of cancer among women with one in eight women developing breast cancer at some point during their lives [1]. Cancer stem-like cells (CSCs) are known to express specific stem cell markers and demonstrate other properties, such as therapeutic resistance and self-renewal, which allows these cells to evade therapy and repopulate the tumor resulting in relapse [2]. However, the factors that contribute to the emergence of CSCs in tumors are still not well understood.

During metastasis, CSCs move through circulation, spread to distant tissues and interact with the perivascular niche, the region directly next to blood vessels. One of the major components of the perivascular niche are the endothelial cells, which secrete factors that regulate stemness properties such as self-renewal and invasion. The perivascular niche also contains a unique metabolic microenvironment, which affects the metabolic behavior of CSCs. There is currently little research on how endothelial cells together with metabolic diffusion affect the metabolism of tumor cells.

To this end, we plan to use a microfluidic cell culture system (Figure 1). Microfluidics will allow us to precisely control metabolic gradients and spatial organization of cells to uncover how perivascular niche factors affect CSC metabolism and subsequent stemness.

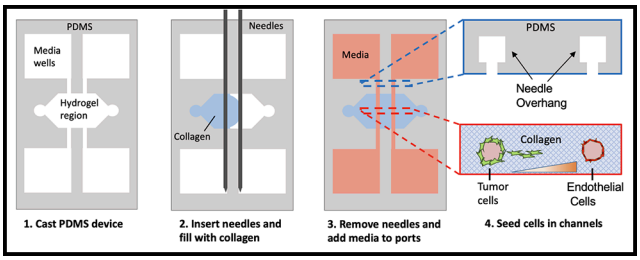

Figure 1: The microfluidic device fabrication process.

Design and Fabrication. The device design consists of three layers: a 100 μm needle buffer layer, a 200 μm needle guide layer, and a 300 μm hydrogel reservoir layer. The needle guide layer helps to keep the needle straight in the channel while the needle buffer layer prevents the needle from touching the bottom of the device. This is essential because cell contact to the plastic or glass device can alter cell behavior.

The microfluidic device mold was fabricated by depositing and exposing three subsequent layers of SU-8 onto a silicon wafer using two fabrication methods: the reverse (Figure 2) and upright (Figure 3) SU-8 processes. Each SU-8 layer of the device design was exposed to UV light using the ABM contact aligner and after all layers were exposed, the wafer was developed.

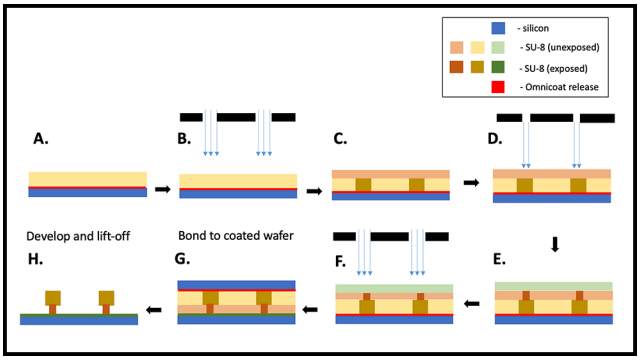

Figure 2: The reverse SU-8 fabrication process steps: a) Coat the wafer with OmniCoat® and SU-8. b) Expose at 350 mj/cm². c) Coat the wafer with a second layer of SU-8. d) Expose devices from 150-600 mj/cm² in 50 mj/cm² increments. e) Coat the wafer with a third layer of SU-8. f) Expose at 450 mj/cm². g) Adhere second wafer to first wafer. h) Develop wafer sandwich and dissolve OmniCoat to remove the first wafer.

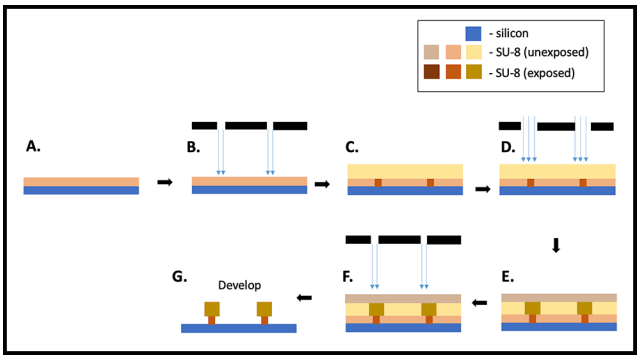

Figure 3: The upright SU-8 fabrication process steps: a) Coat the wafer with SU-8. b) Expose at 300 mj/cm². c) Coat the wafer with another layer of SU-8. d) Expose devices at 150-600 mj/cm² in 50 mj/cm² increments. e) Coat the wafer with a third layer of SU-8. f) Expose at 450 mj/cm². g) Develop wafer.

Device Characterization. The devices were sent to the Biotechnology Resource Center at Cornell University where they were characterized using a CT scanner. The CT scan image shows the devices made from both reverse and upright SU-8 processes. The reverse SU-8 process produced the necessary overhang in the needle guide layer, though slightly elongated, while the upright SU-8 process produced no overhang at all (Figure 4). It was found that the needle buffer and guide had a thickness of about 418 μm, which was close to our estimated 400 μm, while the total thickness of the device is around 745 μm, slightly larger than the 600 μm we had proposed.

Conclusions and Future Steps:

The next phase of this project is to finalize the device fabrication process in order to maximize the effectiveness of the devices. Then, we will cast the PDMS device, insert needles into the channels to fill the collagen reservoir, fill the media reservoirs and lastly seed the channels with tumor and endothelial cells (Figure 1). To increase the strength of the bond between the wafer and substrate, and minimize loss of devices during wafer transfer, we plan to use a substrate bonder. By using metabolic gradient experiments and completing cell culture experiments in our devices, we hope to learn more about the behavior of CSCs and how their properties are affected by the perivascular niche.

Acknowledgements:

Special thanks to Matthew Tan, Claudia Fischbach, Melanie-Claire Mallison, and the CNF Staff. This work was performed at the Cornell NanoScale Facility, as part of the 2021 Research Experiences for Undergraduates (CNF REU) Program, funded by the National Science Foundation via the National Nanotechnology Coordinated Infrastructure (Grant No. NNCI-2025233).

References:

[1] SEER Cancer Stat Facts: Female Breast Cancer. National Cancer Institute. Bethesda, MD, https://seer.cxancer.gov/statfacts/html/breast.html.

[2] Yoo, Y. D., Han, D. H., Jang, J. M., Zakrzewska, A., Kim, S.Y., Choi, C.Y., Lee, Y. J., and Kwon, Y. T. (2013). Molecular characteristics of cancer stem-like cells derived from human breast cancer cells. Anticancer research, 33(3),763-777.

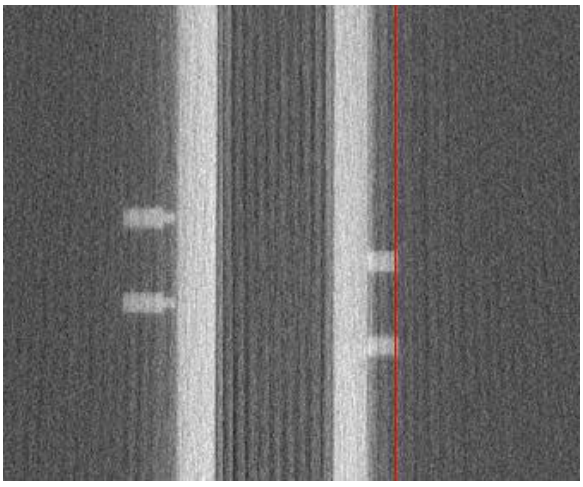

Figure 4: The CT scanner image of the devices from both the reverse (left) and upright (right) SU-8 fabrication methods.

Generating Microfluidic Devices to Study Confined Migration of Cancer Cells

2021 CNF REU Intern: Elisabeth Wang

Intern Affiliation: Biological Sciences and Music, Cornell University

CNF REU Principal Investigator: Jan Lammerding, Meinig School of Biomedical Engineering, Weill Institute for Cell and Molecular Biology, Cornell University

CNF REU Mentor: Richa Agrawal, Biochemistry, Cell and Molecular Biology, Cornell University

Primary Source of Research Funding: 2021 Cornell NanoScale Science & Technology Facility Research Experiences for Undergraduates (CNF REU) Program via National Science Foundation under Grant No. NNCI-2025233

Contact(s): emw239@cornell.edu, jan.lammerding@cornell.edu, ra664@cornell.edu

Primary CNF Tools Used: Heidelberg mask writer - DWL2000, Hamatech-Steag HMP900 mask processor, SÜSS MA6-BA6 contact aligner, Hamatech hot piranha, MVD 100, Anatech plasma asher, Unaxis 770 deep silicon etcher / Oxford Cobra ICP etcher

Abstract:

During metastasis, cancer cells spread from a primary tumor to distal sites. As they travel through interstitial environments, they compress their nucleus to fit through confined areas smaller than themselves. Nuclear deformation can put stress on the cells and have consequences such as nuclear envelope rupture and DNA damage. To study changes induced in cancer cells due to confined migration, polydimethylsiloxane (PDMS) microfluidic devices can simulate the intermittent confinement of an *in vivo* environment. The goal of this research was to create devices which allow for time-lapse imaging and enable collection of cells that had successfully performed confined migration for other characterization. We fabricated devices with constriction areas consisting of a field of heterogeneously spaced pillars by using photolithography techniques to create a wafer with the features for the devices, then creating devices from a PDMS casting of the wafer. We seeded HT1080 fibrosarcoma cells in the devices and allowed them to migrate through the constrictions for up to six days. A study of the cells migrating through the devices over 12 hours showed successful migration. However, over six days, the progress of the cells stalled, possibly due to limited nutrient supply in the confined environment. Overall, the devices successfully model cancer cell migration in a heterogeneous environment, and will be useful for time-lapse microscopy and short-term studies.

Summary of Research:

Cancer cells spread from primary tumors to distal sites during metastasis, which contributes to up to 90% of all cancer-related deaths [1]. As they travel through extracellular matrices, they often must compress their nucleus to fit through tight interstitial spaces [2]. The force required to squeeze through the confined environments can have various consequences for the cells. These effects can include DNA damage from either nuclear deformation that causes increased replication stress [3] or nuclear envelope rupture that allows contents of the cytoplasm and nucleus to mix uncontrollably, leading to greater instability and causing the cancer to advance [4]. However, the full extent that the cells are affected by confined migration is still poorly understood.

To better understand the consequences of confined migration on cancer cells, we designed and fabricated polydimethylsiloxane (PDMS) microfluidic devices with precisely defined confined areas. Previous microfluidic device designs had two main limitations: (1) successive constrictions did not resemble the heterogeneous confinement of tissues, and (2) the small constriction area limited the number of cells for analysis. Our new device designs included the following improvements: (1) the constriction area consisted of a "heterogeneous field" of pillars with varying spacing, which is more physiological (Figure 1), and (2) the constriction area expanded by

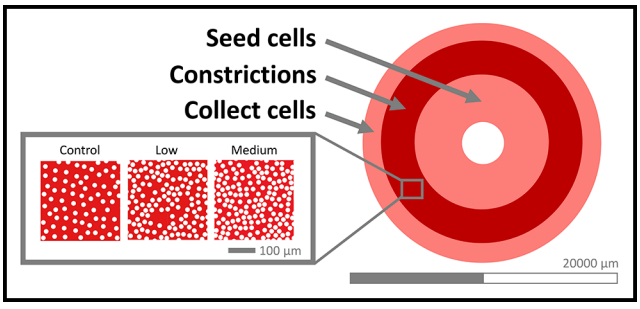

Figure 1: Randomized pillar device design showing the seeding, constriction, and collection areas. Pillars were 5 µm tall and 15 µm in diameter. Modified from Richa Agrawal, submitted to Methods in Molecular Biology.

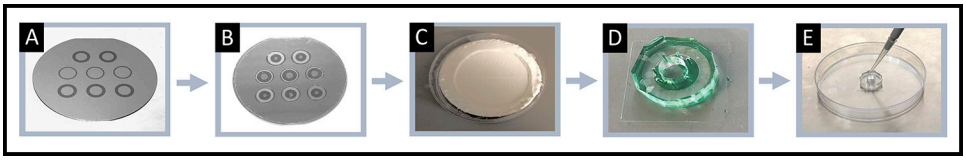

Figure 2: Fabrication workflow for microfluidic devices. (A) First layer of wafer: features for constrictions. (B) Second layer of wafer: features for seeding and collection areas. (C) PDMS casting from plastic mold created from wafer. (D) Devices and seeding ports cut out, then bonded to glass. (E) HT1080 fibrosarcoma cells seeded into device.

100-fold so more cells can be collected after migrating. In addition, the devices have randomized pillars with varying densities, including a relatively "low density" control, to simulate increasing degrees of confinement (Figure 1).

Fabricating microfluidic devices involved making a silicon master mold with two layers. The first layer used reactive ion etching in the Oxford Cobra etcher to create a 5 μm tall constriction area, and the second layer consisted of SU-8 photoresist for 250 μm tall seeding and constriction areas. Microfluidic devices were cut out from a PDMS casting of the wafer and bonded to glass (Figure 2).

Time-lapse imaging of the devices over 12 hours showed that the cells migrate through the constrictions and travel the fastest in the devices with lower pillar densities (Figure 3). Migration was also tracked over several days in another set of devices, and the cells' progress was measured by studying the leading edge of cells. The cells advanced through all of the devices over the first five days, but the average distance from the seeding area decreased on the sixth day, likely due to insufficient nutrient supply that caused some cell death (Figure 4).

However, overall, the devices successfully model migration through a heterogeneous environment and are suitable for time-lapse microscopy and short-term endpoint studies (< four days).

Future Steps:

Decreased migration through the devices after several days most likely indicated insufficient culture media supply or stress from prolonged vertical confinement. Current efforts are focused on creating a version of the devices with a smaller constriction area (< 500 μm) to help with nutrient supply issues, and increased PDMS adhesion area to ensure sufficient bonding to the glass coverslip. We have also created another device with an increased vertical height from 5 μm to 10 μm to eliminate the possibility that cell death was due to prolonged vertical confinement.

Acknowledgements:

I acknowledge the support of the NSF, NNCI, and Cornell NanoScale Facility REU Program (NSF grant no. NNCI-2025233). Special thanks to Dr. Jan Lammerding, Richa Agrawal, Melanie-Claire Mallison, and the staff at the CNF.

References:

[1] Chaffer, C.L., et al. A perspective on cancer cell metastasis. Science (2011).

[2] Keys, J., et al. Assembly and use of a microfluidic device to study cell migration in confined environments. Methods in Molecular Biology (2018).

[3] Shah, P., et al. Nuclear deformation causes DNA damage by increasing replication stress. Current Biology (2021).

[4] Isermann, P., et al. Consequences of a tight squeeze: Nuclear envelope rupture and repair. Nucleus (2017).

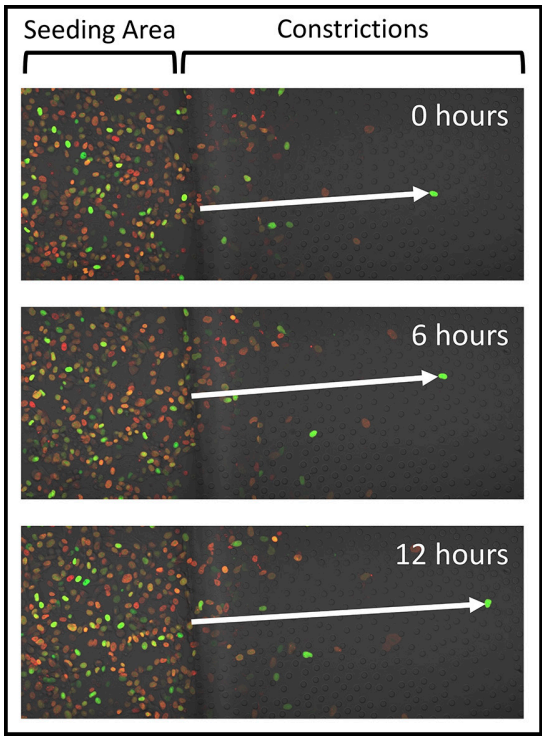

Figure 3: HT1080 fibrosarcoma cells, fluorescently labeled with NLS-GFP (green) and 53BP1-mCherry (red), in a device with a control pillar density region imaged over 12 hours. Migration distance of a single cell inside the constrictions indicated by arrow.

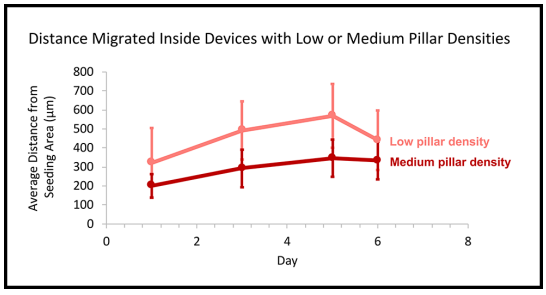

Figure 4: Distance migrated by HT1080 fibrosarcoma cells inside devices with low or medium pillar densities. n=1, 50 cells per timepoint.

Body-on-a-Chip Systems for Drug Development and *in vitro* Interactions

CNF Project Number: 731-98

Principal Investigator(s): Michael L. Shuler, Harold G. Craighead

User(s): Zhu Chen, Paula Miller

Affiliation(s): Nancy E. and Peter C. Meinig School of Biomedical Engineering; Robert Frederick Smith School of Chemical and Biomolecular Engineering, Cornell University

Primary Source(s) of Research Funding: National Center for Advancing Translational Sciences, National Science Foundation, National Institutes of Health

Contact(s): mls50@cornell.edu, hgc1@cornell.edu, zc465@cornell.edu, pgm6@cornell.edu

Primary CNF Tools Used: VersaLaser Engraver/Cutter tool, Samco UV and ozone stripper, hot press, Objet30 Pro 3D Printer, ABM contact aligner, SU-8 hot plates, SUEX/ADEX laminator, PDMS casting station, DRIE system

Abstract:

Organ-on-a-chips are microsystems that through tissue-engineering can model human organs, representing both structure and function [1]. Human cell-based multi-organ on-a-chip systems can be used for drug development [2], studying metastasis and chemotherapy. The microscale biomimetics of human organs with organ-organ interactions can be used to model human physiology and disease progression, and thus offer more accurate predictions of human responses to therapeutics and provide mechanistic insights into human diseases. Also, these models can significantly reduce drug development cost and animal usage [3-5]. Currently, we are developing several microfluidic systems, which are fabricated with tools at Cornell NanoScale Facility (CNF) and will be used to study chemotherapeutic toxicity, model cancer cell metastasis, and simulate immune responses.

Summary of Research:

Single-Pass Chip. We have designed and modified a gravity-driven microfluidic model for studying the extravasation of circulating tumor cells (CTC) through endothelium (either primary human liver sinusoidal endothelial cells (LSEC) or human umbilical cord endothelial cells (HUVEC)) into a chamber with HepG2 C3A (liver cells). The frame of this device is made from PMMA layers patterned using a CO_2 laser (VersaLaser VLS3.50), and bonded together using a hot press after a 15 min UV/Ozone (Samco UV& Ozone stripper) exposure at CNF. The propeller stirring lid of the device is fabricated using the Objet30 Pro 3D Printer from the CNF. Clear silicone sheets are also patterned with laser ablation using the VeraLaser CO_2 laser cutter. The stirring is driven by a small stir bar on a magnetic stir plate. This device allows for a continuous operation up to 24 hours while maintaining a constant concentration of CTC and evaluate of the capability of CTC (large and small clusters) from various sources to enter into the liver chamber. [Fig.1]

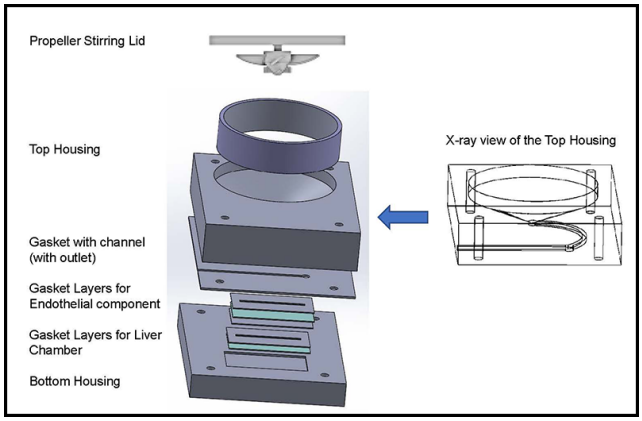

Figure 1: Design of the single pass colorectal/liver metastatic device. Schematic of the single pass device.

Unidirectional Chip Devices. We have two unidirectional chip devices (two-chamber and three-chamber chips) for studying the metastasis and drug effects. Chambers are interconnected and perfused with gravity-driven flow at physiological perfusion rates [3-5]. The flow dynamics are characterized computationally and experimentally. Our pumpless gravity-driven flow is created by using a customized programmable rocker where a common media is recirculated between the two reservoirs. Flow rates were measured to be within 15% of the designed values [6,7]. The prototype devices are initially tested for viability where the goal is to maintain a viability greater than 85%.

Two-Chamber Unidirectional Chip. We have developed and modified our original colon-liver two-chamber unidirectional chip system to model CTC liver metastasis. This two organ system interconnects colon and liver

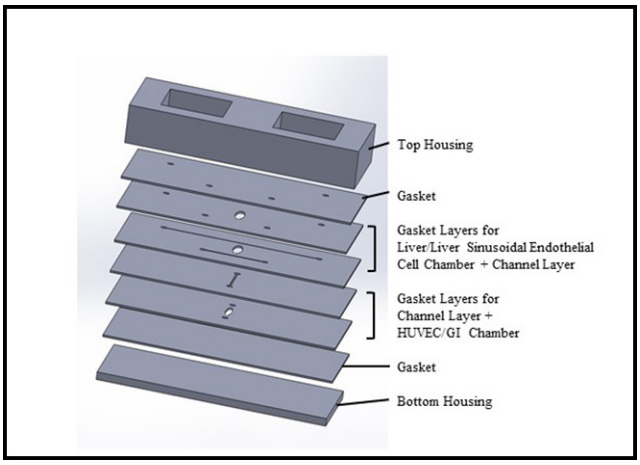

Figure 2: Design of the two-chamber unidirectional chip device. Schematic of the two-chamber unidirectional chip.

chambers. The frame of the modified device is milled out of a polycarbonate (PC) sheet at the Cornell University Olin Hall Machine Shop. Clear silicone sheets are patterned with laser ablation using the VersaLaser CO_2 laser cutter to create the chambers, channels and used for sealing the device. For this device, microfluidic channels were etched into silicone gaskets and designed to mimic human blood flow rates [3-5]. Using this colon-liver platform, we are able to incorporate organotypic CTC model into the colon chamber and create a 3D liver construct by incorporating liver cells in a hydrogel into the liver chamber. Here, we are investigating the ability of CTC from various sources to metastasize to the liver chamber. We will investigate the cellular interaction, differentiation, migration and invasion of primary tumors to evaluate contributing factors in CTC metastasis. [Figure 2]

Three-Chamber Unidirectional Chip. A three-organ microphysiological system (tumor-liver-bone marrow chip) [8] that was initially create to study chemotherapeutic toxicity with relevant drug metabolism and hematological side effects is now being used to study metastasis. We modified this device by changing the biological components of the chambers. First, normal colon cells with colon cancer organoids are plated in the colon chamber, HepG2/C3A hepatocytes (in hydrogel) are plated in the liver chamber and then the third chamber (no cells) is used as a control. For this device, microfluidic channels were etched into a layer of poly (methyl methacrylate) (PMMA) and designed to mimic human blood flow rates [3-5]. The silicone cell culture layer and PMMA channel layer were sandwiched between silicone gaskets and outer PMMA housing pieces. All layers were fabricated using the VersaLaser CO_2 laser cutter at CNF. Using this three-chamber platform, we incorporate organotypic CTC model and 3D liver constructs to investigate the metabolic stress due to CRC liver metastasis. We will investigate contributing factors in CTC metastasis by evaluating cellular interaction, differentiation, migration, invasion of primary tumor, metastatic fibroblast tumor microenvironment, and CTC selectivity. [Figure 3]

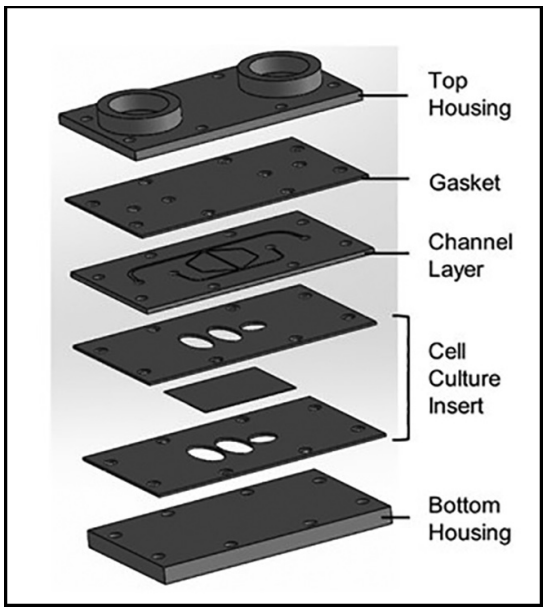

Figure 3: Design of the three-chamber unidirectional chip device. Schematic of the three-chamber unidirectional chip.

Micromechanical Cantilevers for Cell Motion Transduction. New processes were explored for fabricating silicon micromechanical cantilevers for transduction of cell motion. Process development, including addressing issues of uniformity of devices, continues.

References:

[1] NIH/NCATS. What are tissue chips, and why are they important? https://ncats.nih.gov/tissuechip/about/faq#chips.

[2] Wang YI, Carmona C, Hickman JJ, Shuler ML. Multiorgan Microphysiological Systems for Drug Development: Strategies, Advances, and Challenges. Adv Healthc Mater. 2018;7(2):1701000. doi:10.1002/adhm.201701000.

[3] Price PS, Conolly RB, Chaisson CF, Gross E a, Young JS, Mathis ET, Tedder DR. Modeling interindividual variation in physiological factors used in PBPK models of humans. Crit Rev Toxicol. 2003;33(5):469-503. doi:10.1080/713608360.

[4] Brown RP, Delp MD, Lindstedt SL, Rhomberg LR, Beliles RP. Physiological Parameter Values for Physiologically Based Pharmacokinetic Models. Toxicol Ind Health. 1997;13(4):407-484. doi:10.1177/074823379701300401.

[5] Forrester DW, Spence VA, Walker WF. The measurement of colonic mucosal.submucosal blood flow in man. J Physiol. 1980;299(1):1-11. doi:10.1113/jphysiol.1980.sp013106.

[6] Wang YI, Oleaga C, Long CJ, Esch MB, McAleer CW, Miller PG, Hickman JJ, Shuler ML. Self-contained, low-cost Body-on-a-Chip systems for drug development. Exp Biol Med. 2017; (November); 153537021769410; doi:10.1177/1535370217694101.

[7] Sung JH, Kam C, Shuler ML. A microfluidic device for a pharmacokinetic-pharmacodynamic (PK-PD) model on a chip. Lab on a Chip. 2010;10(4):446. doi:10.1039/b917763a.

[8] LaValley DJ, Miller PG, Shuler ML. Pumpless, unidirectional microphysiological system for testing metabolism-dependent chemotherapeutic toxicity. Biotech Prog. 2021. 37(2). doi: 10.1002/btpr.3105.

Silicon Nitride Cantilevers for Muscle Myofibril Force Measurements

CNF Project Number: 1255-04

Principal Investigator(s): Walter Herzog

User(s): Timothy Leonard, Andrew Sawatsky

Affiliation(s): Faculty of Kinesiology, University of Calgary, Calgary, Canada

Primary Source(s) of Research Funding: Canadian Institutes of Health Research, the Canada Research Chair for Cellular and Molecular Biomechanics

Contact(s): wherzog@ucalgary.ca, leonard@ucalgary.ca, ajsawats@ucalgary.ca

Website: https://kinesiology.ucalgary.ca/research/labs-and-centres/human-performance-lab

Primary CNF Tools Used: GCA 5X Stepper, SÜSS MA6-BA6 contact aligner, photolith spinners, Oxford 81 ion etcher

Abstract:

To measure muscle forces in the nano-Newton range, silicon nitride cantilever pairs were manufactured and used. We investigated history-dependent behaviour in cardiac muscle using a single myofibril model. Our experiments demonstrate for the first time that cardiac myofibrils display the same history-dependent properties observed in skeletal muscle, specifically force enhancement following active stretch. The giant molecular spring titin [1] is thought to play a major role in this enhanced force, possibly through interactions of regions of titin with the actin filament. However, titin in cardiac muscle is much smaller than skeletal muscle titin and is missing regions of titin (specifically N2A region) that are suggested to facilitate interactions with actin. We investigated rabbit cardiac myofibrils to see if enhanced force following stretch is present in eight samples. We observed in all tests performed, greater force after stretch compared to force in the isometric condition and at the same sarcomere length. This provides, for the first time, evidence that cardiac muscle displays history-dependent behaviour.

Summary of Research:

The active force produced by skeletal muscle is well described by the Huxley cross-bridge model [2] and the force-length relationship [3] but these well accepted paradigms cannot adequately explain greater force at the identical muscle length when the muscle is lengthened during the contraction (eccentric contraction), compared to a muscle that does not change length (isometric contraction). This history-dependent force has been observed for over 60 years, but no generally accepted mechanism has been put forth to explain it. Recently, titin interaction with other sarcomeric proteins has been proposed as a mechanism and promising work on a mutation mouse model (mdm) has provided evidence that the N2A region of titin is essential for force enhancement [4]. We hypothesize that cardiac muscle will exhibit enhanced force following active stretch because cardiac muscle contains a domain similar to the N2A region (i.e. N2AB) and so cardiac titin will interact with actin, as has been proposed for skeletal muscle.

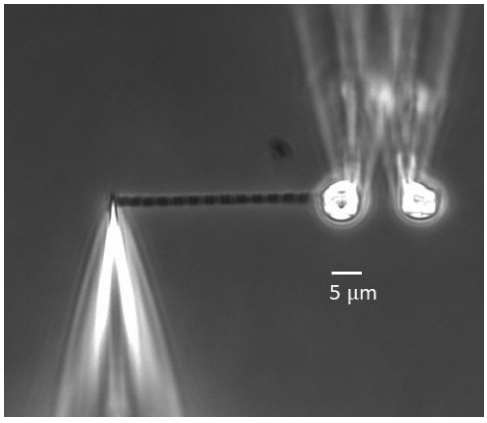

Figure 1: Myofibril attached to a glass needle for stretch-shortening and nano-levers for force measurement. Example of a myofibril with 13 sarcomeres in-series.

Myofibrils were harvested from heart ventricle muscle obtained from New Zealand White rabbits and were chemically and mechanically isolated as described in our previous work [5]. Single myofibrils were attached to nanofabricated silicon-nitride cantilevers (stiffness 150 pN/nm) [6] for force measurement at one end of the myofibril (resolution < 0.5 nN), and at the other end, a glass pipette needle attached to a piezo-motor for controlling specimen length (Figure 1).

Forces were divided by the cross-sectional area of the myofibril and reported as stress (nN/μm^2).

Myofibrils (n=8) were stretched passively from an average sarcomere length (SL) of 1.8 μm to 2 μm, held at that length, and then activated by infusing Ca^{+2} and ATP. After 10 seconds, the specimen was shortened to 1.8 μm and held for 20 seconds to allow the force transients to fade and then the specimen was rapidly stretched to 2.0 μm and held. After the stretch force transients faded, the second force measurement was made.

The isometric (SL=2 μm) and eccentric tests (SL=1.8 μm stretched to 2.0 μm) were combined in a single experiment (Figure 2). The force was recorded at two time-points: once at first vertical-red bar (75 seconds) for the isometric condition and then at the steady-state condition following the active stretch (second vertical bar-blue) at 150 seconds into the test. The eccentric stress was normalized to the isometric stress for each test and the residual force enhancement as a percentage increase (RFE) reported (Figure 3).

In all eight experiments, residual force enhancement following stretch was observed, (average increase 20%).

We show here for the first time, force-enhancement in cardiac myofibrils and this work provides insight into the possible titin-actin interaction in the eccentric condition as the mechanism underlying this phenomenon.

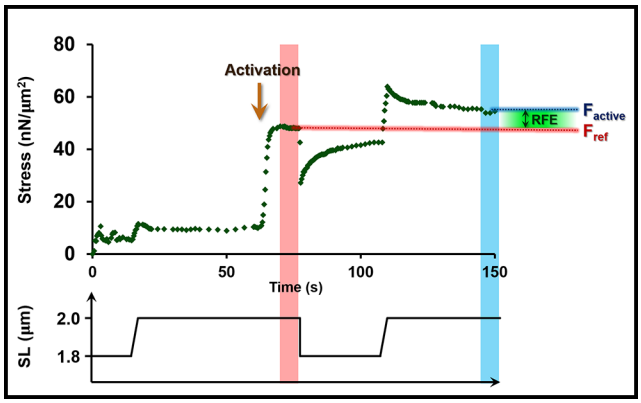

Figure 2: Isometric and steady-state isometric stress following stretch, for a single myofibril test. The residual force enhancement is formalized to the initial isometric stress.

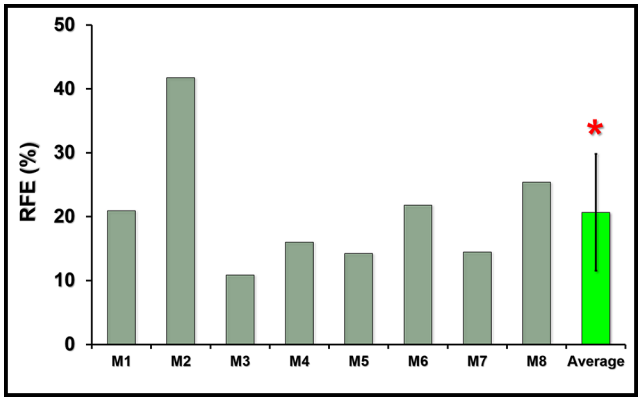

Figure 3: Residual force enhancement values for each of eight myofibrils tested. The increased stress observed following stretch compared to the isometric stress ranged from 11% to 42%, with a mean value of 20%. RFE is statistically greater than the isometric value, Wilcoxon test, a=0.05.

References:

[1] Granzier and Labeit. Muscle Nerve. 36:740-755, 2007.

[2] A.F. Huxley, Prog Biophys Biophys Chem.7:255-318, 1957.

[3] Gordon, et al., J Physiol. 184(1):170-92, 1966.

[4] K. Powers, et al. JEB. 219:1311-1316, 2016.

[5] Joumaa, et al. Eur J Physiol. 455:367-371, 2007.

[6] M. E. Fauver, et al. IEEE Trans Biomed Eng 45(7):891-898, 1998.

Nanophotonic Standing-Wave Array Trap for Single-Molecule Applications

CNF Project Number: 1738-08

Principal Investigator(s): Michelle D. Wang

User(s): Yifeng Hong

Affiliation(s): a) Department of Electrical and Computer Engineering, Cornell University; b) Department of Physics, Cornell University; c) Howard Hughes Medical Institute, Chevy Chase, Maryland

Primary Source(s) of Research Funding: Howard Hughes Medical Institute

Contact(s): mdw17@cornell.edu, yh874@cornell.edu

Website: http://wanglab.lassp.cornell.edu/

Primary CNF Tools Used: ASML DUV stepper, Oxford 100 plasma etcher, Oxford 81 etcher, Oxford 82 etcher, Unaxis 770 deep Si etcher, Heidelberg mask writer - DWL2000, SÜSS MA6-BA6 contact aligner, Gamma automatic coat-develop tool, LPCVD nitride - B4 furnace, wet/dry oxide - B2 furnace, AJA sputter deposition, Oxford PECVD, CVC SC4500 odd--even hour evaporator, Zeiss Supra SEM, Zeiss Ultra SEM

Abstract:

As a fundamental tool in single-molecule science, optical tweezers have been used broadly for decades. The Wang Lab has developed a nanophotonic standing-wave array trap (nSWAT) device, which integrates the functions of a conventional microscope-based optical tweezer into a centimeter-scaled chip. Here, we present our latest progress on nSWAT applications, focusing on high enough force generation. This increased force enables us to unzip an array of DNA molecules along the waveguide, thus providing a platform for parallel single-molecule measurements.

Summary of Research:

In the past few years, the Wang Lab has been working on developing the nanophotonic standing-wave array trap (nSWAT) device, aiming for high-throughput single-molecule manipulations and measurements [1-6]. In principle, the nSWAT is generated by the interference of two counter-propagating waves along a single-mode waveguide. Polystyrene beads attached to biomolecules like DNA can be trapped within the antinodes of the near-field evanescent waves at the waveguide surface (Figure 1). As a result, those biomolecules can be manipulated in parallel by modulation of the trapping array. For instance, a simple application of parallel DNA molecule sorting has been demonstrated [2].

To further make use of the nSWAT platform for fundamental single-molecule studies, such as an unzipping assay for protein-DNA interaction, we have to overcome the force limitation of the existing nSWAT. Recently, a more advanced version of the Si_3N_4 nSWAT (operated at 1064 nm laser) [3] has been developed to enhance the maximum trapping force applied to the biomolecules, and includes features such as minimized absorption and bending loss as well as a fastest heater reset time. Increased trapping force enables us to unzip DNA molecules, and expands opportunities to study protein-DNA interaction in a high-throughput manner.

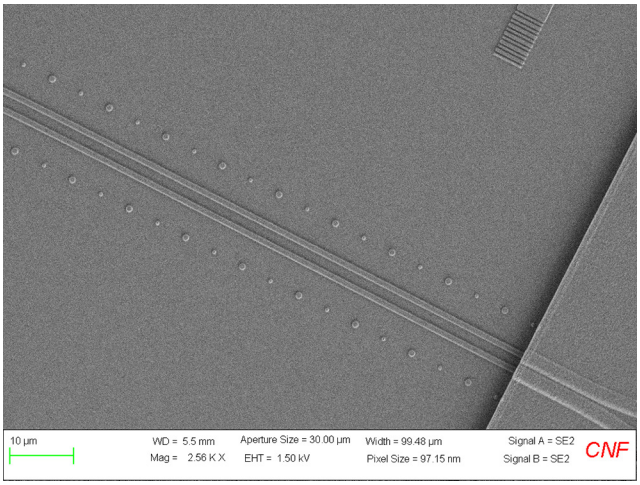

Figure 1: An SEM image of the waveguides at the trapping region (fluid pool). A standing wave is generated along each waveguide, forming a trapping array for 380 nm polystyrene beads. The dot arrays near the waveguides are fiducial marks for monitoring the global drifting during operation. (See cover for more detail.)

So far, this technique has been applied to locate a bound protein with nearly nm spatial resolution, which serves as a benchmark of on-chip optical trapping techniques. We hope this high-throughput technique can become a fundamental tool in other aspects of biological studies.

The achievements based on the nSWAT have led to six publications [1-6]. The latest demonstration of unzipping DNA to map a bound protein has been submitted for publication this year.

References:

[1] J. E. Baker, R. P. Badman, and M. D. Wang, "Nanophotonic trapping: precise manipulation and measurement of biomolecular arrays" WIREs Nanomed Nanobiotechnol. e1477 (2017).

[2] M. Soltani, J. Lin, R. A. Forties, J. T. Inman, S. N. Saraf, R. M. Fulbright, M. Lipson, and M. D. Wang, "Nanophotonic trapping for precise manipulation of biomolecular arrays" Nature Nanotechnology 9(6), 448-452 (2014).

[3] F. Ye, R. P. Badman, J. T. Inman, M. Soltani, J. L. Killian, and M. D. Wang, "Biocompatible and high stiffness nanophotonic trap array for precise and versatile manipulation" Nano Letters 16(10), 6661-6667 (2016).

[4] F. Ye, M. Soltani, J. T. Inman, and M. D. Wang, "Tunable nanophotonic array traps with enhanced force and stability" Optics Express 25 (7) 7907-7918 (2017).

[5] R. Badman, F. Ye, W. Caravan, and M. D. Wang, "High Trap Stiffness Microcylinders for Nanophotonic Trapping" ACS Appl. Mater. Interfaces 11(28), 25074-25080 (2019).

[6] R. Badman, F. Ye, and M. D. Wang, "Towards biological applications of nanophotonic tweezers", Current Opinion in Chemical Biology, 53, 158-166 (2019).

Microfluidics Channels for Zinc Metal Homeostasis

CNF Project Number: 1844-09

Principal Investigator(s): Peng Chen

User(s): Felix Alfonso

Affiliation(s): Department of Chemistry and Chemical Biology, Cornell University

Primary Source(s) of Research Funding: National Institute of Health, National Institute of General Medical Sciences

Contact(s): pc252@cornell.edu, fsa33@cornell.edu

Website: http://chen.chem.cornell.edu/

Primary CNF Tools Used: Heidelberg mask writer - DWL2000, SÜSS MA6-BA6 contact aligner, Oxford Cobra ICP etcher, Plasma-Therm deep silicon etcher, P7 profilometer

Abstract:

We constructed a custom-made microfluidic device for the control growth of *Escherichia coli* (*E. coli*) colonies in microchambers. The confinement of the cells is achieved by matching the height of the microchambers with the diameter of the *E. coli* cells. The objective of our study is to image *E. coli* strain with fluorescent protein reporters to elucidate the role individual cells play in colonies achieving metal homeostasis.

Summary of Research:

Biological processes in the gut microbiome heavily depend on the harmonious balance between microbial communities and a host. This balance is maintained by chemical and biophysical cues that are exchanged between organisms to coordinate behavior. Zinc is an essential micronutrient for all living organisms [1]. It plays a vital role in protein folding, catalysis, and gene regulation [2]. To regulate the uptake/efflux of metal ions, bacterial cells control the transcription of the protein pumps with metal-responsive transcription regulators that sense the cellular concentration of metal ions.

The purpose of this project is to quantify the management of Zn^{2+} in a microbiome and determine the role the individual cells have in the colony achieving metal homeostasis. As a model system, *Escherichia coli* (*E. coli*) will be used to study community-derived zinc metal regulation. *E. coli* cell's motility and poor adherence to a substrate make it difficult to conduct imaging studies with long time scales. Microfluidics technology is a widely accepted method to study bacterial communities in a controlled environment [3]. A microfluidic platform permits tight control of the nutrients influx and has been successfully used for long-timescale imaging studies [4].

The design of the microfluidic device is shown in Figure 1. This study focuses on community behavior; thus, we chose the width and length of the chamber to be about ~ 200 μm. The depth of the microchamber has been chosen to match the diameter of an *E. coli* cell (~ 1 μm) [5]. The high aspect ratio (200:1) is problematic due to the possibility of ceiling collapse [6] caused by the attractive forces between PDMS and the glass coverslip. Therefore, the roof is supported by regularly spaced pillars. The regularly spaced pillars were designed to have the shape of circles or squares with a diameter or length of 4 or 8 μm.

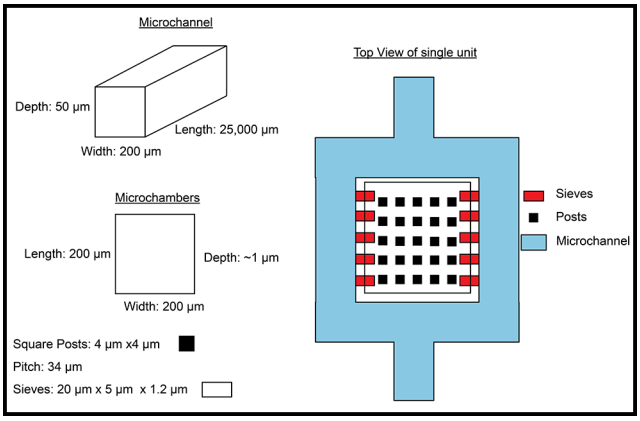

Figure 1: Schematic of the microfluidic device design of the microchannel and microchambers with the desired dimensions.

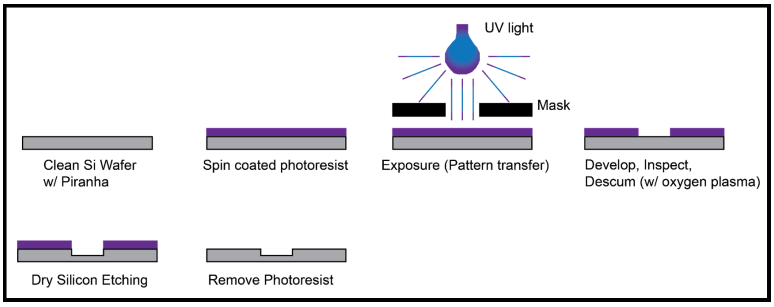

Figure 2: Fabrication scheme of the silicon mold for the microfluidic device.

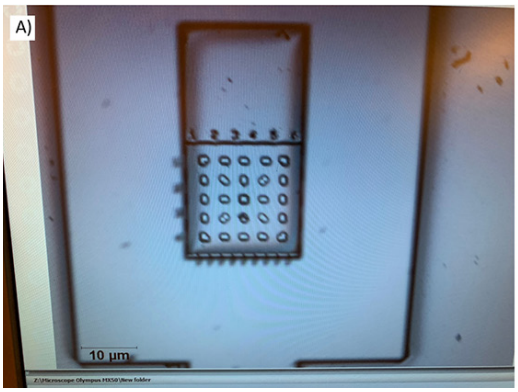

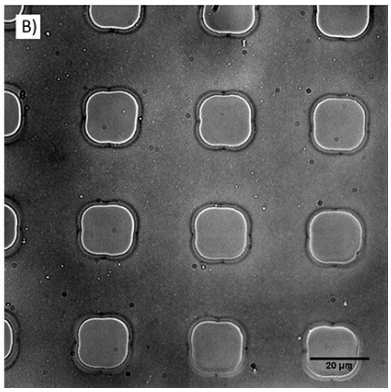

Figure 3: A) A photographed image of a prototype of the microfluidic device. B) Bright-field image of the PDMS posts used to prevent ceiling collapse.

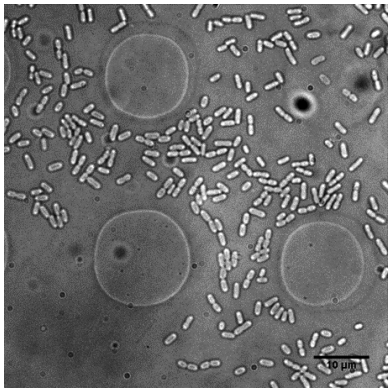

Figure 4: A bright-field image of one growth chamber filled with E. coli *cells.*

The microfluidics devices are constructed using well-established silicon nanofabrication technology. The fabrication scheme is summarized in Figure 2. Briefly, silicon wafers were cleaned with piranha solution from the Hamatech wafer processor. Afterwards, they were spin coated with photoresists. Photoresist was removed 2 mm from the edge of the wafer using the edge bead removal system. The substrate was patterned using a pre-patterned photomask made using the Heidelberg mask writer - DWL2000. The SÜSS MA6-BA6 contact aligner was used for the UV light exposure of the wafer. After developing the wafer and cleaning it with a brief oxygen plasma. The chamber was created by etching about ~ 1 μm of silicon using the Oxford Cobra ICP etcher. The photoresist was removed using the photoresist stripper bath. The height of the chamber was measured using a profilometer. The same process was repeated to create the flow channels; however, the Plasma-Therm deep silicon etcher was used for the etching step to create channels with depths of about 50 μm.

The final step is coating the silicon mold with a hydrophobic molecular monolayer such as tridecafluoro-1,1,2,2-tetrahydrooctyl trichlorosilane (FOTS). An image of the prototype of the microfluidic device is shown in Figure 3A. After casting PDMS on the silicon mold, the microfluidic devices were bonded to coverslips and inspected using a microscope. The brightfield image of the chamber shows a regularly spaced PDMS post preventing the collapse of the ceiling (Figure 3B).

The loading of the cells into the chambers is a challenge. One approach is to increase the gauge pressure inside the devices to inflate the microchannels, and cause the ceiling to bulge up, increasing the height of the channels and allowing the passage of the cells. Reducing the pressure causes the channels to deflate, and the ceilings return to their original height. The brightfield image shown in Figure 4 shows an example of a chamber loaded with *E. coli* using the procedure described previously. The future step is to test this prototype and optimize the conditions for the successful completion of the project.

References:

[1] R. R. Robert B. Saper, Zinc: An Essential Micronutrient. Am. Fam. Physician. 79, 768 (2009).

[2] A. R. Blanden, X. Yu, A. J. Blayney, C. Demas, J.-H. Ha, Y. Liu, T. Withers, D. R. Carpizo, S. N. Loh, Zinc shapes the folding landscape of p53 and establishes a pathway for reactivating structurally diverse cancer mutants. Elife. 9 (2020), oi:10.7554/eLife.61487.

[3] F. Wu, C. Dekker, Nanofabricated structures and microfluidic devices for bacteria: from techniques to biology. Chem. Soc. Rev. 45, 268-280 (2016).

[4] D. Binder, C. Probst, A. Grünberger, F. Hilgers, A. Loeschcke, K.-E. Jaeger, D. Kohlheyer, T. Drepper, Comparative Single-Cell Analysis of Different E. coli Expression Systems during Microfluidic Cultivation. PLoS One. 11, e0160711 (2016).

[5] A. Groisman, C. Lobo, H. Cho, J. K. Campbell, Y. S. Dufour, A. M. Stevens, A. Levchenko, A microfluidic chemostat for experiments with bacterial and yeast cells. Nat. Methods. 2, 685-689 (2005).

[6] Y. Y. Huang, W. Zhou, K. J. Hsia, E. Menard, J.-U. Park, J. A. Rogers, A. G. Alleyne, Stamp collapse in soft lithography. Langmuir. 21, 8058-8068 (2005).

Sample Cells for High Pressure Biological X-Ray Solution Scattering

CNF Project Number: 1940-10

Principal Investigator & User: Richard E. Gillilan

Affiliation(s): Macromolecular Diffraction Facility of the Cornell High Energy Synchrotron Source (MacCHESS), Cornell High Energy Synchrotron Source; Cornell University

Primary Source(s) of Research Funding: National Science Foundation DMR-1829070, National Institutes of Health 1-P30-GM124166-01A1 and NYSTAR

Contact(s): reg8@cornell.edu

Website: https://www.chess.cornell.edu/macchess/hp_more

Primary CNF Tools Used: VersaLaser VLS3.50 engraver/cutter tool

Abstract:

Over 80% of the biomass of Earth consists of organisms living under extreme conditions of temperature, pressure, and chemical environment. As a potentially rich source of new tools and deeper understanding of the history and limits of life, there is much renewed interest in conducting biophysical and structural biological measurements under these types of conditions. We have developed an X-ray transparent, biologically compatible sample environment for conducting small angle X-ray solution scattering at hydrostatic pressures of up to 400 MPa (58,000 psi). The disposable, low-volume cells are designed to allow pressure equalization between the sample and pressurizing medium without excessive flexing of the thin X-ray transparent windows. The current design has been routinely and successfully used at the Cornell High Energy Synchrotron's High Pressure Biology facility (HP-Bio) since late 2019, including a remote "hands-on" training course in April 2021.

Summary of Research:

Though we surface dwellers are rarely aware of it, high hydrostatic pressure is the norm for most of the biomass on Earth. Organisms living in the deep ocean and subsurface experience pressures that can reach beyond 100 MPa (14500 psi). Biomolecules do not merely compress in response to external pressure; they rearrange their structure in informative ways to minimize total volume, including that of the surrounding water [1]. X-ray solution scattering (SAXS) is well-suited to study such changes, but special design considerations are necessary to handle the high pressure.

We recently introduced an easy-to-use SAXS system capable of maintaining up to 400 MPa of hydrostatic pressure on biological samples [2]. The system uses X-ray transparent single crystal diamond windows combined with a quick sample change mechanism (Figure 1A,B). To prevent the pressurizing medium (water) from mixing with the biological samples, we designed disposable laser cut PMMA cells with thin, X-ray transparent 7 μm polyimide film windows. At 400 MPa, the specific volume of water has declined by a significant amount, 11.6%. The chemically inert silicone grease used to seal the cells can flow, allowing pressure between the sample and external pressurizing water to equalize. The cells have also been adapted successfully to hold standard 1.5 mm glass sample capillaries for use in studying phase changes in deep sea lipid samples (Winnikoff and Budin, personal communication, 2021).

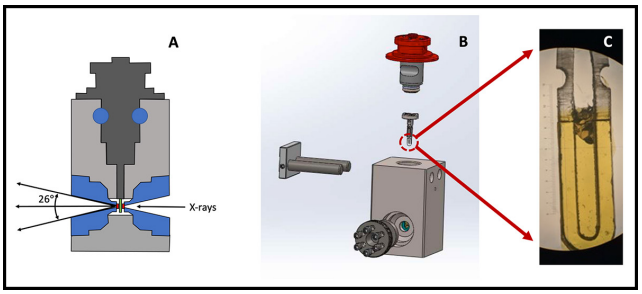

Figure 1: High pressure small-angle solution scattering system. X-rays enter the cell from the right (A) traveling through a single-crystal diamond window, passing through a sealed plastic sample cell at center and emerging from the second diamond window scattered at angles up to 26°. Water is used as a pressure medium. A locking pin and piston-style o-ring system allows easy access to the disposable inner PMMA cell (B), which has 7 µm polyimide windows to minimize X-ray scatter and a grease seal to allow for pressure equalization.

References:

[1] Ando N, Barquera B, Bartlett DH, Boyd E, Burnim AA, et al. 2021. The Molecular Basis for Life in Extreme Environments. Annu. Rev. Biophys.

[2] Rai DK, Gillilan RE, Huang Q, Miller R, Ting E, et al. 2021. High-pressure small-angle X-ray scattering cell for biological solutions and soft materials. Journal of Applied Crystallography. 54(1): 111-22.

Bacterial Mechanics and Mechanobiology

CNF Project Number: 1970-10

Principal Investigator(s): Christopher J. Hernandez

User(s): Christine E. Harper, Junsung Lee

Affiliation(s): Sibley School of Mechanical and Aerospace Engineering, Meinig School of Biomedical Engineering; Cornell University

Primary Source(s) of Research Funding: Army Research Office Grant Number W911NF-19-1-0121

Contact(s): cjh275@cornell.edu, ceh272@cornell.edu, jl3939@cornell.edu

Website: hernandezresearch.com

Primary CNF Tools Used: AJA sputter deposition, ASML stepper, PT 770, Oxford 100, MOS clean anneal

Abstract:

Bacteria naturally experience mechanical forces in the environment. Bacteria experience mechanical forces as they grow and divide, swim in fluids, attach to surfaces, and grow in biofilms. Although it has been well established that mechanical forces are key signals for eukaryotic cell development and physiology, much less is known about the importance of mechanical forces for bacterial cells. This is in part because applying controlled mechanical stimuli to bacterial cells is technically challenging due to the small scale of bacteria (~ 1 μm wide). We developed a microfluidic platform to apply mechanical stimuli to individual, live bacteria cells. We use this microfluidic platform to apply mechanical loads to *E. coli* and *V. cholerae* cells in order to understand how mechanisms of antibiotic resistance respond to mechanical stimuli. Additionally, we use this microfluidic platform in conjunction with finite element modelling to quantify the mechanical properties of the bacterial cell envelope.

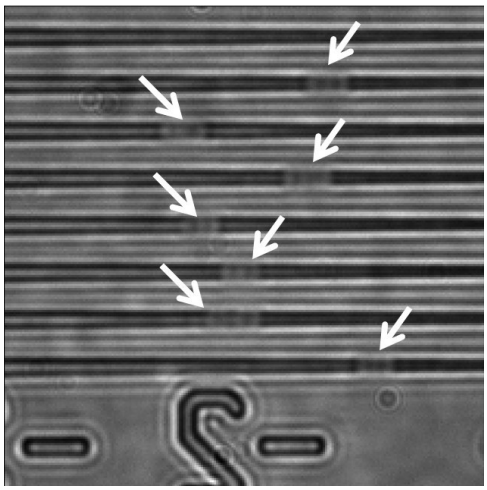

Figure 1: E. coli *cells trapped within the tapered channels of the microfluidic device. Fluid pressure is used to flow the bacteria into the tapered channels.*

Summary of Research:

Our work involves the use of microfluidic devices to apply a mechanical stimuli to individual bacteria. Within our devices, fluid pressure pushes individual bacteria into narrow tapered channels (Figure 1). The bacteria experience mechanical loading from the hydrostatic fluid pressure as well as contact with the tapered channels walls (Figure 2). The amount of mechanical loading a cell experiences depends on the fluid pressure, which is varied strategically within the device. During a single experiment, different cells experiencing different magnitudes of mechanical loading can be observed simultaneously. The bacteria remain alive while trapped in the tapered channels and continue to elongate and divide. Cells remain viable for up to 12 hours in the devices.

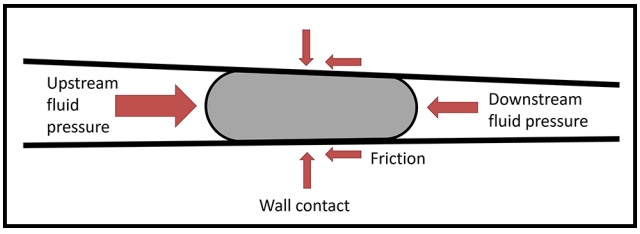

Figure 2: The bacteria cells experience mechanical loading in the tapered channels due to the fluid pressure, which varies from the upstream end to the downstream end.

Key advantages of this microfluidic platform include minimal sample preparation, no chemical immobilization or labeling, and the ability to analyze hundreds of cells at once [1].

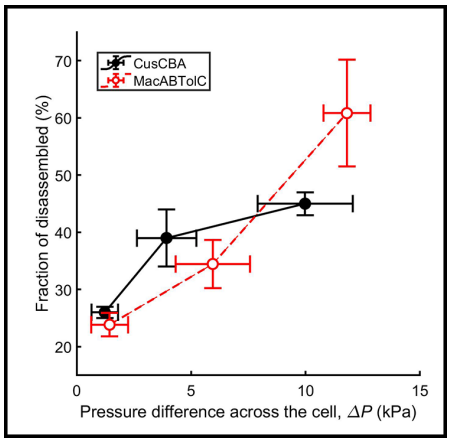

Figure 3: Increased mechanical loading (pressure difference across the cell), was shown to increase disassembly of the multicomponent efflux complexes CusCBA and MacABTolC in E. coli.

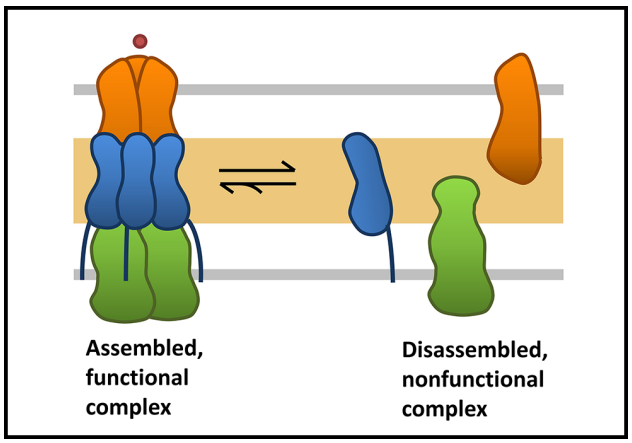

Figure 4: Multicomponent efflux complexes can be in an assembled and functional form or a disassembled and nonfunctional form. Disassembled complexes are unable to efflux toxins and antibiotics.

We manufacture our microfluidic devices on fused silica glass wafers using deep UV photolithography to achieve nano-scale features (250 nm smallest dimension). These glass-on-glass devices are manufactured using the AJA sputter deposition, ASML, PT770, Oxford 100, VersaLaser, and MOS clean anneal tools.

We are investigating the effects of mechanical stress and strain on two systems of antibiotic resistance found in bacteria: multicomponent efflux complexes and two component signal transduction systems. Multicomponent efflux complexes create channels that cross the cell envelope of bacteria and are used to pump toxins and antibiotics out of the cell. Our data suggests that the assembly and function of the multicomponent efflux complex CusCBA in *E. coli*, which effluxes the toxin copper, is impaired by increased mechanical loading (Figure 3) [2].

Preliminary evidence shows that other trans-envelope multicomponent complexes are also sensitive to the mechanical stress experienced by the cell. Disassembly of the multicomponent efflux complex MacABTolC, which effluxes macrolide antibiotics, also increases with the magnitude of mechanical loading (Figure 3) [3]. Disassembled CusCBA and MacABTolC complexes are nonfunctional and incapable exporting copper toxins and antibiotics, suggesting toxin and antibiotic resistance of mechanically stressed cells is reduced (Figure 4).

Two-component signal transduction systems are a key mechanism bacteria use to sense external stimuli and respond by altering gene expression. We are currently investigating a two-component system in *V. cholerae* that controls cell wall homeostasis and is essential for resistance to antibiotics that damage the cell wall. Preliminary work shows that this signaling pathway is activated by mechanical loading in our microfluidic device, providing exciting evidence that mechanical stimuli can affect gene expression in bacteria.

We are also working to better understand bacterial mechanical properties by combining experimental data from the microfluidic devices with finite element modelling to calculate numerical estimates for the Young's Modulus of the bacterial cell envelope. Establishing a reliable method of measuring the mechanical properties of the bacterial cell envelope will help us identify subcellular components that contribute to bacterial mechanics as well as how different environmental factors such as antibiotic treatment can change bacterial mechanical properties.

Conclusions and Future Steps:

So far our research has shown that mechanical stress and strain impairs the proper assembly and function of the cellular machinery needed for toxin and antibiotic efflux in *E. coli*. We also have preliminary evidence that a two-component system in *V. cholerae* regulates gene expression in response to mechanical stimuli.

In the future we will focus on using our microfluidic device to quantify the mechanical properties of different components of the bacterial cell envelope.

References:

[1] X. Sun, W.H. Weinlandt. H. Patel, M. Wu, C.J. Hernandez. (2014) "A Microfluidic Platform for Profiling Biomechanical Properties of Bacteria." Lab on a Chip. 14 (14), 2491-2498. NIHMS600175.

[2] L.A. Genova, M.F. Roberts, Y.C. Wong, C.E. Harper, A.G. Santiago, B. Fu, A. Srivastava, W. Jung, L.M Wang, Krzemiski, X. Mao, X. Sun, C.Y. Hui, P. Chen, C.J. Hernandez. (2019) "Mechanical stress compromises multicomponent efflux complexes in bacteria". Proc. of the National Academy of Sciences U. S. A. 116 (51) 25462-25467.

[3] C.E. Harper, W. Zhang, P. Chen, C.J. Hernandez. (2020) "Mechanical stress promotes disassembly of the antibiotic efflux complex MacAB-TolC". Biophysical Society AM. San Diego, CA, USA.

Design and Application of Microfluidic Devices to Study Cell Migration in Confined Environments

CNF Project Number: 2065-11

Principal Investigator(s): Jan Lammerding

User(s): Richa Agrawal, Maggie Elpers, Elisabeth Wang

Affiliation(s): Meinig School of Biomedical Engineering, CNF, Weill Institute, Cornell University

Primary Source(s) of Research Funding: National Institutes of Health award R01 HL082792; National Institutes of Health award R01 GM137605; National Institutes of Health award 1U54 CA210184; Department of Defense Breast Cancer Research Program Breakthrough Award BC150580; National Science Foundation CAREER award CBET-1254846; 2021 CNF REU Program via National Science Foundation under Grant No. NNCI-2025233 (Wang)

Contact(s): jan.lammerding@cornell.edu, ra664@cornell.edu, mae228@cornell.edu, emw239@cornell.edu

Website: http://lammerding.wicmb.cornell.edu/

Primary CNF Tools Used: Plasma-Therm 770 deep silicon etcher, Oxford Cobra etcher, Heidelberg mask writer - DWL2000, SÜSS MA6 contact aligner, Anatech SCE-110-RF resist stripper, P-7 profilometer, MVD 100

Abstract:

The ability of cells to migrate through tissues is an essential factor during development, tissue homeostasis, and immune cell mobility. At the same time, it enables cancer cells to invade surrounding tissues and metastasize. We have created microfluidic devices that mimic the narrow, heterogeneous interstitial spaces and that can be used to study nuclear mechanobiology during confined migration. Using these devices in combination with fluorescent imaging, we have developed a method to assess the confined migration fitness of varying cell types.

Research Summary:

During *in vivo* migration, cells such as immune cells, fibroblasts, or metastatic tumor cells traverse interstitial spaces as small as 1-2 μm in diameter. This 'confined migration' requires the deformation not only of the soft cell body but also the rate-limiting step of deforming the large (5-10 μm diameter) and relatively rigid nucleus [1]. To study these processes in more detail, we have previously designed and built polydimethylsiloxane (PDMS) microfluidic devices to model the tight three-dimensional constrictions that metastatic cancer cells may encounter during the metastatic process [2]. These devices support a wide range of cell lines and enable high-quality fluorescence imaging of nuclear lamina bucking, chromatin strain, DNA damage and nuclear rupture/blebbing and repair [2-4]. However, these devices require time-consuming single-cell analysis, do not fully mimic the heterogeneously confining nature of interstitial spaces, and do not allow use of sufficient cell numbers for biological and genomic analyses of cells that have migrated through the confined spaces due to their relatively small constriction areas (Figure 1).

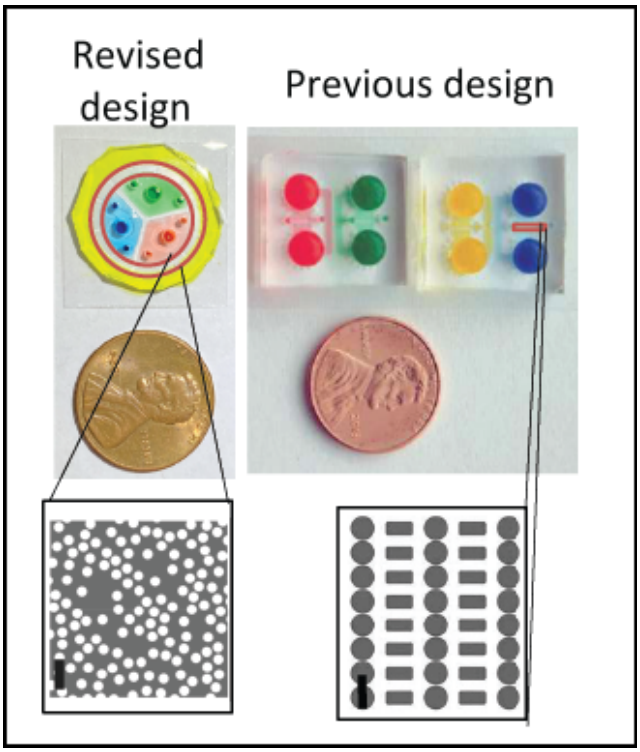

Figure 1: Overview of cancer cell migration device. Top: Partial figure reproduced from Davidson, et al. [2]. Previous PDMS microfluidic devices bonded on glass coverslips and filled with food coloring dye. Bottom: New design of "random pillar" microfluidic devices also bonded to glass coverslip and filled with food coloring. CAD for constriction areas of each design shown (outlined in red on left). Scale bars: 30 µm. All devices have migration areas with 5 µm height. Figure adapted from manuscript submitted to Methods in Molecular Biology.

To overcome these limitations, we have designed novel migration devices that mimic the intermittent confinement of interstitial environments using a precisely controlled but heterogeneous "field of pillars" with variable spacing

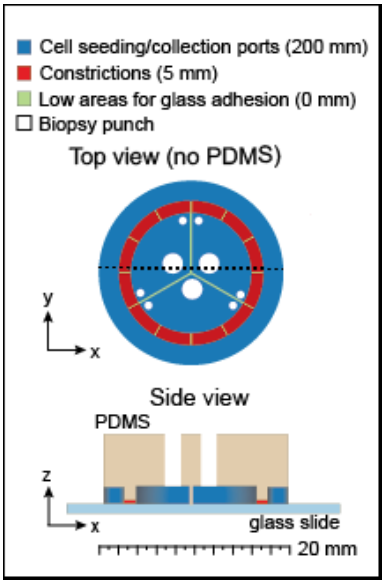

Figure 2: Schematic overview of the PDMS migration device. Top and side view of the device after bonding to glass slide to create a confined environment for cancer cell migration (red area). Figure adapted from manuscript submitted to Methods in Molecular Biology.

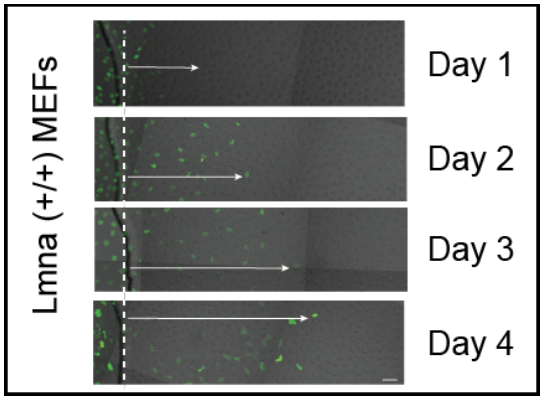

Figure 3: Cell migration in microfluidic device. Representative image series to show usage of microfluidic devices to determine migratory fitness as a function of distance traveled from seeding port into constriction area (white arrows) over four days. Figure adapted from manuscript submitted to Methods in Molecular Biology.

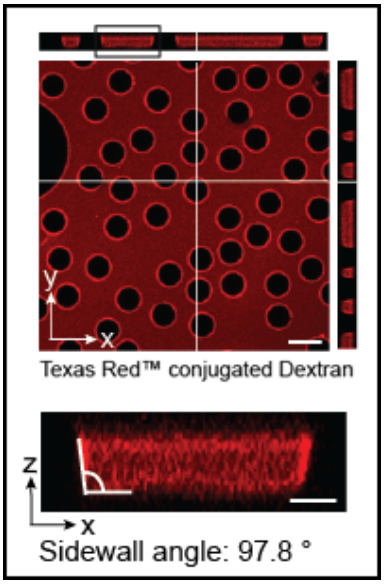

Figure 4: Confocal 3D reconstruction of confined migration area. The PDMS microfluidic device was bonded to a glass coverslip, filled with fluorescent TexasRed-conjugated Dextran, and imaged by confocal microscopy to create a 3D image stacks. Orthogonal projection used to measure sidewall angle, α, of 97.8°. Scale bars: 4 μm. Figure adapted from manuscript submitted to Methods in Molecular Biology.

(Figures 1 and 2). These new devices enable not only time-lapse microscopy, but also straightforward assessment of migratory fitness based on the distance traveled by the cells from the seeding port (Figure 3). These devices are also more amendable to enable collection of large numbers of cells following confined migration. Thus, the new devices present a high-throughput method for observing the short- and longer-term effects mechanically induced nuclear deformation and rupture has on the tumor cells.

In addition to the design, we have also improved the microfabrication methods of wafer used as the mold for the PDMS devices. Wafers for previous device generations were generated using either a thin layer of SU-8 photoresist or reactive ion etching (RIE) fabrication using the photonics etch in the Unaxis 770 deep silicon etcher. However, SU-8 lacked the fidelity to reproduce our fine features (1 μm), and repeated molding and removal of PDMS would, over time, weaken the SU-8/silicon substrate bond, eventually resulting in the delaminating of features. RIE etching in the Unaxis 770 enabled us to create our desired features but required time-consuming seasoning and re-seasoning of the chamber before and after the long photonics etch, as it is traditionally a deep reactive ion etching (DRIE) tool.

For the new devices, we shifted the nanofabrication process to etching using hydrogen bromide in the Oxford Cobra etcher, which has proven to be a highly efficient, reliable method to achieve vertical sidewalls (Figure 4). This revised approach has a faster etch rate than our previous RIE process and enabled us to improve the fidelity of our critical features, while also reducing the fabrication time and costs by more than two thirds.

We highly recommend etching using hydrogen bromide for the creation of PDMS microfluidic devices.

Future fabrication efforts will be focused on transitioning this process to a stepper, as this will enable us to create "taller" constrictions to serve as a vertically "unconfined control" (> 10 μm), which cannot currently be performed using HBr etching. The stepper approach will also enable additional modularity for device layout on wafers and allow us to produce our submicron features with greater ease, instead of the current "trial-and-error" exposure arrays required for the contact lithography process. Taken together, these examples illustrate new uses of the available nanofabrication technologies to create improved *in vitro* models to study cancer cell migration.

References:

[1] Davidson, P. M., Denais, C., Bakshi, M. C., and Lammerding, J. Nuclear deformability constitutes a rate-limiting step during cell migration in 3-D environments. Cell. Mol. Bioeng. 7, 293-306 (2014).

[2] Davidson, P. M., Sliz, J., Isermann, P., Denais, C., and Lammerding, J. Design of a microfluidic device to quantify dynamic intra-nuclear deformation during cell migration through confining environments, Integrative Biology, Volume 7, Issue 12, December 2015, Pages 1534-1546, https://doi.org/10.1039/c5ib00200a.

[3] Shah, P., et al. Nuclear Deformation Causes DNA Damage by Increasing Replication Stress. Curr. Biol. 31, 753-765.e6 (2021).

[4] Denais, C. M. et al. Nuclear envelope rupture and repair during cancer cell migration. Science Vol. 352, Issue 6283, pp. 353-358 (2016).

Microfabrication of Fixed Length Sample Holders for Cryogenic Small Angle X-Ray Scattering

CNF Project Number: 2157-12

Principal Investigator(s): Robert Thorne

User(s): David Moreau, Jonathan Clinger, Liam Barnes

Affiliation(s): Cornell Laboratory of Atomic and Solid State Physics, Cornell University

Primary Source(s) of Research Funding: National Institutes of Health

Contact(s): ret6@cornell.edu, dwm265@cornell.edu

Website: https://www.lassp.cornell.edu/Thorne/

Primary CNF Tools Used: Heidelberg mask writer - DWL2000, SÜSS MA6-BA6 contact aligner, Oxford 81/82, VersaLaser engraver/cutter tool, YES polyimide curing oven, SUEX laminator, Hamatech hot piranha, LPCVD CMOS Nitride - E4, Class II resist room

Abstract:

Small-angle X-ray scattering (SAXS) is a key tool for probing the structure and function of proteins, nucleic acids, and macromolecular complexes. Most synchrotron sources have dedicated BioSAXS beam lines, but efforts to improve their throughput have not kept pace with user demand. Large sample volumes and low duty cycles are critical bottlenecks in the expansion of BioSAXS. Cryogenic sample freezing overcame these bottlenecks in an analogous X-ray technique, macromolecular crystallography. Cryocooling significantly reduces the effects of X-ray radiation damage, reducing the necessary sample volume to collect adequate amounts of data, and eases the sample handling procedure of sensitive or unstable samples. Likewise, CryoSAXS should require much smaller sample volumes per measurement, allow sample preparation in the home lab immediately after purification, easy sample storage and shipping, and automated high-throughput data collection. This will enable dramatically more efficient use of both biomolecules and synchrotron beam time, and significantly expand the potential scope of BioSAXS studies.

Summary of Research:

We envision CryoSAXS as a routine method analogous to cryocooling in macromolecular crystallography (MX). The reduction in radiation damage at T = 100 K significantly reduces the amount of protein required per measurement and sample holders compatible with standard macromolecular cryocrystallography (MX) infrastructure could be transformative step in increasing the throughput and potential of BioSAXS. CryoSAXS could be especially useful for high-throughput parameter and ligand interaction screening, the study of difficult to produce proteins or complexes, and extremely radiation sensitive targets, applications in which BioSAXS may have the greatest impact on human health.

Despite the demonstrations of its potential [1,2], the lack of a robust experimental platform has prevented CryoSAXS from becoming a routine experimental technique. The need to subtract a highly matched background scattering pattern from the macromolecule's scatter and the difficulty in vitrifying bulk-like solutions have posed serious technical challenges for the development of sample holders adequate for routine use. Shown in Figure 1 is a new generation of CryoSAXS devices we recently developed using microfabrication techniques at the Cornell NanoScale Science and Technology Facility (CNF).

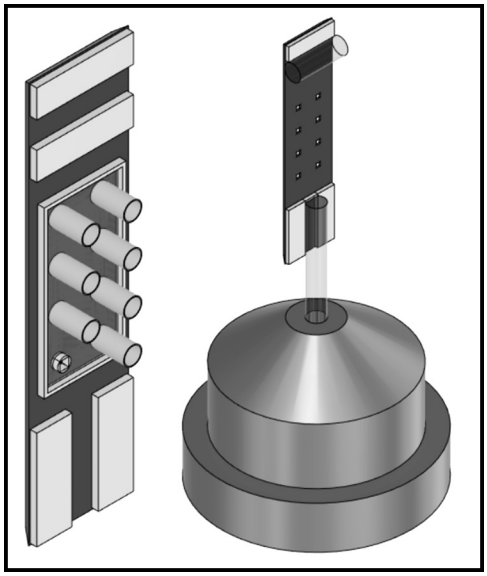

Figure 1: Images of CryoSAXS sample devices. The sample is held in place between two silicon nitride X-ray windows by Kapton® tube. The X-ray passes axially through the tubing. Multiple sample cells are present in a single device in two rows. One row contains solutions with a macromolecule and the other is analogous solutions without the macromolecule to be used for background subtraction.

These devices constrain the sample held between two silicon nitride windows at a 1 mm fixed pathlength. Double-sided polished wafers coated in 500 nm of low-pressure chemical vapor deposition silicon nitride using

the LPCVD CMOS nitride furnace (E4). Using the MA6-BA6 contact aligner, one side of the wafer was patterned with photoresist. The nitride was then dry etched with the Oxford 81 plasma etcher for a later potassium hydroxide (KOH) wet etch. SUEX was laminated onto the other side and patterned with backside alignment using the MA6-BA6 contact aligner. The SUEX features serve as guides for alignment and to help position tubes. A KOH wet etch then formed the X-ray windows and diced the wafer. The VersaLaser was used to cut spacers from 1 mm diameter quartz glass rods and affixed to one wafer pieces. Using jigs for cutting and alignment, 1 mm long Kapton® tubing was cut and glued to the devices. The devices are filled from the open end of the tube, then a second wafer piece is affixed to the top of the device to seal the sample. The samples are then cryogenically frozen in a cold nitrogen gas stream at T = 100 K for data collection.

X-ray data collection was performed at Cornell High Energy Synchrotron Source (CHESS) beamline ID7A and NSLS-II beamline 16ID for the protein apoferritin using 35% w/w propylene glycol as a cryoprotectant. Figure 2 shows results from apoferritin at several protein concentrations.

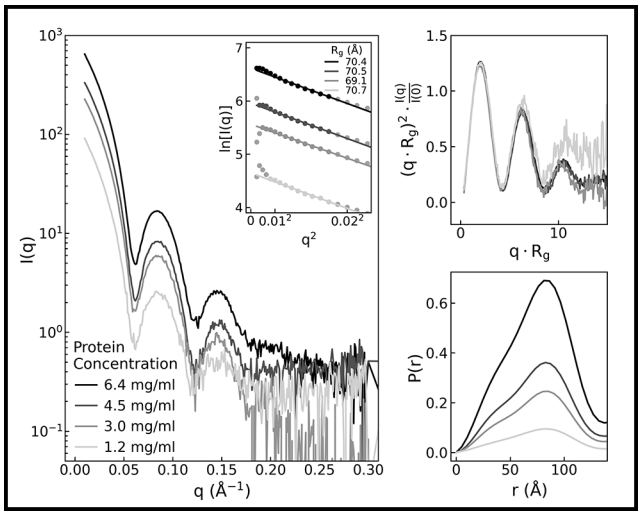

Figure 2: Background subtracted X-ray diffraction intensity from apoferritin at different concentrations.

References:

[1] Meisburger, S. P., et al., (2013) Biophys. J., 104, 227-236.

[2] Hopkins, J. B., et al., (2015) J. Appl. Cryst. 48, 227-237.

Metasurface-Enhanced Infrared Spectroscopy for the Measurement of Live Cells

CNF Project Number: 2472-16

Principal Investigator(s): Gennady Shvets

User(s): Steven He Huang, Po-Ting Shen, Aditya Mahalanabish

Affiliation(s): Applied and Engineering Physics, Cornell University

Primary Source(s) of Research Funding: National Cancer Institute of the National Institutes of Health award number R21 CA251052; National Institute of General Medical Sciences of the National Institutes of Health award number R21 GM138947

Contact(s): gs656@cornell.edu, hh623@cornell.edu, ps944@cornell.edu, am2952@cornell.edu

Website: http://shvets.aep.cornell.edu

Primary CNF Tools Used: JEOL 9500, CVC SC4500 evaporator, Zeiss Supra SEM, PDMS casting station, Anatech resist strip, Oxford PECVD

Abstract:

Infrared (IR) spectroscopy for the label-free, nondestructive analysis of biological samples is a rapidly expanding area of research. We have developed Metasurface-Enhanced Infrared Spectroscopy (MEIRS) as a novel tool to perform spectral analysis of live cells in standard cell culture conditions. The cells are cultured on plasmonic nanoantennas (metasurface), and the plasmonic hotspots are used to enhance the IR signal. We have used MEIRS to track the spectral changes in the cells *in situ* as they are being treated with different chemical compounds. We are also investigating the effect of surface functionalization on the metasurface, with the aim of enhancing cellular signal by increasing the overlap between the cells and the infrared optical field.

Summary of Research:

Infrared (IR) spectroscopy is widely used to identify chemical compounds through their molecular vibration fingerprints and has recently found applications in the biological analysis as a tool for histology and cytopathology, identifying tumor tissues from normal tissues and monitoring the effect of chemotherapeutics on cancer cells. We have developed a novel technique called Metasurface-Enhanced Infrared Spectroscopy (MEIRS) to measure live cells in physiological conditions. In MEIRS, cells are seeded on a planar array of gold plasmonic nanoantennas called metasurfaces. These resonant nano-antennas support plasmonic hot spots in their vicinity, enhancing the light-matter interaction and IR absorption. In the past, we have used MEIRS to detect spectroscopic changes in response to cellular dissociation and cholesterol depletion [1]. Our current work focuses on further extending the application of this technique to the measurement of cellular response from chemotherapeutics, as well as exploring different chemical functionalization to improve the sensing capability of the device.

The plasmonic metasurfaces are fabricated in the CNF cleanroom. Metasurfaces are fabricated on IR-transparent CaF_2 substrates. First, patterns are defined on poly(methyl methacrylate) (PMMA) using electron beam lithography with the JEOL 9500 system. This is followed by gold evaporation and lift-off in acetone to create the gold nanoantennas. Once the fabrication is done, Anatech resist strip is used to clean the metasurface and remove any resist residues. To perform *in situ* spectroscopy with live cells, we use a polydimethylsiloxane (PDMS) based flow chamber to

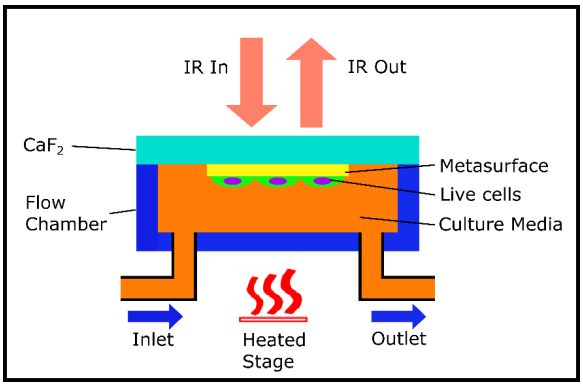

Figure 1: Schematic drawing of the flow-chamber setup for in situ *IR spectroscopy of live cells.*

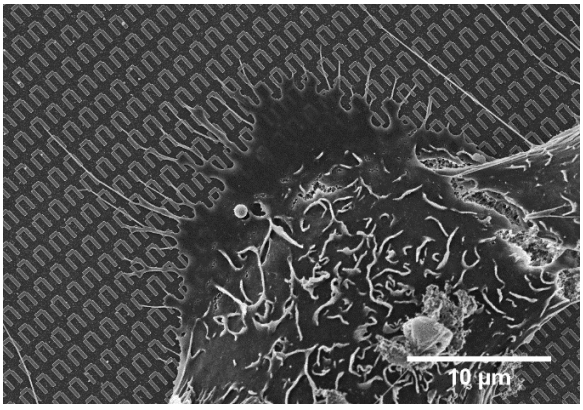

Figure 2: SEM of A431 cells grown on the plasmonic metasurface.

maintain physiological conditions, which is also fabricated at the CNF. A schematic drawing of our measurement setup is shown in Figure 1. We use human squamous carcinoma cell line A431 cells as a model system to investigate the cellular response. Scanning electron microscope (SEM) images of the cells on the metasurface (Figure 2) shows that the cells preferentially attach to the gold nanostructures rather than the CaF_2 substrate.

Using MEIRS, we have investigated the action of tricarbonyl rhenium isonitrile polypyridyl (TRIP) complex [2], a novel chemo-therapeutic developed by our collaborator (Wilson group, Cornell University), on A431 cells. TRIP has been previously shown to induced endoplasmic reticulum (ER) stress that eventually leads to apoptosis. Figure 3 shows the detection of protein absorbance signal with MEIRS in real-time while the cells are being treated by TRIP at different concentrations. The control group showed a slight increase in protein signal, while TRIP-treated cells showed clear reduction in protein signal. The protein signal reduction is larger for a higher dosage of TRIP and this is in line with what we expect, given that TRIP can induce unfolded protein response through ER stress.

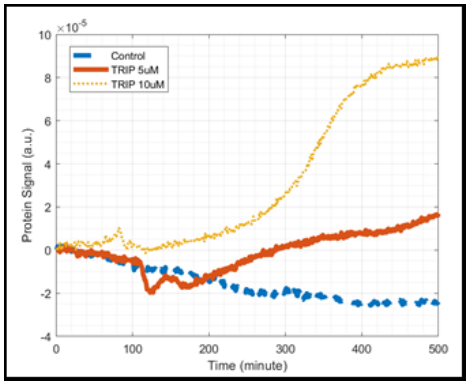

Figure 3: Protein signal from A431 cells in response to TRIP treatment. Infrared spectra collected in real-time are analyzed with principal component analysis (PCA). The spectral features at amide I and amide II absorption peaks are captured by the first principal component, the score from which is shown as the protein signal. The +y direction corresponds to a decrease in protein signal from cells.

To improve the sensitivity of the metasurface we use chemical functionalization to achieve cell blocking on the IR transparent substrate while enhancing their attachment to the metallic antennas. The interaction between the evanescent fields of the metasurface and the cells depends principally on the placement of their focal adhesion on the metasurface. This functionalization process aims to increase the overlap of the cells with the metasurface hotspot, due to which we expect a significant increase in the spectroscopic intensity.

To controllably block cell adhesion on the CaF_2 substrate, it is first coated with a thin layer of silica (~100 nm) using the Oxford PECVD tool, followed by deposition of a self-assembled monolayer of silane conjugated polyethylene glycol (PEG) [3]. The gold nano-antennas are functionalized using n-alkanethiols [3]. This ensures the cells preferentially attach to the nanoantennas. Figure 4 (left) shows A431 cell attachment on an un-functionalized metasurface. We can see how the cells cover the metasurface as well as the substrate. Figure 4 (right) shows A431 cell attachment after the metasurface was functionalized. We can see the cells cover only the metasurface area and are blocked from the substrate region.

References:

[1] S. H. Huang, J. Li, Z. Fan, R. Delgado and G. Shvets. bioRxiv 2021.06.30.450584.

[2] A. P. King, S. C. Marker, R. V. Swanda, J. J. Woods, S. B. Qian and J. J. Wilson, Chem. - A Eur. J., 2019, 25, 9206-9210.

[3] S. Lan, M. Veiseh and M. Zhang, Biosens. Bioelectron., 2005, 20, 1697-1708.

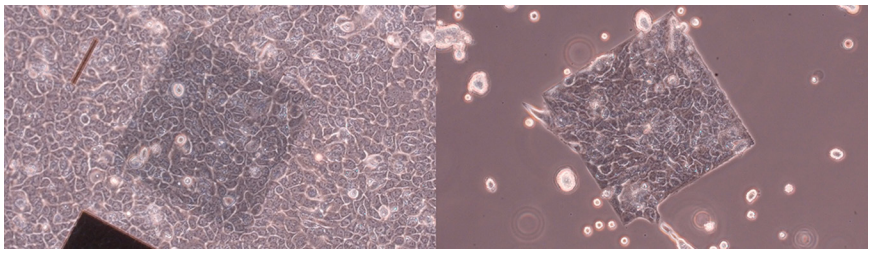

Figure 4: (left) A431 cell attachment on an unfunctionalized metasurface sample. (right) A431 cell attachment on metasurface sample after functionalization.

Retinal Implant Project

CNF Project Number: 2504-16

Principal Investigator(s): Douglas Shire, Ph.D.[1,2,3]

User(s): Marcus Gingerich, Ph.D.[1,3]

Affiliation(s): 1. Department of Electrical Engineering, Cornell University; 2. VA Cleveland Healthcare System; 3. Bionic Eye Technologies, Inc.

Primary Source(s) of Research Funding: NIH R43 NS113708-01

Contact(s): dbs6@cornell.edu, mdg37@cornell.edu

Website: http://www.bostonretinalimplant.org

Primary CNF Tools Used: PT-72, lithography toolset/MA6, Heidelberg mask writer - DWL2000, evaporators, AJA sputter deposition, SEMs, gold electro-plating, Class 2 lithography toolset, Oxford PECVD, Oxford 100 etcher, Oxford Cobra etcher, Glenn 1000, YES polyimide oven, Parylene-C coater, VersaLaser, numerous metrology tools

Abstract:

The purpose of the Retinal Implant Project is to restore useful vision to patients who are blind with degenerative retinal diseases. The primary illnesses we hope to treat are retinitis pigmentosa (a primary cause of inherited blindness) and age-related macular degeneration (the leading cause of blindness in the developed world). Both these diseases cause the eventual destruction of the photoreceptor cells — rods and cones — in the retina, leaving intact the ganglion cells that transmit electrical impulses (and hence visual information) to the brain. The ganglion cells may be stimulated, however, with biphasic current pulses from a microfabricated electrode array. Blind surgical volunteers have consistently described visual percepts that resulted from such stimuli, and this has led our team to develop a wireless, implantable retinal prosthesis. More recently, we have also begun work on developing a system which can induce visual percepts deeper in the brain into the lateral geniculate nucleus.

Summary of Research:

The implanted portion of our device consists of power and data secondary receiving coils, and — in a sealed titanium (Ti) can — a small number of discrete components, and a custom designed application specific integrated circuit (ASIC), which consists of circuitry for clock and data recovery, current drivers for electrodes in a stimulating electrode array, and a programmable function generator capable of stimulating with a wide range of pulse widths and amplitudes. The current outputs drive high-charge capacity sputtered iridium oxide film (SIROF) stimulating electrodes, which in turn give rise to the visual percepts mentioned above.

CNF-fabricated components of this system have included various proof-of-concept test structures and tools used in the research effort and an integrated combination flexible circuit and stimulating electrode array. Silicon (Si) wafers serve as carriers for these freestanding films during processing. The electrode leads are fabricated inside of 'sandwiches' of polyimide and amorphous silicon carbide (SiC), while the SIROF electrodes are reactively sputter-deposited.

Assembly of the intraocular components of the prosthesis is accomplished by flip chip solder ball bonding of the IC and solder attachment of discrete components onto an internal flexible circuit board, which is hermetically sealed into an ultraminiature Ti can. The RF coils are soldered and glued to the integrated external flex-array which is in turn thermosonically bonded to the hermetic feedthrough of the Ti can. Finally, the thermosonic bonds are protected and insulated with an over-mold. An external patient interface unit, will consist of a video camera for capturing images, a digital signal processor, and a radio frequency (RF) transmitter and coil to relay power and data to the implanted device.

Scientific challenges still remain in realizing a chronically implantable retinal prosthesis. While our first-generation device was primarily encapsulated in polymers for short term proof-of-concept implant studies, our second-generation system focused on a system which would last many years *in vivo*. Our past efforts have focused on developing a device with 256+ stimulation channels that is still small enough and of a configuration to be easily implanted in the ocular orbit and continue to function for many years *in vivo*. Thus, a major effort has been the development of a technological platform to build a robust, hermetically packaged, high-density subretinal visual prosthesis with a lifetime of > 10 years in biological saline that is scalable to hundreds of I/O channels.

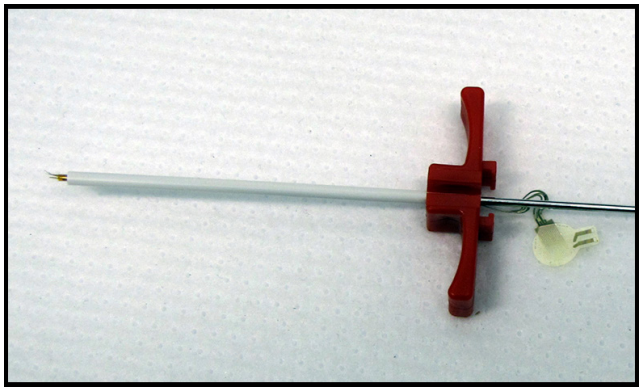

Figure 1: A prototype deep brain insertion sub-assembly is shown which includes a protective split-sheath inserter, the actual electrode array/ signal cable and the tungsten insertion rod.

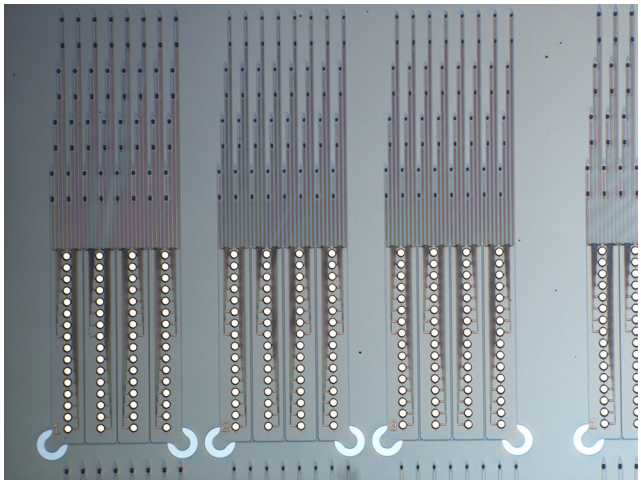

Figure 2: An optical image of three versions of test arrays, which each have four tine lengths and two electrodes per tine.

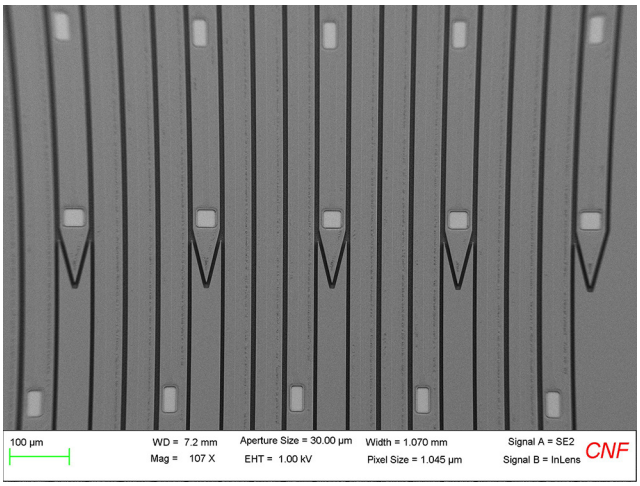

Figure 3: An SEM showing some of the tines just after the outline etching step, but while still on the Si carrier wafer.

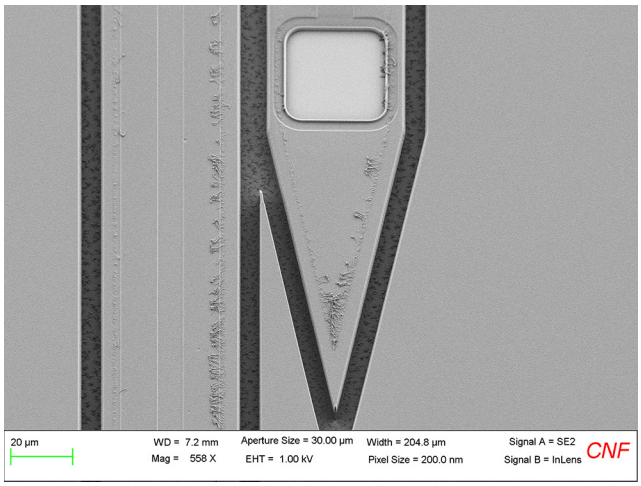

Figure 4: An SEM image of the electrode near the tip of a tine.

Recent efforts at the CNF have turned to developing a microfabrication process for penetrating electrodes for long-term implantation in brain tissue. The goal is to extend the existing retinal stimulator platform to include electrodes which can be placed at different points in the visual tract to enable the restoration of sight due to other causes of blindness. These electrodes can be placed into structures such as the lateral geniculate nucleus (LGN) to produce visual signals at that location. The LGN is a structure located deeper within the brain thus a system of implanting the electrode array into the target location has had to be developed as well.

An early prototype insertion device, shown in Figure 1, includes a protective split-sheath inserter, the actual electrode array/signal cable and the insertion rod. The resulting system has the potential to be utilized in other applications such as those requiring deep brain stimulation including Parkinson's disease, severe depression, morbid obesity, and obsessive-compulsive disorder, to name a few.

Long-term compatible LGN electrodes have been fabricated on a Si carrier wafer using an initial polyimide layer followed by a 2 μm-thick layer of PECVD SiC above and below a metal conductor layer with SIROF electrodes as the electrode/tissue interface material. The devices are shown post-outline-etch in Figures 2-4.

References:

[1] J. F. Rizzo, J. Wyatt, J. Loewenstein, S. Kelly, and D. Shire, "Methods and Perceptual Thresholds for Short-Term Electrical Stimulation of Human Retina with Microelectrode Arrays," Investigative Ophthalmology and Visual Science, vol. 44, no. 12, Dec. 2003, pp. 5355-5361.

Development of Heparin-Based Coacervate Loaded Liposomes as Non-Invasive Therapy for Myocardial Infarction

CNF Project Number: 2754-18

Principal Investigator(s): Yadong Wang

User(s): Chia-Wei Yeh

Affiliation(s): Biomedical Engineering, Cornell University

Primary Source(s) of Research Funding: Cornell Startup Funds

Contact(s): yw839@cornell.edu, cy465@cornell.edu

Primary CNF Tools Used: Heidelberg mask writer - DWL2000, ABM contact aligner, Zetasizer Nano-ZS

Abstract:

Cardiovascular disease is one of the major leading causes of death worldwide. Specifically, myocardial infarction (MI), generally known as heart attack, is the main cause of death in cardiovascular disease. Among them, the major cause of death of MI is due to myocyte necrosis and heart failure. The acute inflammation after MI may be resolved by draining the excessive tissue fluid through lymphatic networks around the heart. However, the high interstitial pressure in the infarcted area may impede the drainage, and the newly formed lymphatic networks due to the MI are not functional. Thus, unresolved inflammation may further exacerbate the damage to the heart tissue.

Vascular endothelial growth factor type C (VEGF-C) is known for inducing lymphangiogenesis both *in vitro* and *in vivo*. Several studies reported that by administrating VEGF-C after MI on rat model can effectively resolve the acute inflammation, and furthermore improve the cardiac function. Therefore, it is of particular promise to deliver VEGF-C to the infarcted heart area, induce lymphangiogenesis, resolve the acute inflammation after MI as well as facilitate injured heart tissue to regenerate.

Summary of Research:

Coacervate is an electrostatically bound complex between cationic and anionic polyelectrolytes. In the extracellular matrix (ECM), glycosaminoglycan such as heparan sulfate proteoglycan (HSPG) binds with several growth factors (GFs) to form HSPG-GF complex. This complex not only serves as reservoir for bonding and stabilization of GFs but also potentiates GFs responsible for maintaining normal cellular function. Due to the similar mechanism of protein-extracellular matrix interaction, it has been shown that heparin-based coacervate is a promising candidate for protein delivery system in biomedical and tissue engineering applications. Nevertheless, coacervate complex is unstable in the blood stream owing to the relatively weak electrostatic interaction within coacervate droplets, leading to the difficulty to systemically administer coacervate via intravenous injection.

In this study, we aim to develop a liposome filled with heparin based coacervate, namely lipocoacervate in short, for protein delivery to treat MI. Polyanion heparin is utilized to complex with vascular endothelial growth factors C (VEGF-C) to form heparin-growth factor complex, which is then mixed with synthetic polycation, ploy(ethylene arginyl aspartate diglyceride) (PEAD) to construct VEGF-C loaded coacervate droplets. Also, staggered herringbone micromixer (SHM) microfluidics is designed to generate lipid vesicles. The VEGF-C loaded coacervate will then be mixed with the lipid vesicles to form lipocoacervate. The therapeutic effect of the lipocoacervate will be evaluated on rat myocardial infarction model.

Research Steps:

The negatively charged lipid vesicles were prepared by mixing DOPC/DSPG/cholesterol (molar ratio = 5/1/3) ethanol solution with 0.9% saline in SHM chip. The flow rate ratio between ethanolic and aqueous phase is 5, resulting negatively charged lipid vesicles (zeta potential = -3.11 ± 0.49 mV) with 70 nm in diameter. In order to facilitate the negatively charged lipid vesicles assemble onto coacervate, different PEAD to heparin (P/H) ratio was tested to figure

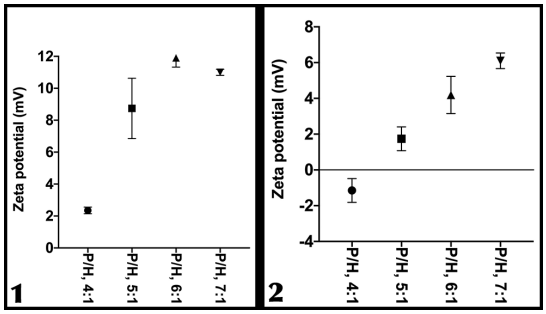

Figure 1, left: Zeta potential of PEAD/heparin coacervate before adding negatively charged lipid vesicles vs. P/H ratio. Figure 2, right: Zeta potential of lipocoacervate vs. P/H ratio.

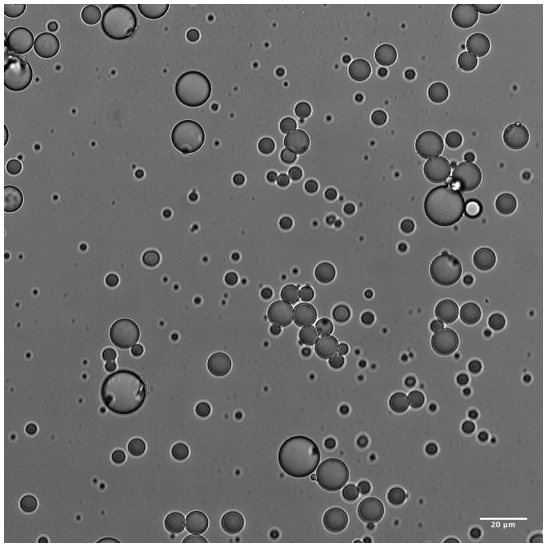

Figure 3: Confocal image of lipocoacervate, bright field. Scale bar, 20 µm.

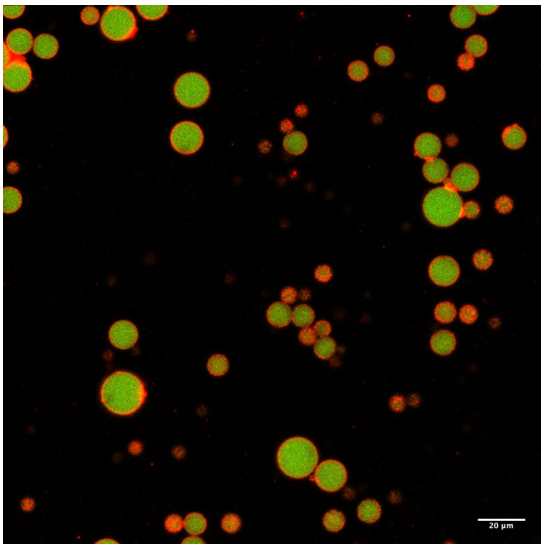

Figure 4: Confocal image of lipocoacervate, red: rhodamine labeled PE; green: fluorescein labeled BSA. The red lipid outside of green coacervate core suggesting the successful assembly of lipocoacervate. Scale bar, 20 µm.

out the zeta potential of coacervate, as shown in Figure 1. As the P/H ratio increased, the zeta potential also increased. When the negatively charged lipid vesicles were mixed with coacervate, the zeta potential was reduced due to the electrostatic adsorption of the negatively charged lipid vesicles on coacervate, as shown in Figure 2. For visualizing the structure of lipocoacervate, rhodamine labeled PE (red) was added into lipid solution during the preparation of lipidvesicles, and fluorescein labeled bovine serum albumin (green) was also incorporated into PEAD/heparin coacervate for visualization.

The confocal images in Figure 3 and Figure 4 showed that the red lipid was indeed outside of green coacervate core, suggesting the successfully assembly of lipocoacervate.

Future works will be focused on investigating the lipid structure outside of coacervate, testing the stability of lipocaocervate, and evaluating the lymphangiogesis efficacy of VEGF-C loaded lipocoacervate.

References:

[1] Hamano, N., et al. "Robust Microfluidic Technology and New Lipid Composition for Fabrication of Curcumin-Loaded Liposome: Effect on the Anticancer Activity and Safety of Cisplatin." Molecular Pharmaceutics 2019, 16, 3957-3967.

[2] Cakmak, F., et al. "Lipid Vesicle-Coated Complex Coacervates." Langmuir 2019, 35, 7830-7840.

[3] Zang, Y., et al. "Giant Coacervate Vesicles as an Integrated Approach to Cytomimetic Modeling." JACS 2021, 143, 2866-2874.

Test Chip for Impedance Spectroscopy of Neuro Excitability

CNF Project Number: 2832-19

Principal Investigator(s): Prof. Huili Grace Xing

User(s): Mohammad Javad Asadi

Affiliation(s): School of Electrical and Computer Engineering, Cornell University

Primary Source(s) of Research Funding: Air Force Office of Scientific Research

Contact(s): grace.xing@cornell.edu, ma2297@cornell.edu

Primary CNF Tools Used: ABM contact aligner, SÜSS MA6-BA6 contact aligner, GCA AutoStep 200 DSW i-line wafer stepper, Heidelberg mask writer, Glen 1000 resist strip, CVC SC4500 odd-hour evaporator, Zeiss Supra SEM

Abstract:

This report focuses on the efforts for fabrication of a test chip containing coplanar waveguides and designed for impedance spectroscopy of neuron excitability. Since there has been a mysterious problem during the fabrication of the chip, we elaborate on the efforts to find the root cause of this issue. Finally, some conclusions will be provided along with suggestions to be tried to alleviate the problem.

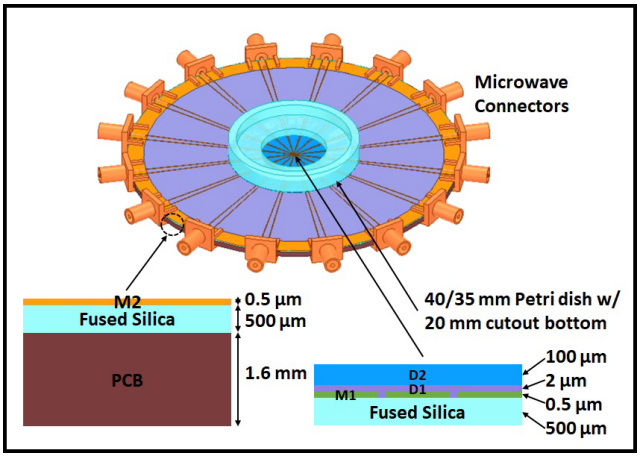

Figure 1: Top view of the designed test chip mated with a Petri® dish.

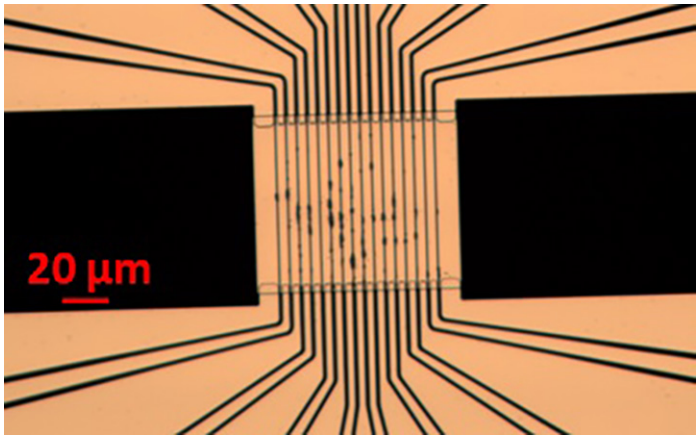

Figure 2: Micrograph of the gold M1 and M2 fabricated on a fused silica wafer.

Summary of Research:

Figure 1 shows the designed test chip. It can be seen that the chip serves as the bottom of a Petri® dish reservoir through a 20-mm-diameter cutout in the bottom of the Petri dish. The chip comprises eight coplanar waveguides (CPWs) fabricated on a 0.5-mm-thick, 100-mm-diameter fused silica wafer. Sixteen microwave connectors of sub-miniature type A (SMA) are attached on the edge of the fused silica wafer in a radial pattern. The fused silica wafer is mechanically strengthened by a 1.6-mm-thick FR4 printed circuit board (PCB) with a 40-mm cutout to allow transmission optical microscopy of the center portion of the fused silica wafer. A microfluidic channel (100 μm long, 20 μm wide, 2 μm high) for axons is formed on the fused silica wafer with 2-μm-thick SU-8 walls and a 100-μm-thick polydimethylsiloxane (PDMS) cover. To electrically insulate the CPWs from the culture medium outside the microfluidic channel, the SU-8 covers most of the fused silica wafer and the PDMS covers most the cutout of the bottom of the Petri dish.

The fabrication process for the entire chip is a four-mask process. The first two layers that were fabricated are metal 1 (M1) at the center of the chip, and metal 2 (M2) for the rest. The photolithography for M1 was done using the GCA AutoStep 200 DSW i-line wafer stepper to create a pattern with gaps of 1 μm. CVC SC4500 odd-hour evaporator was used to deposit 15 nm and 200 nm of titanium and gold, respectively, as M1. The same process but using SÜSS MA6-BA6 contact aligner was done to deposit 15 nm and 500 nm of titanium and gold respectively, as M2. The fabricated two metal layers is shown in Figure 2.

As can be seen in the figure, once M2 is deposited, and lift-off process is done, the M1 starts to develop some mouse bites. However, this kind of defects never observed in M1 before M2 is deposited and lifted off.

As a scanning electron microscopy (SEM) image of the M1, shown in Figure 3 confirms, the metal is severely damaged after fabrication. In order to solve this problem, several suggestions were tried such as not using RCA cleaning, not sonication for lift off, using brand new crucibles and metal sources for evaporation, and prebaking the wafers for several days before fabrication. However, none of these suggestions were helpful.

Successful fabrication without any mouse bite on a silicon wafer instead of fused silica led us to come up with a hypothesis that the problem is due to the electrostatic discharging effect.

In order to verify this hypothesis, half of the coplanar waveguide lines fabricated using aluminum were shorted while kept the rest intact. The result is shown in Figure 4.

As can be seen, the metal lines that are shorted and cannot build up static charge, are not damaged while the others developed mouse bite although not as severe as the case fabricated with gold. This test validates the assumption that the defects (mouse bites) are due to the electrostatic discharging that happens between each two isolated electrodes.

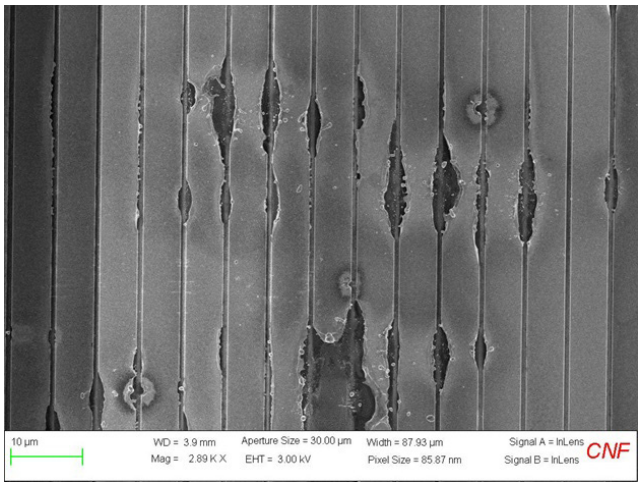

Figure 3: SEM image of the mouse bites in M1.

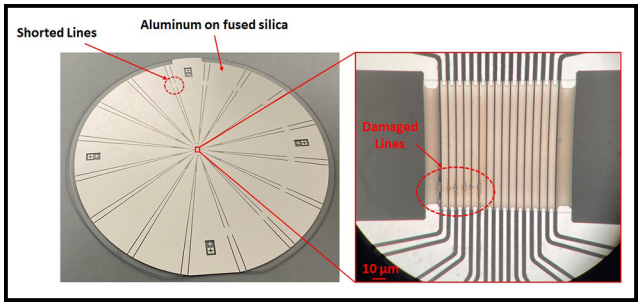

Figure 4: Micrograph of the aluminum M1 and M2 fabricated on fused silica wafer.

Conclusions and Future Steps:

We successfully found the root cause of the mouse bites that developed in the metal layer fabricated on a fused silica wafer. In the future, the isolated metal layers will be temporarily shorted up to the last fabrication step to make sure electrostatic discharging will not happen. Besides that, the fabricated metal layers will be covered with a thin layer of oxide that might help to mitigate the electrostatic discharging effect.

Fabrication of Microchip Devices for Organ-on-a-Chip and Lab-on-a-Chip

CNF Project Number: 2857-19

Principal Investigator(s): Esak (Isaac) Lee, Ph.D.

User(s): Renhao Lu

Affiliation(s): Meining School of Biomedical Engineering, Cornell University

Primary Source(s) of Research Funding: Cornell Start Up

Contact(s): el767@cornell.edu, rl839@cornell.edu

Primary CNF Tools Used: Heidelberg mask writer - DWL2000, ABM contact aligner, MVD 100

Abstract:

Triple-negative breast cancer (TNBC) is one of the most insidious forms of breast cancer. Among multiple metastatic processes, extravasation determines the final site of the metastasis. We developed a rapid multilayer microfabrication method of transferring a three-dimensional (3D) overhang pattern to a substrate with a sacrificial layer to reconstitute a 3D blood vessel surrounded by the extracellular matrix containing organ-specific parenchymal cells. Based on our *in vitro* model, we found that bone-like microenviroment with osteoblasts and mesenchymal stem cells promoted extravasation of the bone-tropic TNBC cells, whereas the lung-like microenviroment promoted extravasation of the lung-tropic TNBC cells.

Summary of Research:

Despite numerous research efforts, triple-negative breast cancer (TNBC) is the most aggressive form of breast cancer and still the leading cause of cancer deaths in breast cancer patients. Physicians have discovered that breast cancer highly prefers to certain organs for metastases [1], referring as organotropic cancer metastasis. To better understand and treat TNBC metastasis, we need to look into TNBC interactions with blood vessels through bio-mimic models.

Needle-based casting method has been used as a conventional tool for fabricating engineered vessels with an ease of obtaining a cylindrical shape in 3D matrices [2]. However, a needle buffer layer has to be prepared, and additionally mix of photo resist is required to produce a blocking layer [2], which significantly harms the purity of the materials and weakens the bonding strength between the layers, thereby deteriorating the durability of the mold.

Here, we developed a novel microfabrication method allows the fabrication of a vascular channel with only single casting mold by transferring a 3D overhang two-layer SU-8 pattern to a substrate with a sacrificial layer. The casting mold with a 3D overhang pattern provides a more reproducible, reliable vascular conduit structure than previous methods described above.

The microfluidic vascular channel device design is shown in Figure 1(a). The device contains a circular inlet and outlet, an extracellular matrix (ECM) hydrogel cavity located in the center, and two ports to access the vessel lumens. The design is made using L-edit computer-aided design software, and the ultraviolet (UV) photomasks for three layers are engraved on 5-inch-chromium masks by a laser pattern generator (Heidelberg mask writer - DWL2000).

Our PDMS microfluidic chip was fabricated using a conventional polydimethylsiloxane (PDMS) casting process. The microfabrication photolithography for PDMS mold began with two 100 mm silicon wafer substrates, one was used as a 'pattern wafer' (Figures 1(b) and (c)), and another was used as a 'mold wafer' (Figure 1(d)). For the pattern layer, firstly, a layer of OmniCoat™ was spin-coated on the whole surface. Next, a 450 μm thick layer of SU-8 2150 for a 100 μm thick gel-top layer and a 350 μm thick needle guide layer was spin-coated and soft-baked. This layer was exposed by two different masks (needle guide layer mask and gel-top layer mask) using ABM manual mask aligner.

After post-exposure baking (PEB) and cooling down, a 100 μm thick layer of SU-8 100 for the needle buffer layer was spin-coated, soft-baked and exposed. Simultaneously, on the mold wafer, a 50 μm thick layer of SU-8 50 for the bonding layer was spin-coated, soft-baked, and flood-exposed with 450 mJ cm^{-2} of UV exposure without a mask (Figure 1(d)).

Consequently, the two wafers were joined together facing each other, and we performed PEB and developed them together (Figure 1(e)). After the development, the wafers were further developed in an alkaline developer MF319 to remove the OmniCoat™ sacrificial layer, completing

the transferring process. The surface of the fabricated mold wafer was treated by a monolayer of FOTS through the molecular vapor deposition system (MVD 100).

Based on our PDMS microfluidic chip, we investigated breast tumor extravasation in distinct organs to recapitulate the critical step in the organotropic metastasis. Our study showed that bone-like microenviroment with osteoblasts and mesenchymal stem cells promoted extravasation of the bone-tropic TNBC cells, whereas the lung-like microenviroment promoted extravasation of the lung-tropic TNBC cells (Figure 2). Given that these organ-specific parenchymal cells do not impact vascular permeability, our results suggest that the parenchymal cells dictate selective extravasation of the bone-tropic or lung-tropic TNBC cells in our system.

Conclusions and Future Steps:

By transferring multilayer pattern to another wafer, we have achieved building SU-8 overhanging structure without any blocking layers. Furthermore, we found the tissue specific TNBS extravasation phenomenon based on our microfluidic chips.

In the future, we plan to dig into the biological mechanisms behind our findings. Also, we hope to expand our microfabrication chip into other biological applications, including lymphatic and glaucoma organ-on-a-chip models.

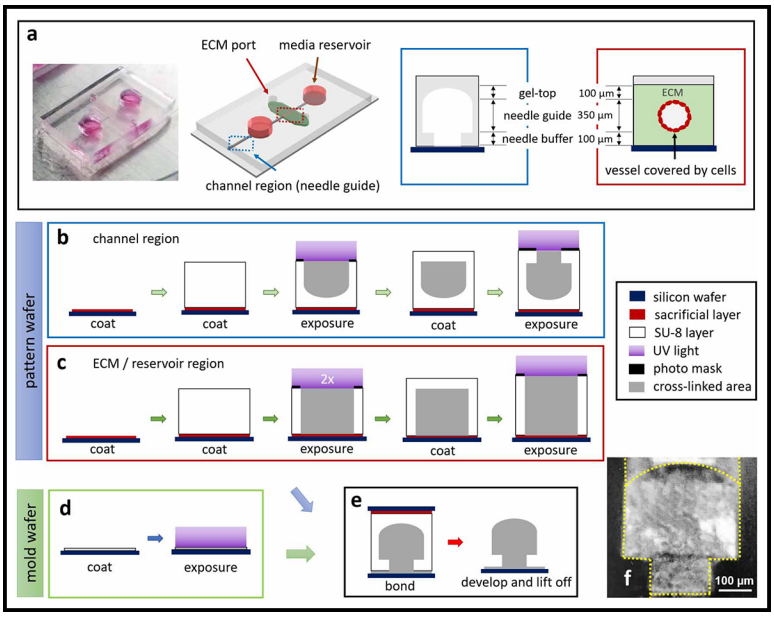

Figure 1: A schematic illustration of the rapid multilayer microfabrication method. (a) A real image of the device and an isometric illustration of the device (left); and in the right, there are cross-section views of the channel region (blue box) and the ECM hydrogel region (red box). (b)-(e) A multi-layer mold fabrication process for the channel region (b) and ECM /reservoir region (c) on the pattern wafer. (d) A flood-exposure is used to form a SU-8 bonding layer on the mold wafer. (e) The two wafers are bonded together by facing during a post-exposure bake (PEB) process and are developed to remove non-crosslinked SU-8 and the sacrificial layer. (f) A cross-section image of a multi-layered overhang structure in the channel region.

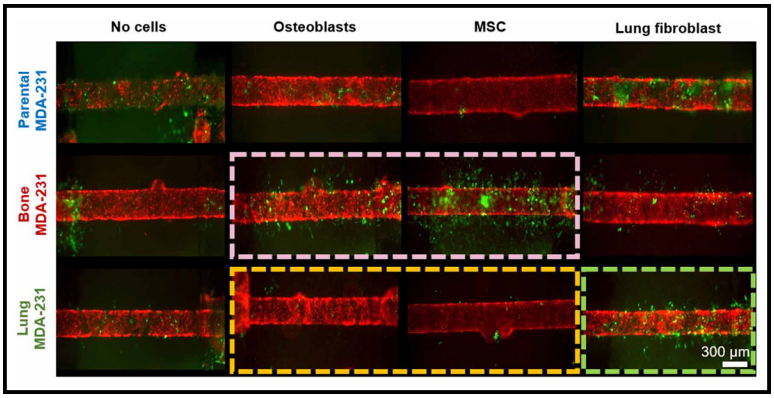

Figure 2: Organ-specific tumor metastasis 3D in vitro. *Parental, bone-tropic, and lung-tropic MDA-MB-231 cells were introduced into blood vessels surrounded by collagen I with no cells, osteoblasts, bone-marrow derived MSC, and lung fibroblasts. The experiment was maintained for six days. Representative images at Day 6 are presented. The highlighted boxes (pink, orange, green) indicate the organ-specific extravasations.*

References:

[1] Patanaphan, V. I. N. I. T. A., Omar M. Salazar, and Rapael Risco. "Breast cancer: metastatic patterns and their prognosis." Southern medical journal 81.9 (1988): 1109-1112.

[2] Polacheck, William J., et al. "Microfabricated blood vessels for modeling the vascular transport barrier." Nature protocols 14.5 (2019): 1425-1454.

[3] Kwak, Tae Joon, and Esak Lee. "Rapid multilayer microfabrication for modeling organotropic metastasis in breast cancer." Biofabrication 13.1 (2020): 015002.

Human MSCs Release Multiple EV Populations Containing Mitochondria

CNF Project Number: 2864-20

Principal Investigator(s): Dr. Michelle L. Delco, DVM, Ph.D., DACVS

User(s): Matthew Thomas

Affiliation(s): College of Veterinary Medicine, Department of Clinical Sciences; Cornell University

Primary Source(s) of Research Funding: Harry M. Zweig Fund for Equine Research National Institute of Health-National Institute of Arthritis and Musculoskeletal and Skin Diseases

Contact(s): mld12@cornell.edu, mt826@cornell.edu

Primary CNF Tools Used: Malvern Nano ZS Zetasizer, Malvern NS300 NanoSight

Abstract:

A growing body of evidence supports intracellular mitochondrial (MT) transfer as an important intercellular signaling mechanism. Further, increasing evidence suggests that mesenchymal stromal cells (MSCs) can rescue injured and dysfunctional cells by donating whole mitochondria, and this phenomenon may explain the beneficial effects of therapeutically implanted MSCs. One possible mechanism for MT transfer involves packaging mitochondria into extracellular vesicles (EVs). This would open the possibility of cell-free MT-targeted regenerative therapies. Confirming that this is possible would be an important step toward therapeutic development. As demonstrated here, human MSCs produce EVs containing MT. We have used the CNF to further characterize these 'mitovesicles' and found that there are multiple populations of different sizes, indicating different modes of biogenesis and/or distinct bio-signaling functions.

Summary of Research:

The phenomenon of intercellular mitochondrial transfer, by which mesenchymal stromal cells donate whole mitochondria (MT) to other cell types undergoing MT dysfunction, is a promising avenue for therapeutic intervention in degenerative disease [1]. Mitochondrial donation has been demonstrated in multiple cell types, including neurons and myocytes. It has been shown to improve MT function and prevent apoptosis *in vitro*, as well as improve tissue repair *in vivo* [2-4].

Our lab studies MSC MT donation in the context of orthopedic disease, using *in vitro* chondrocyte cultures and explanted cartilage tissue as models. Using confocal imaging, we have identified several possible modes of MSC-chondrocyte MT transfer, including direct cell-cell contact (e.g., nanotubule-medial filipodial transfer, gap junction-mediated transfer) and what appears to be non-contact transfer, whereby MSCs release mitochondria into the extracellular space, which are then taken up by chondrocytes. We hypothesize that these are MT are packaged inside of extracellular vesicles (EVs) as so-called 'mitovesicles'.

This strategy of loading MT into EVs has precedent in literature. Phinney, et al., showed that MSCs can use mitovesicles, to outsource mitophagy of depolarized MT to macrophages, boosting bioenergetics for both the donating MSC and the recipient macrophage [5]. Furthermore, Morrison, et al., used cellular staining and flow cytometry to demonstrate that distressed lung epithelial cells can take up MT through EV-mediated transfer, and this ameliorates lung injury *in vivo* [6].

Our goal was to characterize the EVs produced by human MSCs. EVs are an inherently heterogenous population, making specific categorization difficult. However, it is widely recognized that they fall into three size categories: small (15-100 nm, exosomes), medium (150-1000, microvesicles), and large (1 μm+, apoptotic bodies).

We isolated EVs from human bone marrow derived MSCs and used dynamic light scattering (DLS) to analyze their size distribution (Figure 1). As expected, we found the three categories supported by previous work [7] (Figure 1).

Next, we used the Malvern NS300 NanoSight to identify which, if any of these categories, contain MT. We stained hMSC EVs with Mitotracker Red, then performed nanoparticle tracking analysis using the Nanosight's 565 nm fluorescent filter. We were able to validate that this method allows us to track exclusively EVs that contain mitochondrial content (Figure 2.)

Further, we found that mitovesicles make up around 20% of the total EV's released and appear to trend slightly larger than the general population (Figure 2.).

The significance of these findings is not yet clear, but likely reflects distinct modes of biogenesis and cargos for different sub-populations of mitovesicles.

Conclusions and Future Steps:

Our work thus far has confirmed our ability to isolate EVs from MSCs and identify mitovesicles within that population. Our next step is to identify and separate the EVs that contain functional and non-functional MT. This will allow us to begin identifying the role that these particles play in intercellular signaling and to further investigate MSC-EV mediated MT transfer.

References:

[1] Delco, M. L., Bonnevie, E. D., Bonassar, L. J., and Fortier, L. A. Mitochondrial dysfunction is an acute response of articular chondrocytes to mechanical injury. J. Orthop. Res. 36, (2018).

[2] Jiang, D., et al. Mitochondrial transfer of mesenchymal stem cells effectively protects corneal epithelial cells from mitochondrial damage. Cell Death Dis. 7, (2016).

[3] Konari, N., Nagaishi, K., Kikuchi, S., and Fujimiya, M. Mitochondria transfer from mesenchymal stem cells structurally and functionally repairs renal proximal tubular epithelial cells in diabetic nephropathy *in vivo*. Sci. Rep. 9, (2019).

[4] Spees, J. L., Olson, S. D., Whitney, M. J., and Prockop, D. J. Mitochondrial transfer between cells can rescue aerobic respiration. Proc. Natl. Acad. Sci. U. S. A. 103, (2006).

[5] Phinney, D. G., et al. Mesenchymal stem cells use extracellular vesicles to outsource mitophagy and shuttle microRNAs. Nat. Commun. 6, (2015).

[6] Morrison, T. J., et al. Mesenchymal stromal cells modulate macrophages in clinically relevant lung injury models by extracellular vesicle mitochondrial transfer. Am. J. Respir. Crit. Care Med. 196, (2017).

[7] Zhang, X., Hubal, M. J., and Kraus, V. B. Immune cell extracellular vesicles and their mitochondrial content decline with ageing. Immun. Ageing 17, (2020).

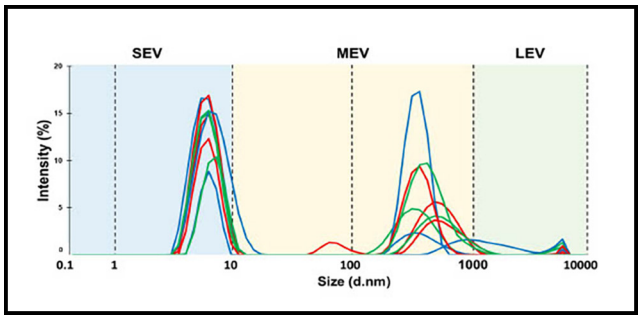

Figure 1: Dynamic Light Scattering of human MSC-derived extracellular vesicles (EVs) reveals three sub-populations of EVs based on size: small, (SEV; ~ 5-10 nm) medium, (MEV; ~ 100-1000 nm) and large (LEV; 5,000-10,000 nm). N = 3.

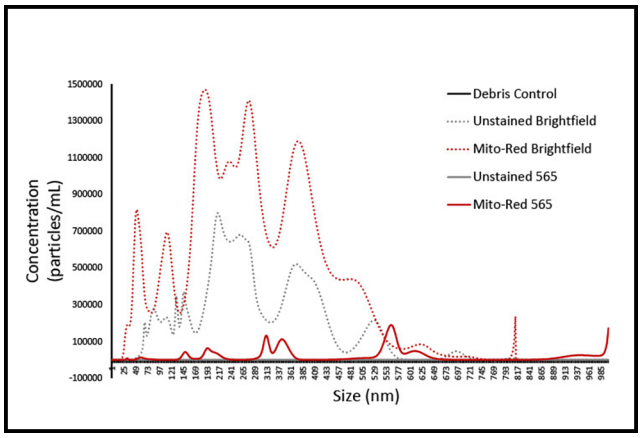

Figure 2: NTA supports trend of larger EVs containing MT. EVs were stained with Mitotracker Red and run with either a non-fluorescent (brightfield) filter, or with fluorescence exciting at 565 nm. These groups were compared to non-stained EVs and a double filtered PBS control. Unstained particles were undetectable using the 565 filter. Mitotracker positive EVs seemed to show a trend towards larger size, with nearly all of the smallest population disappearing altogether. N = 1.

Microfluidic Device to Study Breast Cancer Cell Migration

CNF Project Number: 2912-20

Principal Investigator(s): Claudia Fischbach

User(s): Siyoung Choi

Affiliation(s): Biomedical Engineering, Cornell University

Primary Source(s) of Research Funding: NIH

Contact(s): cf99@cornell.edu, sc2237@cornell.edu

Primary CNF Tools Used: Objet30 Pro 3D Printer

Abstract:

Bone metastasis through the dissemination of cancer cells worsens the prognosis of patients with advanced breast cancer. Migration of breast cancer cells is a fundamental process for breast cancer metastasis and is dependent on surrounding microenvironment. Cancer cell response to chemical signals and extracellular matrix (ECM) has been studied to understand the migration of cancer cells using microfluidic devices [1-2]. How bone ECM, mainly mineralized collagen, regulates breast cancer cell migration, however, is unclear.

Here, we utilized biomimetic approach in conjunction with microfluidic device to investigate the role of bone ECM on breast cancer migration.

Summary of Research:

Three-dimensional computer-aided design (3D CAD) software (Inventor, Autodesk) was used to design a microfluidic device for studying breast cancer migration. The device is composed of central channel for bone ECM deposition and two channels for chemical gradient and breast cancer cell seeding.

To guide the cancer cell entrance into the central channel, arrays of trapezoidal posts were placed between central channel and side channels (Figure 1). CNF's 3D printer (Object30 Pro, Stratasys) was used to fabricate a mold for this microfluidic device, casted with polydimethysiloxane (PDMS, Sylgard 184, Dow Corning) (Figure 2). To verify liquid flow within microfluidic channels, first, holes for liquid flow were punched at the end of each channel. Then, the PDMS microfluidic device and glass coverslip were treated with plasma cleaner and the channels of the device were bonded, facing the surface of a plasma treated glass coverslip for binding.

Aqueous solution containing red dye was injected at the inlet of each channel and filled all microfluidic channels (Figure 3). However, post structure of the device is not enough to provide high resolution and there are striation patterns in the microfluidic channel, which will be an issue for solution leakage (Figure 4).

Conclusions and Future Steps:

The 3D printer is a tool for fast and cost-effective fabrication. However, the resolution is limited to sub-millimeter structures of microfluidic devices.

To increase the resolution of our microfluidic device, a soft photolithography technique is required. In the future, an epoxy-based negative photoresist will be coated on a silicon wafer and patterned using a photomask.

References:

[1] Lab on a Chip (2017), Vol. 17, 3851.

[2] PNAS, 2012, Vol. 109, 13515.

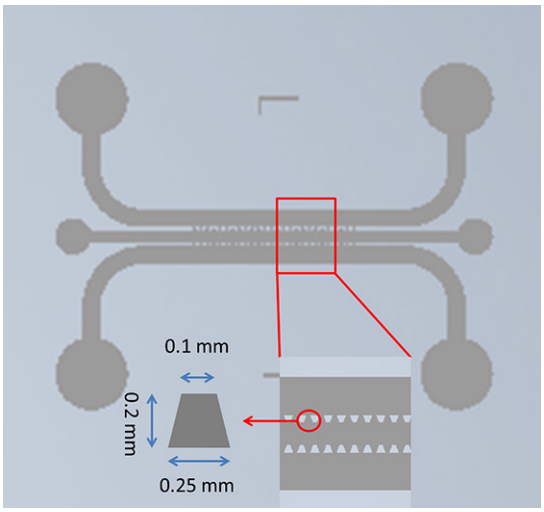

Figure 1: Design and dimension of microfluidic device. The device is composed of three channels and the array of arrays of trapezoidal posts between channels will provide the entrance of breast cancer cells into bone ECM. The smallest dimension of posts is 100 µm.

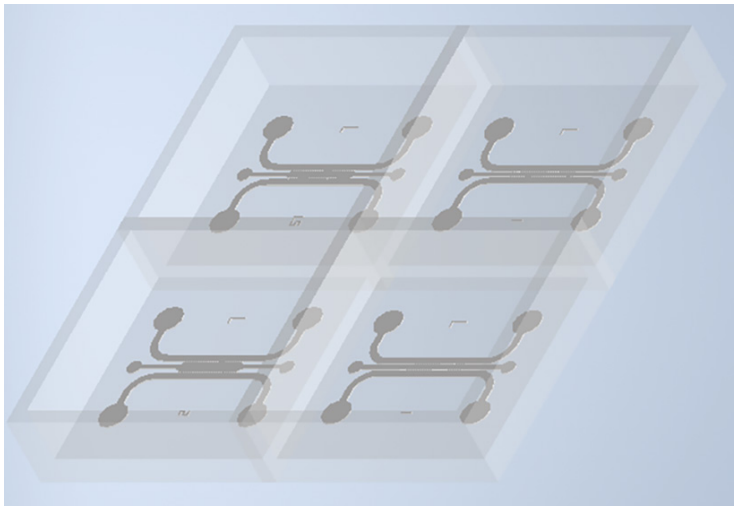

Figure 2: Mold design to cast PDMS microfluidic device. The mold has four microfluidic devices and each device has different central channel widths (1-2 mm).

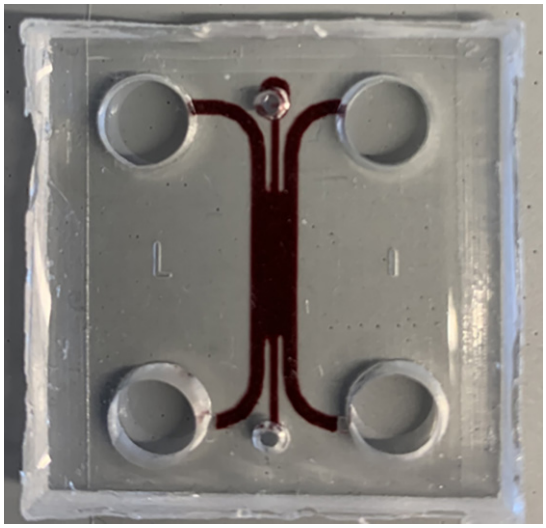

Figure 3: PDMS casted microfluidic device with fluidic channels. Plasma treated PDMS device was bound on plasma treated glass coverslip. Solution containing red dye was injected into holes of each channel.

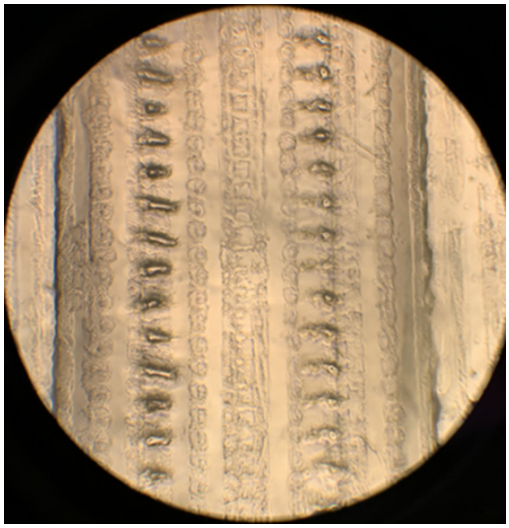

Figure 4: Low resolution of posts within central channel. Each post has different resolution and striation pattern was observed on the surface of PDMS device.

Peptoid Photoresists with Precisely Controllable Length and Composition

CNF Project Number: 2733-18

Principal Investigator(s): Christopher Kemper Ober

User(s): Florian Hermann Ulrich Käfer

Affiliation(s): Department of Material Science and Engineering, Cornell University

Primary Source(s) of Research Funding: JSR

Contact(s): cko3@cornell.edu, fhk28@cornell.edu

Website: https://ober.mse.cornell.edu/

Primary CNF Tools Used: ASML 300C DUV stepper, Woollam RC 2 ellipsometer, JEOL 6300 e-beam

Abstract:

Here we present the synthesis of peptoid with precisely controllable length and composition. Peptoids were synthesized using an automated peptide synthesizer. The 10-mers were purified and protecting groups serving as solubility switches were introduced. MALDI-TOF mass spectrometry was applied to characterize the peptoid structure and molar mass. The photolithographic performance was investigated by DUV and e-beam exposures resulting in a line-space pattern of 1 μm and 50 nm, respectively.

Summary of Research:

Introduction. Today's widely used polymeric resists are typically based on random copolymers. These polymers are polydisperse and relatively large, with molar masses ranging from 5,000-15,000 g/mol [1]. Characteristics such as these can affect resist performance, and therefore it is necessary to explore other architectures for new resist platforms. For sequence-controlled polymers, on the other hand, the monomers are arranged in a specific, user-defined order. Monomer sequence regularity strongly influences the molecular, supramolecular, and macroscopic properties of polymer materials, showing promise for the creation of a new type of small molecule photoresist. In this respect, peptoids represent a particularly advantageous group, since they can be specifically varied in their structure, length and sequence of the amines used [2].

Peptoid Synthesis. A solid-phase peptoid synthesis approach using a 2-chlorotrityl based resin was used [3]. The bromoacetylation step was carried out by adding bromoacetic acid (BAA) in DMF and N, N-diisopropylethylamine (DIPEA) to the resin. The resin was then washed repeatedly with DMF. Amination was performed by reacting the acylated resin with the amine in DMF. After cleaving, protecting, and purifying using preparative high-pressure liquid chromatography (HPLC), the peptoids were characterized using MALDI-TOF mass spectrometry, see Figure 1.

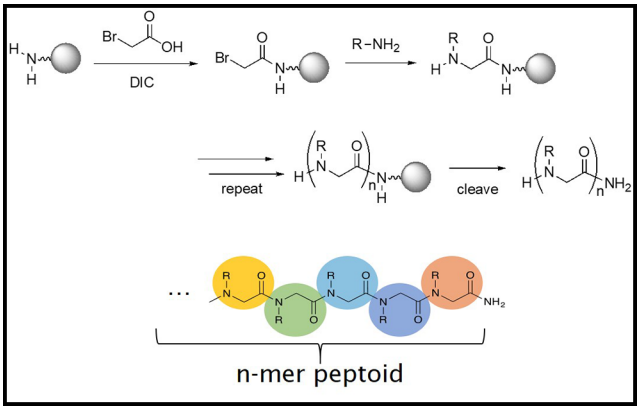

Figure 1: Synthesis and characterization of peptoid photoresists with precisely controllable molecular structure.

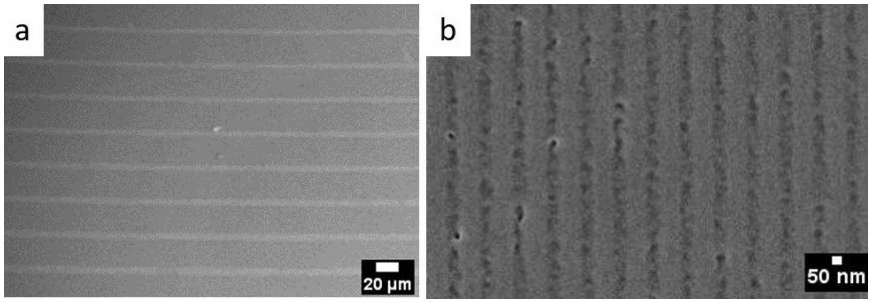

Figure 2: (a) Line pattern measured using scanning electron microscopy; (a) after DUV exposure on an ASML PAS 5500/300C DUV wafer stepper (~ 40 mJ/cm^2), feature size 1 µm, (b) after exposure on a JEOL 6300 to 75 µC/cm2 e-beam radiation. The feature size is 50 nm.

Characterization and Results. Herein we design peptoids that incorporated side chains with a variety of chemical moieties serving functions such as adhesion to the underlying substrate, etch resistance, and solubility switching. Precisely sequence control allowed us to probe not only the optimal composition of the aforementioned moieties but also their order in the peptoid. As the peptoids examined were 10-mers, the structure of the side chains was also carefully chosen to avoid crystallization and tune the glass transition temperature. Protecting groups serving as solubility switches were selected with the goal of groups that possessed a high radical cation acidity, a property that is previously shown to correlate closely with the sensitivity of EUV resists. First DUV photolithography and electron beam exposures of the synthesized 10-mers are showing defined line patterns, see Figure 2.

Conclusions and Future Steps:

Sequence-controlled peptoids with different sequences and compositions of the used amines have been successfully synthesized and the performance as a positive tone photoresist was evaluated performing DUV and e-beam exposures.

While these initial results show the potential of peptoids as photoresist materials, the ongoing research is still at an initial stage. In the future, the length, sequence as well as the effect of different site moieties on the photolithographic performance will be investigated.

References:

[1] Patterson, K.; Yamachika, M.; Hung, R.; Brodsky, C.; Yamada, S.; Somervell, M.; Osborn, B.; Hall, D.; Dukovic, G.; Byers, J.; Conley, W.; Willson, C. G., Polymers for 157-nm photoresist applications: a progress report. SPIE: 2000; Vol. 3999.

[2] Gangloff, N.; Ulbricht, J.; Lorson, T.; Schlaad, H.; Luxenhofer, R., Peptoids, and Polypeptoids at the Frontier of Supra- and Macromolecular Engineering. Chemical Reviews 2016, 116 (4), 1753-1802.

[3] Culf, A. S.; Ouellette, R. J., Solid-phase synthesis of N-substituted glycine oligomers (alpha-peptoids) and derivatives. Molecules (Basel, Switzerland) 2010, 15 (8), 5282-5335.

Controlling the Crystallite Size Distribution of Metal Organic Frameworks (MOFs) Using Base-Mediated Equilibrium Dynamics

CNF Project Number: 2763-19

Principal Investigator(s): Dr. Phillip J. Milner

User(s): Jose Javier Fuentes-Rivera

Affiliation(s): Chemistry and Chemical Biology, Cornell University

Primary Source(s) of Research Funding: Milner Start-Up

Contact(s): pjm347@cornell.edu, jjf255@cornell.edu

Primary CNF Tools Used: Dynamic Light Scattering: Malvern Nano ZS Zetasizer and Malvern NS300 NanoSight

Abstract:

Metal-organic frameworks (MOFs) are crystalline, porous materials with potential applications ranging from gas separations to catalysis. However, the synthesis of MOFs remains a "black box" — which makes it challenging to prepare frameworks with controlled crystallite size distributions. Generally, MOFs are prepared from the conjugate acid of the organic "linker" combined with a metal precursor and a source of base to deprotonate the acid. This is most commonly achieved using the decomposition of the solvent N,N-dimethylformamide (DMF). However, we hypothesized that the slow addition of base could instead be achieved simply by adding base slowly via syringe pump to a reaction mixture.

We have found indeed that the crystallinity of MOFs, specifically the framework Zn-MOF-74, can be improved by adding organic base slowly to the reaction mixture (Figures 1 and 2).

Summary of Research:

The improvement in crystallinity could be observed by powder X-ray diffraction and scanning electron microscopy (not shown). We attempted to further support our findings using the dynamic light scattering (DLS) instruments available at CNF, specifically the Malvern Nano ZS Zetasizer. However, the prepared MOFs were found to form unstable colloids in all tested media (including water and organic solvents), and thus did not yield meaningful data despite numerous attempts (Figure 3).

Unfortunately, the MOFs were also found to rapidly settle from solution, which also negatively impacted the DLS measurements. As such, we have abandoned DLS measurements at CNF for the time being.

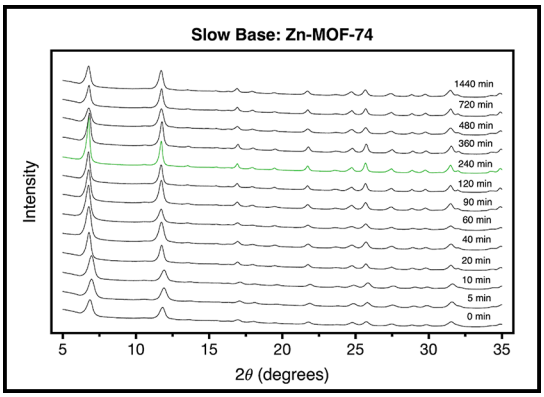

Figure 1: Powder X-ray diffraction patterns of Zn-MOF-74 prepared at a range of base addition times.

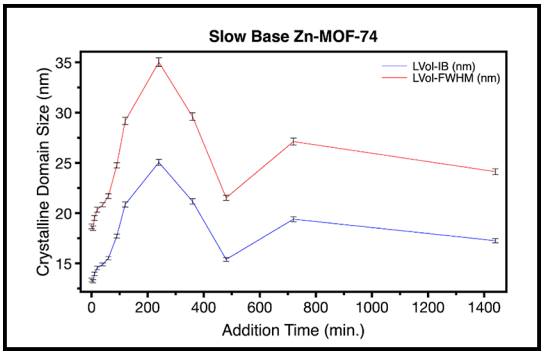

Figure 2: Average crystalline domain sizes of Zn-MOF-74 crystallites prepared by slow addition of base.

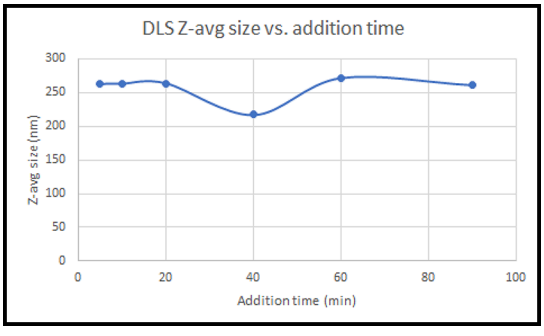

Figure 3: Attempted DLS measurements of MOFs, which yielded unmeaningful results.

Graphene-on-Polymer Flexible Vaporizable Sensor

CNF Project Number: 1121-03

Principal Investigator(s): Amit Lal

User(s): Ved Gund

Affiliation(s): School of Electrical and Computer Engineering, Cornell University

Primary Source(s) of Research Funding: NSF-EFRI

Contact(s): amit.lal@cornell.edu, vvg3@cornell.edu

Website: http://www.sonicmems.ece.cornell.edu/

Primary CNF Tools Used: GSI PECVD, CVC SC4500 odd-hour evaporator, Oxford 81, Unaxis DRIE, spinners, SÜSS MA-6, Zeiss SEM

Abstract:

Wireless sensor nodes integrated on flexible substrates are critical to meet the demands of a burgeoning market of wearable sensors, fieldable environmental sensors, and consumer electronics for Internet-of-Things (IoT) applications. While silicon-based circuits are pervasive, they face critical challenges for the aforementioned new and emerging applications. Wearable sensors necessitate conformality and stretchability to curved surfaces, in contrast to silicon-based sensors which are non-compliant. The use of silicon substrates for sensor nodes in a large, distributed network of sensors, whether for diagnostic and therapeutic biomedical devices or for soil and crop monitoring, also poses a significant concern from a sustainability standpoint since these sensors cannot be reacquired or resorbed easily back into the natural environment which can lead to non-degradable waste accumulation. Hence, it is critical to design sensors and electronics on flexible substrates that can also incorporate mechanisms for vaporization or disintegration which would minimize electronic waste. With this perspective, we have developed a graphene-on-polymer vaporizable and flexible piezoresistive sensor platform. This sensor technology can be used for wearable microsystems and disposable environmental sensors. A proof-of-concept pressure sensor with a high sensitivity of 68 × 10^{-3} kPa^{-1} has been demonstrated. The device needs 22 mW to achieve a temperature of 220°C for the partial vaporization of a 1 mm^2 membrane made of 1.8 μm thick polypropylene carbonate (PPC), thus demonstrating a pathway to sensor self-destruction.

Summary of Research:

It is essential to design flexible sensors with materials that have high mechanical strength for stretchability and conformality as well as excellent electronic properties. Atomically thin two-dimensional graphene is an outstanding candidate for such sensors because of its high Young's modulus of 1 TPa and as zero-bandgap semi-metal with out-of-plane p-orbital electrons for conduction modulation [1]. These properties make it suitable for piezoresistive sensing. Flexible graphene-based piezoresistive sensors with record high sensitivities have previously been reported [2]. Our work (schematic in Figure 1) demonstrates a graphene-on-polymer flexible piezoresistive pressure sensor that uses lithographically defined metal electrodes and membranes while maintaining a high quality of graphene as the piezoresistive sensor. The PPC is a highly compliant and flexible structural layer (Young's modulus of 1 GPa) for the sensor with low-temperature vaporization for potential self-destruction on environmental resorption [3].

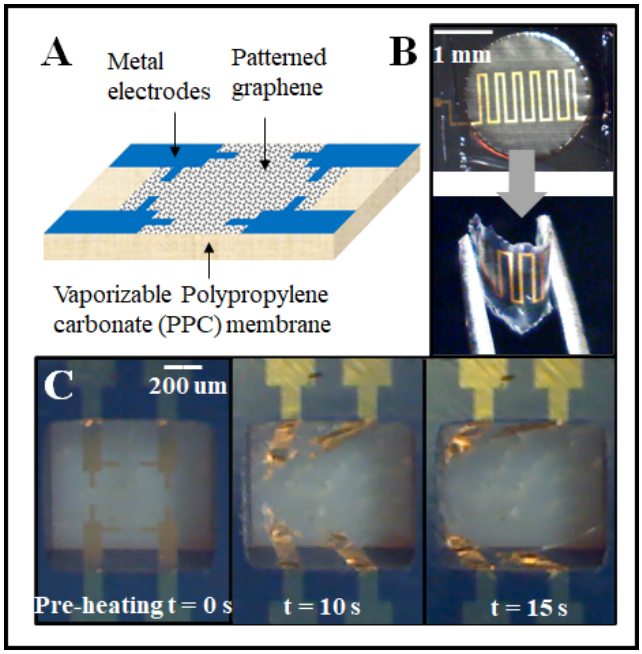

Figure 1: A) Flexible vaporizable pressure sensor architecture with lithographically defined graphene and metal electrodes on PPC. B) Flexibility: Metal-on-PPC piezoresistor on Si wafer (top) and after scribing out and bending with tweezers (bottom) C) Vaporization: Time series of sensor transience by vaporization of PPC in 15 seconds.

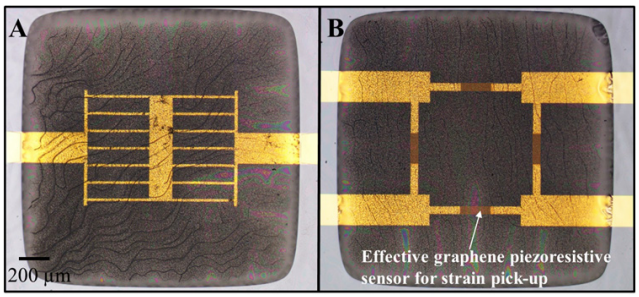

Figure 2: Optical micrographs of (A) Ti/Au metal-on-PPC flexible sensor and (B) graphene-on-PPC with false color between metal electrodes to show the effective graphene pressure sensing region for strain pick-up.

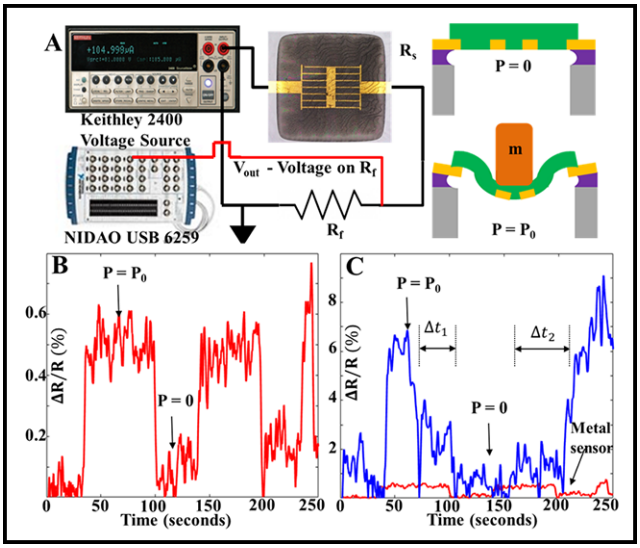

Figure 3: A) Piezoresistive pressure sensor test-setup. B) Fractional change in resistance (ΔR/R) for the metal sensor and C) Graphene sensor for loading and unloading of pressure P_0. The graphene sensor shows delays in response to unloading and loading after the first cycle.

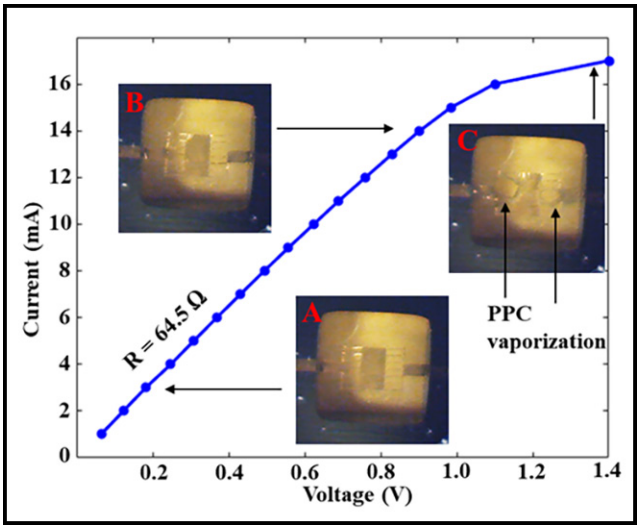

Figure 4: Voltage generated on the sense resistor vs. input current. A) For low input power < 15 mW, the sensor remains intact. B) As the input is increased further, the sensor starts to vaporize. C) Partial vaporization at sensor end-of-life occurs before the resistor breaks, producing an open circuit.

Fabrication:

0.5 μm and 1 μm PECVD oxide (SiO_2) films were deposited on the device side and backside respectively of a 500 μm silicon wafer with the GSI PECVD tool. PECVD oxide on the backside of the wafer was then patterned by reactive etching in the Oxford 81 tool followed by deep silicon etching in the Unaxis DRIE tool to produce oxide membranes on the device side. 10 nm/40 nm Ti/Au was evaporated on the 0.5 μm device side and patterned with lift-off to realize metal contacts to the piezoresistive graphene layer using the odd-hour evaporator. Commercially purchased CVD-grown single layer graphene (SLG) on copper foil was then transferred on the device side with PMMA as a handle layer and patterned with oxygen plasma in the Oxford 81 to confine it to the membrane region. A 5 wt. % PPC solution in dichloromethane (DCM) was then spin-coated on the device side to produce a 1.8 μm PPC film, which eventually serves as the sensor membrane — details of the PPC solution preparation are available in [4]. The graphene-on-polymer and metal-on-polymer devices are shown in Figure 2. Figure 3 shows the electrical configuration for testing the metal-on-polymer and graphene-on-polymer devices with sensitivities of 6.12×10^{-3} and 68×10^{-3} kPa-1 respectively, the graphene sensor showing a more than 10x improvement in performance over the metal strain gauge. Figure 4 shows the DC current vs voltage (IV) sweep and corresponding sensor self-destruction with optical verification.

Conclusions and Future Steps:

Our work demonstrates a graphene-on-polymer flexible sensor architecture for self-destructing electronics with low-voltage operation and high pressure-sensitivity using a representative sensor device. The architecture can be extended other self-destructing sensors such as accelerometers, gyroscopes, and gas sensors for a more ubiquitous self-destructing sensor platform.

References:

[1] H. Tian, et al., "A graphene-based resistive pressure sensor with record-high sensitivity in a wide pressure range," Sci. Rep., vol. 5, no. 1, pp. 1-6, Feb. 2015.

[2] P. Miao, J. Wang, C. Zhang, M. Sun, S. Cheng, and H. Liu, "Graphene Nanostructure-Based Tactile Sensors for Electronic Skin Applications," Nano-Micro Letters, vol. 11, no. 1. SpringerOpen, Sep. 01, 2019.

[3] V. Gund and A. Lal, "Graphene-On-Polymer Flexible Vaporizable Sensor," in Proceedings of the IEEE International Conference on Micro Electro Mechanical Systems (MEMS), Jan. 2021, vol. 2021-January, pp. 521-524.

[4] V. Gund, A. Ruyack, A. Leonardi, K. B. Vinayakumar, C. Ober, and A. Lal, "Spatially Controlled Transience of Graphene-Polymer Electronics with Silicon Singulation," Adv. Funct. Mater., vol. 29, no. 20, p. 1900592, May 2019.

Towards Low-Coercive Field Operation of Sputtered Ferroelectric $Sc_xAl_{1-x}N$

CNF Project Number: 1122-03

Principal Investigator(s): Amit Lal

User(s): Ved Gund, Benyamin Davaji

Affiliation(s): School of Electrical and Computer Engineering, Cornell University

Primary Source(s) of Research Funding: Defense Advanced Research Projects Agency (DARPA)

Contact(s): amit.lal@cornell.edu, vvg3@cornell.edu

Website: http://www.sonicmems.ece.cornell.edu/

Primary CNF Tools Used: AJA sputter deposition, AJA ion mill, PT770, Oxford PECVD, SEM

Abstract:

This work reports on the ferroelectric properties of scandium aluminum nitride ($Sc_xAl_{1-x}N$) thin films with an Sc-concentration between 22-30%. The goal of this work is to engineer a low coercive field in $Sc_xAl_{1-x}N$ for low-voltage post-CMOS compatible RF frontends. Films between 200 and 300 nm $Sc_xAl_{1-x}N$ were deposited on platinum (Pt) and molybdenum (Mo) electrodes. Lateral and vertical capacitors were tested over a range of electric fields, frequencies, and electrode sizes. Measured coercive field (EC) and remnant polarization (Pr) values were between 3.9-6.2 MV/cm and 58-170 $\mu C/cm^2$. Frequency, temperature, and device area-dependence were studied to identify trends towards low coercive field operation of the material. An anomalous observation relating Sc-concentration and film stress, with EC and Pr is reported to present prospects for decoupled tuning knobs to engineer lowered EC in $Sc_xAl_{1-x}N$.

Summary of Research:

Aluminum nitride (AlN) is the material of choice for MEMS RF resonators due to its excellent piezoelectric properties and CMOS compatibility. Fundamental limits in the piezoelectric properties of AlN have inspired the exploration of alloys of AlN towards enhanced piezoelectric properties. One such alloy is scandium aluminum nitride ($Sc_xAl_{1-x}N$), which presents a tuning mechanism to increase the piezoelectric coefficient by ~ 4x with scandium incorporation. Theoretical calculations predict that monotonically increasing Sc-concentration can decrease the energy barrier between the parent wurtzite structure and the hexagonal phase in $Sc_xAl_{1-x}N$ to produce ferroelectric switching. The recent discovery of ferroelectric switching in high Sc-concentration $Sc_xAl_{1-x}N$ ($x > 0.27$), has confirmed these predictions and generated significant interest as the first III-V ferroelectric [1]. Ferroelectricity has been demonstrated with Sc-concentration as low as 10%, and $Sc_xAl_{1-x}N$ has been used for ferroelectric resonators [2,3]. A major challenge to use $Sc_xAl_{1-x}N$ for device applications is the requirement for high on-chip voltages (>100V) due to its high EC. Here, we present results that map the design space of parameters which present a pathway towards lower EC in $Sc_xAl_{1-x}N$ [4,5].

Fabrication. Multiple film stacks were made for testing the impact of bottom electrode and substrate on $Sc_xAl_{1-x}N$. Ti/Pt was deposited on blanket silicon in the AJA sputtering tool followed by $Sc_xAl_{1-x}N$/Mo deposition at an external vendor (OEM). In another variation, SiO_2 was deposited in the Oxford PECVD followed by Mo/$Sc_xAl_{1-x}N$/Mo deposition at OEM. The film stacks were deposited in a cluster-line tool followed by etching of the top Mo and $Sc_xAl_{1-x}N$ in the PT770 etcher. For the bottom electrode, Ti/Pt was etched in the AJA ion mill whereas the Mo was etched in the PT770. For etch-calibration, AlN films were deposited in the OEM Endeavor M1 and etched in the PT770.

Results. A setup with continuous wave positive-up-negative-down (PUND) was used for ferroelectric testing of $Sc_xAl_{1-x}N$ (Figure 1A). The P and N pulses include both switching and leakage currents. The U and D pulses include only the leakage and can be subtracted from P and N pulses respectively to get the switching current (Figure 1B). Representative polarization vs. E-field (PE) loops are shown in Figure 1C.

In situ heating of capacitors on 300 nm $Sc_{0.30}Al_{0.70}N$ shows a monotonic decrease in E_C without a significant change in P_r (Figure 2A). The temperature coefficient of E_C for this sample is ~ 8.8 kV/°C (Figure 2B). Figure 3 shows the area and frequency-dependence of E_C and P_r across a range of electrode sizes and frequencies from 20-100 μm diameter and 1-8 kHz. E_C increases with an increase in

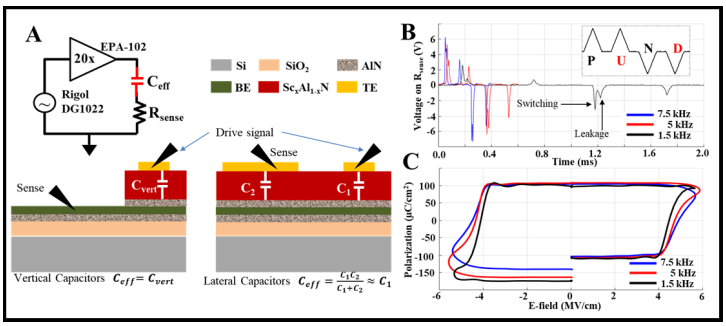

Figure 1: A) Modified Sawyer-Tower circuit for testing ferroelectric ScAlN capacitors and probing configurations for testing vertical and lateral configurations. B) Raw output voltage waveforms at various switching frequencies for PUND test (generic input waveform inset) C) Polarization vs. E-field (PE) loops generated by integrating switching currents from B.

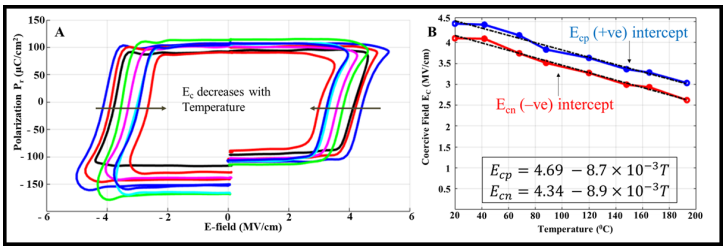

Figure 2: A) Polarization vs. E-field (PE) loops for 40 μm capacitor on 300 nm $Sc_{0.30}Al_{0.70}N$ between RT and 195°C. B) Linear decrease in E_C with increase in temperature with a coefficient of ~ 8.8 kV/cm/°C.

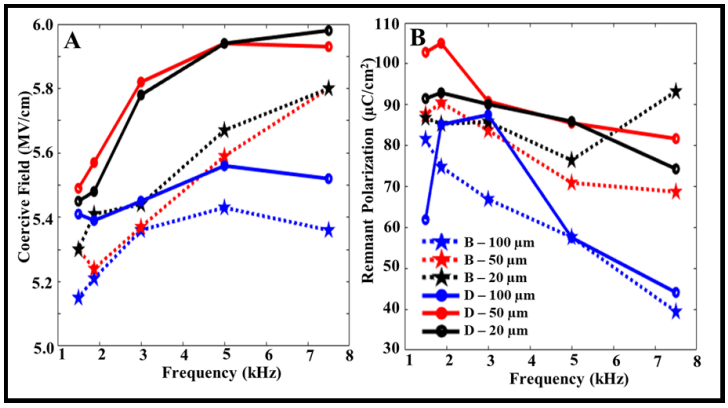

Figure 3: Plots of A) E_C and B) P_r versus frequency for capacitors of 20-100 μm diameter with Sc-concentration of 30% and 22% on Mo and Pt electrodes to map frequency and area-dependence of ferroelectricity.

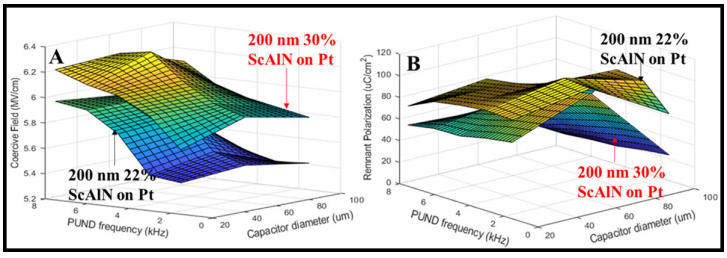

Figure 4: 3D map of A) E_C and B) P_r for 30% and 22% ScAlN on Pt electrodes tested over the range of capacitor sizes and frequencies. The 22% ScAlN has lower E_C and higher P_r due to a favorable tensile film stress of 102 MPa.

frequency and decreases with an increase in electrode size because a larger capacitor has more domains for ferroelectric switching and a lower frequency allows for more complete switching. P_r decreases with an increase in electrode size due to higher leakage in larger devices.

Figure 4 shows an anomalous dependence of E_C on Sc-concentration across a range of electrode sizes and frequencies — a lower Sc-concentration shows lower E_C due to a favorable tensile stress of 102 MPa compared to a compressive stress of 80 MPa. This stress-control shows a path towards decoupled knobs for tuning ferroelectricity, other than Sc-concentration.

Conclusions and Future Steps:

Our work maps out the design space of low E_C-operation (as low as 2.5 MV/cm) in $Sc_xAl_{1-x}N$ with *in situ* heating, and high frequency operation.

The use of this low E_C in ferroelectric transistors, resonators, transducers, and NEMS devices is the subject of on-going research.

References:

[1] S. Fichtner, N. Wolff, F. Lofink, L. Kienle, and B. Wagner, "AlScN: A III-V semiconductor based ferroelectric," Journal of Applied Physics, 2019.

[2] S. Yasuoka, et al., "Effects of deposition conditions on the ferroelectric properties of ($Al_{1-x}Sc_xN$) thin films," Journal of Applied Physics, 2020.

[3] J. Wang, M. Park, S. Mertin, T. Pensala, F. Ayazi, and A. Ansari, "A Film Bulk Acoustic Resonator Based on Ferroelectric Aluminum Scandium Nitride Films," Journal of Microelectromechanical Systems, 2020.

[4] V. Gund, et al., "Temperature-dependent Lowering of Coercive Field in 300 nm Sputtered Ferroelectric $Al_{0.70}Sc_{0.30}N$," IEEE ISAF, 2021.

[5] V. Gund, et al., "Towards Realizing the Low-Coercive Field Operation of Sputtered Ferroelectric $Sc_xAl_{1-x}N$," TRANSDUCERS 2021- 21st Int. Conf. Solid-State Sensors, Actuators Microsystems, 2021.

A High-Performance Epitaxial Transparent Oxide Thin-Film Transistor Fabricated at Back-End-Of-Line Temperature (< 450°C) by Suboxide Molecular-Beam Epitaxy

CNF Project Number: 2543-17

Principal Investigator(s): Darrell Schlom

User(s): Jisung Park

Affiliation(s): Department of Material Science and Engineering, Cornell University, Ithaca, NY 14853, USA

Primary Source(s) of Research Funding: Semiconductor Research Corporation

Contact(s): schlom@cornell.edu, gp359@cornell.edu

Primary CNF Tools Used: PT720/740, PVD75 sputter deposition, Autostep i-line stepper

Abstract:

We fabricated a micron-scale field effect transistor (FET) based on epitaxial In_2O_3 thin film with drain current of 0.2 A/mm and on-off ratio of 1×10^8 at room temperature. The whole device manufacturing process including epitaxial In_2O_3 growth takes place below 450°C, making it suitable for back-end-of-line (BEOL) process.

Summary of Research:

Epitaxial layer of indium oxide (In_2O_3) was formed below the threshold for BEOL process, $T_{sub} < 450$°C, with narrow rocking curve less than 0.05° and low surface roughness of 0.45 nm RMS value, using recently developed version of molecular-beam epitaxy called suboxide MBE [1,2]. At lower carrier concentration regime, an epitaxial In_2O_3 film attained a mobility of 28 $cm^2V^{-1}s^{-1}$ at a carrier concentration of 1.35×10^{19} cm^{-3}. We chose this film to make a FET device because of its low carrier concentration, which is ideal for achieving complete depletion.

We used reactive ion etching using the same conditions we described recently for etching stannate materials for device isolation, and it worked well for In_2O_3 [3]. Contacts at the source/drain and top gate were made with sputtered ITO thin film. For dielectric, ALD-grown HfO_2 was deposited. Figure 1 depicts the device schematic. The characteristics of the devices are shown in Figure 2 and Figure 3.

The hysteresis behavior in the transfer characteristic with respect to the voltage sweep directions is similar to what we saw on $BaSnO_3$-based field effect transistor made with the same technique. It is believed this non-ideal behavior is attributed to the defects in HfO_2. The drain current of the device in the output characteristic is 0.2 A/mm and the on-off ratio is 1×10^8. In Figure 4, we compared the results of our devices to those of the most advanced oxide channel thin film transistor [4-49].

Our result is in the upper left corner, where the expected performance with high drain current and on-off ratio should be found. This indicates that our results are comparable to the best-performing devices based on alternative oxide channel materials, and thus promising.

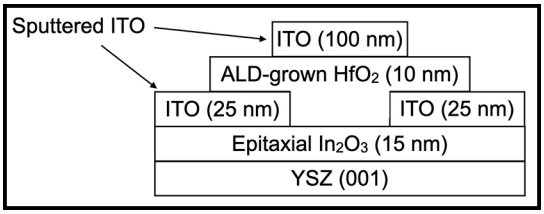

Figure 1: Device schematic.

References:

[1] P. Vogt, et al., APL Materials 9 (2021) 031101.
[2] P. Vogt and O. Bierwagen, Phys. Rev. Mat. 2 (2018) 120401.
[3] J. Park, US Patent 10,868,191 (2020).
[4] Z. Yuan, et al., Thin Solid Films 519, 3254-3258 (2011).
[5] P. K. Nayak, et al., Appl. Phys. Lett. 103, 033518 (2013).
[6] N. Mitoma, et al., Appl. Phys. Lett. 104, 102103 (2014).
[7] L. Wang, et al., 2020 IEEE Symposium on VLSI Technology (2020).
[8] M.Si, et al., IEEE Trans. Electron Devices 68, 1075-1080 (2021).
[9] M. Si, et al., IEEE Electron Device Lett. 42, 184 (2021).
[10] M. Si, et al., Nano Lett. 21, 500-506 (2021).
[11] J. Park, et al., APL Mater. 8, 011110 (2020).
[12] U. Kim, et al., APL Mater. 3, 036101 (2015).
[13] J. Shin, et al., Appl. Phys. Lett. 109, 262102 (2016).
[14] C. Park, et al., Appl. Phys. Lett. 105, 203503 (2014).
[15] Y. M. Kim, et al., APL Mater. 5, 016104 (2017).
[16] Y. M. Kim, et al., Appl. Phys. Exp. 9, 011201 (2016).
[17] Y. Kim, et al., APL Mater. 6, 096104 (2018).
[18] J. Cheng, et al., J. Vac. Sci. Technol. B 38, 012201 (2020).
[19] J. Cheng, et al., IEEE Electron Device Lett. 41. 621 (2020).
[20] J. Cheng, et al., Appl. Phys. Lett. 118, 042105 (2021).
[21] H.-H. Hsieh and C.-C. Wu, Appl. Phys. Lett. 89, 041109 (2006).
[22] E. Fortunato, et al., Adv. Mater. 24, 2945-2986 (2012).
[23] B. Bayraktaroglu, et al., IEEE Electron Device Lett. 30, 946-948 (2009).
[24] B.-Y. Oh, et al., Semicond. Sci. Technol. 26, 085007 (2011).
[25] B. Bayraktaroglu, et al., IEEE Electron Device Lett. 29, 1024-1026 (2008).
[26] K. Nomura, et al., Science 300, 1269-1272 (2003).
[27] K. Nomura, et al., Nature 432, 488-492 (2004).
[28] R. Yao, et al., Appl. Phys. Lett. 112, 103503 (2018).
[29] N. C. Su, et al., IEEE Electron Device Lett. 30, 1317-1319 (2009).
[30] C.-Y. Chung, et al., Appl. Phys. Lett. 106, 123506 (2015) /igzo.
[31] I. Noviyana, et al., Materials 10, 702 (2017).
[32] S. Tomai, et al., Jpn. J. Appl. Phys. 51, 03CB01 (2012).
[33] R. Jany, et al., Adv. Mater. Int. 1, 1300031 (2013).
[34] L. Dong, et al., Proc. IEEE Int. Electron Devices Mtg, 26.4.1-26.4.4. (2010).
[35] H. Zhou, et al., Appl. Phys. Lett. 111, 092102 (2017).
[36] A. J. Green, et al., IEEE Electron Device Lett. 38, 790-793 (2017).
[37] Z. Xia, et al., IEEE Electron Device Lett. 39, 568-571 (2018).
[38] N. Moser, et al., IEEE Electron Device Lett. 38, 775-778 (2017).
[39] K. D. Chabak, et al., IEEE Electron Device Lett. 39, 67-69 (2018).
[40] H. Zhou, et al., ACS Omega 2, 7723.7729 (2017).
[41] N. A. Moser, et al., Appl. Phys. Lett. 110, 143505 (2017).
[42] W. S. Hwang, et al., Appl. Phys. Lett. 104, 203111 (2014).
[43] C. Ju, et al., Curr. Appl. Phys. 16, 300-304 (2016).
[44] R. E. Presley, et al., J. Phys. D: Appl. Phys. 37, 2810-2813 (2004).
[45] S. Li, et al., Nat. Mater. 18, 1091-1097 (2019).
[46] M. Si, et al., ACS Nano 14, 11542-11547 (2020).
[47] J. Zhang, et al., IEEE Electron Device Lett. 40, 1463 (2019).
[48] A. Verma, et al., Appl. Phys. Lett. 105, 113512 (2014).
[49] H. Chandrasekar, et al., ACS Appl. Electron. Mater. 2, 510.516 (2020).

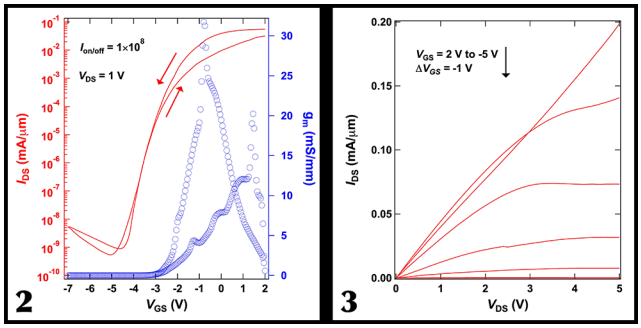

Figure 2, left: Transfer characteristic of the device. Figure 3, right: Output characteristic of the device.

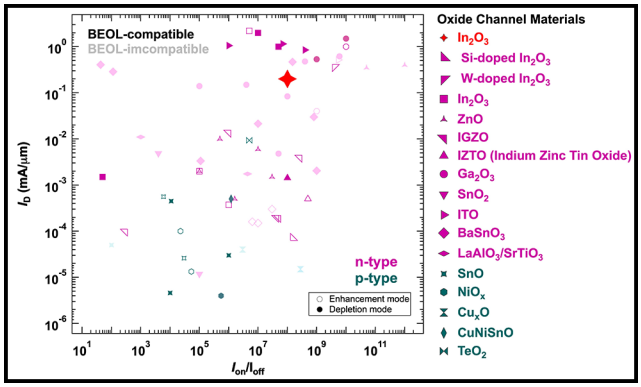

Figure 4: The comparison of device performances based on oxide channel materials in terms of drain current and on-off ratio.

Fabrication and Manipulation of Microscale Opto-Electrically Transduced Electrodes (MOTEs)

CNF Project Number(s): 2578-17, 2836-19

Principal Investigator(s): Prof. Alyosha C. Molnar

User(s): Sunwoo Lee, Sanaz Sadeghi, Shahab Ghajari, Devesh Khilwani

Affiliation(s): Electrical and Computer Engineering, Cornell University

Primary Source(s) of Research Funding: National Institutes of Health (NIH)

Contact(s): am699@cornell.edu, sl933@cornell.edu, ss3842@cornell.edu, sg2367@cornell.edu, dk842@cornell.edu

Website: https://molnargroup.ece.cornell.edu/

Primary CNF Tools Used: ABM contact aligner, AJA sputter deposition, Westbond 7400A ultrasonic wire bonder, Oxford 100, Oxford 81, Oxford 82, Unaxis deep Si etcher, Oxford PECVD, Oxford ALD, Anatech, P7 profilometer, ZEISS Ultra and Supra SEMs

Abstract:

Recording neural activity in live animals *in vivo* is critical in elucidating how the brain functions. However, such recording poses several challenges. Electrical techniques typically require electrodes to be tethered to the outside world directly via a wire, or indirectly via an RF Coil [1], which is much larger than the electrodes themselves. Tethered implants suffer from the residual motions between electrodes and neurons as the brain moves, limiting our ability to measure from peripheral nerves in moving animals, especially in smaller organisms such as zebra fish or fruit flies. On the other hand, optical techniques, which are becoming increasingly potent, are often limited to subsets of neurons in any given organism, impeded by scattering of the excitation light and emitted fluorescence, and limited to low temporal resolution [2]. Here we present an untethered opto-electrical system on chip (SoC), Micro-scale Opto-electrically Transduced Electrodes (MOTEs), which are powered by, and communicating through a microscale optical interface, combining many benefits of optical techniques with high temporal-resolution of electrical recording.

Summary of Research:

Our fabrication starts with about 5 mm × 5 mm, conventional 180 nm complementary metal oxide semiconductor (CMOS) die, which contains the electronics for signal amplification, encoding, and transmission. The CMOS die is then integrated with AlGaAs diode, which acts as a photo-voltaic (PV) as well as light emitting diode (LED), hence the diode is abbreviated as PVLED. The PVLED provides an optical link which powers the electronics and transmits encoded signals in optical pulses. The MOTE utilizes pulse position modulation (PPM) for signal encoding for its high information-per-photon efficiency, where the spacing between the output pulses is proportional to the measured electric field of neuronal signals across the measurement electrodes. Figure 1 depicts a conceptual deployment and system description of such MOTE [3].

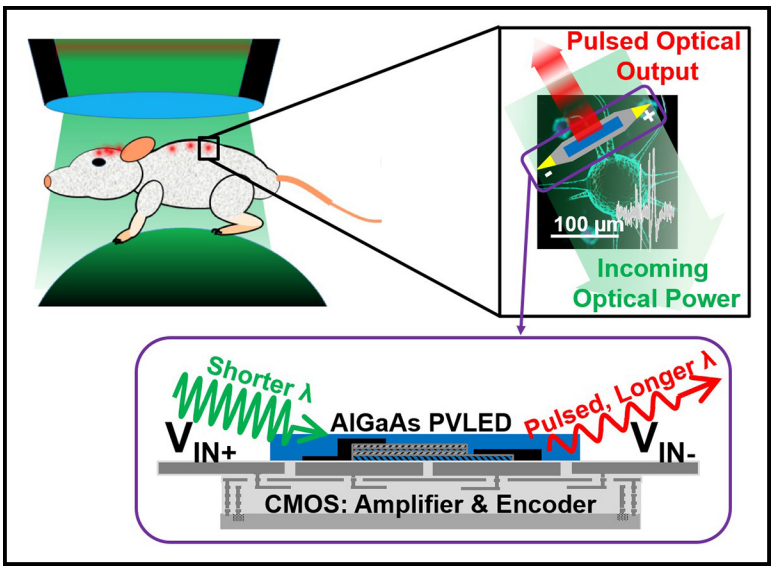

Figure 1: An exemplary implementation and system level description of the MOTEs in a mouse animal model [3].

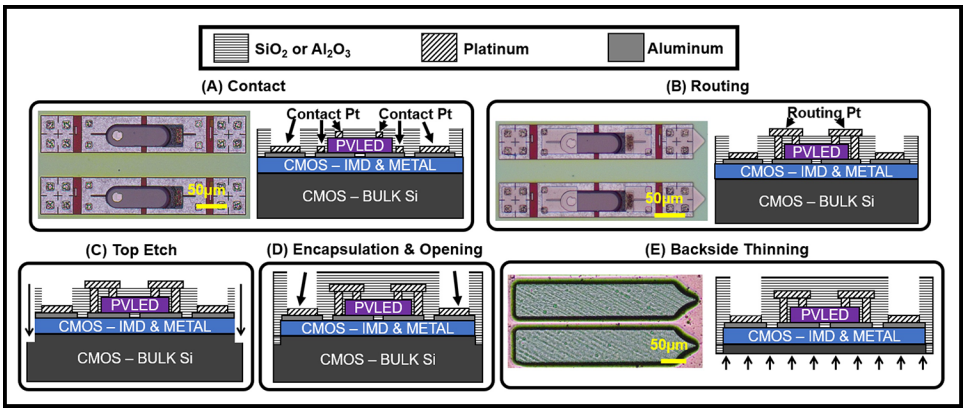

Figure 2: MOTE fabrication process. (A) An AlGaAs μLED (bullet-shaped) array is transferred on top of a CMOS chip containing an array of unit MOTE circuitry, and Pt is deposited over contact areas. (B) Routing Pt electrically connects each μLED with an underlying CMOS. (C) Each MOTE is segregated and (D) encapsulated with SiO_2 and Al_2O_3, except for the measurement electrodes area. (E) The backside Si is thinned so that total thickness is < 30 μm. Adapted from [4].

The AlGaAs diodes are first fabricated on a sapphire wafer, to be later released from the sapphire substrate with a sacrificial poly(methyl methacrylate) (PMMA) polymer. Once the PMMA-coated AlGaAs diodes are transferred onto the CMOS die, the Oxford 81 plasma etcher is used to remove the sacrificial PMMA, leaving only the diodes array intact on the CMOS die. To establish the electrical contact between the PVLED and CMOS, we have used the CNF ABM contact aligner for photolithography with AZ nLof2020UV photoresist for efficient lift-off process that ensues after metal deposition. After the contact fabrication, the contacts of CMOS and PVLED are connected via similar photolithography process, and to maximize the conformality of the metal routing, we employ AJA sputtering. Following the routing step, each MOTE is encapsulated using Oxford ALD and PECVD for SiO_2 and Si_3N_4 deposition, followed by dielectric etching using OXFORD 100 and UNAXIS deep reactive ion etch (DRIE) for release. Figure 2 described the fabrication sequence described herein.

It should be noted that before embarking on the nano/micro-fabrication flow, to confirm the functionality of each module (CMOS and the diode), we use the Westbond 7400A ultrasonic wire bonder for board-level testing. ZEISS Ultra and Supra scanning electron microscopes (SEMs) are also used to inspect the fabricated MOTE for debugging purposes.

Conclusions and Future Steps:

MOTEs are the smallest electrophysiological sensor of its kind, and we are currently testing the MOTEs *in vivo* in mouse animal models. As we accumulate more data on our ongoing *in vivo* efforts, we plan to improve fabrication processes as well as surgical procedures for inserting the MOTEs into the mouse cortex.

References:

[1] Harrison RR, Watkins PT, Kier RJ, Lovejoy RO, Black DJ, Greger B, and Solzbacher F. A Low-Power Integrated Circuit for a Wireless 100-Electrode Neural Recording System. IEEE J. Solid-State Circuits. 2006 Dec 26;42(1): 123-133.

[2] Yang W and Yuste R. *In vivo* Imaging of Neural Activity. Nature Methods. 2017 Mar 31;14(4):349.359.

[3] Lee S, Cortese AJ, Trexel P, Agger ER, McEuen PL, and Molnar AC. A 330 μm × 90 μm Opto-Electronically Integrated Wireless System-on-Chip for Recording of Neural Activities. IEEE ISSCC. 2018 Feb.

[4] Lee S, Cortese AJ, Mok A, Wu C, Wang T, Park JU, Smart C, Ghajari S, Khilwani D, Sadeghi S, Ji Y, Goldberg JH, Xu C, McEuen PL, and Molnar AC. Fabrication of Injectable Micro-Scale Optoelectronically Transduced Electrodes (MOTEs) for Physiological Monitoring. IEEE JMEMS. 2020 June 12;29(5):720.726.

Millimeter-Wave Large Signal Performance of AlN/GaN/AlN HEMTs

CNF Project Number: 2800-19

Principal Investigator(s): Debdeep Jena, Huili Grace Xing

User(s): Austin Hickman, Reet Chaudhuri, Kazuki Nomoto, Lei Li

Affiliation(s): Electrical and Computer Engineering, Materials Science and Engineering; Cornell University

Primary Source(s) of Research Funding: Semiconductor Research Corporation

Contact(s): djena@cornell.edu, grace.xing@cornell.edu, alh288@cornell.edu

Primary CNF Tools Used: AFM, i-line stepper, PT770 etcher, Oxford 81 etcher, CVC SC4500 odd-hour evaporator, JEOL 6300 EBL, Oxford PECVD, AJA sputter deposition, Woollam ellipsometer, Zeiss Ultra SEM, Leica critical point dryer, Glen1000 resist stripper, P7 profilometer

Abstract:

Gallium nitride high-electron-mobility transistors (GaN HEMTs) are ideal for high-power, gigahertz (GHz) frequency applications due to their wide bandgap and high electron saturation velocity. To further improve upon established GaN HEMTs, our group has introduced GaN HEMTs based on the aluminum nitride (AlN) platform using anAlN/GaN/AlN double heterostructure. In this report, we show the first large signal measurements forAlN/GaN/AlN HEMTs at millimeter wave frequencies (30+ GHz).

Summary of Research:

HEMTs were fabricated on the AlN/GaN/AlN heterostructure. The processing is highlighted by JEOL 6300 electron-beam lithography achieving T-gates with gate lengths as short as 60 nm. The AlN/GaN/AlN HEMTs showed on-currents over 3 A/mm and transconductance of over 0.7 S/mm. Small-signal characteristics for this device demonstrated a cutoff frequency (f_t) and maximum oscillation frequency (f_{max}) of 124 and 221 GHz, respectively. The HEMT was measured for large signal power sweep measurements at 30 and 94 GHz. At peak PAE, it showed associated output powers of 2.2 and 1.7 W/mm and gain of 7.1 and 3.1 dB, respectively. At peak output power, the HEMT demonstrated 2.6 and 2.2 W/mm at 30 and 94 GHz, respectively.

These numbers represent the record for HEMT on the AlN platform.

Conclusions and Future Steps:

The HEMTs in this report were limited by degradation in on-current and increased gate leakage during large signal measurement. This is likely caused by the lack of a surface pretreatment before the SiN passivation, leading to excessive surface states. An additional factor could be the thicker GaN channel, which increases the stress in top barrier, leading to degradation when further stressed at high biases. Therefore, the next generation ofAlN/GaN/AlN HEMTs will feature a 30 nm GaN channel to reduce stress in the barrier, and an *in situ* cleaning step to minimize surface states before SiN deposition.

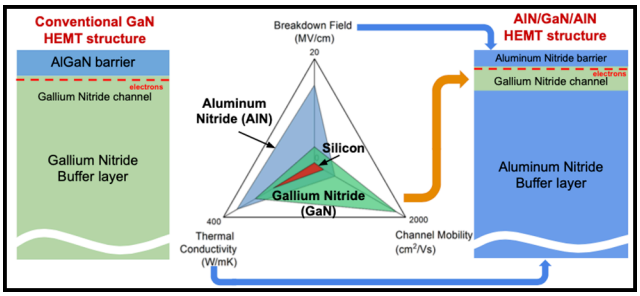

Figure 1: The cross-section of a conventional AlGaN/GaN heterostructure (left) and our group's AlN/GaN/AlN heterostructure (right). As highlighted by the radar plot (center), the AlN/GaN/AlN heterostructure takes full advantage of what both GaN and AlN have to offer.

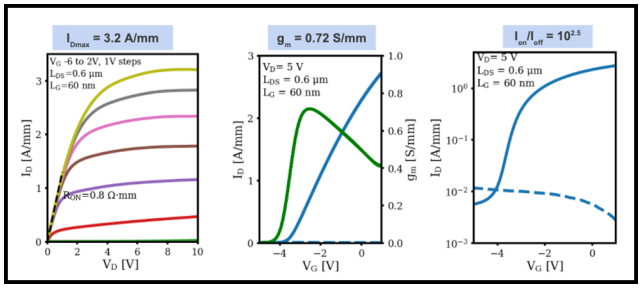

Figure 2: (left) Output characteristics of an AlN/GaN/AlN HEMT showing on-currents over 3 A/mm with high output resistance. (center) The transfer characteristics highlighted by a transconductance of 0.72 S/mm. (right) Log-scale transfer curves with an on/off ratio of $10^{2.5}$.

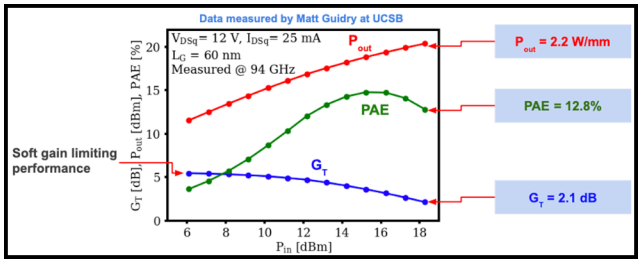

Figure 3: The load-pull power sweep of anAlN/GaN/AlN HEMT at 94 GHz. The result is highlighted by a measured output power of 2.2 W/mm.

Nitrogen Polar III-Nitride Resonant Tunneling Diodes

CNF Project Number: 2801-19

Principal Investigator(s): Huili Grace Xing, Debdeep Jena

User(s): Jimy Encomendero, Yongjin Cho, Shao-Ting Ho

Affiliation(s): Electrical and Computer Engineering, Cornell University

Primary Source(s) of Research Funding: NSF

Contact(s): grace.xing@cornell.edu, djena@cornell.edu, jje64@cornell.edu, yc2343@cornell.edu

Primary CNF Tools Used: Veeco AFM, ABM contact aligner, YES asher, CVC SC4500 odd-hour evaporator, PT770 etcher, P10 and P7 profilometer, Oxford ALD, Oxford 81 etcher, AJA sputter deposition

Abstract:

We report the engineering of resonant tunneling transport in polar III-nitride heterostructures grown along the [000-1] direction of single-crystal GaN substrates. The double-barrier structures, grown by molecular beam epitaxy (MBE), consist of a 3-nm-thick GaN quantum well flanked by two 2.2-nm AlN tunneling barriers. Room temperature electronic transport reveals a peak current density of ~ 7.8 kA/cm^2, measured in multiple resonant tunneling diodes (RTDs) with mesa areas between 36 and 144 μm^2. Electronic quantum interference is confirmed by the presence of repeatable room-temperature negative differential conductance (NDC) under reverse bias injection. The polarization-induced threshold voltage, characteristic in polar RTDs, is also measured at ~ +4.2V. When the devices are biased within the NDC region, microwave electronic oscillations are generated in the external circuit. Owing to the highly non-linear current-voltage characteristics, the oscillatory signal contains not only the fundamental frequency at 10.7 MHz, but also multiple harmonics up to the fifth overtone. These results constitute the first demonstration of robust resonant tunneling injection in III-Nitride N-polar RTDs capable of AC power generation.

Summary of Research:

The recent demonstration of resonant tunneling transport in GaN/AlN heterostructures [1-4] has reignited interest in harnessing this quantum transport regime for the development of ultrafast high-power electronic and photonic devices. Featuring a wide and tunable band gap spanning several electron-volts, III-Nitride heterostructures stand out as a highly versatile platform for tailoring electronic states via quantum confinement. This advantage, coupled with their high breakdown electric-fields, high thermal conductivities, and high longitudinal optical (LO) phonon energies, make nitride materials a promising platform for the development of ultra-fast electronic oscillators and high-power intersubband lasers.

These new functionalities stem from the possibility of engineering ultra-fast carrier injection into discrete energy levels via resonant tunneling, thereby enabling electronic and optical gain over a wide range of frequencies. In non-centrosymmetric semiconductors, however, the engineering of quantum-confined electronic states via heterostructure design, results not only in a discontinuous energy band profile, but also generates built-in polarization charges, whose spatial distribution lacks inversion symmetry [3,5]. Therefore, in the case of Ga-polar RTDs—grown along the [0001] direction—electrons injected from the emitter side undergo enhanced quantum interference effects compared to carriers injected from the collector contact. These natural broken symmetry effects can be exploited as an additional degree of freedom for the realization of novel device functionalities. In this scenario, nitrogen-polar RTDs—grown along the [000-1] direction—offer the possibility of placing the emitter electrode on the top of the resonant tunneling structure, facilitating its integration with other materials such as ferromagnets and superconductors. Despite these advantages, N-polar RTDs have not been demonstrated so far. In this work, we report the growth, fabrication, and transport characteristics of the first N-polar GaN/AlN RTD, exhibiting robust negative differential conductance (NDC) at room temperature [5].

Molecular beam epitaxy (MBE) is employed to grow the GaN/AlN double-barrier resonant tunneling structures under metal-rich growth conditions atop a N-polar single-crystal n-type GaN substrates [6]. The structure consists of a 3 nm GaN quantum well flanked by two 2.2 nm AlN barriers that are sandwiched by heavily doped n-type GaN

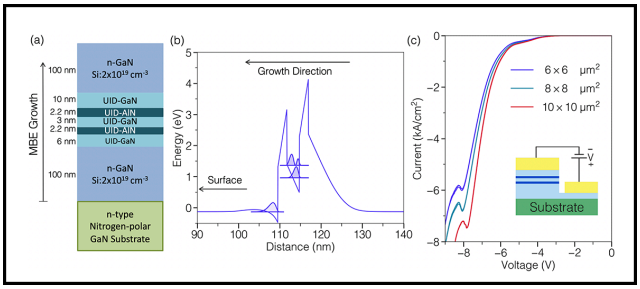

Figure 1: (a) Schematic of the nitrogen-polar RTD structure grown by molecular beam epitaxy. The structure consists of a 3 nm GaN quantum well flanked by two 2.2 nm AlN barriers that are sandwiched by heavily doped n-type GaN contact layers. (b) The band diagram of the structure shows the corresponding energies and wavefunctions of the resonant tunneling levels. (c) Current-voltage characteristics are measured at room temperature, revealing a region of negative differential conductance.

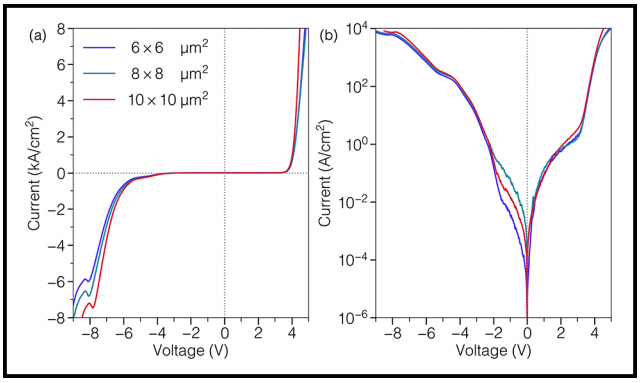

Figure 2: Electronic transport is measured at room temperature in multiple devices with different areas and under both bias polarities. (a) The linear plot shows the onset of negative differential conductance when the diode is biased at ~ -7.8 V, driving a peak tunneling current of ~ 7.8 kA/cm². Under forward bias, the polarization-induced threshold voltage is measured at ~ +4.2 V. (c) The logarithmic plot shows the highly asymmetric exponential modulation of the tunneling current.

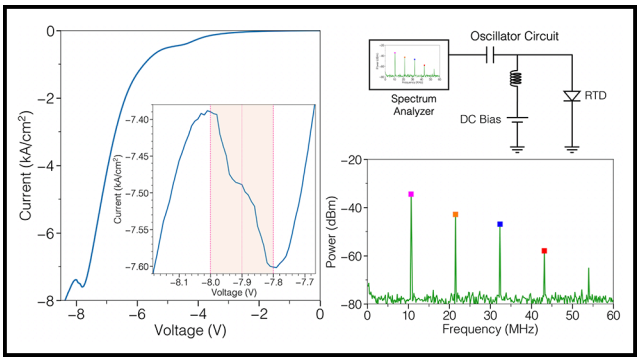

Figure 3: Nitrogen-polar RTD electronic oscillator. When the RTD is biased within the negative differential conductance (NDC) region, AC oscillations build up in the circuit. A bias tee and spectrum analyzer are employed to measure the spectrum of the AC signal. Owing to the highly non-linear characteristics of the NDC region, we measured not only the fundamental frequency at 10.7 MHz, but also multiple harmonics up to the fifth overtone.

layers. *In situ* reflection high-energy electron diffraction (RHEED) showed a (3×3) surface reconstruction at low temperature after growth, indicating the conservation of the nitrogen polarity throughout the whole epitaxial process.

Sharp heterointerfaces are confirmed by the pronounced interference fringes of the symmetric X-ray diffraction (XRD) pattern. The sample also reveals smooth surface morphology with clear atomic steps. After growth, RTDs are fabricated by conventional contact lithography, reactive ion etching, and electron-beam metal evaporation.

Electronic transport is measured at room temperature, revealing negative differential conductance (NDC) due to resonant tunneling injection, in multiple devices with different mesa areas. Under reverse bias, the diodes drive a peak tunneling current of ~ 7.8 kA/cm^2 at a resonant bias of ~ -7.8V, consistent with the energy alignment between the emitter states and the resonant level in the GaN quantum well.

Under forward bias, the polarization-induced threshold voltage is measured at ~ +4.2V. When the device is biased in the NDC-region, room-temperature electronic oscillations are generated, attesting to the robustness of the resonant tunneling phenomena [4]. Owing to the highly non-linear characteristics of the NDC region, the oscillatory signal contains not only the fundamental frequency at 10.7 MHz, but also multiple harmonics up to the fifth overtone.

These results constitute the first demonstration of robust resonant tunneling injection in III-Nitride N-polar RTDs capable of AC power generation.

References:

[1] J. Encomendero, et al. Physical Review X 7, 041017 (2017).

[2] J. Encomendero, et al. Applied Physics Letters 112, 103101 (2018).

[3] J. Encomendero, et al. Physical Review Applied 11, 034032 (2019).

[4] J. Encomendero, et al. Physical Review Applied 13, 034048 (2020).

[5] Y. Cho, et al. Applied Physics Letters 117, 143501 (2020).

[6] J. Encomendero, et al. Journal of Vacuum Science and Technology A 39, 023409 (2021).

CMOS Neural Probe with Multi-Turn Micro-Coil Magnetic Stimulation

CNF Project Number: 2847-19

Principal Investigator(s): Alyosha Molnar

User(s): Edward Szoka

Affiliation(s): Department of Electrical and Computer Engineering, Cornell University

Primary Source(s) of Research Funding: National Institute of Health

Contact(s): molnar@ece.cornell.edu, ecs227@cornell.edu

Primary CNF Tools Used: ABM contact aligner, AJA sputter deposition, Oxford 81, Oxford 100, Oxford ALD, PT770 etcher, P7 profilometer, Unaxis deep silicon etcher, Parylene coater, Westbond 7400A ultrasonic wire bonder

Abstract:

Micro-coil magnetic stimulation has been shown to be an effective method of neurostimulation while circumventing the issues that limit the effectiveness of the more commonly used implantable electrodes [1,2]. This is due to the micro-coils not needing direct contact to the biological tissue allowing for complete device encapsulation. This allows for the stimulation effectiveness to be maintained over long periods of time while eliminating the electrode-tissue interface that is prone to electrochemical effects that can damage the probe or tissue [3]. Recent work has developed programmable micro-coil neural probes integrating complementary metal oxide semiconductor (CMOS) technology with the micro-coil design [4]. However, the design did not utilize multi-turn micro-coils to reduce the necessary stimulation current. This work proposes a neural probe that co-optimizes the micro-coil design with CMOS micro-coil current drivers to maximize the induced electric field gradients. A four-wire interface is used to supply power, deliver the stimulation current, and program the micro-coil current directions using four terminals. Preliminary *in vitro* testing with mouse olfactory bulb slices and a commercial MEA show the probes are capable of producing changes in neural behavior.

Summary of Research:

The circuit implementation of the proposed neural probe is shown in Figure 1. A four-wire interface is implemented to reduce the number of necessary pads to power the probe, drive the micro-coils, and program the location of the stimulation sites by using the supply and differential current inputs as the programming clock and data signals respectively. The clock is generated by a comparator comparing VDD to a bias voltage. The programming data is extracted from the common-mode of the differential input current using a pair of unity gain, high output impedance amplifiers with the outputs connected together. The current drivers use a push-pull topology operating with the bias transistor pairs operating in class AB to balance between the maximum input current range and the quiescent bias current. The output of the current driver is the parallel outputs of cascoded PFET and NFET current mirrors. Cascoded outputs are used to ensure accurate current mirroring over the wide range of coil voltages present during stimulation.

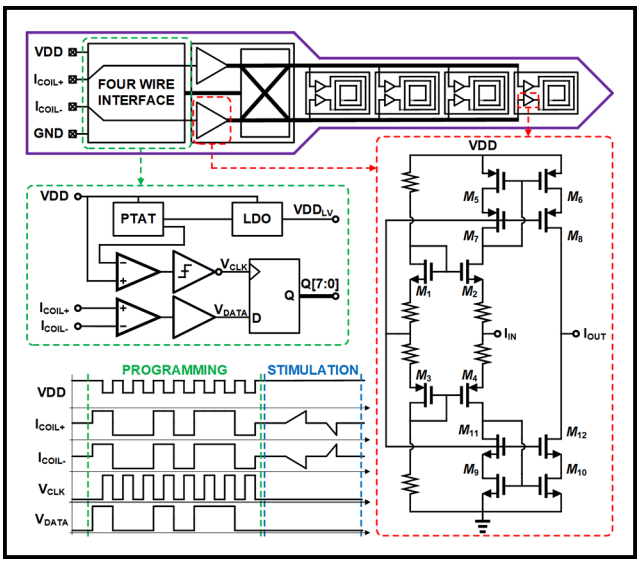

Figure 1: Circuit implementation of the proposed neural probe.

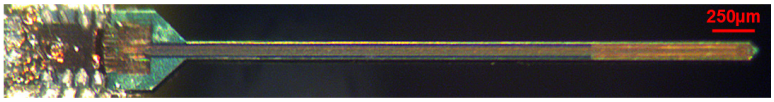

Figure 2: Micrograph of a released and fully encapsulated neural probe.

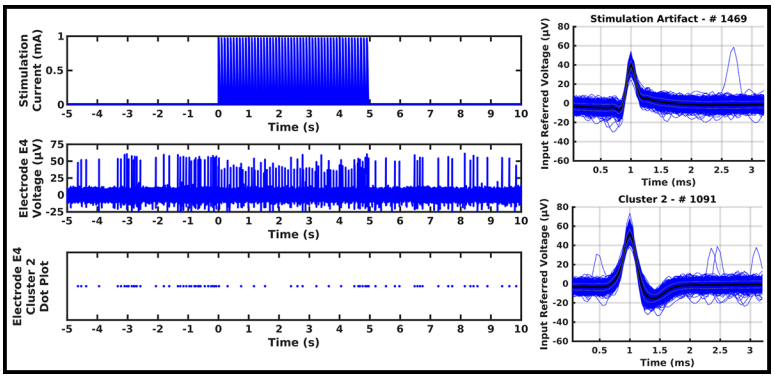

Figure 3: Preliminary data showing inhibitory neural response to stimulation train and time aligned neural spikes and stimulation artifacts.

The neural probes are thinned down and released from the original chip packaging through a series of nanofabrication steps. The neural probes are initially embedded in 5 mm × 5 mm die of foundry CMOS with a thickness of 330 μm. Aluminum oxide and chrome are deposited (used as silicon etching and oxide etching masks respectively) and patterned using conventional photolithography and a combination of wet etching and plasma etching. The oxide is etched in a CHF_3/O_2 plasma sto expose the silicon surface. The exposed topside silicon is etched in a deep reactive-ion etching (DRIE) process down to the desired thickness of the neural probe of 70 μm. The chips are flipped upside-down, and the bulk silicon is etched in the same DRIE process until the micro-coils are released from the rest of the chip. The released probes are mounted to a carrier printed circuit board using conductive silver epoxy and electrically connected using the Westbond 7400A ultrasonic wire bonder. The wire bonds are protected using a clear epoxy before the entire assembly is coated with approximately 4 μm of Parylene-C.

In vitro testing is done on 300 μm-thick mouse olfactory bulb slices with a commercial MEA. Spikes and LFPs are recorded using a 120-electrode microelectrode array with titanium nitride electrodes. The probe is placed on the surface of the slice with the micro-coils located over the region of tissue with visible activity. Testing consisted of driving the micro-coils with stimulation trains of fifty 10 Hz ramp waveforms spaced ten seconds apart while observing changes in neural behavior.

Figure 3 shows preliminary results where the micro-coils are configured to have the two inner coils run current in opposite directions to generate the strongest gradient in the electric field while the outer coils are turned off. The dot plot shows that the stimulation waveform has an inhibitory effect on the recorded activity which is consistent with the results found in [4].

Conclusions and Future Steps:

This work proposes a neural probe that co-optimizes the micro-coil design with CMOS current drivers to maximize the electric field gradients and reduce the necessary stimulation current. Independently driven multi-turn micro-coils allow for spatially programmable neurostimulation sites between adjacent micro-coils. A four-wire interface is used to reduce the number of pads on the probe backend by using the supply and differential current inputs as the programming clock and data signals, respectively. Preliminary *in vitro* testing of the neural probe is done with slices of a mouse olfactory bulb in conjunction with an MEA showing changes in neural behavior.

Future work looks to explore neural probe designs utilizing micro-coil magnetic stimulation with recording electrodes to allow for a closed-loop neuromodulation.

References:

[1] S. W. Lee, F. Fallegger, B. D. F. Casse, and S. I. Fried, "Implantable microcoils for intracortical magnetic stimulation," Science Advances, vol. 2, no. 12, 2016.

[2] S. W. Lee, K. Thyagarajan, and S. I. Fried, "Micro-coil design influences the spatial extent of responses to intracortical magnetic stimulation," IEEE Transactions on Biomedical Engineering, vol. 66, no. 6, pp. 1680-1694, June 2019.

[3] S. F. Cogan, K. A. Ludwig, C. G. Welle, and P. Takmakov, "Tissue damage thresholds during therapeutic electrical stimulation," Journal of Neural Engineering, vol. 13, no. 2, p. 021001, Jan 2016.

[4] E. C. Szoka, J. C. Werth, S. Lee, J.-I. Lee, A. J. Cortese, T. A. Cleland, S. Fried, and A. Molnar, "Neural probe utilizing programmable microcoil magnetic stimulation," in 2021 10th International IEEE/EMBS Conference on Neural Engineering (NER), 2021, pp. 651-654.

New Generation of DUV Photoresists with Precise Molecular Structure

2021 CNF Intern: Francesca Bard

Intern Affiliation: Materials Science and Engineering, Cornell University

Principal Investigator: Prof. Christopher Kemper Ober, Materials Science and Engineering, Cornell University

Mentor: Dr. Florian Hermann Ulrich Käfer, Materials Science and Engineering, Cornell University

Primary Sources of Research Funding: 2021 Cornell NanoScale Science & Technology Facility Research Experiences for Undergraduates (CNF REU) Program via National Science Foundation under Grant No. NNCI-2025233, Intel

Contact(s): fmb54@cornell.edu, c.ober@cornell.edu, fhk28@cornell.edu

Primary CNF Tools Used: ASML 300C DUV stepper, Zeiss SEM, Woollam RC2 ellipsometer, JEOL 6300

Abstract:

This CNF internship project is focused on synthesizing peptoids, with a controlled sequence of amines and chain length, to be used as photoresist materials. As photoresist materials, these peptoids must be UV sensitive, changing solubility when exposed to UV light. 10-mers (peptoids with 10 repeat units) are created with different compositions and sequences of amines to optimize the pattern resolution of the photoresist. These positive tone chemically amplified photoresists are exposed with deep ultraviolet (DUV) to create line patterns ranging from 1-0.1 μm. The line patterns are analyzed to determine the effect of the chosen composition and sequence.

Summary of Research:

Introduction. Photoresists are typically made of polymers that are polydisperse and whose monomers are randomly distributed along the chain. These attributes bottleneck the ability to attain smaller feature sizes since the dispersity and length affects photoresist properties. Therefore, it is imperative to create new materials where the sequence and chain length can be controlled, like peptoids.

Peptoid Synthesis and Characterization. The peptoids are synthesized by adding each amine to 2-chlorotrityl chloride resin. The resin is activated through bromoacetylation, and then the amine is added by displacing the bromine (see Figure 1).

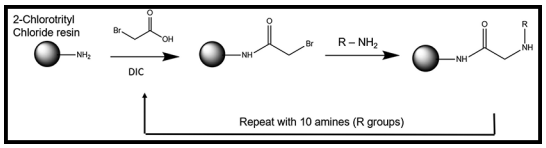

Figure 1: Peptoid synthesis on 2-chlorotrityl chloride resin through bromoacetylation and displacement until all ten amines (R groups) are added.

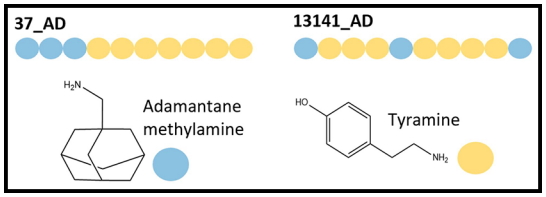

Figure 2: Peptoid amine sequence of samples 37_AD and 13141_AD.

This process repeats until all 10 amines are added to the chain. The samples have different sequences but the same composition — 3 adamantane methylamine (AD) and 7 tyramine (TA). Sample 37_AD has sequence $AD_{(3)}$–$TA_{(7)}$, and sample 13141_AD has sequence $AD_{(1)}$–$TA_{(3)}$–$AD_{(1)}$–$TA_{(4)}$–$AD_{(1)}$ (see Figure 2).

Afterward, the peptoids are cleaved off the resin using mild acid, protected, and purified. The amine, tyramine, present in all samples, is protected using di-*tert*-butyl dicarbonate. Exposure to UV light deprotects tyramine, changing its chemical structure and solubility. The samples are then purified using preparative high-performance liquid chromatography (HPLC). The glass transition temperature of the peptoids is determined through differential scanning calorimetry (DSC), and the mass is verified through liquid chromatography-mass spectrometry (LC-MS).

Exposures. For spin coating, the peptoids are dissolved in organic solvent and a photoacid generator is added. The solution is then sonicated and filtered to degas before spin coating on a silica wafer. The wafer is baked (pre and post) at the glass transition temperature of the peptoids. The wafer is then exposed using the ASML 300C DUV stepper to print line and resolution patterns.

Solubility and SEM Images. Following exposures, the film is tested for different developers at various times to remove the exposed/unprotected regions on the film. To optimize contrast, there must be a great difference in solubility before (protected) and after exposures (unprotected). The

solubility before and after exposures differ between the two samples (see Figure 3). After developing the film, the patterns are observed and analyzed using scanning electron microscopy (SEM). As shown in Figure 4, these peptoids produce clear patterns smaller than 0.4 μm, which is already approaching the limits of DUV lithography (0.2 μm). After being developed in ethyl acetate for 45 seconds, 13141_AD produced clear line patterns of 0.4 μm. Sample 37_AD was developed in ethyl acetate for two minutes and produced clear line patterns of 0.3 μm.

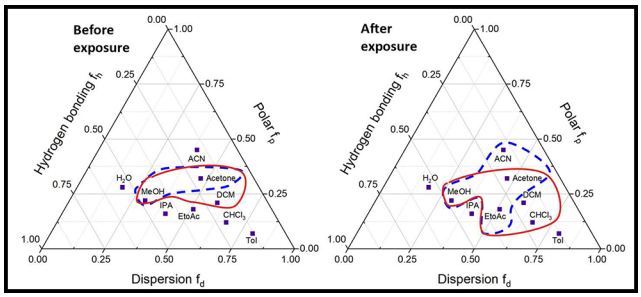

Figure 3: TEAS plots showing the solubility for samples 37_AD (blue dotted lines) and 13141_AD (red solid lines) before and after exposures.

Conclusions and Future Steps:

Although these samples have the same composition, their solubility is different before and after exposures. This suggests that the sequence of amines influences solubility and contrast, and is thus an important factor when optimizing the photolithography performance. Patterns this small (0.4 and 0.3 μm) and clear are promising results for even smaller feature sizes that are possible to print with e-beam and extreme ultraviolet (EUV) exposures. We will perform e-beam exposures with the JEOL 6500 and EUV exposures with Intel. Furthermore, to have greater control over the placement of the photoacid generators, we will be including a photoacid generator as one of the amines of the 10-mer. This will guarantee a more homogenous film and distribution of the photoacid generator.

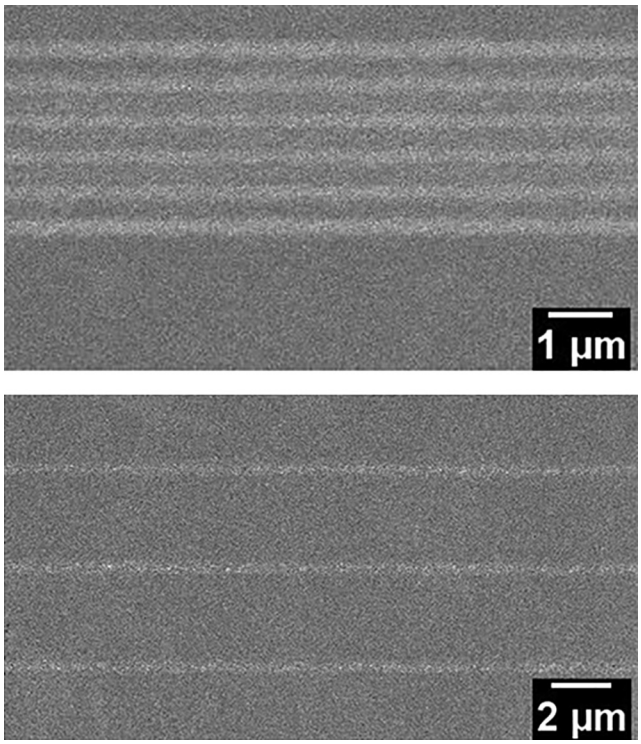

Figure 4: SEM images of line space patterns of (top) 37_AD and (bottom) 13141_AD; developed in ethyl acetate for two minutes and 45 seconds, respectively.

Acknowledgments:

I would like to thank Dr. Florian Käfer, the rest of the Ober group, and the CNF staff for their support this summer. This work was performed in part at the Cornell Center for Materials Research (CCMR) and at Cornell NanoScale Science & Technology Facility (CNF), a member of the National Nanotechnology Coordinated Infrastructure (NNCI), which is supported by the National Science Foundation (Grant NNCI-2025233). I would like to thank Intel for also funding this research.

A New Generation of Small Molecules for EUV Photolithography

2021 CNF REU Intern: Kareena Dash

Intern Affiliation: Biological Sciences, Chemistry, Cornell University

CNF REU Principal Investigator: Professor Christopher Kemper Ober, Materials Science and Engineering, Cornell University

CNF REU Mentor: Dr. Florian Hermann Ulrich Käfer, Materials Science and Engineering, Cornell University

Primary Source of Research Funding: 2021 Cornell NanoScale Science & Technology Facility Research Experiences for Undergraduates (CNF REU) Program via National Science Foundation under Grant No. NNCI-2025233, Intel

Contact(s): kd366@cornell.edu, c.ober@cornell.edu, fhk28@cornell.edu

Primary CNF Tools Used: ASML 300C DUV stepper, JEOL 6300 electron-beam, Zeiss Ultra SEM, RC2 Woollam ellipsometer

Abstract:

Modern computer chips require smaller and smaller feature sizes in the 3 to 5 nm range to reach greater efficiencies. One way to achieve this is by using polymeric resists with well-defined repeat group sequences. In this research, peptoids, made of amine monomers, have been synthesized to contain identical sequences and very small chain sizes in a specific sample, allowing for higher pattern resolution. Azide-alkyne click chemistry has been used on the peptoid backbone to homogeneously introduce new functionalities to the peptoid. Peptoids of two different sequences were synthesized, and the photolithographic properties were investigated through deep ultraviolet (DUV) and electron-beam photolithography exposures.

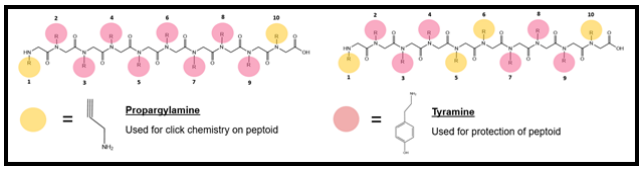

Figure 1: Chosen sequences for peptoid samples, 181-ProT on left and 13231-ProT on right.

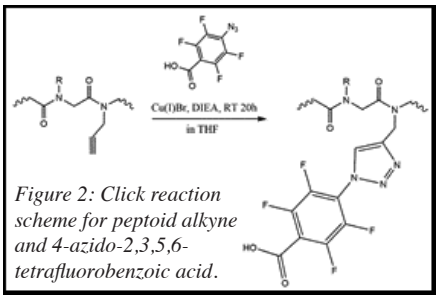

Figure 2: Click reaction scheme for peptoid alkyne and 4-azido-2,3,5,6-tetrafluorobenzoic acid.

Summary of Research:

In this work, we utilize click chemistry on a small, sequence-controllable molecule, called a peptoid, to generate a new polymeric photoresist material. Click chemistry is a category of highly specific, high yield, fast reactions that form a bond between two particular chemical handles [1].

Two peptoids were synthesized to contain 10 units of different compositions of propargylamine (Pro) and tyramine (Tyr). The sequences were 181-ProT and 13231-ProT (Figure 1). The alkyne group of propargylamine served as a click handle, whereas tyramine was protected for photolithography exposures. The peptoid synthesis was performed using repeated acylation and replacement steps on 2-chlorotrityl chloride resin. The peptoid was cleaved from the resin and protected using di-tert-butyl dicarbonate.

For the click reaction, 1 equiv. of protected peptoid was stirred with 40 equiv. N,N-diisopropylethylamine, 2 equiv. Cu(I)Br, and 5 equiv. of 4-azido-2,3,5,6-tetrafluorobenzoic acid (Azo4FBA) in tetrahydrofuran (THF) for 20 hr at room temperature [2] (Figure 2). The fluorinated azido-acid was chosen for the purpose of increasing hydrophobicity of the resist and providing the first step for a homogeneously distributed photoacid generator.

The peptoid samples were characterized by differential scanning calorimetry (DSC), matrix-assisted laser desorption/ionization-time of flight (MALDI-TOF), and nuclear magnetic resonance (NMR) spectroscopy. With DSC, the glass transition temperature of 181-ProT was determined to be 120°C. Through MALDI-TOF, the

theoretical mass of 181-ProT (2425.14 g/mol) was found, verifying the synthesis of the correct peptoid product. 1H-NMR of 181-ProT and 181-ProT-Clicked showed the disappearance of an alkyne-indicative proton peak around 3.03 ppm, while 19F-NMR data for 181-ProT-Clicked displayed a peak around -75 ppm, proving the successful clicking of Azo4FBA. The resist performance was determined through DUV and electron beam photolithography. Isopropanol was found to be the most effective developer for both sets of samples, 181-ProT and 13231-ProT, at a developing time of one minute. The RC2 Woollam ellipsometer was utilized to measure the film thickness of each box on the 181-ProT flat exposure to determine the best dose for DUV photolithography. Scanning electron microscopy (SEM) images were taken of the DUV line-space pattern and electron beam samples for further characterization.

This work found that adjusting the sequence of propargylamine and tyramine monomers changes the solubility and performance of the resist. Clear DUV and electron beam line-space patterns were observed (Figures 3 and 4), signifying good resolution. Additionally, the successful peptoid azide-alkyne cycloaddition indicates that click reactions allow easy modification of peptoid resist properties. In the future, new azides with different functionalities will be clicked on Pro-Tyr peptoids to alter resist properties such as solubility, glass transition temperature, and resist performance. Altogether, this research has explored a promising avenue for polymeric photoresist development for EUV photolithography.

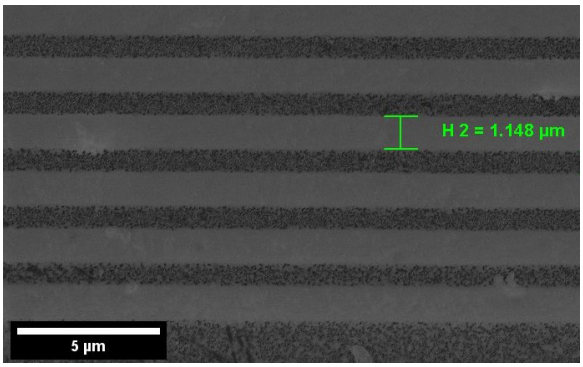

Figure 3: SEM image of 1.15 µm line pattern from DUV exposure on 181-ProT.

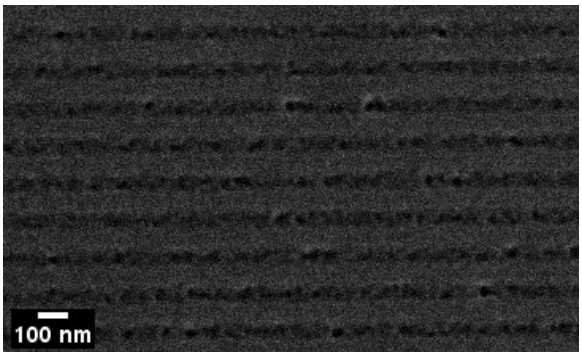

Figure 4: SEM image of 83 nm line pattern from e-beam exposure on 13231-ProT.

Acknowledgements:

The author would like to thank the National Science Foundation, NNCI, and Cornell NanoScale Science & Technology Facility Research Experiences for Undergraduates (CNF REU) Program (NSF grant no. NNCI-2025233). Thank you to Professor Christopher Ober, Dr. Florian Käfer, the whole Ober research group, and the CNF REU Program Coordinator and Staff. Thank you to Intel for also funding this research.

References:

[1] Castro, V.; Rodríguez, H.; and Albericio, F. CuAAC: An Efficient Click Chemistry Reaction on Solid Phase. ACS Comb. Sci. 2016 18 (1), 1-14.

[2] Thundimadathil, J. Click Chemistry in Peptide Science: a Mini-Review. Chimica Oggi -Chemistry Today. 2013 31 (2), 34-37.

Mesoporous Thin Film Quantum Materials via Block Copolymer Self-Assembly Patterned by Photolithography

CNF Project Number: 1356-05

Principal Investigator(s): Ulrich Wiesner

User(s): Fei Yu, R. Paxton Thedford

Affiliation(s): Department of Materials Science and Engineering, Cornell University

Primary Source(s) of Research Funding: U.S. Department of Energy (DOE), Office of Science (Basic Energy Sciences (DE-SC0010560)

Contact(s): ubw1@cornell.edu, fy84@cornell.edu

Website: http://wiesner.mse.cornell.edu/

Primary CNF Tools Used: Oxford 81 etcher, VersaLaser engraver/cutter tool, ABM contact aligner

Abstract:

The use of block copolymers (BCPs) as structure directing or templating agents, offers facile pathways toward quantum metamaterials with highly tunable mesostructures via scalable solution processing. Here, we report the preparation of mesoporous niobium carbonitride-type thin film superconductors through spin-coating of a hybrid solution containing an amphiphilic BCP swollen by niobia sol precursors and subsequent thermal processing in combination with photolithography. Spin-coated as-made BCP-niobia hybrid thin films on silicon substrates after photolithographic definition are heated in air to produce a porous oxide, and subsequently converted to carbonitrides via high temperature treatment in reactive gases including ammonia. Electrical transport measurements show initial exponential rise in resistance before dropping to zero into a superconducting state. Such cost-effective and scalable solution-based quantum materials fabrication approaches may be integrated into existing microelectronics processing, combining the capabilities of soft matter self-assembly with quantum materials.

Summary of Research:

The general solution-based fabrication route toward NbCN-type thin films on silicon substrates is depicted in Figure 1, based upon past efforts to synthesize similar materials in the bulk [1]. The structure-directing BCP in the study is an amphiphilic triblock terpolymer poly(isoprene-*b*-styrene-*b*-ethylene oxide) (PI-*b*-PS-*b*-PEO, referred to as ISO hereafter), synthesized by sequential anionic polymerization. The inorganic niobia sol precursor is prepared from the hydrolytic condensation of niobium (V) ethoxide. Upon mixing the sol with ISO in tetrahydrofuran (THF) and subsequent spin-coating and self-assembly (Figure 1a,b), the niobia sol particles selectively mix with the hydrophilic PEO block of the ISO to form a nanostructured composite thin film.

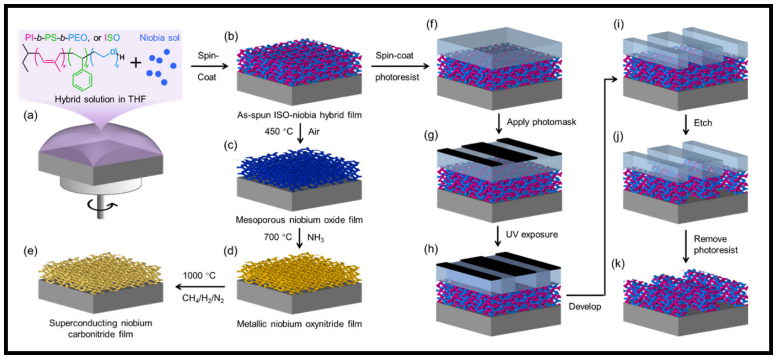

Figure 1: Schematic of solution-based fabrication processes. (a) ISO and niobia sol hybrid solution in THF is spin-coated on a silicon substrate. (b) As-spun ISO-niobia hybrid thin film. (c) Mesoporous niobium oxide thin film after heating in air at 450°C. (d) Metallic niobium nitride thin film after treatment in ammonia at 700°C. (e) Superconducting niobium carbonitride-type thin film after final treatment in carburizing gas at 1000°C. (f) – (k) Photolithography route to patterned thin films that can be further processed along (c) to (e).

Without post-deposition annealing such as solvent vapor annealing, the hybrid films are treated in air at 450°C to further condense the niobia and remove the structure directing ISO. The resulting niobium oxide thin films (Figure 1c) show locally ordered mesoporous structures,

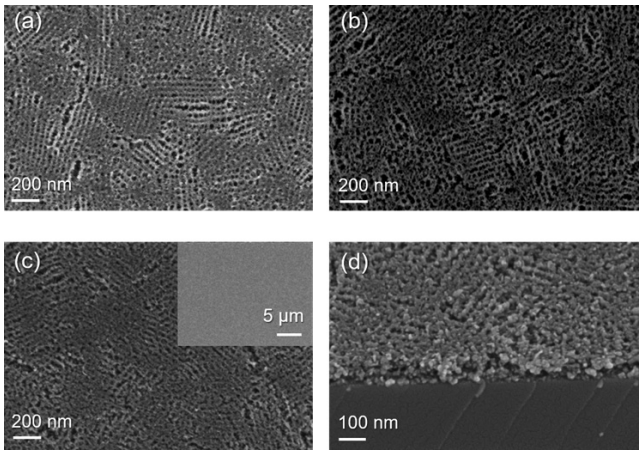

Figure 2: SEM images of thin films at different processing stages. Plan views of (a) the niobium oxide film; (b) the niobium nitride film; (c) the niobium carbonitride film (inset at low magnification). (d) 45-degree cross-sectional view of the niobium carbonitride film displaying the film edge on the cleaved silicon substrate.

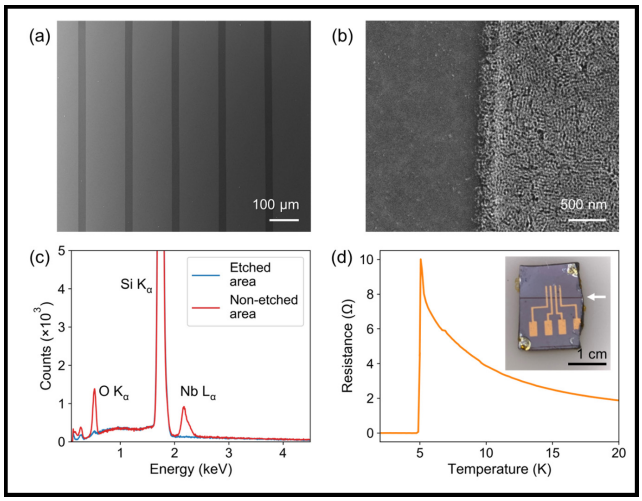

Figure 3: Lithographic patterning of spin-coated thin films. (a) Plan-view SEM image of niobium carbonitride thin film patterned through photolithography, with 25 µm wide strips etched away shown in dark. (b) Higher magnification SEM image of the patterned film showing the edge along with details of the self-assembled mesostructure. (c) EDS spectra of areas of plain film and etched film after 10-min CF_4 plasma etching. (d) Plot of resistance versus temperature from an individual patterned 400 µm wide strip thin film. Inset shows the single lithographically patterned niobium carbonitride strip (white arrow) with four co-linear metal contacts across the strip.

as evidenced by scanning electron microscopy (SEM, Figure 2a). X-ray scattering suggests the morphology is consistent with a deformed alternating gyroid structure, in which the niobia in the original hybrid film is retained as a single inorganic minority network replicating the PEO plus inorganic. To render the thin films electrically conducting, a nitridation step in ammonia (NH_3) at 700°C converts the mesoporous oxide into niobium nitride (NbN, Figure 1d), albeit with some oxygen (and vacancies) likely remaining. The mesostructure appears largely unchanged, with a slight coarsening of the nodes in the network (Figure 2b).

Finally, heating the NbN thin films to 1000°C in a mixture of methane (CH_4), hydrogen (H_2), and nitrogen (N_2), known as carburizing gas ($CH_4/H_2/N_2$), yields a superconducting niobium carbonitride (NbCN)-type material (Figure 1e) without substantial further growth in crystallite size. The overall mesoporous structure is retained, albeit with additional coalescence of struts (Figure 2c). With the simple spin-coating technique, a uniform thin film with arbitrary lateral dimensions can be fabricated without major macroscopic defects (inset of Figure 2c).

Photolithography was performed to illustrate compatibility of our solution-based synthesis approaches to mesoporous superconducting samples with typical semiconductor nanofabrication processing (Figure 1f-k).

First, a photoresist is applied on the ISO-niobia hybrid thin films pre-treated at 300°C to minimize swelling or dissolution by photoresist solution. After exposure using the ABM contact aligner and development, 25 μm wide strips of photoresist layers are removed. Pattern transfers are achieved by a combination of wet etching using buffered oxide etchant (BOE) and dry etching using oxygen plasma. The clear and sharp patterns demonstrate the viability for the superconducting thin films based on solution processing to be incorporated into standard microelectronic processing, with additional self-assembled 3D features at the mesoscale (Figure 3a,b).

A separate pattern was transferred from a shadow mask (fabricated using the VersaLaser engraver/cutter tool) through CF_4 plasma etching using the Oxford 81 Etcher. The CF_4 plasma etching can completely remove the ISO-niobia hybrid materials, as evidenced by the disappearance of the Nb La peak in energy-dispersive X-ray spectroscopy (EDS) spectra (Figure 3c). Films patterned via plasma etching (Figure 3d, inset, white arrow) have a superconducting transition temperature of 5 K (Figure 3d).

In summary, our work opens pathways toward solution-based thin film technologies at the intersection between soft matter self-assembly and quantum materials with tremendous academic as well as industrial potential.

References:

[1] Beaucage, P. A.; Van Dover, R. B.; DiSalvo, F. J.; Gruner, S. M.; Wiesner, U. B. Superconducting Quantum Metamaterials from Convergence of Soft and Hard Condensed Matter Science. Adv. Mater. 2021, 33, 2006975.

[2] Yu, F.; Thedford, R. P.; Hedderick, K. R.; Freychet, G.; Zhernenkov, M.; Estroff, L. A.; Nowack, K. C.; Gruner, S. M.; Wiesner, U. B. Patternable Mesoporous Thin Film Quantum Materials via Block Copolymer Self-Assembly: An Emergent Technology? ACS Appl. Mater. Interfaces 2021, ASAP, DOI: 10.1021/acsami.1c09085.

Nano-Scale Area-Selective Formation of Polymer Brushes

CNF Project Number: 1757-09

Principal Investigator(s): Christopher Kemper Ober

User(s): Yuming Huang

Affiliation(s): Department of Materials Science and Engineering, Cornell University

Primary Source(s) of Research Funding: National Science Foundation

Contact(s): cko3@cornell.edu, yh839@cornell.edu

Website: https://ober.mse.cornell.edu/index.html

Primary CNF Tools Used: E-beam resist spinners, JEOL 9500, FilMetrics F50-EXR, Oxford 81 etcher, Zeiss Ultra SEM, optical microscope, Oxford 81

Abstract:

Polymer brushes can be formed in a location-specific manner via an integrated fabrication of surface-initiated polymerizations and electron-beam lithography, which is a state-of-art patterning tool known for its fine resolution and precision. Dot-patterned polymer brushes was produced on silicon wafers by area-selective deposition of initiators, using patterned e-beam resists as the masks. As a result, "nano-spikes" made of polypeptide (rod) brushes and "blurry bundles" of polystyrene (coil) brushes were formed via two different kinds of surface-initiated polymerizations. This platform can be useful for various applications such as cytoskeleton mimicry and molecular recognition.

Summary of Research:

Introduction. Polymer brushes are polymer chains that have one end covalently anchored to a flat substrate, such as a silicon wafer, with a high grafting density. Due to the unusual molecular arrangements and surface attachments, polymer brushes have exhibited unique surface properties and thus has an active research area in polymer science [1]. Potential applications such as organic thin film devices, optoelectronics, and medical diagnosis have been studied in the past decades. However, there is an increasing need for area-selective functionalization of metal oxide surfaces (for e.g. device fabrications) as lithographic techniques and nanofabrication advance. As such, making nanopatterned polymer brushes by incorporating e-beam lithography with the vapor phase surface-initiated polymerization can be one possible solution to these demands.

In addition to the polypeptide brushes, we have fabricated different polymer brushes by utilizing a new type of living polymerization into the integrated process, which will widen the potential of surface functionalities as well as fundamental studies of polymer brushes.

Fabrication. The polymer brushes were patterned on a silicon wafer via an integrated fabrication process and area-selective deposition of surface-bound initiators for polymerizations.

E-Beam Resist Mask Preparation. Patterned e-beam resist mask (~150 nm) was prepared through JEOL 9500. The sample was then etched ~ 40 nm using the Oxford 81 etcher to remove residual debris in the unmasked area.

Synthesis of the Rod Brushes. The deposition of a silane initiator on the treated substrate was carried out in a closed chamber under vacuum and elevated temperature. The initiator was allowed to vaporize and thus react with the exposed metal oxide surfaces. Afterward, the resist mask was removed by organic solvents. Subsequently, surface-initiated ring-opening polymerization of poly-γ-benzyl-*L*-glutamate (PBLG), a rod-like polymer, was synthesized under vacuum and elevated temperature.

Synthesis of the Coil Brushes. After the deposition of silane initiator, there was one additional step of modifying these surface initiators with allyl 2-bromo-2.methylpropionate (BiBB), which acts as the activation site for the subsequent polymerization. Polystyrene (PS), a coil-like polymer, was then synthesized via surface-initiated Cu(0) mediated controlled radical polymerization (SI-CuCRP) under argon-protected environment and elevated temperature. Similar process was also carried out for other coil brushes such as poly(methyl methacrylate) (PMMA) to test the fabrication's adaptability.

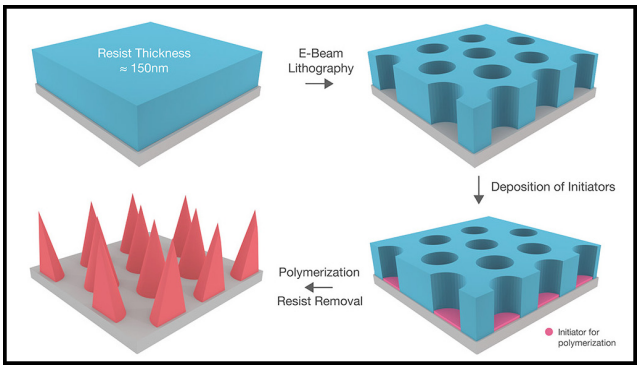

Figure 1: Schematic illustration of the fabrication process.

A schematic illustration of the whole fabrication process is shown in Figure 1.

Characterization and Results:

The e-beam resist thickness was measured by FilMetrics F50-EXR. The patterned e-beam resist (Figure 2), the patterned PBLG brushes (Figure 3) and PS brushes (Figure 4) were characterized using Zeiss Ultra scanning electron microscopy (SEM) and Veeco Icon Atomic Force Microscope (AFM) for topological analysis.

Conclusion and Future Steps:

In conclusion, we demonstrated a novel process for precisely control the spatial arrangement of different kinds of polymer brushes. In the near future, we plan to examine how the surface topography varied with different kind of polymers in terms of molecular structures and physical properties. We also plan to explore the use of these surfaces for various applications, such as cell membrane support, biological simulated model and magnetic storage platforms.

References:

[1] Chen, W. L.; Cordero, R.; Tran, H.; Ober, C. K., 50th Anniversary Perspective: Polymer Brushes: Novel Surfaces for Future Materials. Macromolecules 2017, 50 (11), 4089-4113.

[2] Zhang, T.; Du, Y.; Müller, F.; Amin, I.; Jordan, R., Surface-initiated Cu(0) mediated controlled radical polymerization (SI-CuCRP) using a copper plate. Polym Chem-Uk 2015, 6 (14), 2726-2733.

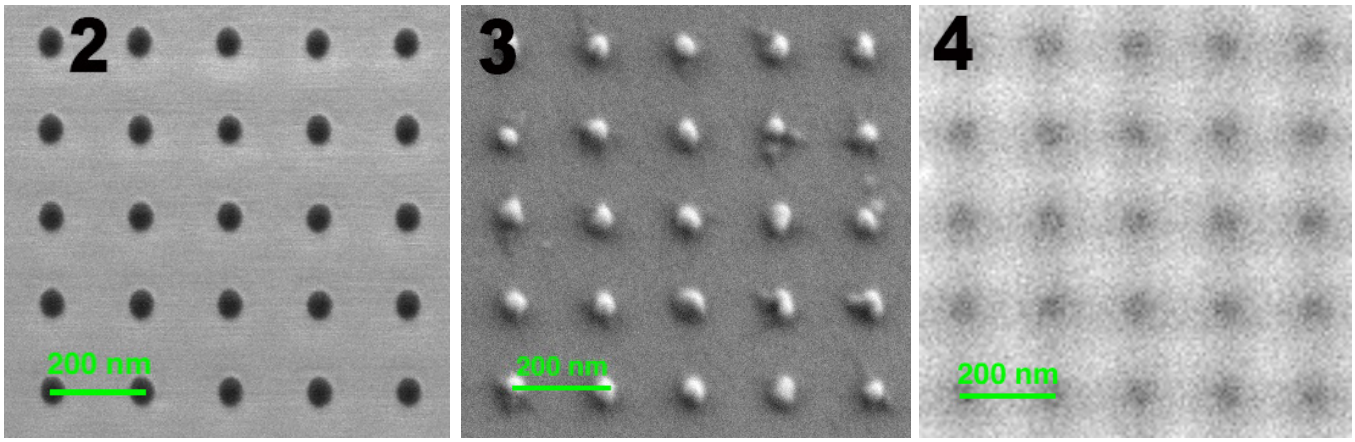

Figure 2, left: SEM of patterned e-beam resist. Figure 3, middle: SEM of the patterned PBLG rod brushes. Figure 4, right: SEM of the patterned PS brushes.

Raman Spectroscopy and Aging of the Low-Loss Ferrimagnet Vanadium Tetracyanoethylene

CNF Project Number: 2126-12

Principal Investigator(s): Gregory D. Fuchs[1]

User(s): Hil Fung Harry Cheung[2], Michael Chilcote[2]

Affiliation(s): 1. School of Applied and Engineering Physics, 2. Department of Physics; Cornell University

Primary Source(s) of Research Funding: Department of Energy (Grants No. DE-SC0019250)

Contact(s): gdf9@cornell.edu, hc663@cornell.edu, mac578@cornell.edu

Website: http://fuchs.research.engineering.cornell.edu

Primary CNF Tools Used: GCA 5x stepper, AJA sputtering deposition system, P10 profilometer, Westbond 7400A ultrasonic wire bonder

Abstract:

Vanadium tetracyanoethylene ($V[TCNE]_x$, x~2) is a low loss organic-based ferrimagnet with a magnetic ordering temperature T_C > 600 K and growth compatibility with many substrates. These properties make it an attractive candidate for coherent magnonics and quantum transduction applications. However, like other organic materials, it is sensitive to air. Encapsulation extends its lifetime in ambient conditions from hours to weeks, but its aging mechanism is not well understood. Here we report micro-focused Raman spectroscopy of $V[TCNE]_x$ as it ages to understand the structural changes accompanying aging and the corresponding changes in magnetism. We also study laser-induced degradation, which enables laser patterning by removing magnetism. These findings enable a local optical probe of $V[TCNE]_x$ quality when local magnetization characterization is impossible, and they enable a new form of patterning.

Summary of Research:

$V[TCNE]_x$ is an organic-based material with low magnetic damping comparable to that of yttrium iron garnet (YIG) at room temperature [1]. It can be grown on a variety of substrates and is an attractive alternative to YIG for coherent magnonics applications. One challenge of working with $V[TCNE]_x$ is its air sensitivity. While encapsulation extends its lifetime from hours to weeks, its aging mechanism is not well understood.

In this work we use a combination of confocal microscopy, micro-focused Raman spectroscopy, ferromagnetic resonance (FMR) and *ab initio* calculations to study $V[TCNE]_x$ and its aging mechanisms [2].

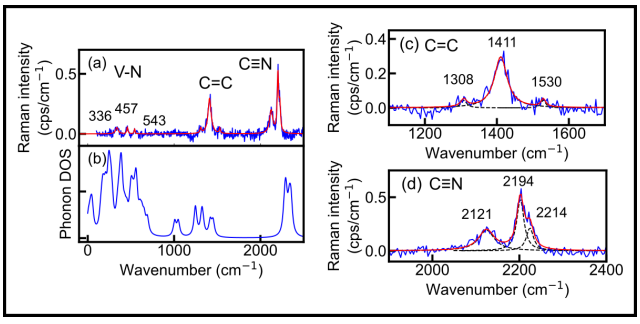

Figure 1: (a) Experimental $V[TCNE]_x$ Raman spectrum. (b) Ab initio *density functional theory (DFT) calculated density of states where each mode is broadened as a Lorentzian with a full width half maximum (FWHM) of 20 cm^{-1}. (c) C=C, (d) C≡N peaks. Individual Lorentzian fits (dashed).*

We characterize $V[TCNE]_x$ using Raman spectroscopy to study its structure. By comparing the spectrum with density functional theory (DFT) calculations, we assign the experimental Raman peaks to V-N (336, 457, 543 cm^{-1}), C=C (1308, 1411, 1530 cm^{-1}), C≡N (2121, 2194, 2214 cm^{-1}) vibrational modes (Figure 1). These Raman peaks reflect the bonding between vanadium ion and TCNE group and are relevant for magnetism.

Having characterized a pristine $V[TCNE]_x$ film, we next study the effects of aging by laser-induced damage. This allows us to study the effect of aging in the absence of diffused oxygen and water. The response of $V[TCNE]_x$ under high intensity light is particularly relevant for quantum applications requiring coupling between $V[TCNE]_x$ and defect centers [3]. Under focused laser illumination, the sample shows an increase in photoluminescence, which we characterized by a laser damage susceptibility χ_{PL}. This laser damage susceptibility increases with laser power, indicating that the damage is not a single photon process (Figure 2). Instead, this suggests it is a heating effect, where chemical reaction rate increases nonlinearly with temperature.

Next we examine the Raman spectra after the sample has been laser damaged. Raman intensity near 2121 cm^{-1} reduces while intensity near 2202, 2225 cm^{-1} increases. Peaks near 1308, 1530 cm^{-1} increases in intensity and linewidth. Low wavenumber peaks (300-600 cm^{-1}) vanishes. These features

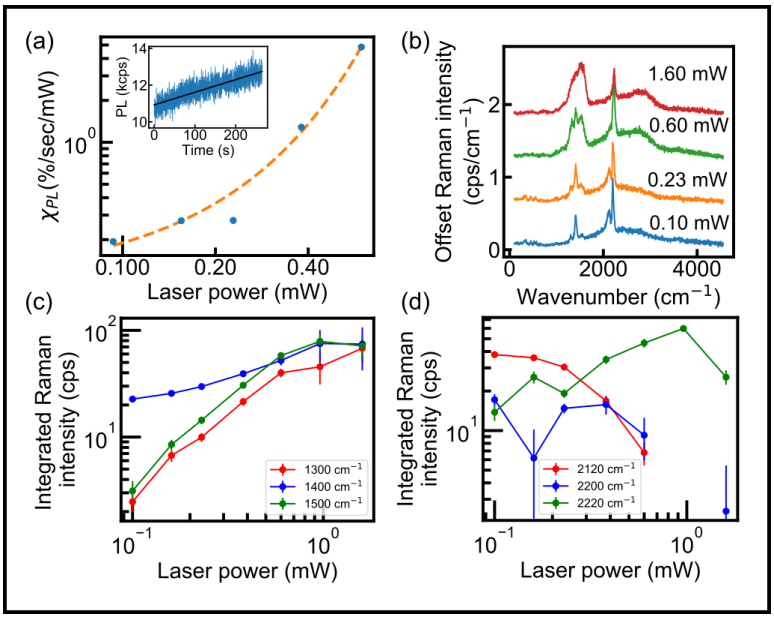

Figure 2: (a) Laser damage susceptibility increases with optical power. (Dashed) A guide to the eye showing an exponential dependence with optical power. (Inset) Photoluminescence over time and a linear fit. (b) Raman spectra at different optical power. (c), (d) Integrated intensity from individual Raman peaks for C=C and C.N peaks.

are clear signatures of aging and suggest a reduction in bonding between vanadium and TCNE. This may reduce spin exchange and magnetization.

We next study V[TCNE]$_x$ aging at room temperature in ambient atmosphere. One clear visual signature of aging is the film turning from opaque to transparent, as shown in Figure 3 where the transparency front advances from sample edges to the center, which we attribute to diffused oxygen and water across the encapsulation epoxy. In comparison, the central region does not show a strong color change, suggesting it has not been oxidized. We observe similar changes in Raman spectra for both a laser damaged sample and a naturally aged sample, indicating similar reactions are happening in both processes. A more drastic signature of aging is the increase in laser damage susceptibility χ_{PL}, which increases exponentially in time while the effective magnetization reduces over time. This establishes a link between optical properties and magnetic properties and show that optical measurement can be a local probe of V[TCNE]$_x$ film quality.

With the findings of V[TCNE]$_x$ laser damage, we explore using it for patterning by selectively damaging V[TCNE]$_x$ to remove magnetism. We show a proof-of-concept demonstration by writing the collaboration's affiliations on a V[TCNE]$_x$ film (Figure 4). Laser damaged regions have a higher photoluminescence. This also turns the material transparent which appears bright in the optical micrograph.

This work shows optical measurement can be used to assess V[TCNE]$_x$ film quality. In the future, we plan to study the anisotropy and spin wave modes of patterned V[TCNE]$_x$.

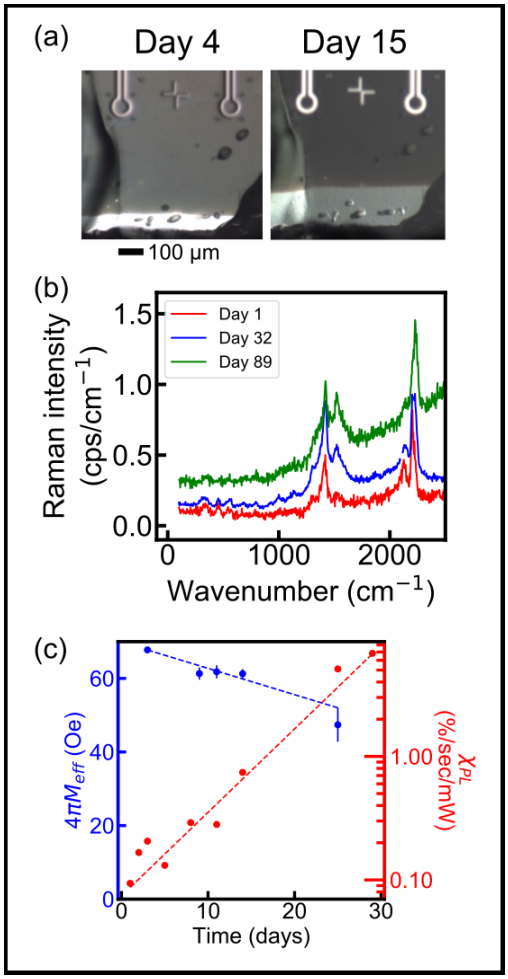

Figure 3: (a) Visual indication of aging, where the transparency front advances from sample edges to the center, revealing the underlying reflective aluminum layer. (b) Raman spectra without baseline subtraction at the central region. Fluorescence background increases and peaks at 1300, 1500 cm^{-1} (C=C) increases. Low wavenumber (300-600 cm^{-1}, V-N) and 2120 cm^{-1} (C≡N) peaks vanish. (c) A reduction in the effective magnetization $4\pi M_{eff}$ and an increase in laser damage susceptibility. Fitted decay rate of 0.72 Oe/day and laser damage susceptibility increases with a 1/e time constant of 6.4 days.

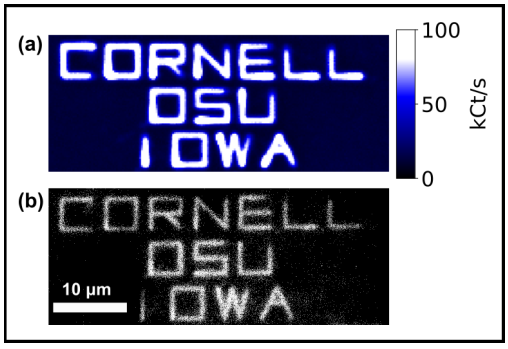

Figure 4: Laser patterning of a 400 nm V[TCNE]$_x$ film. (a) Photoluminescence map of the patterned sample. High photoluminescence regions are laser damaged. (b) Optical micrograph. Laser damaged regions are more transparent and appear brighter in this image.

References:

[1] H. Yu, et al. "Ultra-Narrow Ferromagnetic Resonance in Organic-Based Thin Films Grown via Low Temperature Chemical Vapor Deposition" Applied Physics Letters 2014, 105, 012407.

[2] H. F. H. Cheung, et al. "Raman Spectroscopy and Aging of the Low-Loss Ferrimagnet Vanadium Tetracyanoethylene" 2021, arXiv:2101.10240.

[3] D. R. Candido, et al. "Predicted Strong Coupling of Solid-State Spins Via a Single Magnon Mode" Materials for Quantum Technology 2020, 1, 011001.

Encapsulation of Photocathodes in Two-Dimensional Materials

CNF Project Number: 2584-17

Principal Investigator(s): Melissa A. Hines

User(s): Qingyuan "Amy" Zhu, Dulanga Somaratne

Affiliation(s): Department of Chemistry and Chemical Biology, Cornell University

Primary Source(s) of Research Funding: Center for Bright Beams, an NSF Science and Technology Center

Contact(s): Melissa.Hines@cornell.edu, qz337@cornell.edu, dulanga.somaratne@cornell.edu

Website: http://hines.chem.cornell.edu

Primary CNF Tools Used: CVC SC4500 odd-hour evaporator, Glen 1000 resist strip

Abstract:

We are developing a new technique for encapsulating highly reactive photocathodes in an atomically thin membrane that protects them from oxidation and degradation without affecting their photoemission properties or chemical purity.

Summary of Research:

Photocathodes are materials that eject electrons under illumination. By their very nature, high-performance photocathodes must be made from materials that lose electrons easily — in other words, materials that are easily oxidized. For example, many photocathodes are either coated with alkali metals (e.g., Cs/GaAs) or comprised of alkali metals (e.g., Cs_3Sb). This presents a technical challenge, as exposure to even trace amounts of O_2 or H_2O will destroy or degrade the photocathode. For highest performance, the photocathodes must also be atomically flat and extremely homogeneous.

To meet these challenges, we are developing a technique to produce photocathodes encapsulated in two-dimensional materials, such as graphene or hexagonal boron nitride. The key challenge in this project is ensuring that every step of the fabrication leaves no residue on the surface, as even monolayer levels of contamination could significantly reduce photoelectron transmission and beam brightness.

In the first step of fabrication, commercial two-dimensional materials, which are grown on a copper foil, are coated with a thin gold layer in the CVC SC4500 thermal/e-beam evaporator. The two-dimensional material on the backside of the copper foil is then removed using 100W of oxygen plasma in the YES oxygen plasma asher. The copper foil is then removed with an aqueous etchant, allowing the graphene side of the gold-coated graphene to be adhered to a low energy substrate. The gold film is then removed by a second aqueous etch.

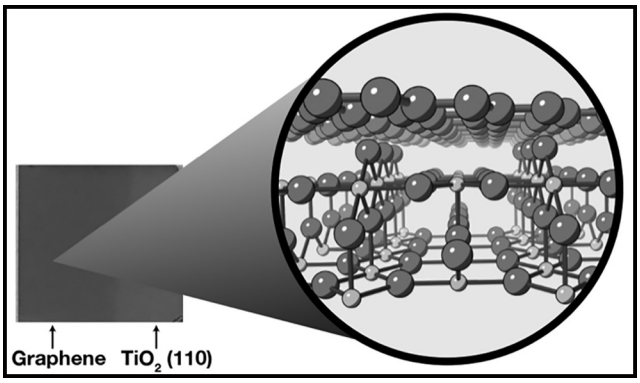

Figure 1: Optical image of TiO_2(110) with single-layer graphene on left side. The inset is a model of single-layer graphene on TiO_2(110).

Fabricating Planar Microwave Resonators for On-Chip Electron Spin Resonance Spectroscopy

CNF Project Number: 2705-18

Principal Investigator(s): Farhan Rana

User(s): Arjan Singh

Affiliation(s): Electrical and Computer Engineering, Cornell University

Primary Source(s) of Research Funding: Air Force Research Lab (AFRL) Grant No. FA9550-18-1-0529

Contact(s): farhan.rana@cornell.edu, as2995@cornell.edu

Primary CNF Tools Used: AJA sputter deposition tool, CVC SC4500 odd/even evaporator, copper electroplating hood, Logitech Orbis chemical-mechanical-polisher (CMP)

Abstract:

Electron spin resonance (ESR) spectroscopy has been a useful tool for measuring defect spins in semiconductors [1-6]. We are utilizing the robust capabilities of the Cornell NanoScale Facility (CNF) to develop an ESR spectrometer with the capability to measure defect spins in MBE-grown films as thin as 100 nm. Here, we demonstrate a planar microwave resonator, the principal device to be used in the spectrometer, with an internal *Q*-factor over 150 at ~ 10 GHz, fabricated completely at CNF. We use a unique "photoresist-mold-defined" fabrication process to pattern copper thicker than 5 μm.

Summary of Research:

Electron spin resonance (ESR) spectroscopy is based on exploiting the Zeeman interaction between a magnetic field and a spin. Ever since it was proposed to study nuclear spins nearly a century ago [8], it has been a useful tool to study spins in materials [1-7].

A (non-oscillating) magnetic field splits degenerate spin states by an energy, $E = \gamma_s B$ (assuming spin-1/2 particles), where γ_s is the gyromagnetic ratio (the ratio between the magnetic moment of a particle to its angular momentum) and B is the applied magnetic field. The energy E for magnetic fields on the order of 1 T can easily be supplied by microwaves of frequencies, $f \sim$ 1-10 GHz.

Thus, the essential idea of ESR spectroscopy is that by supplying microwave radiation to semiconductor samples subject to a magnetic field, we can induce transitions between spin states of defects when the condition, $hf = \gamma_s B$ is met, where h is Planck's constant.

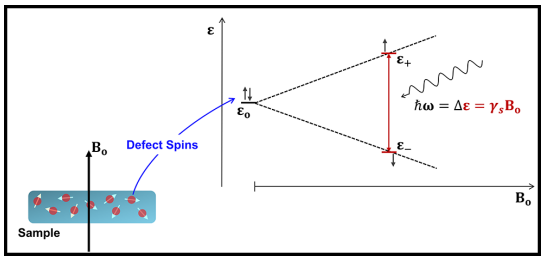

Figure 1: Schematic showing the basic principle of electron spin resonance (ESR) spectroscopy.

By observing these transitions, we can extract the gyromagnetic ratio, γ_s, associated with a defect-spin state, giving us insight into its electrical/magnetic properties. Figure 1 shows a schematic of such an ESR experiment.

ESR spectrometers, by and large, use a 3-D microwave resonator to deliver microwaves to samples subject to a DC magnetic field. 3-D microwave resonators, owing to their large magnetic field mode volumes, are not sensitive to MBE grown thin films. Using a 2-D, planar microwave resonator we can minimize the magnetic field mode volume, and thus minimize the magnetic field fill factor (represents the fraction of magnetic field seen by the film being probed). A small magnetic fill factor (close to unity) will allow us to probe defect spins in semiconductor films as thin as ~ 100 nm. However, the small mode volume of a 2-D planar resonator also means, that much of the magnetic field is within the substrate on which the resonator is patterned. To minimize the dielectric loss resulting from this, we use a sapphire substrate, owing to sapphire's small loss-tangent and high dielectric constant. To minimize the conductor loss, we use thick copper (~ 5 μm) to define our resonating circuit. Figure 2 shows the experimental setup we use for ESR spectroscopy.

Methods and Results:

We used the Cornell NanoScale Facility (CNF) to fabricate this 2D resonator. Since we had to pattern copper 5 μm thick, we adopted a unique fabrication process [9], which is schematically described in Figure 3a.

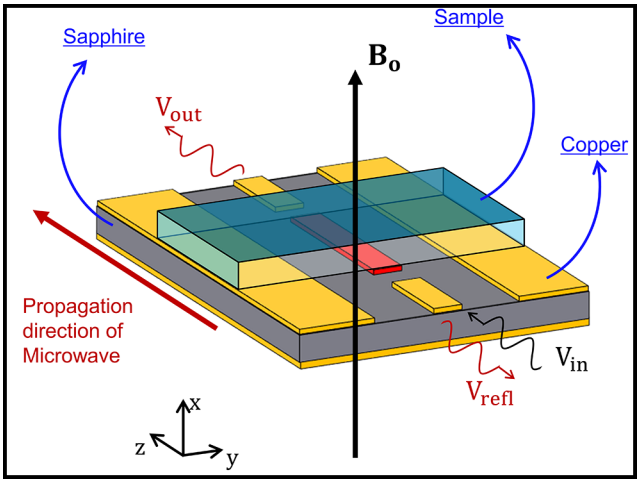

Figure 2: Basic layout of our ESR measurement. The planar microwave resonator lies at the heart of the setup and is fabricated at the Cornell NanoScale Facility (CNF).

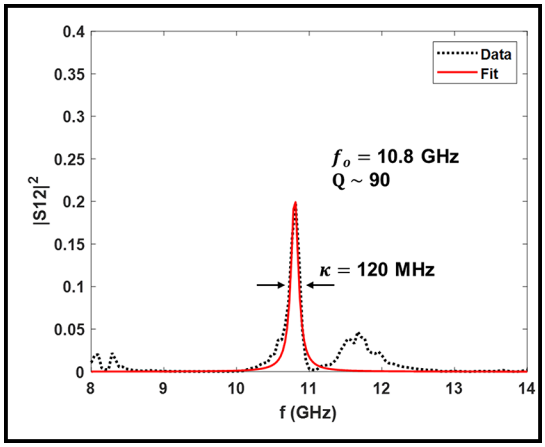

Figure 4: The S21 parameter (transmission coefficient) of our resonator, along with a Lorentzian fit to the data.

The basic principle is as follows. (1) We first define a mold by patterning thick (~ 6 μm) photoresist on a 600 μm sapphire substrate, using *contact photolithography*. (2) We then deposit a thin (~ 80 nm) film of platinum using the *sputter deposition tool*. (3) This platinum film serves as the seed to then *electroplate* ~ 8 μm of copper. (4) We then use the *chemical-mechanical-polisher* (CMP) in the cleanroom to lap and polish the copper film down to ~ 5 μm and make it smooth (roughness on the order of 10 nm). (5) Finally, we strip the photoresist, which leaves us with our patterned devices. A picture of the finished devices can be seen in Figure 3b.

Figure 4 shows the S21 (transmission coefficient) parameter of our device. We clearly see a sharp resonance at 10.8 GHz, which we fit using a Lorentzian lineshape. This resonance corresponds to a linewidth of 120 MHz, a loaded Q-factor of 90, and an internal Q-factor of ~ 162.

Conclusion and Future Steps:

This microwave characterization shows that our devices are functioning well with high quality factors. We hope to now use these devices to do ESR measurements on semiconductor thin films.

Future work at CNF will also involve fabricating devices that use a superconducting metal (niobium or aluminum), instead of copper, to define out resonators. This will allow us to reduce our conductor loss to a point that we can approach the quantum limit of spin detection [10].

Acknowledgements:

I would like to thank the CNF staff, without whom this work would not have been possible and will not be able to continue. I especially thank Chris Alpha, Aaron Windsor, Tom Pennell, Garry Bordonaro, and Jeremy Clark for their invaluable input and support.

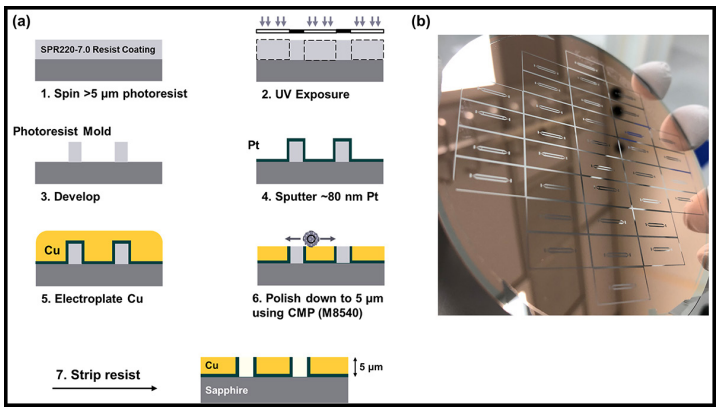

Figure 3: (a) Shows the schematic of the fabrication process used to fabricate our microwave resonator. (b) Shows the finished devices made using said process.

References:

[1] M Baeumler, et al, J. Phys. C: Solid State Phys. 20 L963 (1987).
[2] W. E. Carlos, et al., Phys. Rev. B 48, 17878 (1993).
[3] J H N Loubser and J A van Wyk, Rep. Prog. Phys. 41 1201 (1978).
[4] W. V. Smith, et al., Phys. Rev. 115, 1546 (1959).
[5] B. E. Kananen, et al., Applied Physics Letters 110, 202104 (2017).
[6] Nguyen Tien Son, et al., Applied Physics Letters 117, 032101 (2020).
[7] Conrad Clauss, et al., J. Phys.: Conf. Ser. 592 012146 (2015).
[8] G. Breit and I. I. Rabi, Phys. Rev. 38, 2082 (1931).
[9] Y. Shin, et al., Journal of Microelectromechanical Systems vol. 19, no. 3 (2010).
[10] A. Bienfait, et al., Nature Nanotechnology, volume 11, pages 253-257 (2016).

Scissionable Polymer Photoresist for Extreme Ultraviolet Lithography

CNF Project Number: 2751-18

Principal Investigator(s): Christopher Kemper Ober

User(s): Jingyuan Deng

Affiliation(s): Materials Science and Engineering, Cornell University

Primary Source(s) of Research Funding: Intel Corporation

Contact(s): c.ober@cornell.edu, jd966@cornell.edu

Primary CNF Tools Used: ASML 300C DUV stepper, JEOL-6300 e-beam lithography, P10 profilometer

Abstract:

Extreme ultraviolet (EUV) is one of the most promising methods to create nano-size patterns below 10 nm. Numerous EUV resists have been developed in last decades to accommodate EUV lithography. The main challenge of EUV lithography lies in RLS tradeoff, which specify the tradeoff among resolution (R), line edge roughness (L) and sensitivity (S). In addition, EUV lithography suffers from low photon numbers, which may cause stochastic issues. In this work, we developed chemically amplified chain scissionable polymers to tackle these issues. Polyphthalaldehyde (PPA) based photoresists have been synthesized and their lithographic performance have been investigated.

Summary of Research:

Scissionable polymers are polymers that will depolymerize under different stimuli including acid, base, and free radicals [1]. These polymers have been investigated in the development of photoresists and other degradable materials. This work focuses on the poly(phthalaldehyde), PPA, family of scissionable polymers. The PPA backbone consists of acetal linkages that are very sensitive to acids. Upon exposure to acids, the polymer chain depolymerizes to its corresponding monomers.

This depolymerization behavior makes PPAs excellent candidates as photoresist materials. Several new architectures are being explored. For example, PPAs with tethered photoacid generators (PAG)s, which release acid upon irradiation, depolymerize upon exposure followed by a post exposure bake step. The depolymerized monomers in exposed areas could be easily removed using appropriate organic solvents while the unexposed areas remain unchanged. Therefore, both unsubstituted and substituted PPAs may equally serve as a positive tone photoresist.

This study focuses on the development of low exposure dose, sensitive PPA photoresists, which do not suffer from materials stochastic issues related to non-uniformities at nanoscale present in multi-component systems for EUV lithography.

In order to improve the lithographic performance of the PPA photoresists, the structure of the polymer backbone as well as photoacid generators (PAG)s are being investigated and tailored for EUV lithography. Aryl sulfonates were prepared as non-ionic PAGs for PPA photoresists [2]. The steric and electronic nature of the aryl sulfonate PAGs can be easily tuned to optimize acid generation efficiency and their compatibility with a polymer photoresist matrix.

The homogenous solution of PPA polymers and PAGs were prepared and spin coated on a silicon wafer. The coated silicon wafers were then exposed using ASML 300C DUV stepper. After exposure, the exposed film was baked and developed.

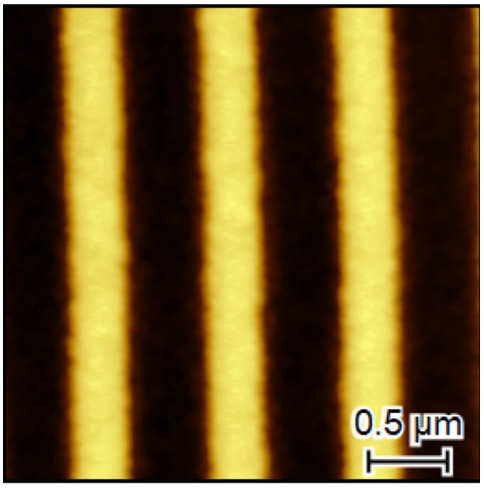

Figure 1. 1:1 Line space pattern with feature size 512 nm observed under AFM after exposure of 100mJ/cm² deep UV exposure.

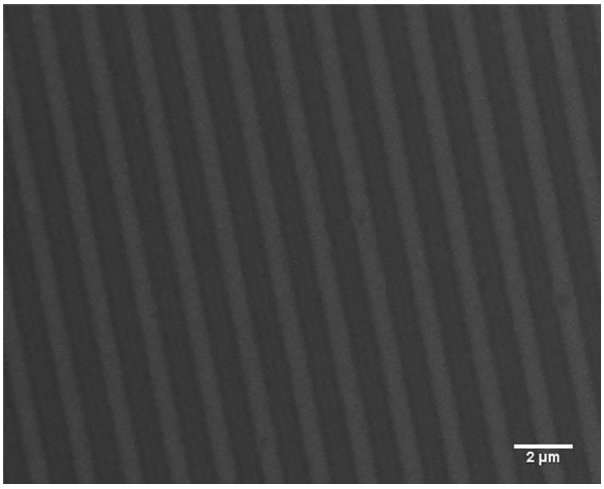

Figure 2. 1:1 Line space pattern with feature size 512 nm observed under SEM after exposure of 100mJ/cm² deep UV exposure.

Results and Discussions:

The resulting line-space patterns were characterized using AFM and SEM. The images are shown in Figure 1 and 2, respectively.

As seen from these figures, the relatively rough line edge roughness was caused by the acid diffusion, which could be alleviated by changing the chemical structure of the photoacid generator.

Next, we plan to explore the resolution limit of these photoresists with different photoacid generators using e-beam and EUV. These samples are currently under preparation.

Summary:

In summary, preliminary results were obtained with chain scissionable photoresists. With these results in hand, the lithographic performance of newly developed functionalized PPAs will be investigated under DUV, e-beam and EUV to pursue higher resolution and improved LER.

References:

[1] Yardley, R. E.; Kenaree, A. R.; Gillies, E. R. Macromolecules 2019, 52, 6342.

[2] Sulc, R.; Blackwell, J. M.; Younkin, T. R.; Putna, E. S.; Esswein, K.; DiPasquale, A. G.; Callahan, R.; Tsubaki, H.; Tsuchihashi, T. Proc. SPIE, 2009; 7273, 72733.

Control of Water Adsorption via Electrically Doped Graphene

CNF Project Number: 2767-19

Principal Investigator(s): Scott Schiffres

User(s): Morteza H. Bagheri, Rebecca T. Loibl

Affiliation(s): Department of Mechanical Engineering, Binghamton University, State University of New York, Binghamton, NY 13902, USA; Materials Science and Engineering Program, Binghamton University, State University of New York, Binghamton, NY 13902, USA

Primary Source(s) of Research Funding: State University of New York at Binghamton's Transdisciplinary Area of Excellence Seed Grant, State University of New York Startup Funds, National Science Foundation Award 1846157

Contact(s): sschiffr@binghamton.edu, mortezahb@binghamton.edu

Website: http://ws.binghamton.edu/schiffres/

Primary CNF Tools Used: Oxford ALD FlexAL, CVC SC4500 odd/even evaporator, YES asher

Abstract:

The interaction of graphene with water molecules under an applied electric field is not thoroughly understood, yet this interaction is important to many thermal, fluidic, and electrical applications of graphene. In this work, the effect of electrical doping of graphene on water adsorption was studied through adsorption isotherms and current-voltage (IV) characterizations as a function of the Fermi level. The water adsorption onto graphene increased ~ 15% and the doping levels increased by a factor of three with a gate-to-graphene voltage of +20 or -20V compared to 0V for sub-monolayer adsorption. This change in uptake is attributed to the increase in density of state of graphene upon electrical-doping, which changes the Coulombic and van der Waals interactions. The water adsorption onto graphene is either *n*- or *p*-doping depending on the applied gate-to-graphene voltage. The ambi-doping nature of water onto graphene is due to the polar nature of water molecules, so the doping depends on the orientation of the water molecules.

Summary of Research:

Being extremely thin and thermally stable, graphene is an appealing method of surface modification [1-3]. It has been noted that water adsorption onto a supported graphene changes graphene's electronic structure. However, how water adsorption changes with altering the graphene Fermi level has never been studied experimentally [4].

We set out to test the hypothesis that the water adsorption behavior onto graphene can be tuned by electrically shifting the Fermi level, and hence the energetics of adsorption. In order to test this hypothesis, water adsorption onto back-gated graphene field effect transistors (GFETs) was studied as a function of electrical-doping via a quartz crystal microbalance (QCM) and current-voltage (IV) curve measurements.

Back-gate GFETs were fabricated onto 5 MHz AT-cut QCMs. An adhesion layer, 100 nm of Ti, was deposited onto the top electrode of the QCM via e-beam evaporation (AJA International). A 100 nm Al_2O_3 was deposited via atomic layer deposition (ALD) with trimethylaluminum (TMA) and oxygen plasma at 200°C (Oxford Flex AL) to form the dielectric onto the QCM.

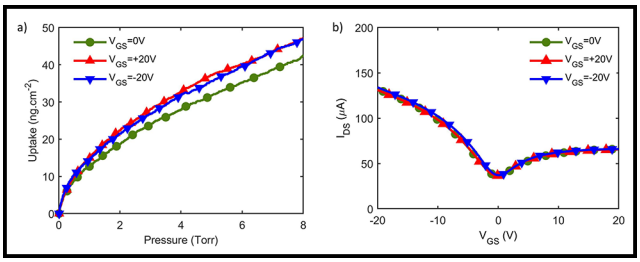

Figure 1: Adsorption isotherms were measured in an environmental vacuum chamber using the shift in the resonance frequency of the QCM upon water vapor exposure. (a) Shows the adsorption isotherms of water onto graphene for three different gate voltages: 0V, +20V, and -20V. (b) The three applied gate voltages during water adsorption induced no doping, n*-doping, and* p*-doping, respectively.*

Then, PMMA-backed CVD graphene was transferred onto the QCM. After the PMMA removal, the source and drain (5 nm Cr / 100 nm Au) were deposited on top of graphene via e-beam evaporation (AJA International), creating a 7.1 mm × 7.1 mm channel.

Adsorption isotherms were measured in an environmental vacuum chamber using the shift in the resonance frequency of the QCM upon water vapor exposure. Figure 1a shows the adsorption isotherms of water onto graphene for three different gate voltages: 0V, +20V, and -20V. The three applied gate voltages during water adsorption induced no doping, *n*-doping, and *p*-doping, respectively (Figure 1b). It can be seen in Figure 1a that the non-zero-gate voltages led to higher uptakes. However, switching the gate voltage polarity resulted in similar uptakes.

This change in uptake for the doped graphene is attributed to the change in the Coulombic and van der Waals interactions due to the increase in density of state (DOS) of graphene upon doping [5].

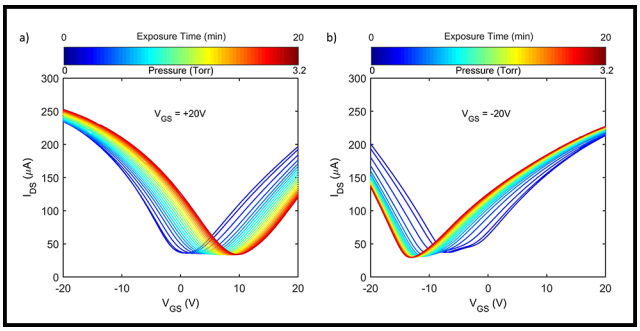

Figure 2: The IV curves after water vapor exposure with different applied gate voltages. (a) The adsorption of water molecules shifted the V_{CNP} in the positive direction and made the graphene less n*-doped. (b) The adsorption of water molecules moved the V_{CNP} in the negative direction and made the graphene less* p*-doped.*

In a different set of experiments, IV scans were periodically conducted after *x* minutes of water vapor exposure ($x = 0, 1, 2, \ldots, 20$). Figure 2 shows the IV curves after water vapor exposure with different applied gate voltages.

During the adsorption with an applied gate voltage of +20V, the graphene was initially *n*-doped; however, the adsorption of water molecules shifted the V_{CNP} in the positive direction and made the graphene less *n*-doped (Figure 2a), i.e., water adsorption induced holes in graphene. On the other hand, when the applied gate voltage was kept at -20V during adsorption, the graphene was initially *p*-doped; however, the adsorption of water molecules moved the V_{CNP} in the negative direction and made the graphene less *p*-doped (Figure 2b), i.e., water adsorption induced electrons in graphene.

When the applied gate voltage (V_{GS}) is greater than the V_{CNP}, electrons are the dominant charge carriers in graphene, so that water molecules tend to adsorb onto graphene with the positive side of the dipole (the H atoms) towards graphene. This creates a dipole layer of water molecules with their positive charge next to the graphene that induces *p*-doping. Figure 2a supports this hypothesis, as when V_{GS} = +20V was greater than V_{CNP}, the V_{CNP} shifted in the positive direction, which indicates water is *p*-doping graphene.

Conversely, when the gate voltage is less than the V_{CNP}, the water molecules adsorb onto graphene with their negative charges toward the graphene (the OH bonds upward), which creates a dipole layer of water molecules and induces *n*-doping. This agrees with Figure 2b, where V_{GS} = -20V was less than V_{CNP}, and the V_{CNP} shifted in the negative direction, which indicates water is *n*-doping graphene (Figure 3).

A detailed discussion of this research can be found at Ref 4.

References:

[1] Rafiee, J.; Mi, X.; Gullapalli, H.; Thomas, A. V.; Yavari, F.; Shi, Y.; Ajayan, P. M.; Koratkar, N. A. Wetting Transparency of Graphene. Nat. Mater. 2012, 11 (3), 217-222. https://doi.org/10.1038/nmat3228.

[2] Preston, D. J.; Mafra, D. L.; Miljkovic, N.; Kong, J.; Wang, E. N. Scalable Graphene Coatings for Enhanced Condensation Heat Transfer. Nano Lett. 2015, 15 (5), 2902-2909. https://doi.org/10.1021/nl504628s.

[3] Bagheri, M. H.; Loibl, R. T.; Boscoboinik, J. A.; Schiffres, S. N. Adsorption Transparency of Supported Graphene. Carbon 2019, 155, 580-586. https://doi.org/10.1016/j.carbon.2019.08.083.

[4] Bagheri, M. H.; Loibl, R. T.; Schiffres, S. N. Control of Water Adsorption via Electrically Doped Graphene: Effect of Fermi Level on Uptake and H_2O Orientation. Adv. Mater. Interfaces n/a (n/a), 2100445. https://doi.org/10.1002/admi.202100445.

[5] Hong, G.; Han, Y.; Schutzius, T. M.; Wang, Y.; Pan, Y.; Hu, M.; Jie, J.; Sharma, C. S.; Müller, U.; Poulikakos, D. On the Mechanism of Hydrophilicity of Graphene. Nano Lett. 2016, 16 (7), 4447-4453. https://doi.org/10.1021/acs.nanolett.6b01594.

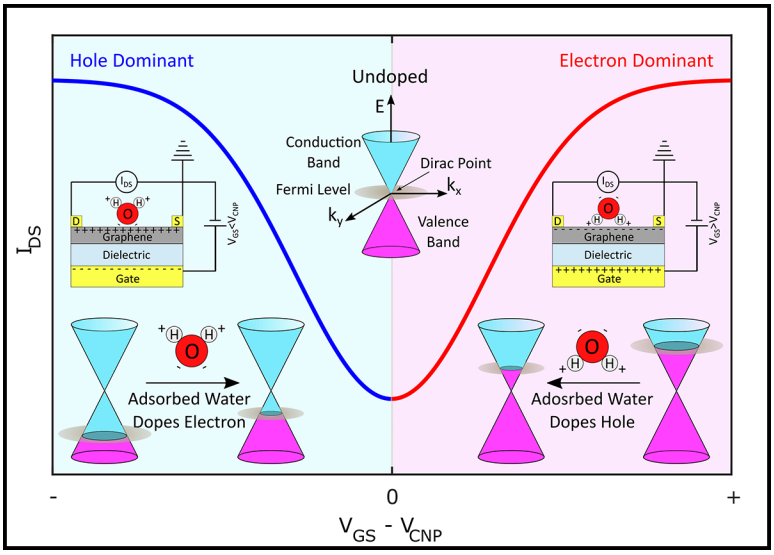

Figure 3: V_{GS} = -20V was less than V_{CNP}, and the V_{CNP} shifted in the negative direction, which indicates water is n*-doping graphene.*

Driving Structure Selection in Colloidal Particles Through Confinement

CNF Project Number: 2794-19

Principal Investigator(s): Julia Dshemuchadse

User(s): Rachael S. Skye

Affiliation(s): Department of Materials Science and Engineering, Cornell University

Primary Source(s) of Research Funding: National Science Foundation Graduate Research Fellowship under Grant No. DGE-1650441

Contact(s): jd732@cornell.edu, rss364@cornell.edu

Primary CNF Tools Used: CNF Computer Cluster

Abstract:

We use Monte Carlo simulations of hard tetrahedral particles to examine the effects of external confinement and particle shape on the self-assembly process. We examine a set of particles related to tetrahedra by vertex truncation. Through simulating self-assembly in a spherical container, we show that confined tetrahedral particles assemble in distinct concentric shells up to hundreds of particles. We also show that the curvature of the container can drive the local environment of particles towards specific motifs, allowing researchers to selectively induce the self-assembly of particular structures.

Summary of Research:

This work uses numerical simulations to explore the effect of confinement on the self-assembly behavior of hard colloidal particles — in particular tetrahedral particles. In experiment, advancements in synthesis of anisotropic particles have allowed the development of an array of shaped nanoparticles [1]. This raises the question: what structures do these different shapes assemble?

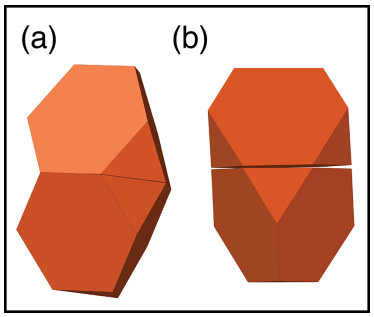

Figure 1: (a) The aligned motif (ca. 70.5°) vs. (b) the anti-aligned motif (90°).

Computational studies enable the exploration of the bulk behavior of particles with different shapes [2], replicating, for example, an experiment with particles floating in solution. However, the non-bulk case is less well explored. Here, we investigate the behavior of hard (non-attractive) tetrahedral particles confined in spherical walls, and the effects of wall curvature and particle shape on interparticle motifs. In experiment, this mimics assembly mechanisms such as confinement in an evaporating droplet [3].

To explore shape space, we apply vertex truncation to hard tetrahedra. Three shapes were given particular attention: the Platonic tetrahedron, the Archimedean truncated tetrahedron (ATT), and the space-filling truncated tetrahedron (STT). These shapes mark different regions in self-assembly space: the Platonic tetrahedra assemble a dodecagonal quasicrystal, the ATTs a diamond-type crystal, and the STTs lie on the boundary between to the two structures, in a region of structural competition [4]. We use a continually shrinking, hard spherical wall, compressed to high pressure to induce assembly. Simulations were performed with the HOOMD-blue Hard-Particle Monte Carlo (HPMC) package [5-7], using the resources provided by the CNF Computer Cluster, among others.

To explore the effects of container size — and therefore curvature — at equal pressure, we increase the number of particles in the system. We observe that concentric shells of particles form, conforming to the curvature of the wall. At small N, the vertices cluster in the center. Additional particles are added in the outer shell until the container is large enough that a two-shell structure forms. We have shown that this process repeats for a third shell, and organization into distinct layers continues up to thousands of particles.

The core-shell structure drives the particles towards local motifs that conform to the container wall. In tetrahedral particles, there are two dominant motifs, characterized by their misorientation angle: the angle through which a particle must be rotated in order to match the orientation of a reference particle. For tetrahedral particles, there are two important local motifs, both with facet-to-facet alignment (Figure 1): in one motif, the vertices of both particles align with one another (misorientation angle = *ca.* 70.5°), while in

the second motif, the vertices of one particle align with the edge midpoints of the other (misorientation angle = 90°) [8]. The "anti-aligned" misorientation angle is characteristic of a diamond-type structure formed in the bulk by ATTs, whereas Platonic tetrahedra favor the "aligned" motif, characteristic of a dodecagonal quasicrystal.

Plotting the change in predominant motif as the system size increases gives information on how the container drives the assembled structure. At small *N*, the clustering of vertices near the center of the containers drives the particle motif towards aligned for all shapes. For Platonic tetrahedra, the bulk motif is identical, so there is no overall transition with increasing *N* (Figure 2a).

In contrast, the ATT bulk motif is anti-aligned, leading to a gradual transition in which the frequency of the anti-aligned motif increases and the aligned motif decreases (Figure 2c). The intermediate shape — STT — lies in a region that exhibits both aligned and anti-aligned motifs in the bulk.

In confined systems, we see first an increase in the frequency of the anti-aligned motif, followed by a decrease towards the bulk system, again persisting up to thousands of particles (Figure 2c). By mapping where different motifs occur, we see that in very large containers, the anti-aligned motif is clustered near the surface. This indicates that low-curvature walls favor the diamond-type structure.

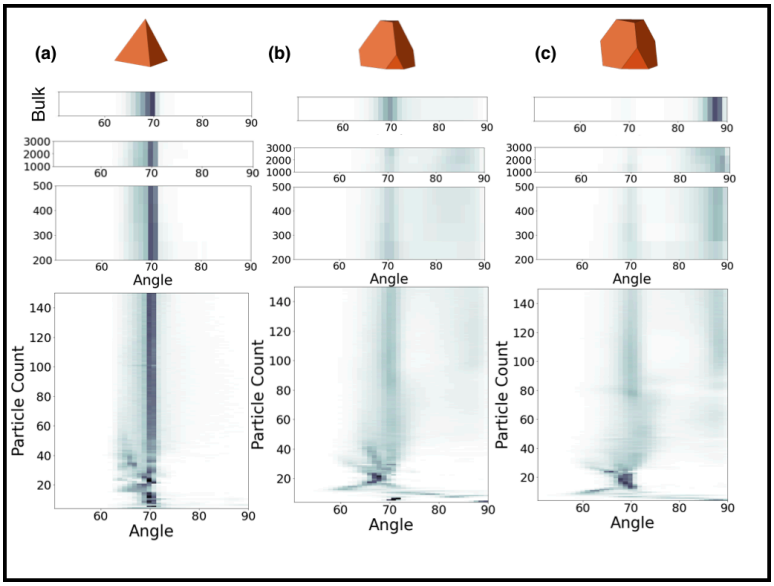

Figure 2: The distribution of misorientation angles for (a) Platonic tetrahedra, (b) space-filling truncated tetrahedra, and (c) Archimedean truncated tetrahedra with increasing container size. Color intensity corresponds to the frequency of that angle.

Conclusions and Future Steps:

We have shown that it is possible to influence structure selection through changing the curvature of the walls of confined systems, driving assembly towards desirable structures. Going forward, we intend to study the effects of other confinement geometries.

References:

[1] J. Henzie, M. Grünwald, A. Widmer-Cooper, P. L. Geissler, P. Yang, Nature Materials 11, 131-137 (2012).

[2] P. F. Damasceno, M. Engel, S. C. Glotzer, Science 33, 453-457 (2012).

[3] B. de Nijs, S. Dussi, F. Smallenburg, J. D. Meeldijk, D. J. Groenendijk, A. Imhof, L. Filion, A. van Blaaderen, M. Dijkstra, Nature Materials 14, 56-60 (2015).

[4] D. Klotsa, E. R. Chen, M. Engel, S. C. Glotzer, Soft Matter 14, 8692-8697 (2018).

[5] J. A Anderson, C. D. Lorenz, A. Travesset, Journal of Computational Physics 227, 5342-5359 (2008).

[6] J. Glaser, T. D. Nguyen, J. A. Anderson, P. Lui, F. Spiga, J. A. Millan, D. C. Morse, S. C. Glotzer, Computer Physics Communications 192, 97-107 (2015).

[7] J. A. Anderson, M. E. Irrgang, S. C. Glotzer, Computer Physics Communications 204, 21-30 (2016).

[8] E. G. Teich, G. van Anders, S. C. Glotzer, Nature Communications 10, 64 (2019).

Elucidating the Chemical Crypsis Mechanism in South African Snakes by Determining Microscale and Nanoscale Structure-Function Relationships in Snake Skin Sheds and Replicas

CNF Project Number: 2819-19

Principal Investigator(s): Robert Shepherd

User(s): Rachel Miller

Affiliation(s): Materials Science and Engineering, Cornell University

Primary Source(s) of Research Funding: National Science Foundation, Contract: EFMA-1830924

Contact(s): rfs247@cornell.edu, rm973@cornell.edu

Website: orl.mae.cornell.edu

Primary CNF Tools Used: NanoScribe GT2

Abstract:

Humans have been studying and mimicking animal's visual crypsis using wearable camouflage since the 18th century. Yet, only recently we have documented and attempted to understand the origins of chemical crypsis, the ability to become imperceptible to olfaction. Specifically this work aims to elucidate the mechanism of chemical crypsis in the first vertebrate shown to exhibit this trait, a snake known as the Puff adder (*Bitis arietans*).

The major feature distinguishing the Puff adder from its non-cryptic brethren such as the Night adder (*Causus rhombeatus*) is the skin surface structure. The skin's micron-scale, high aspect ratio, curved features known as 'fingers' create an array of wells for odorants to pool, significantly reducing odorant volatility and therefore rendering the Puff adder imperceptible to smell. To study and quantify this phenomena independent of snakeskin material, snakeskin surface biomes, and environmental contaminants, we employ various imaging and 3D printing processes to create a variety of detailed and accurate scaled models of both the puff adder skin and night adder skins. Nano-focused computed tomography (nano-CT) is used to create three-dimensional renderings of skins. To maximize accuracy of replicas, nano-CT image segmentation is informed by focused ion beam (FIB) and scanning electron microscopy (SEM) images. These digitally rendered surfaces are printed in epoxy using 3D printing, requiring the use of two photon polymerization (2PP) on the NanoScribe GT2 for micron-scale feature resolution.

We show the use of 2D Fourier transform analysis sequentially along the long axis as a means to quantify periodicity and investigate the degree of quasi-ordered orientation as a predictor for surface thermodynamic phenomena. Physical experiments on printed models and topographical analysis of digital renderings are used together to analyze and quantify the effects of structure periodicity and surface-area-to volume ratio on adhesion, wetting, and evaporation.

Summary of Research:

It has been shown that many snakes may actually hide not in plain sight using visual camouflage, but instead in plain "smell". Instead of being visually cryptic, these South African snakes are chemically cryptic [2]. Specifically, work done by A.K. Miller et al demonstrates that the Puff adder relies on chemical crypsis in order to effectively ambush its prey [1]. Extensive behavioral studies by A.K. Miller et al have suggested that additionally, current unpublished work by A.K. Miller is showing that many snakes in South Africa and the surrounding region also are chemically cryptic.

Previously, Puff adder skins have also been noticed for their microornamentation. Their skins have high aspect ratio "fingers" that protrude out from the skin base. It has been proposed that these types of ornamentation on a similar species were used to create optical effects in the skin. Snakeskin is home to large amounts of bacteria and other odorant producing biota. We hypothesize that these skins are not chemically cryptic because of their lack of odorants, but rather because there is a structure to their skin that keeps odorants from vaporizing and being detected by predators,

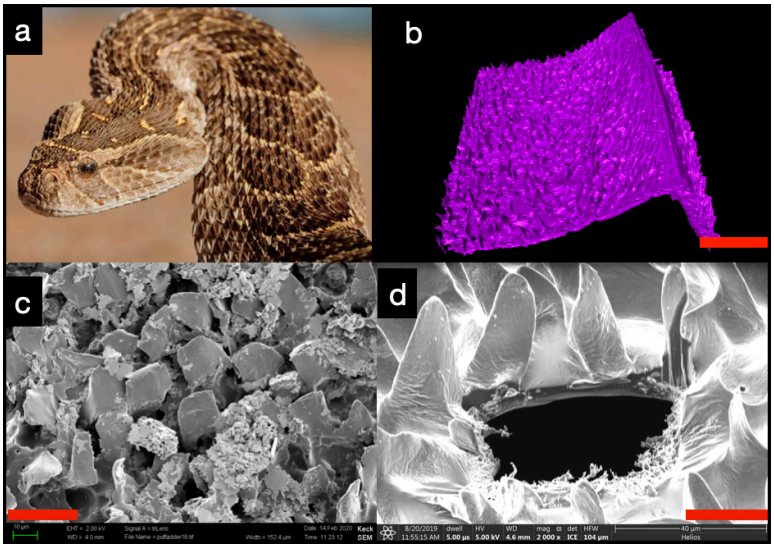

Figure 1: (a) Bitis arietans *(Puff adder), chemically cryptic snake1. (b) Nano CT scan reconstruction of Puff adder skin section with 'fingers,' Scale bar = 100 µm. (c) SEM image of puff adder skin to show pores are more visible than in CT or FIB, Scale bar = 20 µm. (d) FIB image of Puff adder skin. Further reveals structure of 'fingers' on skin, Scale bar = 20 µm.*

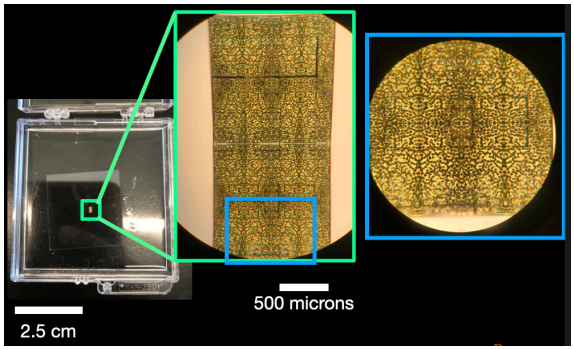

Figure 2: 2PP 3D printed Puff adder snakeskin replicas, photograph and optical microscope images.

prey, or even mates. The high aspect ratio features on Puff adder skin creates an environment on the surface of snake skin which decreases the volatility of odorants, rendering them chemically cryptic.

Using imaging techniques — including but not limited to nano-focused X-ray computed tomography (nano-CT) (Figure 1b), scanning electron microscopy (SEM) (Figure 1c), and focused ion beam microscopy — further reveals structures of 'fingers' on skin (Figure 1d, scale bar = 20 μm (FIB), and we can comprehensively probe Puff adder skin sheds. Together these techniques enable us to render and fabricate accurate digital and physical 3D renderings of skin features via nanoscopic 3D printing on the NanoScribe Photonic Professional GT2 (Figure 2).

Chemical treatment of these nano- and microscale features will be performed using thiolate mediated self-assembled monolayer chemistry, with a final test to be performed using modified substrates that chemically mimic the original skin.

To test these structures' impact on odorant volatility it would be beneficial to be able to fabricate consistent, large area replicas of these features. This could potentially involve reactive ion etching to achieve high aspect ratio features or wet etching methods, depending on the material chosen for these replicas. It is currently being debated as to whether or not it is possible to make these replica structures out of materials that are not silicone, epoxy, or other commercial plastics and instead out of keratin itself or another functionally and/or structurally similar material.

Conclusions and Future Work:

We have successfully created 0.1 cm × 0.1 cm footprint 1:1 Puff adder skin replica prints with submicron scale resolution using the NanoScribe GT2 printing apparatus (Figure 2). Nanoscopic prints and snakeskin sheds will serve as masters for replica molding, the former being non-destructive technique and the latter being a destructive technique.

References:

[1] McKay S, Glaudas X, Alexander GJ, Miller AK, Maritz B. An ambusher's arsenal: chemical crypsis in the puff adder (*Bitis arietans*). Proceedings of the Royal Society B, 282, 2015.

[2] Graeme D Ruxton. Non-visual crypsis: a review of the empirical evidence for camouflage to senses other than vision. Philosophical Transactions of The Royal Society, 364(1516), 2008.

Programmable Magnetic Microsystems

CNF Project Number: 900-00

Principal Investigator(s): Paul L. McEuen[1,2], Itai Cohen[1,2], Michael Brenner[3]

User(s): Tanner Pearson[4], Conrad Smart[5], Chrisy Xiyu Du[3], Hanyu Alice Zhang[4]

Affiliation(s): 1. Laboratory of Atomic and Solid State Physics, Cornell University; 2. Kavli Institute for Nanoscale Science, Cornell University; 3. School of Engineering and Applied Sciences, Harvard University; 4. School of Applied and Engineering Physics, Cornell University; 5. Department of Physics, Cornell University

Primary Source(s) of Research Funding: This work was supported by NSF grant DMR-1921567, Air Force Office of Scientific Research (AFSOR) multidisciplinary research program of the university research initiative grant FA2386-13-1-4118, Cornell Center for Materials Research (CCMR) through NSF MRSEC program (DMR-1719875), and the Kavli Institute at Cornell for Nanoscale Science. This work was performed in part at the Cornell NanoScale Science & Technology Facility (CNF), a member of the National Nanotechnology Coordinated Infrastructure NNCI, which is supported by the National Science Foundation (Grant NNCI-2025233)

Contact(s): plm23@cornell.edu, itai.cohen@cornell.edu, brenner@seas.harvard.edu, tgp34@cornell.edu, cs2239@cornell.edu, xiyudu@seas.harvard.edu, hz496@cornell.edu

Primary CNF Tools Used: Oxford FlexAL ALD, ASML DUV stepper, JEOL 6300, CVC e-beam evaporators, Oxford 81/82/100 etchers, PT770 and PT740 etchers, Anatech asher, Zeiss SEMs, Veeco atomic force microscope, Tencor P7 profilometer, Filmetrics UV, DISCO dicing saw, Heidelberg mask writer - DWL2000, AJA sputter deposition

Abstract:

We develop programmable microscopic systems based on nanomagnetic information. By taking advantage of magnetic shape anisotropy, we sequentially program the orientation of magnetic dipole moments on rigid panels. We can connect these panels with flexible glass hinges to develop actuatable structures capable of locomotion. Additionally, we can leave panels detached from each other and agitate them to demonstrate smart handshake self-assembly based on dipole-dipole interactions. These programmable systems have a diverse range of applications ranging from microrobotics to synthetic DNA assembly and replication.

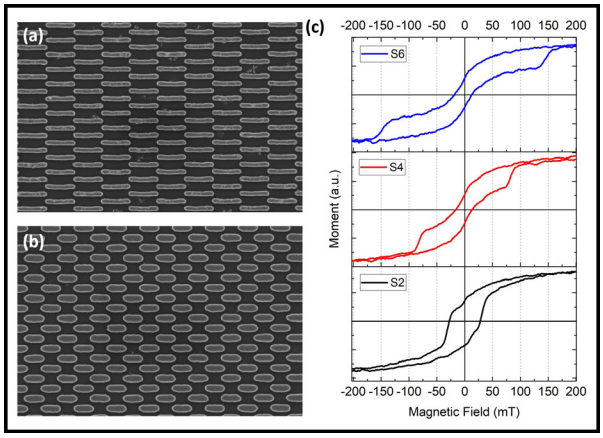

Figure 1: (a) SEM image of high AR nanomagnets. (b) SEM of low AR nanomagnets. (c) Magnetic hysteresis loops for different AR nanomagnets (S2 AR = 3, S4 AR = 5, S6 AR = 9). Width of hysteresis, and therefore coercive field, increases with increasing AR.

Summary of Research:

We create systems embedded with complex magnetic information by utilizing electron beam lithography (EBL) to fabricate single domain cobalt nanomagnets with varying aspect ratios (Figure 1a-b) [1]. The coercive fields of these nanomagnets and the orientations of their moments are intrinsically tied to shape anisotropy. Since magnetic moments prefer to be oriented along the long axis of a magnet, high aspect ratio (AR) magnets will exhibit higher coercive fields along their long axes than those with smaller aspect ratios. We tune the nanomagnet dimensions to achieve magnetic dipoles with coercive fields ranging from 30 mT to 140 mT (Figure 1c).

We sequentially program multiple magnetization directions by using two species of nanomagnets with disparate coercive fields [1]. With the long axis of the two species oriented along the same global axis, we apply a magnetic field greater than the coercivity of the high aspect ratio magnets to program all the magnets in one direction. We then use an opposing field with a magnitude between the coercivities of the two magnet species to reverse the orientation of the lower aspect ratio magnets. With an orthogonal pair of magnet species, we can achieve up to four discrete moment orientations ($\pm x$, $\pm y$). Superpositions of these moments provide additional orientations. We confirm dipole moment orientations with magnetic force microscopy (MFM) (Figure 2b).

We have previously shown that nanometer-thick glass deposited by atomic layer deposition (ALD) is an ideal material for flexible microsystems due to its incredibly low

bending stiffness [2]. By combining EBL and deep ultraviolet (DUV) lithography, we can integrate programmable nanomagnets onto rigid panels connected by flexible glass hinges to create a variety of actuatable devices. Here we show a device consisting of two panels, comprised of arrays of 800 nanomagnets with opposing moments, connected by two 5 nm thick glass hinges (Figure 2a-b). We can apply a uniform external field in z to torque both panels up or down, demonstrating the basic mountain-valley fold essential for microscopic origami and origami-inspired metamaterials.

Moreover, we can apply a combination of sinusoidal in-plane and out-of-plane fields to achieve a crawling motion akin to that of an inchworm (Figure 2c). Starting with both legs on the substrate, these fields continuously cycle through the following sequence of motions: the device tilts to its back leg, stretches the front leg forward, tilts to its front leg, pulls the back leg forward, and returns to its start position. In this way the device achieves net forward motion (Figure 2d). We can increase the frequency of this cyclic motion to achieve impressive crawling speeds of over a body length per second. Additionally, the phase and amplitudes of the in-plane field components can be modulated to achieve direction reversal and turning, respectively. This deceptively simple device illustrates how even a small amount of magnetic information can enable complex actuation dynamics necessary for robotic microsystems.

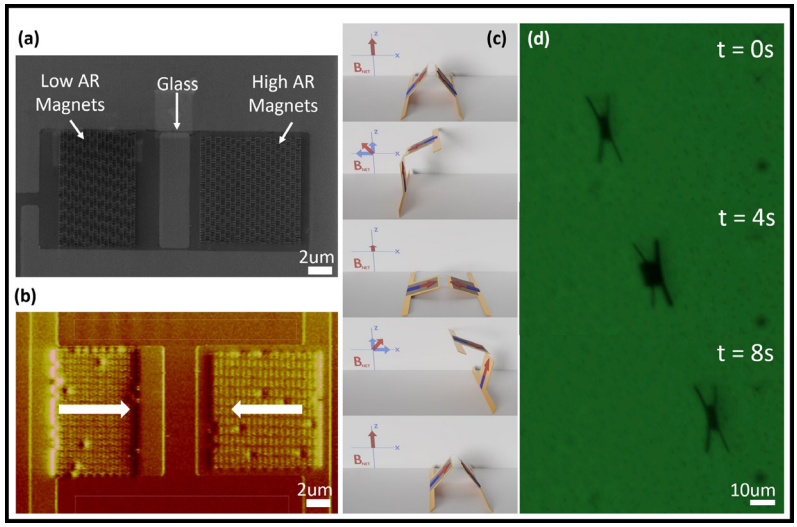

Figure 2: (a) SEM image of inchworm device. Glass hinges (dark grey) are each 250 nm × 2.5 µm. Panels are (10 µm)² and each consist of 800 magnets. (b) MFM image confirming the opposing net magnetic moments of each panel. (c) Cartoon illustrating stepping sequence of device. (d) Position over time of device cycled at 1 Hz, demonstrating net forward motion.

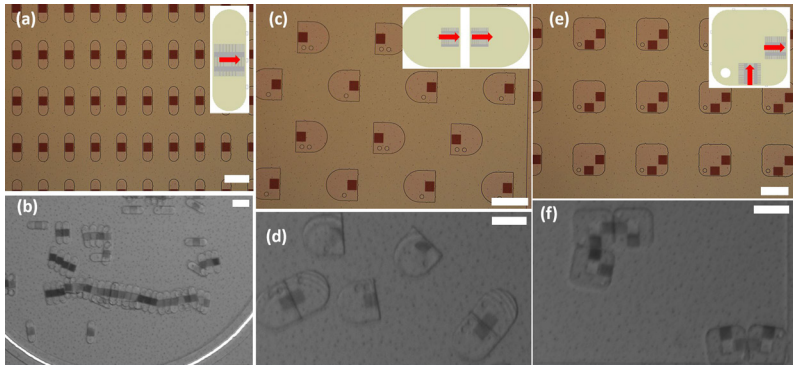

Figure 3: (a-b) Panels assembling into simple polymer chains. (c-d) Panels assembling into dimers. (e-f) Assembly of square panels with two dipole moments. Full assembly would yield 2 × 2 panel arrays. Insets show cartoons of panel magnetizations. Scale bars 30 µm.

We also use programmable nanomagnets to develop microscopic handshake systems capable of smart self-assembly (Figure 3) [3]. The fabrication process consists of embedding one or more nanomagnetic dipoles into thick, disconnected glass panels. When released from the substrate, panels are sonicated to facilitate lock-key binding of dipoles at the sides of complementary panels. With careful design of the panel geometry and magnetic dipole-dipole interactions, we can enable a wide range of well-defined assemblies. As the number of dipoles per panel increases, the lock-key binding becomes more specified, and more complex assemblies are possible. Moreover, these systems can be influenced by external magnetic fields at any point during or after the assembly process, providing a unique mechanism to manipulate assembled structures.

The possible applications for programmable nanomagnetic microsystems are immense. Magnetic panels connected by flexible glass hinges can be used to create mechanical and optical metamaterials and explore magnetically induced defects in those metamaterials. They can also be integrated into locomotive microrobots.

By eliminating the connective membranes between panels, we can further develop intelligent handshake systems governed by lock-key dipole-dipole interactions. These can be used to create assemblies that behave analogous to polymers and DNA.

References:

[1] J. Cui, T. Huang, Z. Luo, P. Testa, H. Gu, X. Chen, B. J. Nelson, L. J. Heyderman, Nature 2019, 575, 164.

[2] K. J. Dorsey, T. G. Pearson, E. Esposito, S. Russell, B. Bircan, Y. Han, M. Z. Miskin, D. A. Muller, I. Cohen, P. L. McEuen, Adv. Mater. 2019, 31, 1901944.

[3] R. Niu, C. X. Du, E. Esposito, J. Ng, M. P. Brenner, P. L. McEuen, I. Cohen, PNAS 2019, 116 (49), 24402.

Smart Microscopic Robots

CNF Project Number: 900-00

Principal Investigator(s): Paul L. McEuen[1,2], Itai Cohen[1,2], Alyosha C. Molnar[3], Marc Z. Miskin[4]

User(s): Michael F. Reynolds[1], Alejandro J. Cortese[1,3], Qingkun Liu[1], Wei Wang[1,5], Samantha Norris[1], Zhangqi Zheng[1], Sunwoo Lee[3]

Affiliation(s): 1. Laboratory of Atomic and Solid State Physics, Cornell University, Ithaca NY USA;
2. Kavli Institute at Cornell for Nanoscale Science, Cornell University, Ithaca NY USA;
3. Department of Electrical and Computer Engineering, Cornell University, Ithaca NY USA;
4. Department of Electrical and Systems Engineering, University of Pennsylvania, Philadelphia, PA, USA;
5. Sibley School of Mechanical and Aerospace Engineering, Cornell University, Ithaca NY USA

Primary Source(s) of Research Funding: CCMR, MURI, KIC, CNF REU Program (NSF grant NNCI-2025233)

Contact(s): plm23@cornell.edu, mfr74@cornell.edu

Primary CNF Tools Used: ABM contact aligner, Oxford 100 ICP dielectric etcher, Oxford 80 etchers, Oxford Cobra ICP etcher, AJA sputter deposition (1&2), Arradiance ALD Gemstar-6, Oxford ALD FlexAL, Oxford PECVD, Gamma automatic coat-develop tool, Xactic xenon difluoride etcher

Abstract:

Research on microscopic robots — robots a few hundred micrometers in size or smaller — has demonstrated a variety of approaches for locomotion and simple functions but has not produced "smart microscopic robots" that can perform complex tasks autonomously. Recently, our group has demonstrated the first smart microscopic robots by integrating microactuators with complementary metal oxide semiconductor (CMOS) electronics. These robots can actuate their legs independently and walk autonomously without any input of information. This work paves the way for smart microscopic robots that can sense and respond to their environment, receive commands, perform complex functions, and communicate with the outside world.

Summary of Research:

Figure 1 shows the first smart microscopic robot. An optical micrograph of one of these robots with labeled parts is shown in Figure 1A. Its body consists of photovoltaics for powering the robot and a 180-nm node CMOS circuit with approximately 1000 transistors to control the robot. The legs of the robot consist of surface electrochemical actuators (SEAs), microactuators developed at Cornell made of ultrathin atomic layer deposition platinum that bend to micrometer-scale radii of curvature in response to small voltages in aqueous environments [1,2]. Rigid panels of SiO_2 on either side of the actuator restrict the bending direction of the SEA to form a hinge. At the top and bottom of the robot are large, exposed platinum ground pads that serve as the counter electrodes to the actuators. Figure 1B shows a microscope image of the circuit of a released robot. Using infrared light and viewing a released robot from underneath, we can see parts of the CMOS circuit that controls the robot (Figure 1B). We fabricate many robots in parallel — Figure 1C shows an array of microscopic robots with a variety of designs prior to release. Each robot is inside a 300 μm by 300 μm square, meaning that almost 100,000 robots could be fabricated on a 4-inch wafer.

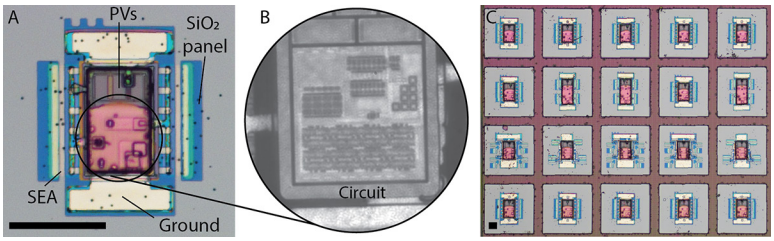

Figure 1: (A) Optical micrograph of a smart microscopic robot. (B) Infrared microscope image of a released microscopic robot showing the onboard CMOS circuit. (C) Optical micrograph of an array of microscopic robots. They are photolithographically fabricated in parallel on a silicon-on-insulator wafer. Scale bars are 100 μm.

Figure 2 shows an optical image of the circuit that controls the robot. This circuit is designed at Cornell and fabricated by X-FAB Silicon Foundries with a 180 nm node CMOS process on silicon-on-insulator (SOI) wafers. It has a simple function: to output phase-shifted square waves to the legs of the robot, allowing it to walk. We set the gait of the robot by wiring the legs of the robot to square wave outputs on the circuit with different phases. We set the frequency of the square wave outputs by wiring the I-shaped pins to the bar above them during post-processing, with frequencies ranging from about 1 Hz to about 128 Hz by factors of two.

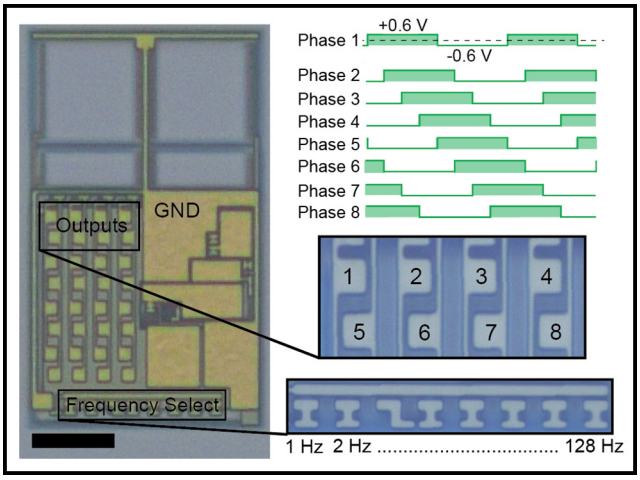

Figure 2: Optical micrograph of clockbot's integrated circuit showing the output pins for the eight phase-shifted square waves and the pins for selecting the output wave frequency. Scale bar is 20 µm.

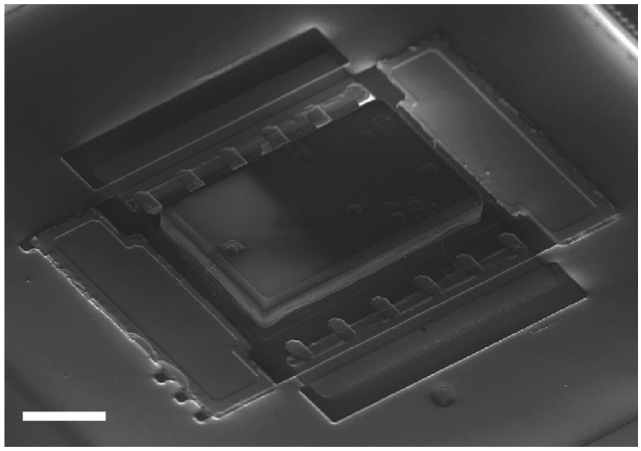

Figure 3: A scanning electron microscope image of a completed microscopic robot. The body of the robot, containing the photovoltaics and circuit, is about 15 µm tall. Scale bar is 30 µm.

After receiving the circuits from X-FAB, we perform post-processing on them to etch out the body (circuit and PVs) of the robot, create wires out from the circuit, shield the circuit from light, build legs and connect them to the circuit, and release the robots from the silicon substrate. This process is based on a variety fabrication protocols developed in our group [1-3], requires 13 layers of photolithography, and makes use of more than twenty CNF tools. A scanning electron microscope image of a completed robot is shown in Figure 3. This image shows the large topography resulting from etching out the body of the robot, about 15 μm tall. This creates several challenges during the fabrication process, requiring us to use the spray coater on the Gamma automatic coat-develop tool to coat the large vertical features completely with photoresist.

Upon completion of the fabrication process, we undercut the silicon beneath the robot and release it into an aqueous environment. Figure 4A shows a 3D model of a released robot. Upon release, the legs bend under the body of the robot. When we illuminate the robot with light, the robot moves autonomously without any additional inputs. Its design is inspired by the Purcell three-link swimmer [4]; instead of swimming, this robot walks by alternately moving its front and back legs. These robots operate in light intensities of about 1 kW/m^2, equivalent to direct sunlight outside on a sunny day. Figure 4B shows time-lapse images of a clockbot walking, with images taken at 25 s intervals.

Conclusions and Future Steps:

The robots shown here are only the beginning for CMOS-integrated smart microscopic robots. We are currently pursuing work on faster robots with more legs and more complex gaits and robots that respond to commands or following light gradients. Future designs will include robots with alternate propulsion mechanisms, additional sensors, and ways to communicate with each other and the outside world. As smart microscopic robots increase in complexity and capability, they have incredible potential for positive impact in numerous fields, from studying emergent behaviors in swarms of smart particles to performing medical procedures at the micron-scale.

References:

[1] Miskin, M. Z., et al. Electronically integrated, mass-manufactured, microscopic robots. Nature 584, 557-561 (2020).

[2] Liu, Q., et al. Micrometer-sized electrically programmable shape-memory actuators for low-power microrobotics. Science Robotics 6, (2021).

[3] Cortese, A. J., et al. Microscopic sensors using optical wireless integrated circuits. PNAS 117, 9173-9179 (2020).

[4] Purcell, E. M. Life at low Reynolds number. American Journal of Physics 45, 3-11 (1977).

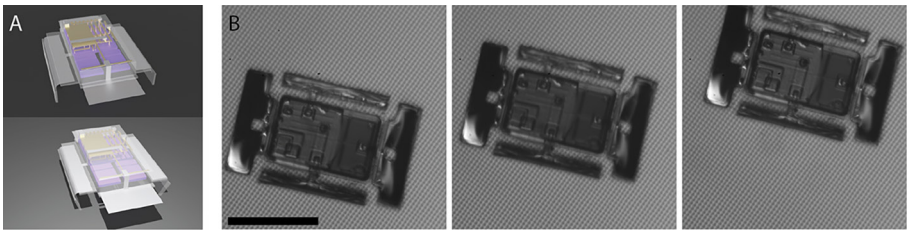

Figure 4: (A) Schematic of a CMOS integrated microscopic robot. The robot moves autonomously when powered by light. (B) A released microscopic robot walking on a glass substrate. Scale bar is 100 µm.

Characterizing Disjoining Pressure of Water in SiO_2 Nanochannels by Wicking Experiments

CNF Project Number: 2123-12

Principal Investigator(s): Shalabh C. Maroo

User(s): An Zou, Durgesh Ranjan

Affiliation(s): Department of Mechanical and Aerospace Engineering, Syracuse University, Syracuse, NY 13244

Primary Source(s) of Research Funding: National Science Foundation Career Award NO. 1454450; Office of Naval Research Grant NO. N000141812357

Contact(s): scmaroo@syr.edu, azou@syr.edu, dranjan@syr.edu

Website: http://maroo.syr.edu

Primary CNF Tools Used: Heidelberg mask writer - DWL2000, manual photoresist spinner, Gamma coat-develop tool, GCA auto stepper, ASML stepper, YES image reversal oven, ABM contact aligner, SÜSS MA6-BA6 contact aligner, e-beam evaporator, Oxford PECVD, GSI PECVD, Glen 1000 Plasma, Anatech resist strip, Oxford 81/82/100 etchers, P-T deep silicon etcher, Unaxis 770 deep silicon etcher, optical microscope, SEM, AFM

Abstract:

We characterized disjoining pressure of water in SiO_2 nanochannels by studying water wicking in 59 nm channels. The wicking in nanochannels was dominated by disjoining pressure. Wicking distance is proportional to square root of time, and the slope can be used to calculate the disjoining pressure, which can be as high as ~ 1.5 MPa in 59 nm channel. The work reported here is part of an article that is currently under review [1].

MECHANICAL DEVICES

Summary of Research:

The pressure in a thin liquid film, with thicknesses ranged from a few nanometers to hundreds of nanometers, differs from its bulk due to the considerable, if not dominant, intermolecular interactions. This pressure difference is characterized by disjoining pressure, which plays a fundamental role in a wide range of engineering and natural systems involving bubbles, foams, emulsions, and membrane, etc. Since disjoining pressure is originated from intermolecular interactions, it is significantly affected by the material of surrounding surfaces, which could be any combination of solid, liquid, and vapor. Although disjoining pressure in a non-polar liquid film has been well understood, comprehensive knowledge for polar liquids, like water on a silicon dioxide (SiO_2) surface, is still lacking. Here, we report an experimental characterization of disjoining pressure of water in 1D SiO_2 nanochannels (height: 59 nm) with all walls made of SiO_2, by studying the water wicking process in nanochannels.

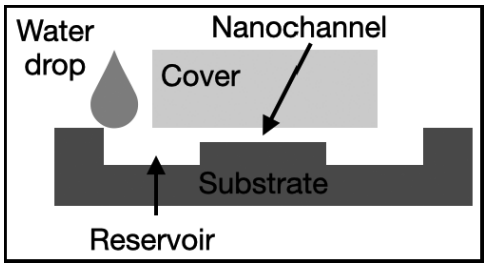

Figure 1: Sketch of cross-sectional view of the sample.

Figure 1 shows a cross-sectional view sketch of the nanochannel sample. The nanochannels, between two reservoirs, are ~ 2 cm long, 10 μm wide with 10 μm spacing between two adjacent channels. The channel height is 59 nm. The nanochannels were closed by bonding two wafers together. The fabrication process started from a silicon (Si) wafer — then ~ 3 μm thick photoresist (PR) was spin-coated and patterned through a standard photolithography process. The wafer was etched down for a certain depth to form open nanochannels, using patterned PR as mask. After removing the remaining PR, ~ 1 μm thick SiO_2 film was deposited using plasma enhanced chemical vapor deposition (PECVD), and was patterned by standard photolithography followed by dry etching, to serve as the hard mask for deep Si etching (Bosch process) for reservoirs (~ 30 μm deep). Then, after removing the remaining PECVD SiO_2 film using buffered oxide etchant, a new 300 nm thick PECVD SiO_2 film was deposited prior to bonding. The nanochannels were closed by bonding a glass piece above the channels using standard anodic bonding. The image from atomic force microscope (AFM) showing channel profile prior bonding was shown in Figure 2.

To perform wicking experiments, the sample was cleaned using deionized (DI) water, followed by oxygen plasma cleaning for 30 min. A DI water drop was placed in the reservoir, and water would wick into the channels, flow forward to fill the channel until reaching the other end. This wicking process was recorded using high speed camera

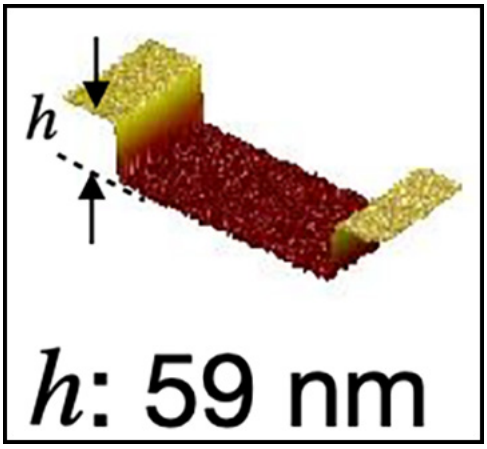

Figure 2: AFM image of channel profile prior bonding.

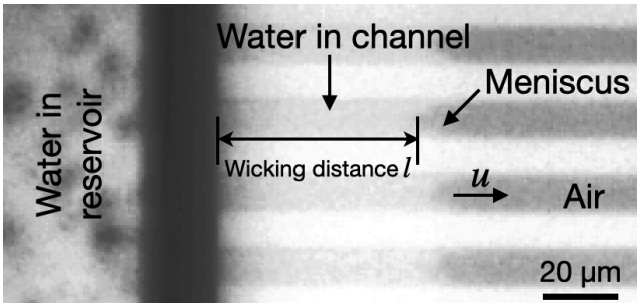

Figure 3: A typical image of the wicking from high speed video.

from the top. From the obtained video, the wicking distance l can be obtained by measuring the distance between the entrance and the position of the meniscus. Figure 3 shows a typical high speed image of the wicking. After finishing one test, the sample was heated to ~ 200°C on a hot plate in the open air to dry, which would take several minutes up to several hours. The wicking experiments for each sample were conducted at least four times to ensure repeatability.

The wicking distance (l) is proportional to square root of wicking time ($t^{1/2}$), as predicted by the simplified analytical solution (Eq. 1) of Navier-Stokes equation for wicking in a low specific ratio (height << width) rectangular cross-sectional channel [2].

$$l = \sqrt{\frac{h^2 \Delta P}{6\mu}} \cdot t^{1/2} = C \cdot t^{1/2}$$

where h is the channel height; ΔP is the total pressure difference driving the wicking; and μ is the fluid dynamic viscosity.

Figure 4 shows experimental results for both 59 nm and 1015 nm channels. As expected, the wicking distance is linear to square root of time with a slope C of 1.00 mm/s$^{1/2}$. As shown in Eq. 1, this slope is a function of channel geometry (height), liquid property (viscosity), and

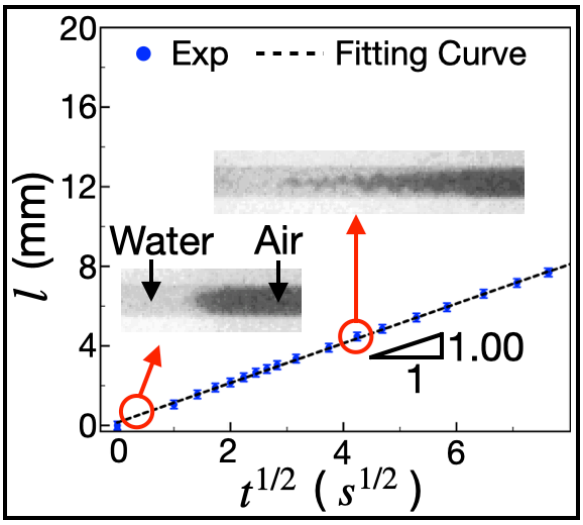

Figure 4: Variation of wicking distance with square root of time.

pressure difference. As both channel height and viscosity are known, the pressure difference can be calculated from experimentally obtained slope.

There are two potential contributions to the total pressure difference driving the wicking: disjoining pressure (due to the intermolecular interactions) and capillary pressure (due to the curvature of the meniscus). An interesting observation of wicking in 59 nm channels is that two types of meniscus were observed: regular-curved shape and wedge shape (Figure 4). The regular-curved meniscus occurred only within the first few hundreds of microns from the entrance. Beyond this initial distance, water was seen to flow much faster at the corners, forming the wedge-shape meniscus, which also led to air or vapor being momentarily trapped within the wicking liquid front. The different meniscus shape implies varied capillary pressure, however, constant slope C was observed during entire wicking process. Thus, capillary pressure was not major contribution to the total pressure difference; while disjoining pressure drove the wicking. With the estimation of capillary pressure in Ref. [1] and Eq. 1, disjoining pressure was calculated as 1.51 MPa. This is a first experimental characterization of disjoining pressure of water in SiO_2 nanochannels.

Conclusions and Future Steps:

We studied the water wicking in SiO_2 nanochannels, from which the disjoining pressure was characterized as 1.51 MPa in 59 nm channels.

References:

[1] A. Zou, S. Poudel, S.C. Maroo, arXiv preprint arXiv:2010.09928 (2020).

[2] B. E. Rapp, Microfluidics: Modelling, Mechanics and Mathematics. Micro and Nano Technologies, Oxford: Elsevier, 2017.

Origami-Inspired Micro-Robotic Arm

CNF Project Number: 2416-16

Principal Investigator(s): Itai Cohen

User(s): Baris Bircan

Affiliation(s): School of Applied and Engineering Physics, Laboratory of Atomic and Solid-State Physics, Kavli Institute at Cornell for Nanoscale Science; Cornell University

Primary Source(s) of Research Funding: National Science Foundation, Contract DMR-1719875; Army Research Office, Contract W911NF-18-1-0032

Contact(s): itai.cohen@cornell.edu, bb625@cornell.edu

Primary CNF Tools Used: Arradiance ALD Gemstar-6, Oxford ALD FlexAL, Oxford PlasmaLab 80+ reactive ion etchers, ABM contact aligner, AJA sputter deposition, AJA ion mill, Heidelberg mask writer - DWL2000

Abstract:

Origami, the Japanese art of paper folding, has recently found use in various engineering applications, leading to the development of origami-inspired systems ranging from the macro to the microscale. At and below the microscale, origami-inspired designs have allowed the use of planar lithographic fabrication methods to build systems that can self-fold into complex three-dimensional (3D) geometries. In our work, we make use of origami design principles to create a microscale robotic arm, which can be fabricated in large numbers using standard lithographic techniques. We envision that these devices will find uses in lab-on-a-chip devices, tissue manipulation and minimally invasive surgery.

Summary of Research:

Our group has previously demonstrated an approach capable of creating complex self-folding microsystems based on atomic layer deposition (ALD) nanofilms [1]. The method we have developed automatically generates photomasks for arbitrarily complex origami-inspired designs, which can then be used to fabricate self-folding microdevices based on ultra-thin ALD films.

One application being pursued with this approach is a microscale robotic arm based on ultra-thin, ALD based surface electrochemical actuators (SEAs) [2,3]. SEAs, which consist of 7.5 nm of platinum, deposited using the Arradiance ALD Gemstar-6, and a 2 nm thick titanium capping layer, deposited using the AJA sputter deposition system, operate in electrolyte and can bend down to several micron scale radii of curvature in response to electrical signals.

To microfabricate our design for the origami-inspired robotic arm (Figure 1A-B), we generate photomasks suitable for SEAs (Figure 2). Our design for the micro-robotic arm incorporates the origami-inspired surgical forceps (Oriceps) [4] as the gripping element, and includes folding hinges to generate translation and tilt, resulting in a total of three degrees of freedom. The leftmost photomask pattern shown in Figure 2 defines the regions that will be used to create upward bending, while the photomask pattern shown in the middle defines the regions that will be used to create downward bending. The rightmost photomask pattern defines the rigid, flat panels that will be used to restrict bending. These patterns are generated as BMP files and imported into L-Edit to create the full mask layout, which is then used to fabricate photomasks with the Heidelberg mask writer - DWL2000.

Figure 3 shows the first prototypes for our origami-inspired micro-robotic arm design, which include three electrodes to address the translation, tilt, and gripping degrees of freedom, and thin, isolated strips of platinum to carry applied electrical signals throughout the device. The three electrodes are permanently bonded to the substrate, which makes the devices semi-tethered. After the devices are released by wet etching the underlying Al release layer, the electrodes make it possible to apply driving voltages by making contact with a Pt/Ir micromanipulator probe.

We envision that the microscale manipulation capabilities offered by this SEA-based, origami-inspired micro-robotic arm will find uses in lab-on-a-chip devices, tissue manipulation and minimally invasive surgery.

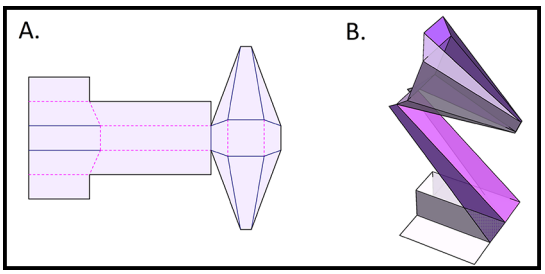

Figure 1: (A) Fold pattern and (B) 3D model for our origami-inspired robotic arm design, which incorporates the Oriceps [4] as the gripping element, and includes folding hinges to generate translation and tilt.

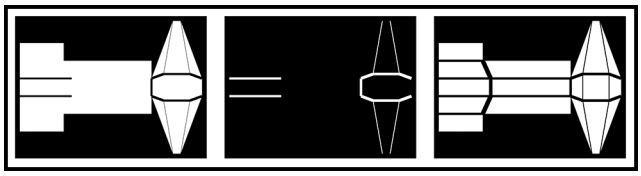

Figure 2: Photomask patterns used in fabrication of the micro-robotic arm design. The leftmost photomask defines the regions that will be used to create upward bending, while the photomask shown in the middle defines the regions that will be used to create downward bending. The rightmost photomask defines the rigid, flat panels that will be used to restrict bending.

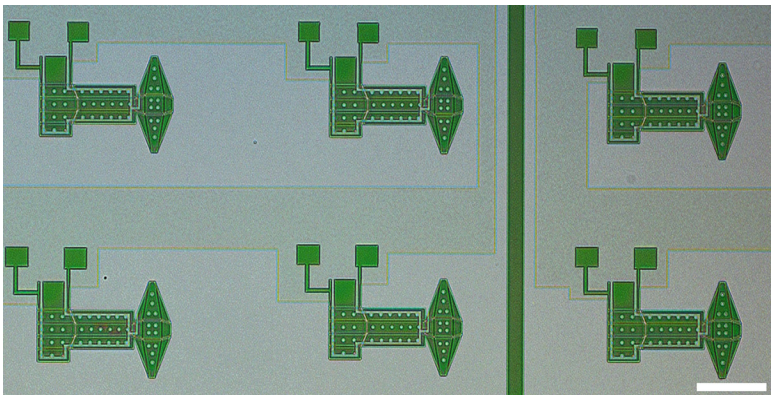

Figure 3: An array of microscale robotic arm devices prior to release. Each device is attached to three fixed electrodes that address the translation, tilt, and gripping degrees of freedom. Scale bar is 200 µm.

References:

[1] Bircan, B., Miskin, M. Z., Lang, R. J., Cao, M. C., Dorsey, K. J., Salim, M. G., Wang, W., Muller, D. A., McEuen P. L., and Cohen, I., "Bidirectional self-folding with atomic layer deposition nanofilms for microscale origami," Nano Letters, vol. 20, no. 7, pp. 4850-4856, 2020.

[2] Miskin, M. Z., Cortese, A. J. Cortese, Dorsey, K., Esposito, E. P., Reynolds, M. F., Liu, Q., Cao, M., Muller, D. A., McEuen, P. L., Cohen, I., "Electronically integrated, mass-manufactured, microscopic robots," Nature, vol. 584, no. 7822, pp. 557-561, 2020.

[3] Liu, Q., Wang, W., Reynolds, M. F., Cao, M.C., Miskin, M.Z., Arias, T.A., Muller, D.A., McEuen, P.L., and Cohen, I., 2021. Micrometer-sized electrically programmable shape-memory actuators for low-power microrobotics. Science Robotics, 6(52), 2020.

[4] Edmondson, B. J., Bowen, L. A., Grames, C. L., Magleby, S. P., Howell, L. L., Bateman, T. C., "Oriceps: Origami-inspired forceps," in ASME 2013 conference on smart materials, adaptive structures and intelligent systems, American Society of Mechanical Engineers Digital Collection, 2013.

Electrically Controllable Micro-Machines

CNF Project Number: 2416-16

Principal Investigator(s): Itai Cohen, Paul L. McEuen

User(s): Qingkun Liu, Wei Wang, Jacob Thomas Pelster, Hanyu Alice Zhang

Affiliation(s): Kavli Institute at Cornell for Nanoscale Science, School of Applied and Engineering Physics, Laboratory of Atomic and Solid-State Physics, Department of Physics; Cornell University

Primary Source(s) of Research Funding: National Science Foundation, Contract DMR-1719875; DMR-1435829 Army Research Office, Contract W911NF-18-1-0032

Contact(s): itai.cohen@cornell.edu, plm23@cornell.edu, ql59@cornell.edu, ww459@cornell.edu, jtp246@cornell.edu, hz496@cornell.edu

Primary CNF Tools Used: Oxford ALD FlexAL, Arradiance ALD Gemstar-6, Oxford 81/100 etchers, ABM contact aligner, CVC SC4500 odd-hour, AJA sputter deposition, AJA ion mill, Oxford Cobra ICP etcher, Heidelberg DWL2000

Abstract:

Electromechanically adaptive materials are poised to revolutionize microscopic robots, robotic materials, and bio-implantable devices. Previously, we have demonstrated that the electrochemical micro-actuators made by atomically thin layers of metals and dielectrics could bend in response to a low voltage of ~ 1V. Here, we utilized this new type of micro-actuators to develop complex microstructures and micromachines, such as auxetic mechanical metamaterials, neural probes, and artificial cilia.

Summary of Research:

Nanofabrication of electromechanically active materials could create micromachines with unparalleled properties and functionalities [1]. The core of these devices consists of a nanometer-thin platinum layer as an electrochemically active material capped on one side by titanium as an inert layer. To demonstrate their broad applications, our team has developed three types of such micro-devices: auxetic mechanical metamaterials, neural probes, and artificial cilia.

Our team first developed micro-sized auxetic mechanical metamaterials by using origami design principles [2]. Auxetic mechanical metamaterials comprised of rigid panels that can locally splay, have the ability to yield reconfigurable curved surfaces and generate different locomotion gaits for robotics applications. We show that such electrically actuated auxetic metamaterials can be utilized to design micro-scale robots. As in their macroscopic counterparts, the expansions and contractions in our devices are achieved by splaying neighboring panels. To achieve this splay actuation we developed an origami hinge based on a single mountain and two valley folds. The actuation of the hinges is controlled by applying voltage to a nm thin surface electrochemical actuator. The local expansions and contractions alter the local Gaussian curvature of the metamaterial sheet allowing it to reconfigure into a continuous set of three-dimensional shapes. We modeled the target shapes using a reversed design approach in which the shapes are iterated towards target shapes by selecting optimal actuations of the splay hinges. We then show experimentally we are able to generate 2D and 3D shapes by actuating the hinges. Based on these proof of principle results, we are working towards manufacturing untethered metamaterial-based micro-scale robots with integrated photovoltaics and timing circuits that control the sequence of hinge actuations and resulting global shapes and locomotion gaits.

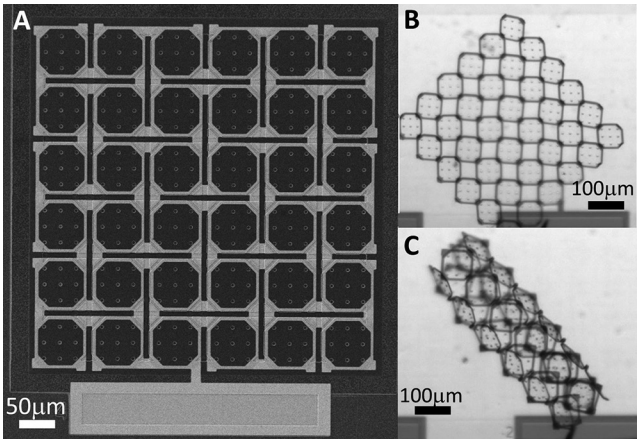

Figure 1: Electrically programmable auxetic mechanical metamaterials. (A) SEM image of a mechanical metamaterial sheet. (B,C) The sheet could deform into two-dimensional and three-dimensional shapes.

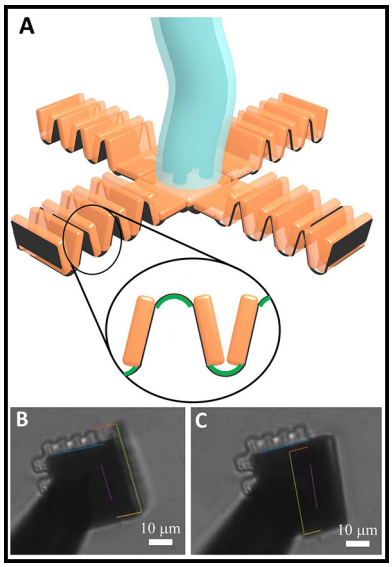

Figure 2: Robotic neural probe. (A) Schematic of an origami-based deployable neural probe. (B,C) Optical images of the bendable probe actuated from -88° to 134° when varying the voltage from 0.6V to -1.2V in phosphate buffer solution.

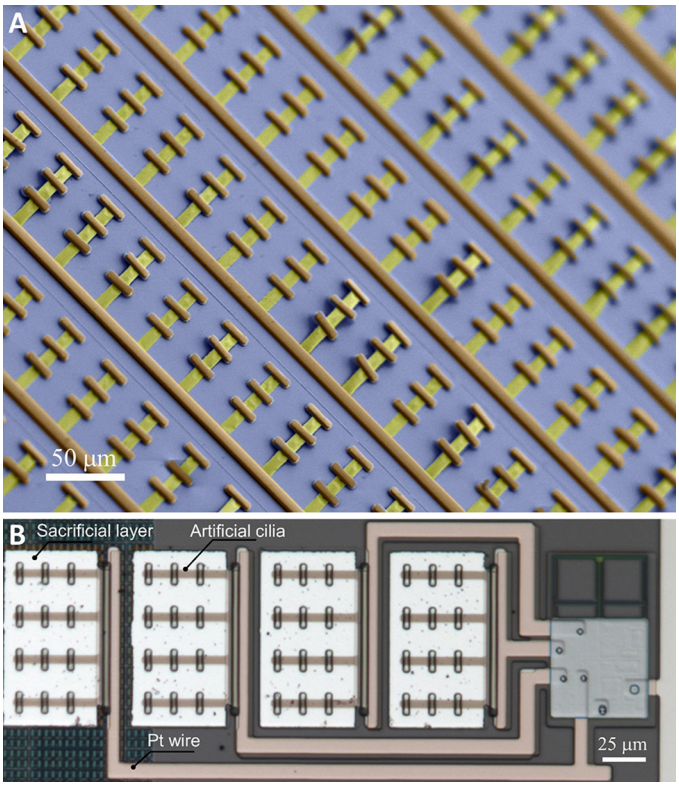

Figure 3: Electrically actuated artificial cilia. (A) SEM image of artificial cilia arrays. (B) Optical image of artificial cilia integrated with control circuit.

Our second project is to use the micro-actuator and origami principle to design robotic neural probes. The ability to actuate the non-toxic materials in the brain paves the way for neural sensing probes that do not require an invasive borehole the size of the area to be sensed, through the cranium and pia-mater. Although the platinum-based micro-actuator we developed previously works perfectly in PBS solution, the fact that the oxidization reaction that drives the actuation of platinum is not scalable with the thickness of the platinum, meaning only the same amount of strain energy can be held in a platinum beam regardless of the thickness (implying a smaller curvature). This limitation presents a challenge with the group's current actuation design if used for neural probes. Since the brain, or brain-like gel, requires much more force to move through compared to the aqueous solution currently used by the group, an actuator needs to store enough energy to effectively displace a gel, while still being able to actuate over a wide range of angles. For this reason, we explored bulk electrochemical micro-actuators that utilize hydrogen adsorption/desorption effect to generate the strain in the thin film. In this system, hydrogen diffuses into the bulk of actuator, creating a bulk stress in the composite that scales with the thickness of the actuator. This new type of micro-actuator has much larger output force than the preview platinum micro-actuator while keeping the bending radius as small as the platinum counterpart.

Last, our team designed microfluidic devices that comprise arrays of such micro-actuators [3]. Microfluidic patterns are crucial in aspects from regulating cerebrospinal fluid in brain, guiding chemical reactions to manipulating particles. The traditional microfluidic devices use micro-channels and external pumps to guide the flow motion. The flow direction is determined by the micro-valves and cannot be changed once fabricated. Here, a new type of integrated microfluidic manipulation system which is built on the electrically actuated artificial cilia is proposed to achieve reprogrammable flow motions. The electrical chemical platinum actuator which has low voltage, low power and fast response time is used to fabricate the artificial cilia. The artificial cilia are compatible with CMOS fabrication and packaging technology and can be easily manipulated by computer software and micro-processor through tethered or untethered control. It gives a new platform to make powerful microfluidic devices and study the programmable motion of micro robotics.

References:

[1] Liu, Q., Wang, W., Reynolds, M.F., Cao, M.C., Miskin, M.Z., Arias, T.A., Muller, D.A., McEuen, P.L. and Cohen, I., 2021. Micrometer-sized electrically programmable shape-memory actuators for low-power microrobotics. Science Robotics, 6(52), 2020.

[2] Liu, Q., Wang, W., Sinhmar, H., Cortese, A., Griniasty, I., Reynolds, M., Taghavi, M., Apsel, A., Kress-Gazit, H., McEuen, P. and Cohen, I., Electrically Programmable Micro-scale Morphing Robots Based on Mechanical Metamaterials. Bulletin of the APS 2021.

[3] Wang, W., Liu, Q., Reynolds, M., Miskin, M., McEuen, P. and Cohen, I., 2021. Electrically actuated artificial cilia for microfluidic applications. Bulletin of the American Physical Society, 2021.

Nanoscale Hot-Wire Anemometer Probe with Contoured Silicon Probe Body

CNF Project Number: 2532-17

Principal Investigator(s): Gregory P. Bewley

User(s): Edmund T. Liu

Affiliation(s): The Sibley School of Mechanical and Aerospace Engineering, Cornell University

Primary Source(s) of Research Funding: The Sibley School of Mechanical and Aerospace Engineering, Cornell University

Contact(s): GPB1@cornell.edu, ETL46@cornell.edu

Primary CNF Tools Used: Heidelberg mask writer - DWL2000, SÜSS MA-6, Oxford PECVD, CVC SC4500 odd-hour evaporator, Oxford 82, Plasma-Therm Versaline deep silicon etcher, Unaxis 770 deep silicon etcher

Abstract:

Turbulence measurements are difficult to take due to the large separation of scales present in a flow. At the smallest scales, where conventional probes are limited by spatial and temporal resolution, measurements are a result of the physical dimensions and thermal mass of the sensing element. Semiconductor fabrication equipment enables the manufacturing of hot-wires much smaller than their conventional counterparts in volume, driving down costs while increasing measurement sensitivity. We report on the successful creation of such a probe with a sensing element measuring 60 × 2 × 0.1 μm supported by a contoured silicon body. The probe is compared to a conventional probe 1.27 μm in diameter in jet turbulence generated by a calibration tank and exhibits higher temporal resolution. The high-throughput process is found to have a yield rate > 95%.

Summary of Research:

Hot-wire anemometry is a method to measure flow velocities and is commonly used for turbulent flows due to high frequency response, spatial resolution, and ease of use. Hot-wires operate by heating up a small wire with electrical current. Placed in a flow, generated heat is convected from the wire to the fluid, with higher flow velocities corresponding to greater amounts of heat convection. By exploiting the wire material's temperature-dependent resistance, the measured voltage across the wire is correlated to the flow velocity.

Sensor performance is significantly impacted by the physical dimensions and material of the wire. Smaller wires exhibit high frequency response due to a small thermal mass, and shorter lengths lead to less spatial filtering. Moreover, a large length-to-diameter ratio is desired to mitigate the effects of end-conduction, where generated heat is conducted to the wire supports, rather than convected to the flow of interest. The smallest conventional wires available measure 0.6 to 1.27 μm in diameter and require labor-intensive soldering and chemical etching, thereby limiting probe throughput. Semiconductor manufacturing equipment is promising because it allows for the fabrication of sensing elements unachievable by conventional means at high-throughput and repeatability. On a single 4-inch wafer, hundreds of such probes may be created.

Initial work on hot-wire probes manufactured with semiconductor processing equipment was performed at Princeton University, resulting in the development of the nanoscale thermal anemometry probe (NSTAP) [1]. Unlike the sharp features used in the NSTAP, we designed a contoured metal film and probe body using AutoCAD and MATLAB. Original NSTAP processes relied on deep reactive-ion etching (RIE) and exploited RIE-lag to produce a 3D aerodynamic probe body. A similar process is used to create in-house probes.

First, 500 nm and 4 μm of silane-based silicon dioxide is formed through plasma-enhanced chemical vapor deposition (PECVD) on either side of a double-side polished wafer with the Oxford PECVD. 100 nm of platinum with a 10 nm titanium adhesion layer is then evaporated onto the 500 nm oxide and lifted off with a LOR bi-layer exposed with the SÜSS MA-6 contact aligner. On the backside, a fine pattern consisting of trenches used to induce RIE-lag is transferred from a SPR220-3.0 photoresist softmask to the 4 μm oxide to form a hardmask. Softmask exposure is performed with the MA-6 in vacuum contact mode, and the hardmask is etched with the Oxford PlasmaLab 82. Through-wafer etching is then performed with both the Plasma-Therm VersaLine and the Unaxis 770 deep silicon etchers, and the profile is smoothed with isotropic silicon etching. Finally, the remaining 500 nm oxide layer is etched to release the probes and free-standing platinum wire.

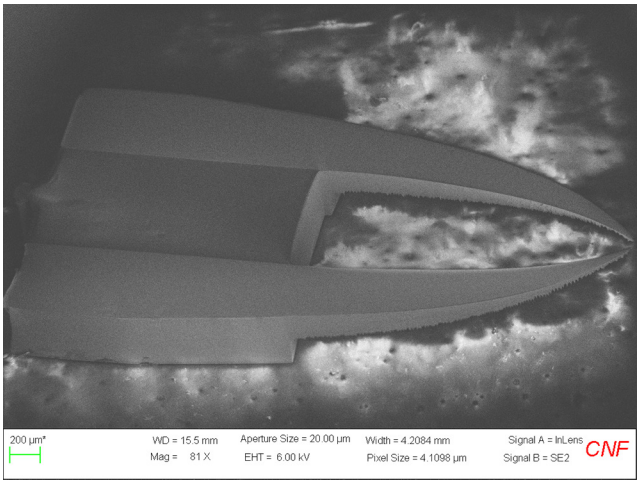

Figure 1: Probe following release from the wafer. The platinum trace and supporting silicon body are contoured, and the three-dimensional taper, a result of RIE-lag, is visible.

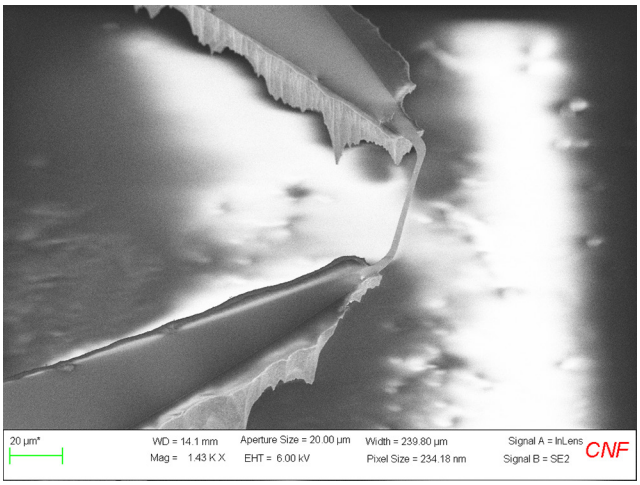

Figure 2: Magnified SEM image of the thin free-standing platinum wire.

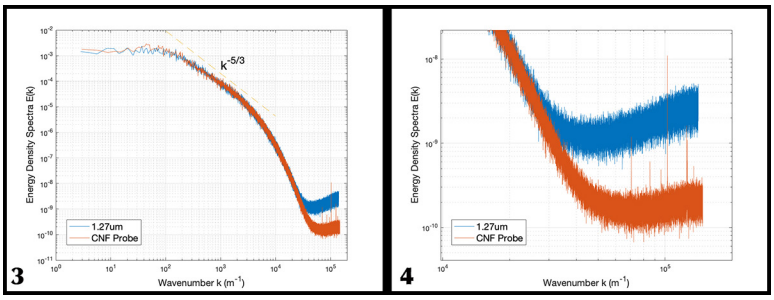

Figure 3, left: Comparison of turbulent spectra from a jet measured with a CNF probe and conventional 1.27 µm hot-wire. We observe a high degree of agreement in the collected spectra. Figure 4, right: Magnified image of the high-frequency spectra. Compared to the conventional hot-wire, the CNF probe is able to resolve more of the dissipation range. The spectra appear to flatten at higher frequencies, most likely due to the noise floor of external electronics.

Figures 1 and 2 show the final probe following release from the wafer and a magnified image of the free-standing wire, respectively. The tapered profile created using RIE-lag is visible and extends downstream from the wire, where there is minimal supporting silicon. The probe is verified using jet turbulence produced by a calibration tank. Placed about twelve opening diameters away from the jet outlet, the probe successfully measures a turbulent spectra, with high agreement with a conventional 1.27 μm hot-wire as shown in Figure 3.

Looking more closely at the high-frequency components of the spectra, we see that the microfabricated probe resolves even more of the dissipation range.

References:

[1] Vallikivi M. and Smits A.J., "Fabrication and Characterization of a Novel Nanoscale Thermal Anemometry Probe," Journal of Microelectromechanical Systems, vol. 23, no. 4, pp. 899-907, Aug. 2014, doi: 10.1109/JMEMS.2014.2299276.

Hot-Wire Anemometer Probe with SU-8 Support Structure

CNF Project Number: 2532-17

Principal Investigator(s): Gregory P. Bewley

User(s): Edmund T. Liu

Affiliation(s): The Sibley School of Mechanical and Aerospace Engineering, Cornell University

Primary Source(s) of Research Funding: The Sibley School of Mechanical and Aerospace Engineering, Cornell University

Contact(s): gpb1@cornell.edu, etl46@cornell.edu

Primary CNF Tools Used: Heidelberg mask writer - DWL2000, SÜSS MA-6, Oxford PECVD, CVC SC4500 odd-hour evaporator, SU-8 hot plates

Abstract:

Nanoscale hot-wire anemometer probe fabrication processes have focused largely on the micromachining of silicon substrates to form support structures, an etch-heavy procedure. We detail the development of a hot-wire probe constructed through additive means with SU-8. An additive approach to manufacturing holds a number of advantages over silicon etching, including the ability to precisely define the probe structure with photolithography and control the final thickness of the supports.

Summary of Research:

Significant benefits in the sensing capabilities of hot-wire anemometer probes, including improved temporal and spatial resolutions, may be achieved by shrinking physical wire dimensions. Semiconductor manufacturing tools are well-suited to this task, allowing for the fabrication of wires measuring only tens of microns in length, microns in width, and hundreds of nanometers thick, previously unachievable or impractical with conventional means. Existing hot-wire probes created through such means rely on silicon etching to produce the probe support structures, utilizing deep reaction-ion etching (RIE) and RIE-lag effects to produce a 3D aerodynamic structure.

Etched silicon structures are the result of subtractive processes, where the substrate is meticulously sculpted and forms an integral component of the final sensor. Associated processes are proven and have resulted in successful probe fabrication at high yield and throughput. However, it is found that the final probe outline after etching seldom resembles the original mask design, and the process requires multiple design iterations to achieve a desired shape. Moreover, due to the thin silicon supports near the wire and the lack of an etch stop, the process is sensitive to over-etching that may undercut and thus jeopardize the sensor.

To address these issues, additive processes are used instead. Rather than using the substrate as a support material, structures are built upon a silicon wafer and subsequently lifted off. By using SU-8, a negative photoresist with a wide range of possible thicknesses, the final probe shape may be precisely defined by light, avoiding an iterative design process. SU-8 also allows for control over the final thickness of the supports by using formulations with different viscosities and modifying spin parameters.

SU-8 probes are manufactured by first depositing a 500 nm silicon dioxide film on a single-side polished silicon wafer using plasma-enhanced chemical vapor deposition (PECVD). This film acts as a sacrificial layer on which the probes lie. 100 nm of platinum with a 10 nm titanium adhesion layer is then evaporated and lifted off with a LOR bi-layer. Two SU-8 layers of varying thickness are processed. First, a layer of SU-8 2035 is spun to about 16 μm and soft-baked according to datasheet guidelines. Only the arms and solder pads of the evaporated metal trace, excluding the wire, are exposed. Next, a second layer of SU-8 2035 is spun on the exposed first layer and soft-baked, reaching a thickness of about 100 μm. This layer serves to hold both arms of the probe in fixed positions. After exposure of the second layer, a post-exposure bake (PEB) is performed at 55°C overnight. The low PEB temperature is used to minimize residual stress in the final SU-8 structure [1].

Finally, the probes are lifted from the wafer by immersion in concentrated 49% HF, which etches the PECVD oxide underneath each probe. Following lift-off, the probes are rinsed in water and dried in air.

A probe lifted from the substrate is displayed in Figure 1. The relatively thin probe arms and the thicker support structure are visible, as is the platinum wire. A prominent feature of the probe is the peeling of the metal film. Due to residual stresses during processing, the SU-8 will tend to

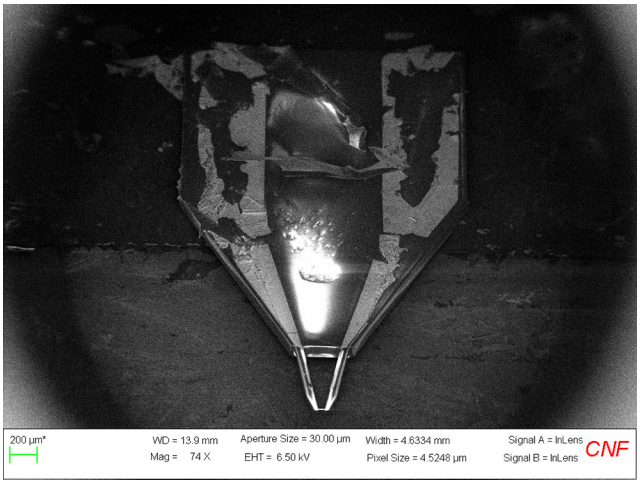

Figure 1: An SU-8 probe lifted from the substrate shows significant metal tearing, an effect of deflection of the SU-8 probe arms.

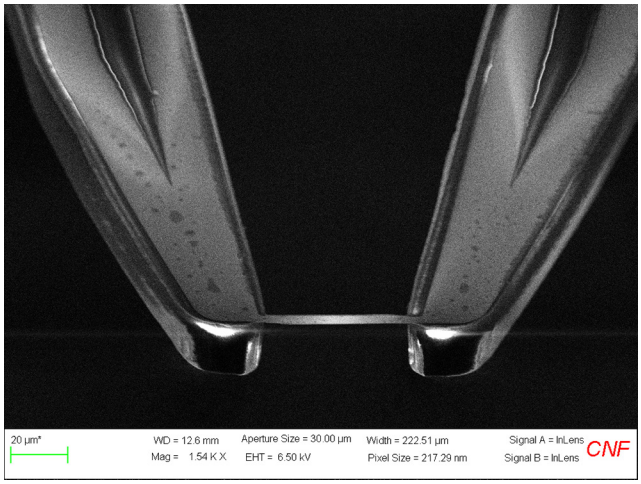

Figure 2: Magnified image of an SU-8 probe. The arm outline is precisely defined by photolithography and the thickness set by SU-8 processing parameters. Metal film peeling is visible along the center of the arms.

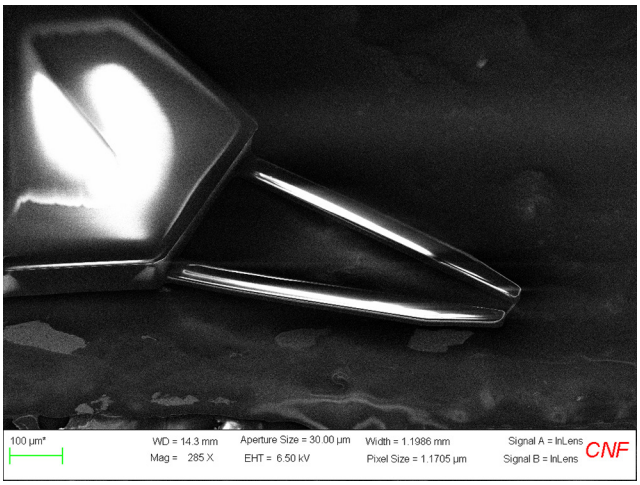

Figure 3: Backside of probe showing varying thickness of SU-8 layers.

deflect, pulling the metal film from the substrate and leading to tearing. This tearing is also visible along the probe arms in Figure 2. However, we see that the SU-8 arms are well-defined, with a controlled thickness. Figure 3 shows the underside of the probe, where the varying thickness of the SU-8 layers is clear.

Future work will focus on modifying the metal film stack and SU-8 processing to minimize stress and tearing.

References:

[1] Li B., Liu M. and Chen Q., "Low-stress ultra-thick SU-8 UV photolithography process for MEMS," J. Micro/Nanolith. MEMS MOEMS, vol. 4, no. 4, 043008, Oct. 2015, https://doi.org/10.1117/1.2117108.

Limit Cycle Oscillations in Silicon Structures Using Opto-Thermal Excitation

CNF Project Number: 2732-18

Principal Investigator(s): Prof. Alan Taylor Zehnder

User(s): Aditya Bhaskar

Affiliation(s): Sibley School of Mechanical and Aerospace Engineering, Cornell University

Primary Source(s) of Research Funding: National Science Foundation (NSF), United States, grant number CMMI-1634664

Contact(s): atz2@cornell.edu, ab2823@cornell.edu

Primary CNF Tools Used: Heidelberg mask writer - DWL2000, Hamatech hot piranha, DISCO dicing saw, GCA 6300 DSW 5x g-line wafer stepper, Unaxis 770 deep silicon etcher, Anatech plasma asher, Leica CPD300 critical point dryer, Zygo optical profilometer, Zeiss Supra SEM

Abstract:

Self-sustaining micro-oscillators may find applications in fields such as time-keeping and sensing, due to their high quality factors and frequency stability. This work involves the study of pairs of opto-thermally driven oscillators and their characteristics such as synchronization to each other and frequency entrainment to an external drive. The experimentally observed phenomena are complemented by theoretical and numerical studies.

Summary of Research:

Our work involves the study of the nonlinear characteristics of limit cycle oscillators (LCO's) and the emergence of synchronization in such systems. A limit cycle oscillator consists of a resonating element supplied by a constant energy source with a built-in positive feedback between the LCO's motion and the external energy source. Such active oscillations can be distinguished from a resonance response caused by an external periodic force applied to a passive resonating element [1].

We focus on single and pairs of clamped-clamped beam micro-resonators which were fabricated on a 0.75″ × 0.5″ silicon-on-insulator (SOI) chip with a 205 nm silicon device layer. The steps of general photolithography were followed with the exposure done on a GCA 5x g-line stepper.

After development, the silicon device layer was etched using the Bosch process. The devices were released using a buffered oxide etch (BOE) of the 400 nm silicon dioxide layer underneath followed by critical point drying. An image of the released devices taken using scanning electron microscopy (SEM) is shown Figure 1.

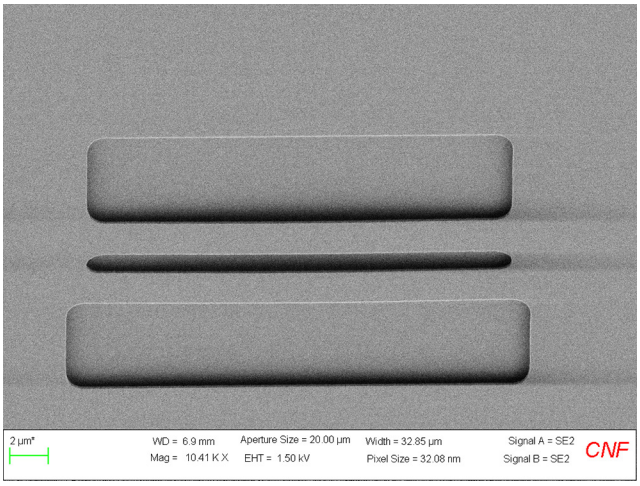

Figure 1: SEM image of clamped-clamped silicon beams fabricated from an SOI stack with 205 nm silicon device layer and 400 nm silicon dioxide.

The SOI chip with the micro-resonators is indium-bonded to a piezoelectric shaker housed in a vacuum chamber at a pressure of approximately 1e-7mBar. A continuous-wave laser beam with wavelength 633 nm is focused at the center of the microresonators, and part of the light is absorbed by the resonator, while part is transmitted and reflected back to it, thus setting up a Fabry-Perot interference cavity. The absorbed light causes the beam to undergo thermal expansion, which in turn modulates the amount of light absorbed. Thus, the microresonator undergoes self-sustaining limit cycle oscillation. The reflected laser beam modulated due to the oscillations is directed to a high-speed photodetector and its frequency content is recorded using a spectrum analyzer. The analyzer also serves a second purpose of providing the input signal to the piezoelectric shaker when an external inertial drive is required [2].

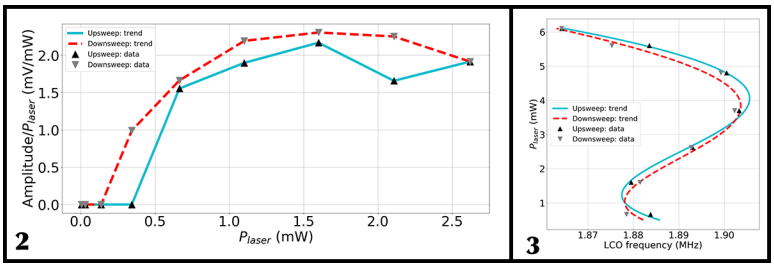

Figure 2, left: The birth of LCO in a Hopf bifurcation: variation of normalized signal amplitude with laser power upsweep and downsweep. Figure 3, right: Variation of the LCO frequency with laser power upsweep and downsweep.

From the resonance response it can be noted that the resonator exhibits spring softening, i.e. the frequency decreases with increasing amplitude of motion. The external drive amplitude is kept fixed and the frequency is swept up and down. The plateaus in the drive LCO curves correspond to entrainment regions. Hysteresis can again be noted in this experiment. It is expected that the frequency span for entrainment will become larger for higher drive amplitudes.

The appearance of a limit cycle response is shown in Figure 2. The laser is focused on a silicon beam 36 μm long and 2 μm wide and the laser power hitting the sample is swept up and then down. In the laser upsweep, we see that the LCO appears at around 0.3 mW of incident power and the signal amplitude normalized by the laser power is approximately constant. The transition to limit cycle is accompanied by a Hopf bifurcation [3], which is seen in numerical models for this system. The downsweep curve shows hysteretic behavior of the oscillator with laser power. For the same device, the frequency response of the LCO with laser power is shown in Figure 3. The response is non-monotonic with laser power. It is also noted that at low laser power the LCO's have greater frequency stability than at higher powers.

Frequency entrainment refers to the phenomenon of an external periodic driving force causing the frequency of the LCO to match that of the drive. The key parameters that determine entrainment of an LCO is the frequency detuning between the LCO and the external drive and the drive amplitude. Figure 4 shows the results of an entrainment experiment on a single LCO. The external drive is provided by the piezoelectric shaker and the swept frequency and amplitude are controlled by the spectrum analyzer [4]. The undriven LCO response and the resonance responses are plotted as a reference for the entrainment curves.

Conclusions and Future Steps:

Opto-thermally driven limit cycle oscillations are observed in the clamped-clamped silicon microresonators. They show other nonlinear behavior such as frequency entrainment to an external inertial drive. Further experiments will be conducted on pairs of beams coupled elastically via silicon bridges. Coupling between two frequency-detuned oscillators is expected to result in self-synchronization of the beams. Further parameter spaces such as coupling strength, frequency detuning between two LCO's, and the influence of the external drive will be explored.

References:

[1] Pikovsky, Arkady, et al. "Synchronization: a universal concept in nonlinear sciences." No. 12. Cambridge university press, 2003.

[2] Blocher, David. "Optically driven limit cycle oscillations in MEMS." (2012).

[3] Aubin, Keith, et al. "Limit cycle oscillations in CW laser-driven NEMS." Journal of microelectromechanical systems 13.6 (2004): 1018-1026.

[4] Blocher, David B., Alan T. Zehnder, and Richard H. Rand. "Entrainment of micromechanical limit cycle oscillators in the presence of frequency instability." Journal of Microelectromechanical Systems 22.4 (2013): 835-845.

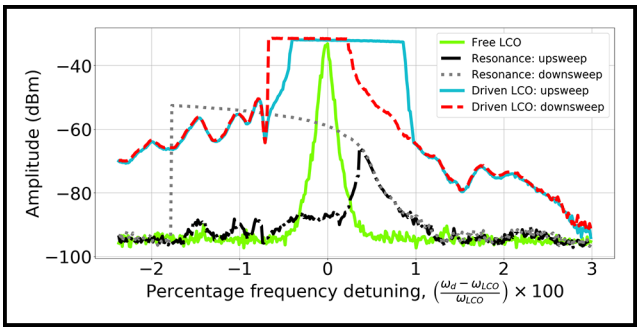

Figure 4: Frequency entrainment of an LCO by an external inertial drive on frequency upsweep and downsweep. The regions of entrainment correspond to the plateaus in the peak tracking signals. The free LCO response and resonance response on frequency upsweep and downsweep are also plotted for reference.

Ultra-Broadband Entangled Photons on a Nanophotonic Chip

CNF Project Number: 1997-11

Principal Investigator(s): Qiang Lin[1,2]

User(s): Usman A. Javid[1], Jingwei Ling[2], Mingxiao Li[2], Yang He[2]

Affiliation(s): 1. Institute of Optics, University of Rochester, Rochester NY;
2. Department of Electrical and Computer Engineering, University of Rochester, Rochester NY.

Primary Source(s) of Research Funding: National Science Foundation (Grants No. EFMA-1641099, ECCS-1810169, and ECCS-1842691); Defense Threat Reduction Agency, Joint Science and Technology Office for Chemical and Biological Defense Grant No. HDTRA11810047; Defense Advanced Research Projects Agency (DARPA) Agreement No. HR00112090012

Contact(s): qiang.lin@rochester.edu, usman.javid@rochester.edu, jling8@ur.rochester.edu, mli53@ur.rochester.edu, yhe26@ur.rochester.edu

Primary CNF Tools Used: JEOL 9500, AJA ion mill, CVC SC4500 odd-hour evaporator

Abstract:

Integrated photonic devices have shown great promise in scalable implementation of quantum technologies for applications in information processing, communication, computing, metrology, and sensing. Particularly, for applications in metrology and sensing, a broadband source of quantum entanglement is desired. To that end, we demonstrate an integrated source of entangled photon pairs with record-high bandwidth and efficiency not seen on chip-scale platforms before. This source is fabricated on thin-film lithium niobate-on insulator wafer at the Cornell NanoScale Facility.

Summary of Research:

One of the most widely used methods to generate quantum entanglement in light is by using a nonlinear optical process called spontaneous parametric down conversion (SPDC). In this process, a laser photon spontaneously breaks into two daughter photons inside a nonlinear optical material, which are entangled in time and energy [1]. The efficiency of this process and its bandwidth is determined by the dispersion of the material used in the interaction. Efforts to generate this entanglement over a broad spectral region is primarily confined to bulk materials where the control over material dispersion is severely limited. Due to this, the only feasible method of increasing the bandwidth is to create inhomogeneity in the medium [2,3]. This severely reduces the generated spectral brightness of the photons creating a tradeoff between brightness and bandwidth of the source [2,4]. Nanophotonics, on the other hand, does not have any such limitation since the wavelength-scale geometry of thin-film devices can be exploited for precise control of the refractive index. Here, we are reporting on fabrication of a nanophotonic waveguide on thin-film lithium niobate-on-insulator wafer (LNOI), which has been engineered to produce an entanglement bandwidth exceeding 100 terahertz (THz).

The waveguide is designed for 600 nm thick lithium niobate film with X-cut orientation of the crystal axis. In order to produce a broad parametric down-conversion spectrum, the dimensions of the waveguide are engineered to have zero group velocity dispersion (as shown in Figure 1) at an optical wavelength of 1550 nm, which will form the center of the generated spectrum. The resulting waveguide has a width of 1.5 μm and an etch depth of 300 nm. The waveguide is subsequently patterned on the wafer using electron-beam lithography on the JEOL 9500 using ZEP520A as the resist mask for the waveguide.

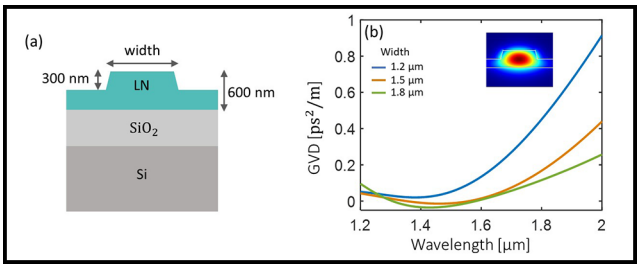

Figure 1: (a) Geometry of the lithium niobate waveguide on a 600 nm LNOI wafer. (b) Group velocity dispersion (GVD) of the waveguide at different widths with the inset showing the fundamental quasi-TE mode of the waveguide at a 1550 nm wavelength.

After development, the waveguide is etched using argon ion milling on the AJA ion mill achieving a 50% (300 nm) etching depth. The resist is then stripped using standard resist remover chemistry and the chip is prepared for a second electron-beam exposure. This is to pattern electrodes on both

sides of the waveguide so that the material can be poled by applying high voltage electrical pulses that permanently alter the material's optic axis. This is done to bridge the refractive index gap between the pump laser photons, which are at a wavelength of 775 nm to the generated photon pairs which are centered at 1550 nm. The material is coated with PMMA resist and exposed again with electron-beam lithography to pattern the electrodes. After development, the chip is deposited with a 400 nm layer of gold using an evaporator (CVC SC4500). The electrode pattern is subsequently created by a resist liftoff process.

Figure 2 shows scanning electron microscope images of a fabricated device.

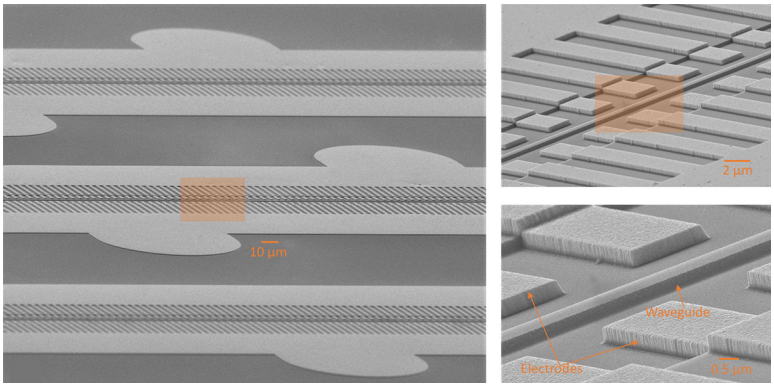

Figure 2: SEM images of a fabricated device at different magnifications.

After fabrication, the waveguide is pumped by a laser with a tunable wavelength. The laser wavelength is scanned, and the generated photon pairs are detected using superconducting single-photon detectors. At 770.4 nm, we observe a parametric down-conversion spectrum spanning from the central wavelength of 1540.8 nm all the way to 1100 nm as shown in Figure 3(a), giving a half spectral-width at half maximum of 50 THz (300 nm).

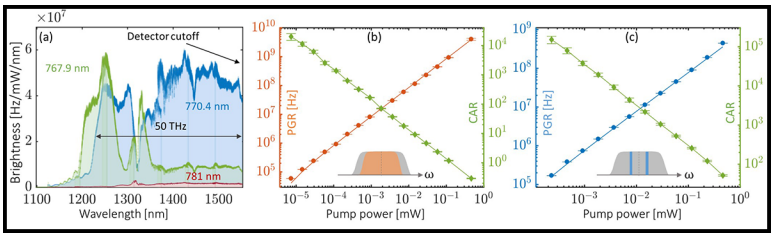

Figure 3: (a) Measured spectrum of the generated photon pairs at different pump wavelength with the blue curve plotting the highest (100 THz) bandwidth. The pair generation rate (PGR) and coincidence-to-accidental ratio (CAR) are plotted for the full spectrum in (b) and a 20 nm filtered section in (c).

The full spectrum is then expected to span up to 2000 nm, given the symmetry of the interaction, giving a total bandwidth of 100 THz. This is more than an order of magnitude larger than a typical chip-scale SPDC source. The device also shows a high efficiency of 13 GHz/mW of pump power, owing to such a large bandwidth and strong confinement of light as expected of a wavelength-scale device.

Another important metric of an entangled photon source is its signal-to-noise ratio, also known as coincidence-to-accidental ratio (CAR), which determines its performance in communication and computing applications. Figure 3(c) plots this measurement for a 20 nm filtered section of the spectrum. This is done to counter dispersive effects in the experimental setup to get the true noise characteristics. We observe a highest CAR of 152,000 the highest achieved for any chip-scale photon-pair source to date [5,6], indicating excellent noise performance, even at high pair generation rates. Additional measurements to verify quantum entanglement in the generated light are also done (not shown here) to verify our claims.

Conclusions:

To conclude, we have designed and fabricated an efficient waveguide source of ultra-broadband entangled photons. The large bandwidth of entanglement produced from this device along with its record efficiency and noise performance make such nanophotonic sources ideal for applications in quantum communication and computing.

Furthermore, we envision that this demonstration will motivate experiments in chip-scale metrology and spectroscopy with non-classical light.

References:

[1] Reports on Progress in Physics 66.6 (2003): 1009.

[2] Physical review letters 100.18 (2008): 183601.

[3] Optics express 20.23 (2012): 25228-25238.

[4] European Quantum Electronics Conference. Optical Society of America, 2019.

[5] Physical review letters 124.16 (2020): 163603.

[6] Optics Express 25.26 (2017): 32995-33006.

Narrow Linewidth, Widely Tunable Integrated Lasers from Visible to Near-IR

CNF Project Number: 2364-15

Principal Investigator(s): Michal Lipson

User(s): Xingchen Ji, Mateus Corato-Zanarella

Affiliation(s): Department of Electrical Engineering, Columbia University, New York City, NY 10027

Primary Source(s) of Research Funding: Defense Advanced Research Projects Agency

Contact(s): ml3745@columbia.edu, xj53@cornell.edu

Primary CNF Tools Used: PECVD, e-beam lithography, Oxford 100 etcher, AJA sputter deposition, mask writer, furnace, Oxford 82 etcher

Abstract:

We demonstrate a chip-scale platform for narrow-linewidth lasers, tunable across the whole spectrum from blue to near-IR. We show powers up to 10 mW, intrinsic linewidth less than 8 kHz, tuning up to 12 nm and high side-mode suppression ratio up to 38 dB.

Summary of Research:

Integrated photonics platforms for light sources in the visible range are promising for applications including trapping, quantum photonics [1], biosensors [2], and spectroscopy. To date, narrow linewidth, tunable visible sources either rely on bulky external free-space cavities and components [3] or are limited to the long wavelength portion of the spectrum (red) and have large footprint [4].

Here, we demonstrate a chip-scale laser platform designed for lasing with narrow linewidth and tunability over a large spectral range covering the whole visible spectrum up to near-IR. We design the platform to be based on high confinement, high quality factor (Q) silicon nitride (Si_3N_4) resonators and commercially available Fabry-Perot (FP) laser diodes. We leverage the large transparency window of Si_3N_4 for high confinement low-loss light propagation at visible wavelengths and commercial FP laser diodes for robust self-injection locking [5]. We show that by coupling laser diodes to a low-loss ring resonator with an optical feedback path, self-injection locking causes the collapse of the multiple longitudinal modes of the diode into a single longitudinal mode, with further linewidth reduction induced by the high Q of the resonator. We achieve lasing at different wavelengths by tuning the resonator's resonance to align to different longitudinal modes of the laser.

We design our photonic components to operate over the whole visible to near-IR spectral range using a platform of 175 nm-thick Si_3N_4 waveguide core surrounded by silicon oxide (Figure 1a). We design a ring resonator with tapered dimensions from 300 nm to 1500 nm to ensure near-single mode operation and good coupling for all the wavelengths while maintaining high Q (Figure 1b) [6]. We leverage the high confinement to design the ring with small radius (10 μm). The resulting large free-spectral range (FSR) of several nm across the whole visible range allows the feedback of a specific wavelength within the gain bandwidth of the laser diodes without the need for a Vernier filter [4]. Such a frequency-selective feedback over a large range eliminates mode-hopping between longitudinal modes of the laser diodes when they are self-injection locked by our resonator. The feedback wavelength can be continuously tuned within the FSR by tuning the resonator. We optimize the feedback loop at the drop port for broad bandwidth, leveraging that the self-injection locking of FP laser diodes is robust to the amount of reflection [5]. We design inverse taper edge couplers to provide good laser-to-chip and chip-to-fiber coupling without inducing spurious reflections.

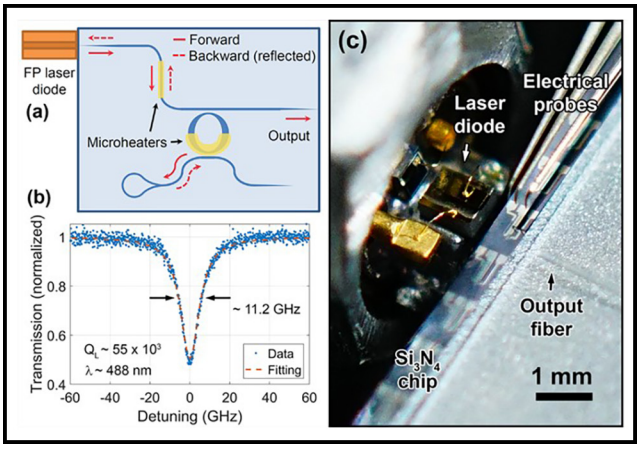

Figure 1: (a) Schematic of the integrated laser. An FP laser diode is butt-coupled to the chip, where a ring resonator with a feedback loop at the drop port acts as a wavelength selective reflector. (b) Ring resonance in blue measured with a Toptica DL Pro 488 nm laser. The loaded quality factor is ~ 5.5 × 10^4 and the extinction is ~ 50%. (c) Image of the laser setup.

We achieve broadband, narrow linewidth, tunable lasing by butt-coupling commercial FP laser diodes to our chip and

controlling the position of the ring resonator's resonance using thermo-optic phase shifters (Figure 1c). We tune the lasing wavelength by tuning the resonator to different longitudinal modes of the laser diodes. When the resonator is detuned from the modes of the laser, the power dropped to the feedback loop is negligible and the laser diode lases with multiple longitudinal modes (Figure 2a). When we align the resonator to a mode of the laser, power is dropped to the feedback loop and then reflected back to the diode. We adjust the phase of the reflected light to cause the self-injection locking by using the phase-shifter on the bus waveguide in between the diode and the resonator. When the laser is locked, the longitudinal modes of the laser diode collapse into a single one (Figure 2b).

We show narrow linewidth, tunable integrated lasers covering blue (~492 nm), green (~522 nm), red (~660 nm) and near-IR (~785 nm) wavelengths with output fiber-coupled powers up to 10 mW, intrinsic linewidth < 8 kHz, wavelength tuning up to 12 nm and side-mode suppression ratios (SMSR) up to ~38 dB. We achieve coarse tuning ranges/SMSRs of ~3.21 nm/~30 dB in blue, ~3.2 nm/~30 dB in green, ~3.7 nm/~37 dB in red, and ~12 nm/~38 dB in near-IR (Figure 3).

We measure the intrinsic linewidths at the two extremes of the spectrum, blue and near-IR, and obtain (8 ± 2) kHz and (601 ± 227) Hz respectively, both limited by our instruments. We determine the linewidth in blue by measuring the RF beat note between our integrated laser and a commercial narrow-linewidth laser using a spectrum analyzer. The beat note represents the lineshape of our integrated laser, limited by the lineshape of the commercial laser. By fitting the beat note with a Voigt profile, we extract the Lorentzian contribution, which corresponds to the white noise that defines the intrinsic linewidth, and the Gaussian contribution, which corresponds to the flicker and technical noises that broaden the effective linewidth. The Voigt fitting of the lineshape (see Figure 4a) gives an intrinsic (Lorentzian) linewidth of (8 ± 2) kilohertz and a Gaussian linewidth of (250 ± 20) kilohertz. We measured the lineshape and frequency noise of our integrated near-IR laser with a linewidth analyzer. The Voigt fittings of the lineshapes (see Figure 4b) for different measurements give an intrinsic linewidth of (601 ± 227) hertz, limited by the linewidth analyzer sensitivity.

Our results show that chip-scale visible lasers can exhibit key specifications such as linewidth, tuning range, power, and SMSR comparable to bulky commercial laser systems. We envision our platform to be a key enabler for fully integrated visible light systems in applications including quantum photonics, trapping, AR/VR, biosensing, atomic clocks, and spectroscopy.

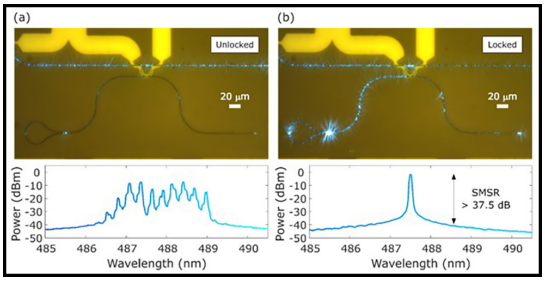

Figure 2: Microscope images of the ring resonator-based feedback loop and optical spectra of the chip output before and after self-injection locking. (a) Ring resonance is detuned from the Fabry-Perot (FP) laser diode modes, so no light is in the feedback loop (top). The chip output resembles the usual output of the FP laser with multiple lasing modes. (b) Ring resonance is tuned to one of the FP modes, so the feedback loop reflects part of the light back to the diode. Self-injection locking causes all the longitudinal modes to collapse into a single frequency, narrow linewidth lasing mode with high (> 37.5 dB) side mode suppression ratio (SMSR). The optical spectra are measured with an optical spectrum analyzer (Ando AQ6314A).

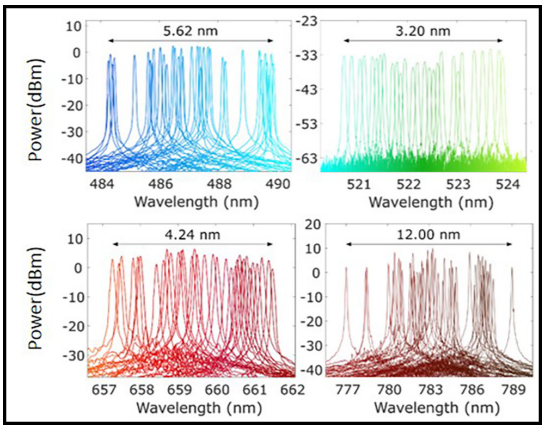

Figure 3: Coarse tuning ranges at blue, green, red and near-IR. The optical spectra are measured with an optical spectrum analyzer (Ando AQ6314A) and overlaid to show the tuning.

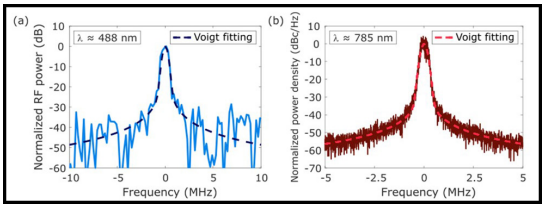

Figure 4: Linewidth characteristics of the blue and near-IR integrated lasers. RF beat note between our integrated blue laser and a commercial narrow-linewidth blue laser (Toptica DL Pro 488 nm). The beat note represents the lineshape of our integrated laser, limited by the lineshape of the commercial laser. By fitting the beat note with a Voigt profile, we extract the Lorentzian contribution, which corresponds to the white noise that defines the intrinsic linewidth, and the Gaussian contribution, which corresponds to the flicker and technical noises that broaden the effective linewidth. The Voigt fitting results in an intrinsic (Lorentzian) 8±2 kHz linewidth and Gaussian linewidth of 250±20 kHz.

References:

[1] R. J. Niffenegger, et al., "Integrated multi-wavelength control of an ion qubit," Nature, vol. 586, no. 7830, Art. no. 7830, Oct. 2020, doi: 10.1038/s41586-020-2811-x.

[2] A. Mohanty, et al., "Reconfigurable nanophotonic Si probes for sub-millisecond deep-brain optical stimulation," NatBiomedEng, V4, #2, Art. #2, 2/20, doi: 10.1038/s41551-020-0516-y.

[3] P. S. Donvalkar, et al., "Self-injection locked blue laser," J. Opt., vol. 20, no. 4, p. 045801, Feb. 2018, doi: 10.1088/2040-8986/aaae4f.

[4] C. A. A. Franken, et al., "A hybrid-integrated diode laser for the visible spectral range," ArXiv201204563 Phys., Dec. 2020, Accessed: Apr. 07, 2021. Available: http://arxiv.org/abs/2012.04563.

[5] A. Gil-Molina, et al., "Robust Hybrid III-V/Si_3N_4 Laser with kHz-Linewidth and GHz-Pulling Range," in Conference on Lasers and Electro-Optics (2020), paper STu3M.4, May 2020, p. STu3M.4, doi: 10.1364/CLEO_SI.2020.STu3M.4.

[6] M. Corato-Zanarella, et al., "Overcoming the Trade-Off Between Loss and Dispersion in Microresonators," in Conference on Lasers and Electro-Optics (2020), paper STh1J.1, May 2020, p. STh1J.1, doi: 10.1364/CLEO_SI.2020.STh1J.1.

Development of Single and Double Layer Anti-Reflective Coatings for Astronomical Instruments

CNF Project Number: 2458-16

Principal Investigator(s): Gordon Stacey[1]

User(s): Bugao Zou[2], Nicholas Cothard[2]

Affiliation(s): 1. Department of Astronomy (Stacey), 2. Department of Applied and Engineering Physics; Cornell University

Primary Source(s) of Research Funding: NASA Grant NNX16AC72G

Contact(s): stacey@cornell.edu, bz332@cornell.edu, nc467@cornell.edu

Primary CNF Tools Used: Oxford PECVD, Anatech resist strip, Oxford 81/82 etcher, Oxford 100 etcher, manual resist spinners, resist hot strip bath, Plasma-Therm deep silicon etcher, ASML 300C DUV stepper

Abstract:

We have been developing silicon-substrate based mirrors for Fabry-Perot Interferometers (FPI) for astronomical instruments in the mid-infrared to sub-mm/mm wavelength regime. The mirrors are patterned with double-layer metamaterial anti-reflection coatings (ARC) on one side and metal mesh reflectors on the other side. The double-layer ARC ensures a reflectance of less than 1% at the surface substrate over the FPI bandwidth.

Summary of Research:

The goal of the project is to develop microfabricated, silicon-substrate based mirrors for use in cryogenic Fabry-Perot Interferometers for astronomical instruments in the mid-infrared to sub-mm/mm wavelength regimes. The mirrors consist of high-purity, float-zone, 500-μm-thick silicon wafers that are lithographically patterned with frequency-selective, gold mesh reflectors. We use a combination of inductive and capacitive meshes to maintain uniform high reflectance and hence nearly uniform resolving power over the FPI bandwidth. Due to the high index of refraction of silicon, the other side of the mirror must be patterned with an ARC to achieve broadband capability and to mitigate contaminating resonances from the silicon surface [1,2].

The bulk of our work this year has been the development of the fabrication methods of the ARC. Figure 1 shows our current recipe for a two-layer ARC.

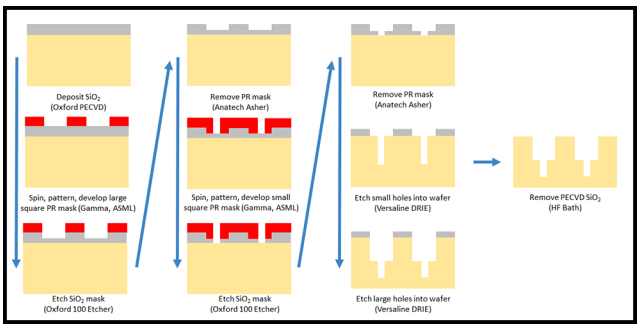

Figure 1: Process flow for fabricating a double-layer ARC on Si wafer.

A scanning electron microscope (SEM) image of the cross section of the ARC is shown in Figure 2. We are currently working to improve our control of this method. In addition, our fabrication process for metal mesh reflectors has been improved over this past year. We have successfully deposited 10-micron scale capacitive and inductive gold meshes on samples using AZ nLOF 2020 photoresist and the CHA evaporator. The lift-off procedure is done using heated Microposit 1165 Remover.

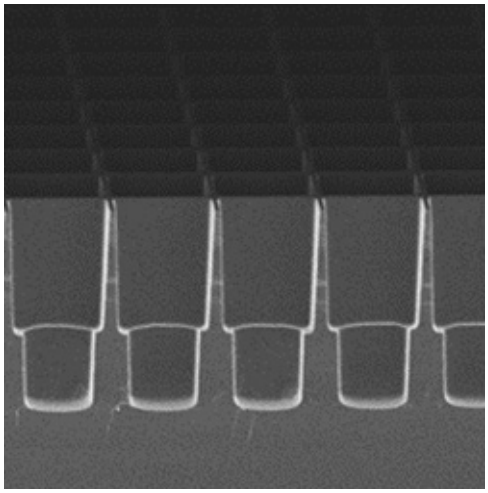

Figure 2: CNF Zeiss Ultra SEM image showing the two-layer structure of anti-reflection coatings.

We have fabricated both ARC and metal mesh reflectors on several optical quality silicon wafers and are now measuring their frequency dependent transmittances in the mid-infrared to sub-mm/mm wavelength regimes using Fourier transform spectrometers. Our progress on these devices is discussed in a paper published in Journal of Low Temperature Physics, which illustrates the design of the CCAT-prime Epoch of Reionization Spectrometer instrument and how the microfabricated FPI fits in the module and enables spectroscopic observations of the early universe [1].

The silicon-substrate based mirrors that are developed in CNF will be used in the upcoming scanning FPI instrument Prime-Cam in the CCAT-prime observatory, which is located at 5600 meters elevation on Cerro Chajnantor in the Atacama Desert in Chile [3]. CCAT-prime will use our FPI for one of its main science goals, that is to study the Epoch of Reionization of the universe via [CII] intensity mapping in the 750-1500 μm regime. Our instrument will enable the intensity mapping observations by providing high-sensitivity, wide-field, broadband spectroscopy. These measurements will tell us about how the first stars and galaxies evolved in the early universe.

Conclusions and Future Steps:

In the past year we have made great steps towards achieving our goals at CNF. We have demonstrated our ability to fabricate double-layer ARCs for different wavelengths and metal meshes with different feature sizes. We have used many of the fabrication and metrology tools at CNF. Our next steps are to better characterize our etched geometries and improve our metamaterial ARCs. We will be using Fourier transform spectrometers to measure our sample's optical performance and using the results to iterate on our fabrication design.

References:

[1] Cothard, N.F., Choi, S.K., Duell, C.J., et al. The Design of the CCAT-prime Epoch of Reionization Spectrometer Instrument. J Low Temp Phys (2020). https://doi.org/10.1007/s10909-019-02297-1.

[2] N.F. Cothard, M. Abe, T. Nikola, G.J. Stacey, G. Cortes-Medellin, P.A. Gallardo, B.J. Koopman, M.D. Niemack, S.C. Parshley, E.M. Vavagiakis, and K. Vetter, "Optimizing the efficiency of Fabry-Perot interferometers with silicon-substrate mirrors," Adv. in Optical and Mechanical Tech. for Telescopes and Instrumentation III (2018).

[3] http://www.ccatobservatory.org/

Electrically Actuated Zoom-Lens Based on a Liquid-Crystal-Embedded Semiconductor Metasurface

CNF Project Number: 2472-16

Principal Investigator(s): Gennady Shvets

User(s): Melissa Bosch, Maxim Shcherbakov

Affiliation(s): School of Applied and Engineering Physics, Department of Physics; Cornell University

Primary Source(s) of Research Funding: Office of Naval Research (ONR), National Science Foundation (NSF)

Contact(s): gs656@cornell.edu, mb2583@cornell.edu, mrs356@cornell.edu

Website: http://shvets.aep.cornell.edu

Primary CNF Tools Used: JEOL 9500, Zeiss Ultra SEM, Oxford Cobra ICP etcher, Oxford PECVD

Abstract:

Planar metamaterials, or metasurfaces, offer an ultrathin and adaptable platform for modulating spatial and spectral properties of light. We engineer semiconductor-based metasurfaces which exhibit tunable optical resonances for photonic applications in near-infrared. We report on the design, fabrication, and characterization of resonant amorphous silicon (a-Si) metasurfaces that act as a voltage-tunable dynamic-focus lenses likely to find uses in augmented reality and other imaging technologies.

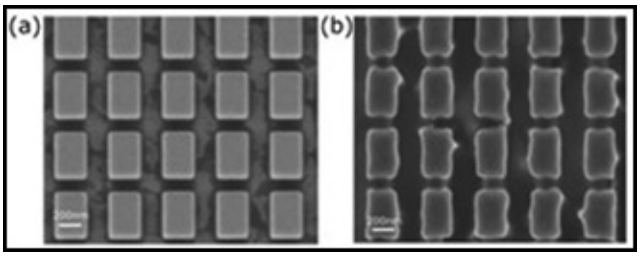

Figure 1: (a) A scanning electron microscope image of a typical a-Si-based resonant metasurface on an ITO-coated SiO_2 substrate. (b) Same as (a), but before improving the fabrication process.

Summary of Research:

Fabrication of a-Si Metasurfaces. Metasurfaces present a compact and scalable alternative to conventional free-space optical elements. Dielectric and semiconductor metasurfaces, such as those consisting of germanium or silicon, can generate near-arbitrary spatial phase profiles with low absorptive losses, leading to high-performance waveplates, beam deflectors, and lenses with subwavelength-thickness [1]. Our project focuses on the design and fabrication of resonant amorphous silicon (a-Si) metasurfaces with sub-100 nm feature sizes and high (up to 1:6) aspect ratios, useful for numerous applications where compact and efficient light modulators are sought. Figure 1a shows a representative a-Si metasurface, consisting of an array of rectangular a-Si prisms patterned on a fused silica substrate. Such regular semiconductor nanoarrays support localized electric and magnetic Mie-type resonant optical modes, which may be spectrally-tuned by modifying the permittivity of the media (e.g., liquid crystals: LC) adjacent to the array. The metasurface fabrication consisted of six steps: plasma-enhanced chemical vapor deposition (Oxford PECVD) of a-Si onto an ITO-coated fused silica substrate and surface treatment with SurPass 3000 adhesion promoter; standard HSQ 6% spin-coat, baking, and e-beam exposure at 6 mC/cm^2 (JEOL 9500FS); development in TMAH/NaCl (0.25/0.7N) salty solution; and pattern transfer to the a-Si layer through an inductively coupled HBr plasma reactive ion etch (Oxford Cobra). The resulting samples were characterized with a scanning electron microscope (Zeiss Ultra). The resulting structures show excellent accuracy in geometric dimensions, a significant improvement over our first-generation metasurfaces produced with MIF300 developer (Figure 1b).

Tunable-Focus Lens Based on a Liquid-Crystal-Embedded a-Si Metasurface. In one application, we apply a-Si metasurfaces towards the design of metalenses with tunable focal lengths. Compact lenses with adjustable focal lengths are essential to modern imaging technologies such as adaptive vision devices and wearable augmented reality displays; however, most metalenses exhibit static functionalities post-fabrication. Our work uses a-Si metasurfaces infiltrated with liquid crystals (LCs) to demonstrate a varifocal metalens with voltage-actuated focal length [2]. This is accomplished through the design of a resonant a-Si metasurface encapsulated in a LC cell. The latter behaves as an anisotropic dielectric medium with

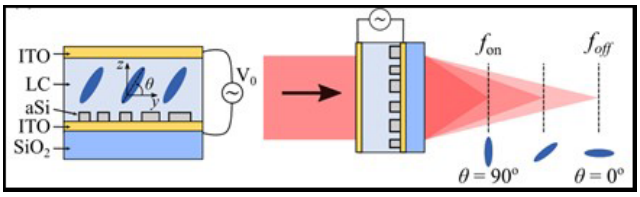

Figure 2: Schematic of the device. Left: A silicon-based metalens is encapsulated in a liquid crystal cell between two transparent conducting oxide electrodes. An AC voltage is applied to the electrodes, driving the orientation of the LC molecules at angle θ with respect to y. Right: Illustration depicting the θ-dependent focal length of light transmitted through the metalens.

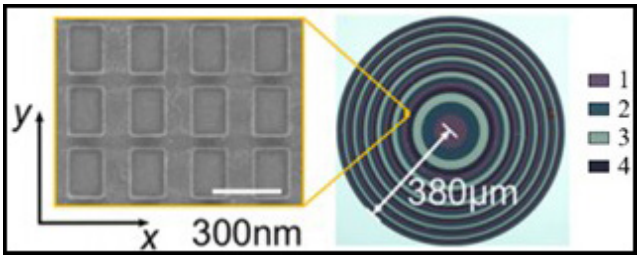

Figure 3: Left: A SEM image of the first metalens subzone. Right: Optical microscope image of the fabricated spherical metalens. The different shades of the metalens correspond to its four different metasurface geometries.

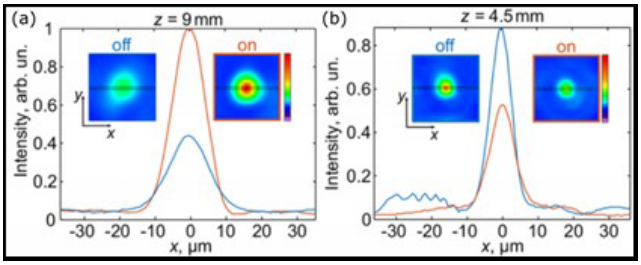

Figure 4: Experimental voltage-dependent focal spot profiles of the metalens (a) Intensity linecuts of the z = 9 mm focal spot image at the 'off' and 'on' voltages of 2.2V_{pp} and 9.8V_{pp}, respectively. The insets show the respective camera images. (b) Same as (a), but for z = 4.5 mm.

voltage-dependent optical axis orientation angle θ of the LC molecules, as depicted in Figure 2. The metalens exploits the electro-optic properties of LCs to tailor the local phase response of the silicon meta-atoms, resulting in continuous and reversible modulations of the metalens focal length.

For the design of a switchable-focus LC metalens, we present a metasurface unit cell template consisting of rectangular silicon pillars encapsulated in a nematic LC between two conductive plates, as shown in Figure 2. The meta-atom geometries are optimized to impart phase shifts to achieve the required hyperbolic phase profile for a spherical lens with focal distance $f = f_{off}$ for $\theta = 0°$, while simultaneously engineered to impart the phase profile of a lens with $f = f_{on}$ for $\theta = 90°$. Therefore, this selection enables voltage-controlled switching between two discrete focal distances of the lens.

We validate this concept by designing and fabricating a 2D metalens that emulates a transition between two distinct concave lenses with focal lengths of f_{off} = 9 mm and f_{on} = 4.5 mm, respectively. Figure 3 shows an SEM image of the fabricated lens. The experimental focal spot tuning is shown in Figure 4. By increasing the AC voltage bias across the LC cell from 2.0V_{pp} ('off') to 9.8V_{pp} ('on'), the focal spot intensity increases by 58% at $z = f_{on}$ and decreases by 37% at $z = f_{off}$.

References:

[1] Soref, Richard. "Mid-infrared photonics in silicon and germanium." Nature photonics 4.8 (2010): 495.

[2] Bosch, M., Shcherbakov, M. R., Won, K., Lee, H. S., Kim, Y., and Shvets, G. "Electrically actuated varifocal lens based on liquid-crystal-embedded dielectric metasurfaces". Nano Letters 21.9 (2021): 3849-3856.

Lithium Niobate Ring Resonator Device for Adiabatic Wavelength Conversion

CNF Project Number: 2524-17

Principal Investigator(s): Jaime Cardenas

User(s): Xiaotong He

Affiliation(s): The Institute of Optics, University of Rochester

Primary Source(s) of Research Funding: National Science Foundation

Contact(s): jaime.cardenas@rochester.edu, xhe20@ur.rochester.edu

Website: https://www.hajim.rochester.edu/optics/cardenas/

Primary CNF Tools Used: JEOL 9500, AJA ion mill, Oxford 100 PECVD, Plasma-Therm 72 and 740 etchers, AJA sputter deposition, CVC SC4500 evaporator, Zeiss SEM, Xactix xenon difluoride etcher, ABM contact aligner, Heidelberg mask writer - DWL2000, DISCO dicing saw

Abstract:

We are working on a brand-new method to change the frequency of light after its emission from laser by applying an electrical signal to ring resonators. Such a novel device will get rid of an optical pump or a gain medium in nonlinear frequency conversion.

Summary of Research:

Changing the frequency of light outside the laser cavity is typically done by nonlinear process like four wave mixing. However, integrating a system with high power optical pump into a photonic chip is a challenge. To achieve on-chip optical frequency conversion, we are working on a method of electrically tuning of ring resonator to go through adiabatic wavelength conversion. With this technique, we can dynamically control light in cavity within photon lifetime by tuning coupling between ring resonators electrically. Moreover, such a novel device will simplify and compact telecommunication components like wavelength-division multiplexing (WDM) with single frequency light input.

In previous work, adiabatic wavelength conversion (AWC) is achieved in silicon ring resonators [1-3] by using strong optical pumps incident on the cavity from above the chip. Similar to tuning frequency of sound by changing the length of the string, we can do the same to light wave by modulating the refractive index of the cavity. The light trapped inside the cavity shifts its frequency with resonance shift of the resonator. In silicon platform, the optical pump is absorbed and generates free carriers, which causes a change in the refractive index of the cavity. However, AWC in silicon introduces an optical loss, which reduces the photon lifetime and limits the conversion efficiency. It also requires a femtosecond timescale high power pulsed laser, which limits the scalability of AWC platform.

We are developing a method for electrical frequency conversion on a lithium niobate on insulator (LNOI) integrated photonic platform, the existence of which enables ultra-high quality resonators for long photon lifetime. Besides, lithium niobite has a large electro-optic effect and allows instantaneous changes in the refractive index, making it an ideal material for electrical AWC.

The LNOI sample we use consists of 600 nm thick lithium niobate (LN), 4.7 μm thick thermal SiO_2 bottom isolation layer and 0.5 mm thick silicon handle. We deposit electron -beam resist maN-2405 on the top of the sample with Surpass 4000 as adhesion. Ring resonators and waveguides are patterned with e-beam lithography process. Lithium niobate is usually etched physically with argon ions to avoid the non-volatile lithium fluoride byproducts shown in fluorine based etching techniques [4]. We etch 350 nm of LN in AJA ion mill and left a 250 nm LN slab. The resist is stripped with oxygen plasma in the PT72 etcher. However, we found that oxygen plasma can hardly remove the micro-masking formed by the interaction between argon and resist. Hence, we put the sample in RCA-1 silicon wafer cleaning process for 45 min to fully remove the residue on the sidewall. We check the sample with a scanning electron microscope (SEM) to make sure that micro-masking is completely removed before further moving on.

After the waveguide pattern is defined, we deposit a thin layer of SiO_2 with plasma-enhanced chemical vapor deposition (PECVD) to protect the waveguides. To pattern the bottom electrodes besides the waveguide, we deposit double layered PMMA and went through another e-beam process, which ensures a tolerance within tens of nanometers. We chose an evaporator as the metallization method to deposit Pt with Cr as an adhesion layer, which can further reduce the production of debris.

After an overnight lift-off, we deposit 2 μm SiO_2 with PECVD. Via holes are patterned with contact aligner and etched with a CHF_3/O_2 recipe of PT72 to expose the bottom electrodes. Top electrodes, designed to be bridges connecting two bottom electrodes and serve as contact pads to probes, are also patterned with contact aligner because the tolerance can be up to several microns. The AJA sputter tool is needed because the sidewalls of the via holes have to be covered or it will be an open circuit. And then a second lift-off process is proceeded.

We found that the top cladding oxide will break and fall off when the dicing saw goes through it, making the input coupling fairly poor. We also tried polishing, but realized that it's not easy for a holder to clamp a 1 mm wide chip. As a result, we tried to use etching method to get smooth facets. The facet is also patterned with contact aligner. Before the dicing, we used PT740 to etch the top and bottom SiO_2 cladding as well as LN slab with ion mill. After the dicing process, chips are put into the xenon difluoride etcher to undercut the silicon substrate.

We test the spectrum of the ring resonators we produced. It shows the loaded quality factor of around 100k, which corresponds to intrinsic quality factor of 170k. We also applied voltage to the device to test the electro-optics efficiency. As shown in Figure 1, the blue curve is the original spectrum without voltage applied. Red and yellow ones are the spectrum when we apply positive and negative 30V. It shows that the electro-optic efficiency is around 7pm/V. These results meet the criteria for an AWC device. We are now working on experiments to get the wavelength converted signal.

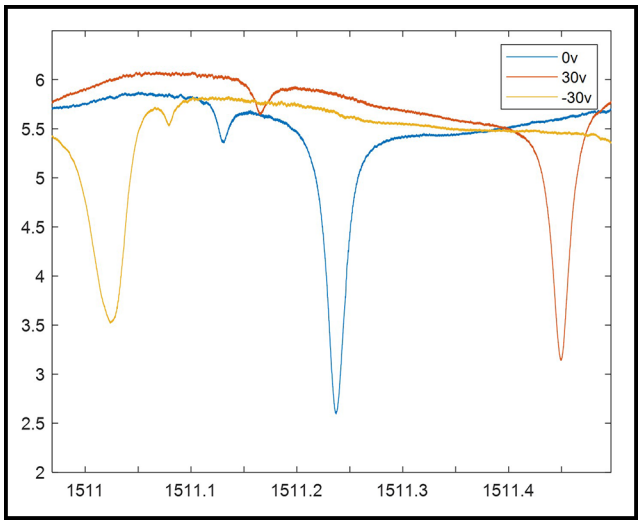

Figure 1: Spectrum of ring resonator when applying voltage.

Conclusions and Future Steps:

We fabricated devices that show possibility for electrical AWC. We are now working on the experiments to get the wavelength converted signal. In the future, we will try to improve the quality factor and electro-optical efficiency of the devices.

References:

[1] Preble S F, Xu Q, Lipson M. Changing the color of light in a silicon resonator. J. Nature Photonics, 2007, 1(5):293-296.

[2] Daniel B A, Maywar D N, Agrawal G P. Efficient adiabatic wavelength conversion in Gires-Tournois resonators. J. Optics Letters, 2011, 36(21):4155.

[3] B. A. Daniel, D. N. Maywar, and G. P. Agrawal, J. Opt. Soc. Am. B 28, 2207 (2011).

[4] Luke K, Kharel P, Reimer C, et al. Wafer-scale low-loss lithium niobate photonic integrated circuits. J. Optics Express, 2020, 28(17): 24452-24458.

Precise Phase Measurement with Weak Value Amplification on Integrated Photonic Chip

CNF Project Number: 2524-17

Principal Investigator(s): Jaime Cardenas

User(s): Meiting Song

Affiliation(s): The Institute of Optics, University of Rochester

Primary Source(s) of Research Funding: DRS, Andrew Jordan LLC

Contact(s): jaime.cardenas@rochester.edu, msong17@ur.rochester.edu

Website: https://www.hajim.rochester.edu/optics/cardenas/

Primary CNF Tools Used: Low pressure chemical vapor deposition (LPCVD), plasma-enhanced chemical vapor deposition (PECVD), JEOL 9500 e-beam lithography, ASML stepper, Oxford 100 inductively coupled plasma reactive ion etching (ICP-RIE), AJA sputter deposition

Abstract:

We show, for the first time, phase measurement with weak value amplification on an integrated photonic chip. We demonstrate 9 dB improvement of signal over an on-chip Mach-Zehnder interferometer with equal amount of detected optical power.

Summary of Research:

Weak value amplification has shown the ability to make sensitive measurements with a small portion of the light signal, including beam deflection measurement of 400 frad with 63 μW out of 3.5 mW light power [1], frequency sensitivity of 129 kHz/√Hz with 85 μW out of 2 mW [2] and temperature sensor with 4-fold enhancement [3]. By introducing a perturbation and post-selection of the light, weak value can amplify the interferometric signal without amplifying the noise, resulting in a higher signal-to-noise ratio (SNR). Therefore, in a detector saturation limited system, weak value amplification can further increase the SNR. However, tabletop setups are space consuming and vulnerable to environmental changes. By taking this technique to the integrated photonics regime, we can largely improve its robustness and compactness, making it a good candidate for precision metrology.

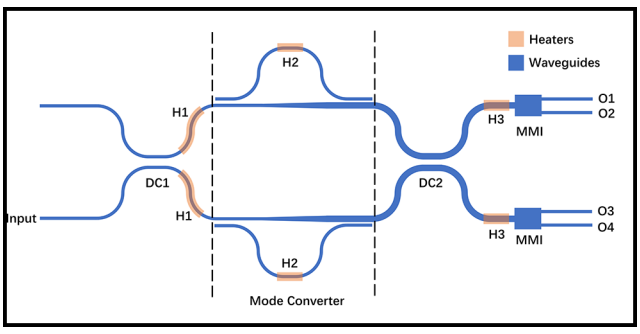

Figure 1: Layout of the device with heaters (not to scale). DC: directional coupler; H: heater; MMI: multi-mode interferometer; O: output.

We used an integrated Mach-Zehnder interferometer (MZI) followed by a multi-mode interference waveguide (MMI) (Figure 1) to achieve inverse weak value measurement. For traditional weak value amplification in optical interferometers, a propagation phase shift between the two paths is introduced to amplify spatial phase front tilt signal introduced by a tilted mirror. However, in integrated photonics, sensing is usually achieved with propagation phase. Therefore, we apply "inverse" weak value amplification (IWVA), which uses spatial phase front tilt to amplify propagation phase signal. To introduce a spatial phase tilt in a waveguide, we designed the mode converter in Figure 1 to couple a small part of the light from TE_0 mode to TE_1. This is based on that the Hermite-Gaussian (HG) expansion of free space IWVA output beam is mainly a combination of HG_0 and HG_1 modes [4]. Since eigenmodes of a waveguide are similar to Hermite-Gaussian modes, we applied the theory on waveguide eigenmodes TE_0 and TE_1.

We design a multimode coupler to couple light from fundamental mode to higher order mode. As shown in Figure 1 (between dashed lines), the straight branch is a single mode waveguide which transits to a multimode waveguide through an adiabatic taper. Therefore, TE_0 mode in the lower waveguide stays in TE_0 mode. The bending branch couples a slight portion of light from TE_0 in lower waveguide. Then it couples back into the lower waveguide, but to TE_1 mode, since the TE_1 mode supported by the multimode waveguide is designed to be phase matched with TE_0 in the bending branch.

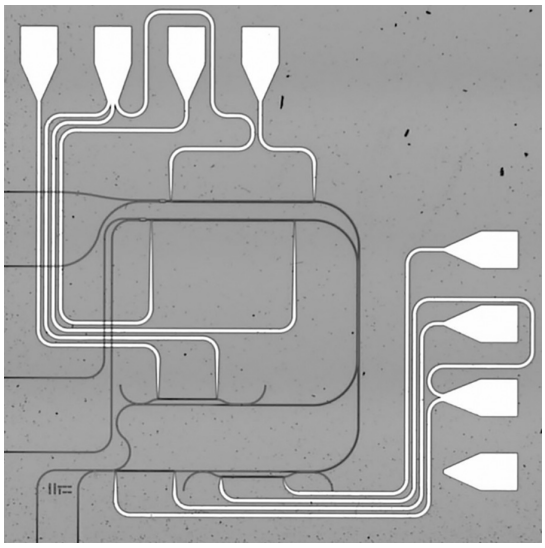

Figure 2: Microscope capture of the device. The device is wrapped around to reduce footprint.

To readout the phase shift introduced by heater 1 in Figure 1, which translates to measuring the ratio of TE_0 and TE_1 modes, we design a multimode interferometer (MMI). We used an MMI as simulation shows that its output power is dependent on the ratio of the input TE_0 and TE_1 modes.

We then fabricated the device with CMOS compatible process (Figure 2). The fabrication started with a 4-inch silicon wafer with 4 μm of thermal grown silicon dioxide. We deposited a layer of 289 nm silicon nitride with low pressure chemical vapor deposition (LPCVD). Then we used e-beam lithography to pattern the waveguides and etched the silicon nitride with inductively coupled plasma reactive ion etching (ICP-RIE). We deposited 2.6 μm of silicon dioxide with plasma enhanced chemical vapor deposition (PECVD).

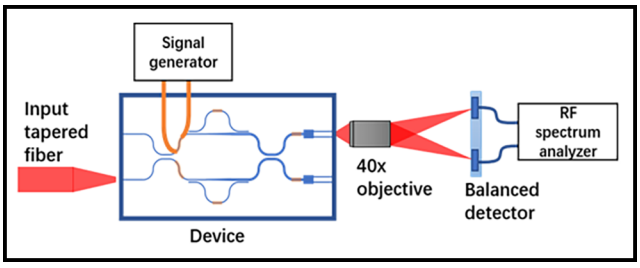

Figure 3: Illustration of testing setup.

Finally, we sputtered 100 nm of platinum, patterned with deep UV lithography, and used lift-off method to form the heaters.

We compare our weak value device with a standard on-chip MZI with same footprint working in quadrature (Figure 3). We launch 1 mW of laser power at 1570 nm with a tapered optical fiber. The phase signal is introduced by applying a modulated 1V, 10 kHz sinusoid voltage to heater 1.

The outputs of the waveguides are imaged onto a balanced detector, and we measure the signal on an RF spectrum analyzer.

We demonstrate 9±1.9 dB signal improvement over the regular MZI in the weak value device with equal amount of detected optical power. When detected powers are 14 μW, weak value device has a signal of 66.17 dBm, while the regular MZI shows 75.33 dBm. For the regular MZI to also show a signal of 66.17 dBm, it requires a higher detected power of 40.5 μW.

Conclusions and Future Steps:

In conclusion, we have shown that on-chip weak value device is a good candidate for phase related metrology, including temperature drift and frequency shift. As it provides higher signal with same amount of optical power, it can monitor the optical signal in a system without consuming a large portion of the light. On the other hand, in a detector saturation limited system, weak value device is able to further increase the signal.

References:

[1] P. B. Dixon, D. J. Starling, A. N. Jordan, and J. C. Howell, "Ultrasensitive Beam Deflection Measurement via Interferometric Weak Value Amplification," Phys. Rev. Lett. 102, 173601 (2009).

[2] D. J. Starling, P. B. Dixon, A. N. Jordan, and J. C. Howell, "Precision frequency measurements with interferometric weak values," Phys. Rev. A 82, 063822 (2010).

[3] L. J. Salazar-Serrano, D. Barrera, W. Amaya, S. Sales, V. Pruneri, J. Capmany, and J. P. Torres, "Enhancement of the sensitivity of a temperature sensor based on fiber Bragg gratings via weak value amplification," Opt. Lett., OL 40, 3962-3965 (2015).

[4] J. Steinmetz, K. Lyons, M. Song, J. Cardenas, and A. N. Jordan, "Precision frequency measurement on a chip using weak value amplification," in Quantum Communications and Quantum Imaging XVII (International Society for Optics and Photonics, 2019), Vol. 11134, p. 111340S.

Engineered Second-Order Nonlinearity in Silicon Nitride

CNF Project Number: 2524-17

Principal Investigator(s): Jaime Cardenas

User(s): Yi Zhang

Affiliation(s): The Institute of Optics, University of Rochester

Primary Source(s) of Research Funding: National Science Foundation

Contact(s): jaime.cardenas@rochester.edu, yzh239@ur.rochester.edu

Website: https://www.hajim.rochester.edu/optics/cardenas/

Primary CNF Tools Used: JEOL 9500, ASML PAS 5500/300C DUV stepper, Oxford PECVD, Oxford 100 etcher

Abstract:

We induce a permanent second order nonlinearity up to 26 fm/V in silicon nitride via electrical poling at a high temperature. We demonstrate electro-optic modulation on the engineered silicon nitride device up to 15 GHz.

Summary of Research:

Silicon nitride (Si_3N_4) is a low loss, CMOS-compatible material that has revolutionized many fields including integrated photonics and nonlinear optics, but the lack of a significant electro-optic response limits its applications. Second harmonic generation (SHG) [1-3] is promising; however, these platforms do not show feasible signal modulation at gigahertz or higher speed. Building an electro-optic response available for gigahertz (GHz) modulation in Si_3N_4 will create a new photonic platform with great potential in silicon photonics and quantum optics.

We propose to align the Si-N bonds in Si_3N_4 and induce an electro-optic effect by electrically poling the Si_3N_4 device. Khurgin hypothesized that the Si-N bonds in Si_3N_4 possess a second-order hyperpolarizability comparable to Ga-As bonds in gallium arsenide (GaAs) [4], whose $\chi^{(2)}$ is as large as 300 pm/V. However, the centro-symmetric structure of Si_3N_4 — meaning the bonds are oriented isotropically — leads to the absence of a second-order nonlinearity ($\chi^{(2)}$) and Pockels effect. A non-trivial $\chi^{(2)}$ will naturally emerge in Si_3N_4 if an applied force can align the bonds towards a certain direction, even by just a few degrees, and thus break the structural symmetry of the material.

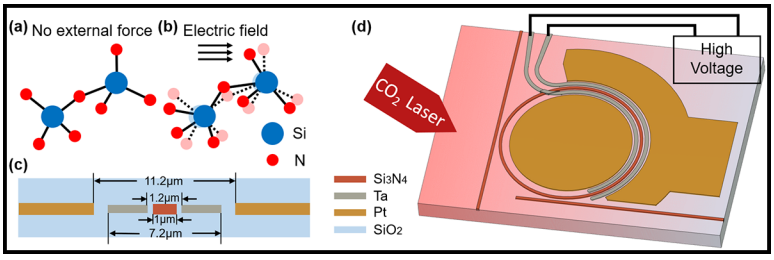

Figure 1: (a-b) Si_3N_4 lattice without (a) and with (b) an electric field applied. (c) Schematic of poling the Si_3N_4 ring with device heated by CO_2 laser. (d) Cross section of the device.

The Si-N bonds are electrically asymmetric and behave as dipoles (Figure 1(a-b)). We place a pair of tantalum (Ta) electrodes 100 nm (edge-to-edge) away from the waveguide (cross section 1 μm × 300 nm) to provide a horizontal electric field strong enough to efficiently align the Si-N bonds (Figure 1(d)). The maximum bias we can apply before arcing happens is 200V, generating a field 1 MV/cm in the Si_3N_4, very close to its electrical breakdown threshold.

To further enhance the poling process, we heat up the Si_3N_4 ring by focusing a 10W CO_2 laser beam at the device (Figure 1(d)) as the poling begins. The temperature reached is approximately 700°C, estimated based on the incandescent color of the device. Such high temperature makes the Si-N bonds more susceptible to the applied field. The poling lasts for five minutes before the heating laser is switched off, and the sample cools down while the poling field stays on. The rapid cooling prevents the aligned bonds from a complete reversal and 'freezes' them at their new positions permanently even after the removal of the poling field.

The fabrication of our device starts from depositing 300 nm of Si_3N_4 using low pressure chemical vapor deposition (LPCVD) over 4 μm thermally grown SiO_2 on a 4-inch silicon wafer. We pattern the ring resonator using electron-beam lithography and inductively coupled plasma reactive-ion etching (ICP-RIE). The temporary Ta electrodes and another pair of permanent platinum (Pt) electrodes for high-speed modulation (Figure 1(c)) are then separately patterned using DUV photolithography and deposited by sputtering.

We examine the induced electro-optic coefficient (EOC) in our device by applying a modulation

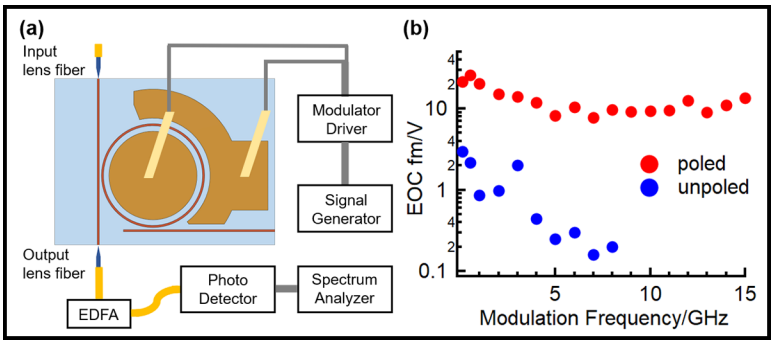

Figure 2: (a) Schematic of measuring the introduced second order nonlinearity in the Si_3N_4 ring resonator. (b) Measured r_{zzz} versus modulation frequency.

What we derive is the ZZZ component of EOC since the working mode is polarized in the same direction as the poling field as well as the modulation field.

We measure the r_{zzz} to be up to 26 fm/V in the device we engineered using this method, and we present non-decaying electro-optic modulation up to 15 GHz (Figure 2(b)). Compared to the pre-poling value, our engineering induces a > 50X enhancement at high frequency regime (> 4 GHz). Furthermore, we track the quantity of the induced r_{zzz} for 120 hours and no decay is observed.

signal on it and examine its performance. As shown in Figure 2(a), a signal generator sends modulation signal, amplified by a modulator driver, to the Pt electrodes sandwiching the ring (Ta electrodes removed by XeF_2 etching) through a pair of micro probes. We set the working wavelength properly so that the modulation efficiency is optimized.

A photodetector converts the output optic signal, pre-amplified by an erbium-doped fiber amplifier (EDFA), into electric signal and the following spectrum analyzer extracts the high-frequency component $P(\omega)$ of interest. The EOC (r_{zzz}) of the poled Si_3N_4 can be derived from [5]:

$$P(\omega) = \eta[G(\frac{\partial P}{\partial \lambda})|_{\lambda=\lambda_0} \frac{\lambda_0 L}{2n_{\text{eff}} L_{tot}} n_{SiN}{}^3 r_{zzz} E_Z(\omega)]^2$$

where $\partial P/\partial\lambda$ is the slope of transmitted power spectrum of the device at λ_0, n_{eff} is the effective index of the working mode of our device, n_{SiN} is the refractive index of Si_3N_4, L_{tot} is the total length of the ring and L the length of where modulation field is applied, η is the power conversion efficiency of the photodetector, G is the gain of EDFA and $E_Z(\omega)$ is applied modulation field.

Conclusions and Future Steps:

In conclusion, we demonstrate a permanent second order nonlinearity, up to 26 fm/V, built in silicon nitride available for modulation as fast as 15 GHz. We are working on fabrication of high-performance Si_3N_4 modulator based on this technique.

References:

[1] E. Timurdogan, C. V. Poulton, M. J. Byrd, and M. R. Watts, "Electric field-induced second-order nonlinear optical effects in silicon waveguides," Nature Photon 11, 200-206 (2017).

[2] A. Billat, D. Grassani, M. H. P. Pfeiffer, S. Kharitonov, T. J. Kippenberg, and C.-S. Brès, "Large second harmonic generation enhancement in Si_3N_4 waveguides by all-optically induced quasi-phase-matching," Nat Commun 8, 1016 (2017).

[3] X. Lu, G. Moille, A. Rao, D. A. Westly, and K. Srinivasan, "Efficient photoinduced second-harmonic generation in silicon nitride photonics," Nature Photonics 1-6 (2020).

[4] J. B. Khurgin, T. H. Stievater, M. W. Pruessner, and W. S. Rabinovich, "On the origin of the second-order nonlinearity in strained Si-SiN structures," J. Opt. Soc. Am. B 32, 2494 (2015).

[5] M. Borghi, et al., "High-frequency electro-optic measurement of strained silicon racetrack resonators," Opt. Lett. 40, 5287 (2015).

Description of the Thermal Control using Metamaterials Project

CNF Project Number: 2527-17

Principal Investigator(s): Dr. David Crouse

User(s): Golsa Mirbagheri

Affiliation(s): Electrical and Computer Engineering Department, Clarkson University

Primary Source(s) of Research Funding: National Science Foundation (NSF)

Contact(s): dcrouse@clarkson.edu, gmirbagh@clarkson.edu

Primary CNF Tools Used: AJA sputter deposition, plasma enhanced chemical vapor deposition (PECVD)

Abstract:

In this project, we are going to fabricate a temperature-based metamaterial structure composed of vanadium oxide (VO_2) grating with the benefit of semiconductor to metal phase change. The thermochromic VO_2 is transparent, which acts as semiconductor in temperatures lower than critical temperature, but emits the light in higher temperature as a metal. The deposition of VO_2 film is under investigation by changing the oxygen and argon pressure along with applying temperature changes *in situ* in a sputtering chamber and also, by changing annealing methods.

Project Description:

In this project we show the capabilities of metamaterials-based thermal controlling films. The metamaterial structure composed of VO_2 grating on top of SiO_2/Al substrate can retain heat when desired, while dissipate heat at other times, shown in Figure 1. VO_2 as a thermochromic material undergoes a semiconductor (monoclinic structure) to metal (rutile structure) transitions at a critical temperature of 68°C, accompanied by change in IR reflectivity and in resistivity, shown in Figure 2. The technology is unique such that it allows for passive thermal control of space-based instruments. We also developed a fabrication plan at the Cornell NanoScale Science and Technology Center (CNF) that allows for large-area fabrication of films, and designed the lithography mask for grating layer of the filter. If methods are developed to develop large-area films, then the technology can coat space-based instruments, as optical solar reflector (OSR), shown in Figure 3. The optical setup and reflector in addition to thermal control device is already accomplished to measure the reflection of filter at different temperatures in Clarkson University lab. Current thermal control systems require onboard electronics that add weight, size, complexity (i.e., SWaP-C).

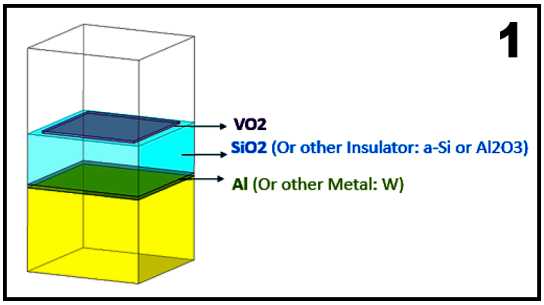

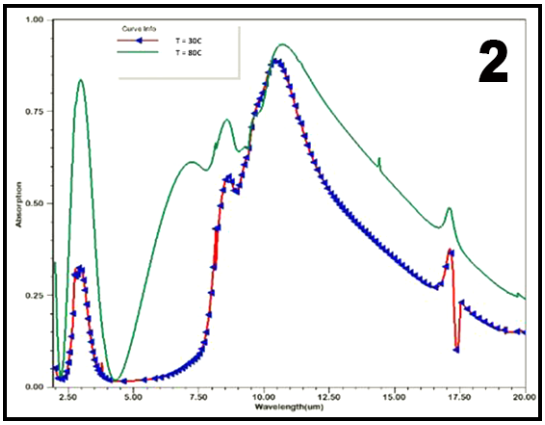

References:

[1] K. Sun, C. Riedel, A. Urbani, M. Simeoni, S. Mengali, M. Zalkovskij, B. Bilenberg, C. d. Groot and O. L. Muskens, "VO_2 Thermochromic Metamaterial-Based Smart Optical Solar Reflector," American Chemical Society Photonics, vol. 5, p. 2280-2286, 2018.

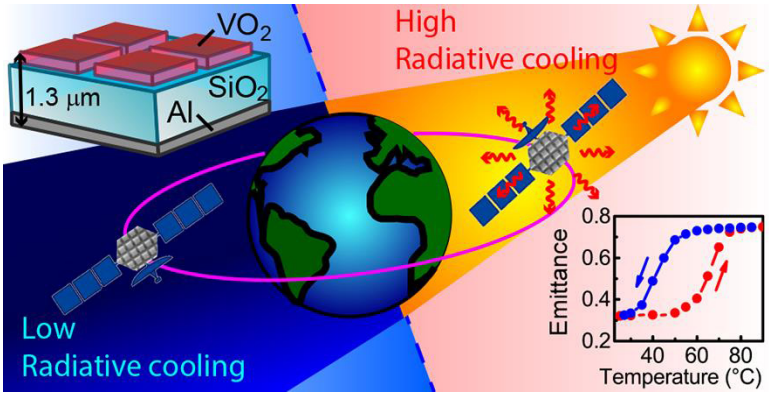

Figure 1, top: Metamaterial structure composed of VO_2 grating on top of insulator/metal substrate. Figure 2, middle: Absorption spectra of VO_2 increased in higher temp in comparison with lower temp. Figure 3, right: VO_2 based metamaterial structure as OSR shows the phase transition above and below 68°C critical temperature [1].

Metamaterial Spectrometer: A Low SWaP, Robust, High Performance Hyperspectral Sensor for Land and Atmospheric Remote Sensing

CNF Project Number: 2661-18

Principal Investigator & User: Lori Lepak

Affiliation(s): Phoebus Optoelectronics LLC

Primary Source(s) of Research Funding: National Aeronautics and Space Administration (NASA)

Contact(s): llepak@phoebusopto.com

Website: www.phoebusopto.com

Primary CNF Tools Used: ASML DUV stepper, Oxford 81 etcher, Logitech CMP, Zeiss Supra SEM

Abstract:

Since 2003, Phoebus Optoelectronics has enabled custom R&D solutions in the fields of Plasmonics, Metamaterials, Antennas, and Sensors. We work closely with our customers throughout device development, from simulation and design, to prototype realization, testing, and small volume manufacturing. Our R&D portfolio spans the spectral ranges of visible light, infrared, terahertz, and microwave radiation, for applications in high resolution imaging systems, wavelength and polarization filtering, tunable optical components, beam forming and steering, solar cells, renewable energy devices, and chemical and biological toxin sensors. We routinely partner with large, industry-leading businesses to develop products in all of these areas, jointly performing advanced testing and working together to scale up to medium- and large-volume manufacturing. Our agile team makes extensive use of the resources at the CNF for our nano/micro fabrication and testing, to provide cost efficiency and rapid turnaround. In the present report, we discuss the ongoing development of a metamaterial-based hyperspectral imaging filter.

Summary of Research:

Phoebus uses the resources of the CNF to fabricate plasmonic chips patterned with a metamaterial surface to enable Extraordinary Optical Transmission (EOT), a phenomenon unique to metastructures in which light is transmitted through apertures much smaller than the incident wavelength, at anomalously large intensities relative to the predictions of conventional aperture theory. EOT was first observed by T.W. Ebbesen in 1998 [1]. Since its founding in 2003, Phoebus has successfully harnessed EOT by incorporating metasurfaces into devices used to perform light filtering [2,3], photon sorting [4,5], polarimetric detection [6], high speed optical detection [7], and SPR plasmonic sensor chips [8].

In our current project, we are developing a hyperspectral imaging system, shown schematically in Figure 1. Our technology (Figure 1b) uses a metasurface to precisely target very narrow spectral bands of interest, enabling a significant reduction in the size and number of optical components relative to current state-of-the-art imaging systems (Figure 1a), which in turn will enable integration of our high-performance sensor onto weight-sensitive platforms (i.e., satellites) far more readily than existing systems. Our initial goal is to detect and image trace gases in the Earth's atmosphere in the midwave infrared (MWIR) region (defined as 3-5 μm wavelength), while reducing adjacent channel latency to less than 10 ms.

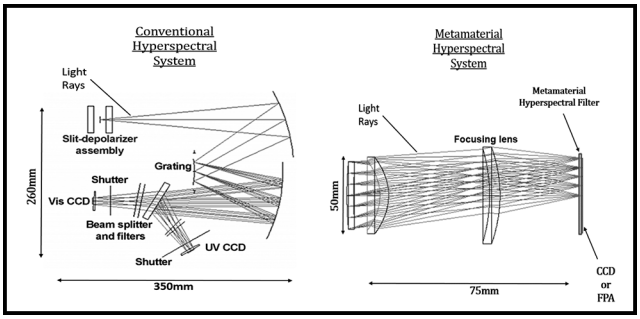

Figure 1: Phoebus's Metamaterial Spectrometer (MS) technology (right) eliminates much of the size and weight of conventional hyperspectral spectrometer technologies (left). Note the significant difference in scale of the two images.

Using the ASML DUV stepper, an entire wafer can rapidly be lithographically patterned with arrays of metastructures, as shown in Figure 2. In general, the optimal feature size and period of these metastructures depends primarily upon the desired wavelength of operation and the refractive indices of the constituent materials. In the MWIR, typical feature sizes are on the order of ~ 1 μm. As we can see in the optical microscope image in Figure 3, the ASML can easily produce highly uniform, large-area arrays of

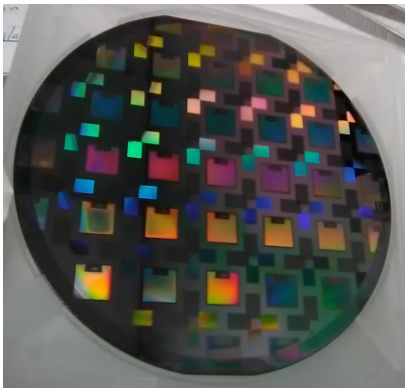

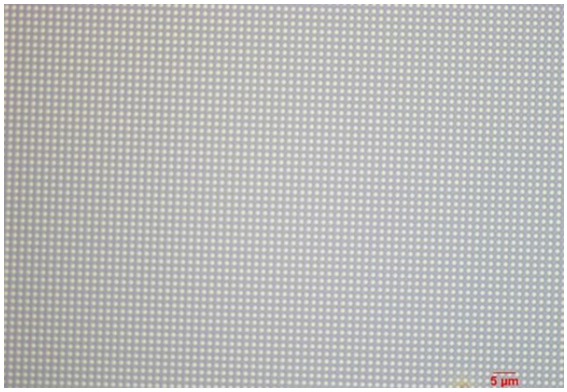

Figure 2, left: Wafer lithographically patterned with optical metastructures, using the ASML DUV stepper, Figure 3, right: Optical microscope image of test pattern of array of ~ 1 µm pillars, also patterned on the ASML.

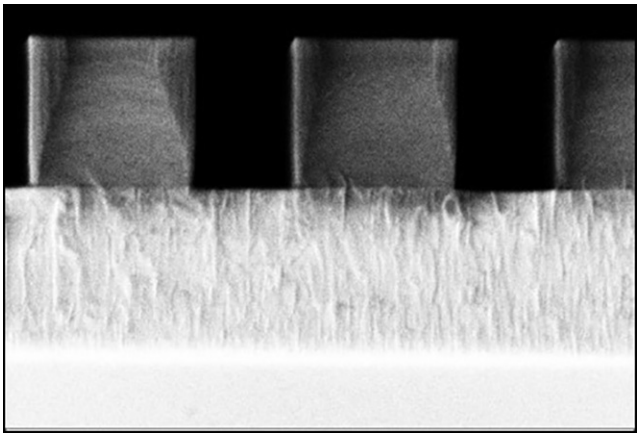

Figure 4: SEM image (cross section) of etched pillars with near-vertical sidewalls. Imaged at ~ 90 kX in the Zeiss Supra SEM, the grain structure of the etch stop layer is clearly visible.

test features of an appropriate size. Equally critical for photonics applications, relatively narrow spaces between these features can be etched with moderately high aspect ratios, to form structures with nearly vertical sidewalls, as shown in Figure 4. These vertical structures both minimize optical losses, and ensure that the real fabricated devices will perform as closely as possible to the optimal designs predicted by simulations.

Conclusions and Future Steps:

With strong, ongoing support from the National Aeronautics and Space Administration (NASA), we have successfully tested our first generation of MWIR devices. Having identified a few key areas for process improvements, we have begun fabrication of a second generation to fully optimize our MWIR device performance.

In addition, we have begun to adapt our overall metasurface technology to other spectral ranges, from the visible to the microwave, by substituting appropriate materials, and scaling feature sizes in proportion to the desired wavelength of imaging. We have just completed the fabrication of a visible/NIR-wavelength counterpart of the current technology, and are about to begin optical testing. The NIR/vis devices are fabricated using all of same tools as the MWIR project, plus the Oxford PECVD and AJA sputter tool to deposit the thin films. Thus, the extensive resources of the CNF are enabling us to rapidly develop our Metamaterial Spectrometer technology for a broad range of imaging and sensing applications.

References:

[1] Ebbesen, T.W., et al., "Extraordinary optical transmission through sub-wavelength hole arrays." Nature, (1998). 391(6668): p. 667-669.

[2] Crouse, D. "Numerical modeling and electromagnetic resonant modes in complex grating structures and optoelectronic device applications." Electron Devices, IEEE Transactions on 52.11 (2005): 2365-2373.

[3] Crouse, D., and Keshavareddy, P. "Polarization independent enhanced optical transmission in one-dimensional gratings and device applications." Optics Express 15.4 (2007): 1415-1427.

[4] Lansey, E., Crouse, D., et al. "Light localization, photon sorting, and enhanced absorption in subwavelength cavity arrays." Optics Express 20.22 (2012): 24226-24236.

[5] Jung, Y.U; Bendoym, I.; Golovin, A.B.; and Crouse, D.T. "Dual-band photon sorting plasmonic MIM metamaterial sensor." Proc. SPIE 9070, Infrared Technology and Applications XL, 90702X (June 24, 2014); doi:10.1117/12.2050620.

[6] Crouse, D., and Keshavareddy, P. "A method for designing electromagnetic resonance enhanced silicon-on-insulator metal-semiconductor-metal photodetectors." Journal of Optics A: Pure and Applied Optics 8.2 (2006): 175.

[7] Mandel, I.; Gollub, J.; Bendoym, I; Crouse, D. Theory and Design of a Novel Integrated Polarimetric Sensor Utilizing a Light Sorting Metamaterial Grating. Sensors Journal, IEEE, (2012): Vol. PP, 99.

[8] Lepak, L., et al. "Handheld chem/biosensor using extreme conformational changes in designed binding proteins to enhance surface plasmon resonance (SPR)" Proc. SPIE 9862, Advanced Environmental, Chemical, and Biological Sensing Technologies XIII, 9862-7 (April 17, 2016); doi:10.1117/12.2222305.

Stoichiometric Silicon Nitride Growth for Nonlinear Nanophotonics

CNF Project Number: 2920-20

Principal Investigator & Remote User: Kartik Srinivasan

Affiliation(s): Joint Quantum Institute, NIST/University of Maryland, College Park, MD 20742, USA

Primary Source(s) of Research Funding: Defense Advanced Research Project Agency (DARPA), National Institute of Standards and Technology (NIST)

Contact(s): kartiks@umd.edu

Website: https://groups.jqi.umd.edu/srinivasan/

Primary CNF Tools Used: Low pressure chemical vapor deposition (LPCVD) furnaces

Abstract:

Chip-integrated optical frequency combs based on integrated photonic resonators are an important technology for realizing precision measurement instrumentation, such as optical atomic clocks, in a compact and deployable format. The combs utilize nonlinear-wave mixing to spectrally redistribute a single-frequency pump laser into a spectrum of equally spaced parametric sidebands and have a behavior that depends on the interplay between dispersion, nonlinearity, dissipation, and gain. Dispersion depends on both the material chosen for the resonator and the geometry of the resonator. Stoichiomeric silicon nitride grown via low-pressure chemical vapor deposition (LPCVD) has been a common choice for this application, but the precise growth conditions have varied in the literature. Here, we study the impact of varying growth conditions, all within the nominally stoichiometric growth regime, on dispersion and frequency comb generation.

Summary of Research:

We received several LPCVD-grown silicon nitride wafers from CNF, with the silicon nitride films grown on a 3 μm thick SiO_2 layer, all on a Si substrate. The parameter varied between the different growth runs was the ratio of the precursors gases, which we stepped between 3:1 (ammonia:dichlorosilane) and 15:1 (ammonia:dichlorosilane).

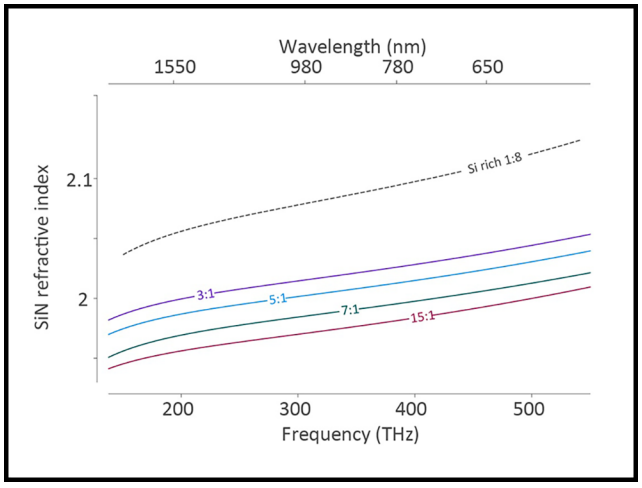

Figure 1: Wavelength/frequency-dependent refractive index values for silicon nitride films grown with varying ammonia:dichlorosilane ratios. 3:1, 5:1, 7:1, and 15:1 films are considered in this work. The refractive index of a Si-rich film (1:8 gas ratio) is shown for reference.

The rest of the processing to create microring resonators was done at NIST, and the fabricated geometries were tested at UMD.

Figure 1 shows results of fits to spectroscopic ellipsometry data, revealing the wavelength-dependent refractive index behavior of the grown films. Although all films were grown within the typical precursor range claimed for stoichiometric films (e.g., ammonia:dichlorosilane > 2:1), there are clear differences between the films, both in terms of the range of refractive index values and the manner in which the refractive index varies (i.e., the dispersion). The impact of the precursor gas ratio on dispersion can be described by a quantity called the integrated dispersion, which in the context of microresonator frequency combs, describes the separation between cavity resonances and an equally spaced grid. This integrated dispersion, which we calculate using finite-element simulations that take the measured refractive index data into account, largely controls the frequency bandwidth of the comb, and is shown in Figure 2 (left side) for a fixed resonator geometry.

We see that both the maximum value of the integrated dispersion and the position of its zero crossings significantly differ as the gas ratio goes from 3:1 to 5:1 to 7:1.

We then model the expected microcomb behavior using the Lugiato-Lefever Equation, which takes these integrated dispersion curves as an input. The predicted comb spectra in Figure 2 (right side) clearly show a significantly different comb bandwidth, with peaks at the extremities of the spectra, known as dispersive waves, having significantly different spectral positions and amplitudes.

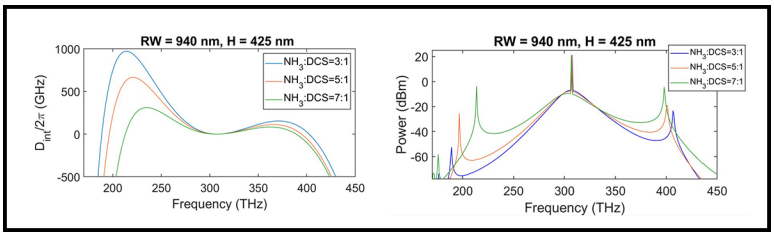

Figure 2: Simulation of the integrated dispersion (left) and expected soliton microcomb spectrum (right) for ring resonators with a fixed geometry and differing SiN films.

To compensate for the shifts in the dispersive wave positions for differing growth gas ratios, we can tune the resonator geometry.

Figure 3 shows the results of measurements indicating such an effect, for resonators fabricated in 3:1 and 7:1 ammonia:dichlorosilane films. Here, the thickness of the two resonators differs by about 10 nm, but the high frequency dispersive waves are at nearly the same position (within 2 THz). In contrast, two resonators with a thickness differing by 10 nm, but fabricated in a fixed gas ratio film (e.g., 7:1), would be expected to show a > 15 THz shift.

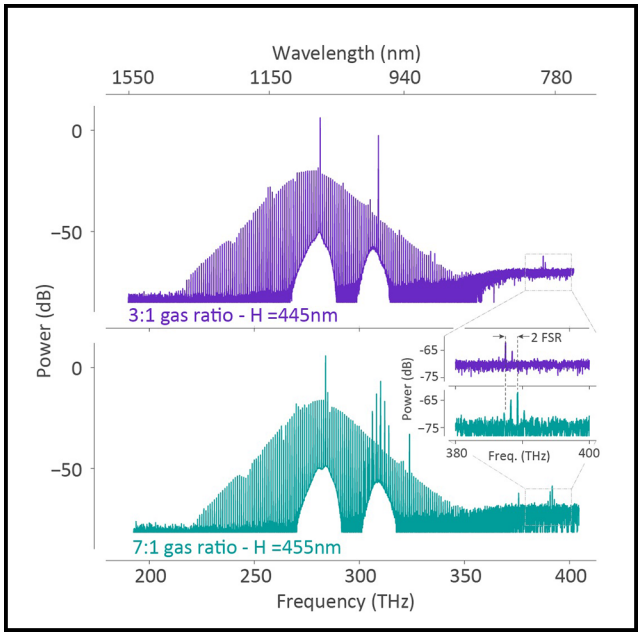

Figure 3: Measured soliton comb spectrum for two devices. The top (bottom) device is grown in a 3:1 (7:1) film, and the bottom device has a 10 nm greater film thickness.

Conclusions and Future Steps:

We have shown that the specific gas ratio within the nominally stoichiometric regime of LPCVD SiN growth has an impact on dispersion and microresonator frequency comb generation. Future work will utilize this ability to adjust material dispersion in combination with geometric dispersion engineering to create broadband microresonator combs to be used in compact optical atomic clocks.

References:

[1] G. Moille, et al, CLEO, SF2A.4 (2021).

Controlling the Pre-Curvature of Surface Electrochemical Actuators for Microscopic Robots

2021 CNF REU Intern: Zhangqi Zheng

Intern Affiliation: Engineering Physics (intended), Cornell University

CNF REU Principal Investigator: Paul L. McEuen, Department of Physics, Cornell University

CNF REU Mentors: Samantha Norris, Department of Physics, Cornell University; Michael F. Reynolds, Department of Physics, Cornell University

Primary Source of Research Funding: 2021 Cornell NanoScale Science & Technology Facility Research Experiences for Undergraduates (CNF REU) Program via National Science Foundation under Grant No. NNCI-2025233

Contact: zz365@cornell.edu, plm23@cornell.edu, sn588@cornell.edu, mfr74@cornell.edu

Primary CNF Tools Used: ABM contact aligner, Arradiance ALD Gemstar-6, AJA sputter deposition (1&2), AJA ion mill, Heidelberg mask writer - DWL2000, Oxford 80 etchers, Xactic xenon difluoride etcher

Abstract:

Smart microscopic robots, capable of performing complicated tasks while at a few hundred microns in size, have revolutionary potential in many fields. Recent research in our group has developed a promising approach towards producing such smart microscopic robots [1]. One important component of this kind of robot is the Surface Electrochemical Actuators (SEAs) [1,2], which function as the legs of the robots. With the current recipe, the SEAs have an innate pre-curvature, causing the legs to bend underneath the bodies of the robots right after release, while ideally, we would like to control the angle of this bending. In this research, we were able to change the pre-curvatures by varying the deposition pressure of titanium during the fabrication of the SEAs, showing that we can tune the pre-curvatures of the legs of smart microscopic robots through the fabrication process.

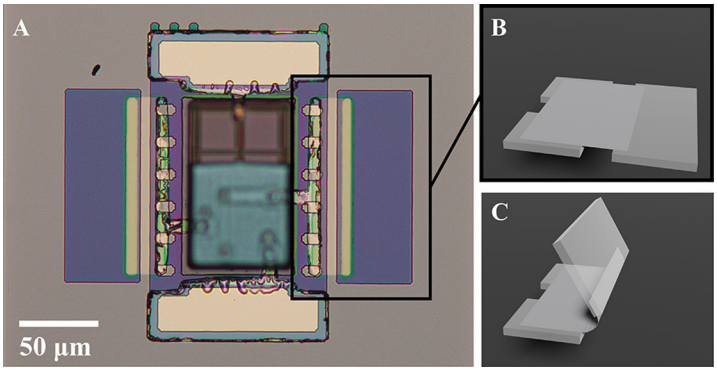

Figure 1, above: (A) Image of a smart microscopic robot before release. (B) 3D illustration of a leg of the microscopic robot before release. (C) 3D illustration of a leg of the microscopic robot after release. Figure 2, right: Fabrication process (A) metal layer, (B) polymer panel, (C) aluminum release layer, (D) after XeF_2 etching, and (E) after release.

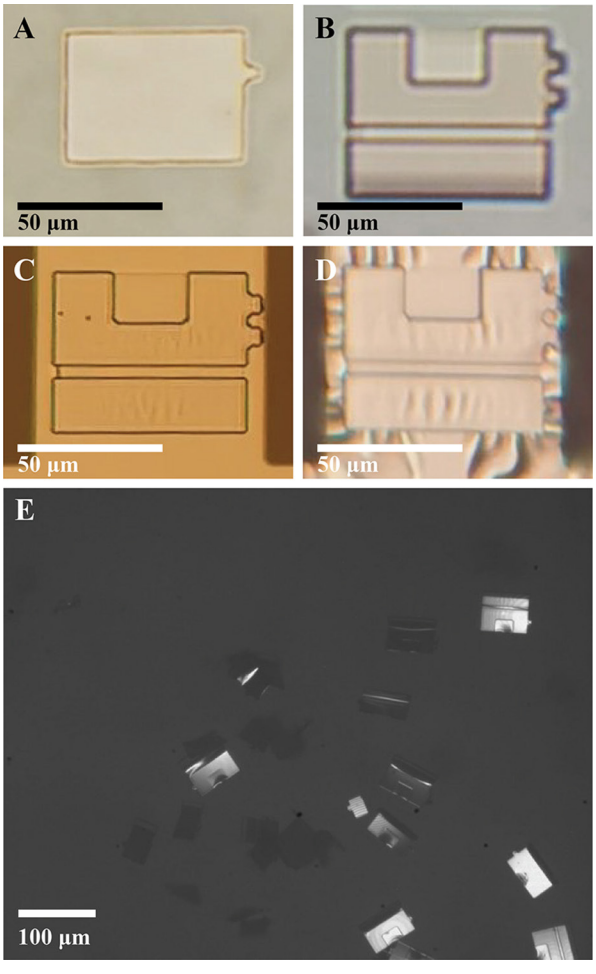

Summary of Research:

These microscopic robots developed by our group are the first of their kind, integrated with on-board circuitry that controls the motions of the robot, photovoltaics that provide power for the robot, and legs that make the robots move. Figure 1A shows an image of one of these robots when it is fully fabricated, prior to release (Reynolds, M.F. et al. Unpublished). Inside the box on the right side of the image is one of its legs, which is also shown with a 3D illustration in Figure 1B. The key component of such leg that provides its functionality is the Surface Electrochemical Actuator (SEA). Made of a 7 nm thick platinum (Pt) thin film capped on one side with about 3 nm thick of titanium (Ti), the SEAs actuate under

a voltage supply [1]. Before any actuation, however, the SEAs naturally bend towards the Pt side of the film when they are released, as shown in Figure 1C. This pre-curvature is caused by the stress of the metal films, which is largely influenced by the deposition pressure of the Ti. We use the AJA sputter deposition #2 at the CNF for depositing the Ti. Previous data collected by the CNF staff show that the pre-stress of an over 200 nm thick Ti film deposited at 3 mTorr is -178 MPa, while that of the same thickness deposited at 7 mTorr is 28 MPa. Through this research, we investigated how this difference in pre-stress due to different Ti deposition pressure causes variation in the pre-curvature of the SEAs. By fabricating SEAs with various Ti deposition pressure and measuring and comparing the pre-curvature of them, we confirmed that we can tune the pre-curvature of SEAs by changing Ti deposition pressure.

Figure 2 demonstrates the fabrication process for the leg hinges that are used for testing the pre-curvature of the SEAs. We start by depositing the Pt and Ti metal films and etching them to a rectangular shape (Figure 2A). For the purpose of this research, we deposited Ti at three different deposition pressures — 3 mTorr, 5 mTorr, and 7 mTorr — on three different silicon (Si) chips. After depositing the metal film, we fabricate the polymer panels that keeps the rest of the SEAs film in these leg hinges straight, ensuring that only the exposed SEAs film in the 3 μm gap between the panels bend when actuated (Figure 2B). We then sputter a layer of aluminum covering the hinges (Figure 2C). After we etch the Si substrate underneath, the hinges are tethered only by the aluminum (Al) on top of them (Figure 2D). For the last step we release the hinges by putting the chips upside down in Al etchant, and the chips fell off of the substrates to the bottom of the Petri® dish (Figure 2E).

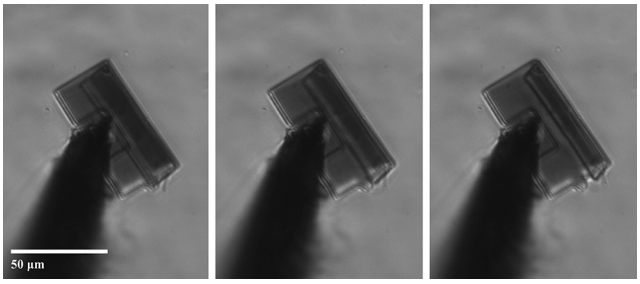

Figure 3: Optical images of a leg hinge during actuation.

We then tested the hinges for actuation by touching down to the SEAs with a Pt/Ir probe and applying a voltage through the probe. We observed actuation of hinges with Ti deposited at all three deposition pressures when we applied a triangular wave with 1.2 V amplitude (Figure 3), showing that the hinges can function as expected with the different deposition pressures.

Figure 4 shows a plot of the pre-curvatures measured from the leg hinges against the Ti deposition pressure of the hinges. Above each Ti deposition pressure is an image of a hinge fabricated with the deposition pressure. The average pre-curvature for each deposition pressure has a clear trend

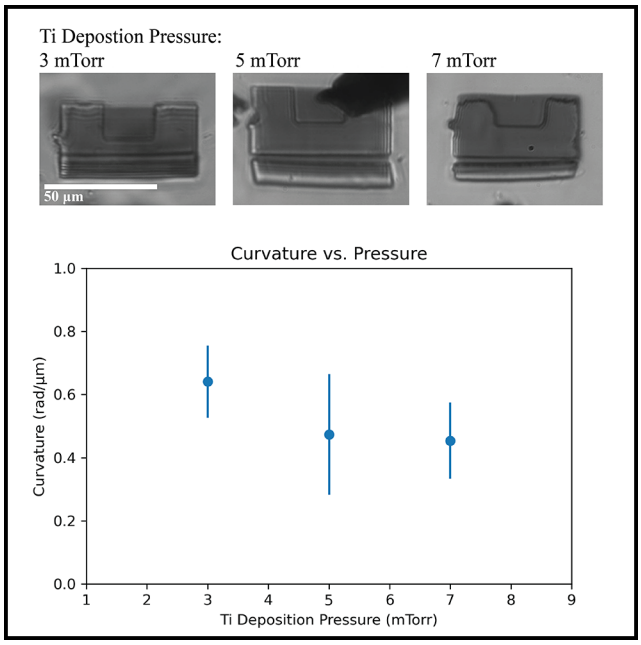

Figure 4: Data of pre-curvatures of SEAs hinges at different Ti deposition pressures.

where lower deposition pressure produces a larger pre-curvature, which matches the behavior of the pre-stresses measured at 3 mTorr and 7 mTorr. This indicates that we can tune the pre-curvature of the SEAs by changing Ti deposition pressures, and that the hinges fabricated with Ti deposited at all three deposition pressures function as expected.

Conclusions and Future Steps:

Overall, the tunability of the pre-curvature of the SEAs via changing Ti deposition pressure demonstrated in this research allows us to have better control of the initial leg shapes for smart microscopic robots. Instead of having a fixed arbitrary bending after release, this tunability allows us to fabricate future generations of smart microscopic robots with their legs bent at the angle we prefer upon release.

Acknowledgements:

I would like to acknowledge the support of the National Science Foundation, National Nanotechnology Coordinated Infrastructure, and Cornell NanoScale Facility Research Experiences for Undergraduates (CNF REU) Program (NSF grant no. NNCI-2025233). I give special thanks to my PI Dr. Paul McEuen, mentors Samantha Norris and Michael F. Reynolds, and the staff at the CNF.

References:

[1] Miskin, M. Z., et al. Electronically integrated, mass-manufactured, microscopic robots. Nature 584, 557-561 (2020).

[2] Liu, Q., et al. Micrometer-sized electrically programmable shape-memory actuators for low-power microrobotics. Science Robotics 6, (2021).

Current-Induced Magnetization Switching in a Ferrimagnetic Layer

CNF Project Number: 111-80

Principal Investigator(s): Robert A. Buhrman, Daniel C. Ralph

User(s): Qianbiao Liu, Lijun Zhu

Affiliation(s): School of Applied and Engineering Physics, Cornell University

Primary Source(s) of Research Funding: Office of Naval Research

Contact: dcr14@cornell.edu, QL63@cornell.edu

Primary CNF Tools Used: 5x stepper, AJA sputter deposition, DISCO dicing saw

Abstract:

Ferrimagnets with strong perpendicular magnetic anisotropy are interesting for their exotic spin-orbitronic effects and technological potential in high-performance magnetic storage and computing. Here we demonstrate efficient switching of ferrimagnetic layers by in-plane charge current. This result indicates the presence of a strong current-induced spin orbit torque.

Summary of Research:

Using ultraviolet photolithography (5X stepper with resist S1813) and ion milling, we patterned sputter-deposited ferrimagnetic FeTb single layers into Hall bar devices ($5\times60\ \mu m^2$) at the Cornell NanoScale Science &Technology Facility. We then fabricated electrical contacts of Hall bars by ultraviolet photolithography (5X stepper with resist S1813), AJA sputter deposition of 5 nm Ti and 150 nm Pt, and lift-off in acetone. Finally, we diced the samples into chips using the dicing saw with a silicon only blade.

As we show in Figure 1, the FeTb single layers can be switched sharply at a low current density of 8×10^6 A/cm^2. During the measurement, we applied a bias magnetic field of -3 kOe along the current direction. This finding indicates that the in-plane current induces a strong spin orbit torque in the ferrimagnetic layers.

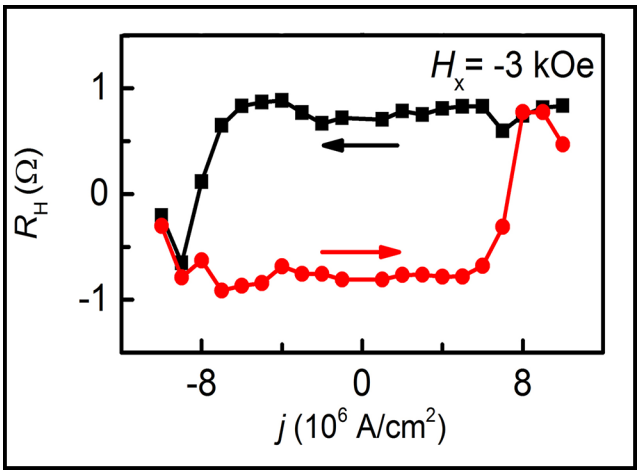

Figure 1: Anomalous Hall resistance of a ferrimagnetic FeTb thin film plotted as a function of the in-plane current density. An in-plane bias field of -3 kOe was applied along the current direction.

Separation of Artifacts from Spin-Torque Ferromagnetic Resonance Measurements of Spin-Orbit Torque for the Low-Symmetry Semi-Metal $ZrTe_3$

CNF Project Number: 598-96

Principal Investigator(s): Daniel C. Ralph

User name(s): Thow Min Jerald Cham

Affiliation(s): Laboratory of Atomic and Solid State Physics, Cornell University

Primary Source(s) of Research Funding: National Science Foundation/Division of Materials Research, Agency for Science Technology and Research (Singapore)

Contact: dcr14@cornell.edu, tc676@cornell.edu

Primary CNF Tools Used: Zeiss Supra SEM, Nabity Nanometer pattern generator, AJA sputter deposition, CVC SC4500 even-hour evaporator

Abstract:

We report measurements of spin-orbit torque generated by exfoliated layers of the low-symmetry semi-metal zirconium tritelluride ($ZrTe_3$), using the spin-torque ferromagnetic resonance (ST-FMR) technique. When the $ZrTe_3$ has a thickness greater than about 10 nm, artifacts due to spin pumping and/or resonant heating cause the standard ST-FMR analysis to give inaccurate values, indicating incorrectly that the spin-orbit torque depends strongly on the $ZrTe_3$ layer thickness. Artifact-free measurements can still be achieved over a substantial thickness range by the method developed recently to detect ST-FMR signals in the Hall geometry as well as the longitudinal geometry. For $ZrTe_3$/Permalloy samples, we measure a conventional in-plane antidamping spin torque ratio $\xi_{\parallel}^{DL} = 0.015 \pm 0.003$, and an unconventional in-plane field-like torque ratio $\xi_{\parallel}^{FL} = 0.003 \pm 0.001$. The out-of-plane antidamping torque is negligible.

Summary of Research:

We illustrate, using $ZrTe_3$/Permalloy bilayers, that extra care is required when employing the spin-torque ferromagnetic resonance (ST-FMR) technique in devices with thicker spin-orbit layers, because the magnitude of artifacts due to spin pumping and resonant heating grow relative to the spin-orbit-torque signals as a function of increasing layer thickness. One signature of such artifacts is an apparent dependence of the spin-torque efficiency on the spin-orbit layer thickness for layers much thicker than a typical spin diffusion length. We demonstrate that a recently-introduced modification of the ST-FMR technique [1], in which the ST-FMR signals are measured in the Hall geometry [2,3] as well as the usual longitudinal geometry, allows more-accurate measurements of the spin-orbit torques, separated from artifacts due to spin pumping and resonant heating. The device geometries for the measurements are shown in Figure 1.

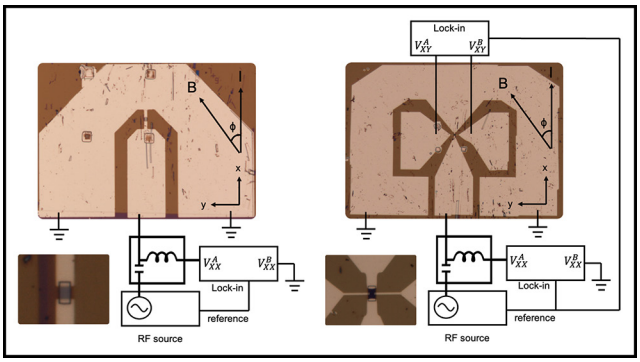

Figure 1: Schematic of a) conventional ST-FMR and b) Hall ST-FMR experimental set-ups. An additional lock-in amplifier connected across the hall leads of the device is used to read out the mixing voltage due to the change in PHE and AHE resistances.

The results of this (incorrect) standard analysis, which neglects artifact effects, are shown in Figure 2 as a function of the thickness of the $ZrTe_3$ layer. For the thinnest $ZrTe_3$ layers, the standard in-plane antidamping torque efficiency $\xi_{\parallel}^{DL}$ is weakly positive, with a value $\xi_{\parallel}^{DL} = 0.015 \pm 0.002$ for the 3 nm $ZrTe_3$ layer, but as a function of increasing $ZrTe_3$ thickness it becomes negative, with strong thickness dependence through 100 nm. At the largest $ZrTe_3$ thicknesses, the apparent magnitude of $\xi_{\parallel}^{DL}$ appears to become extremely large $|\xi_{\parallel}^{DL}| > 0.4$, even larger than the value for pure W.

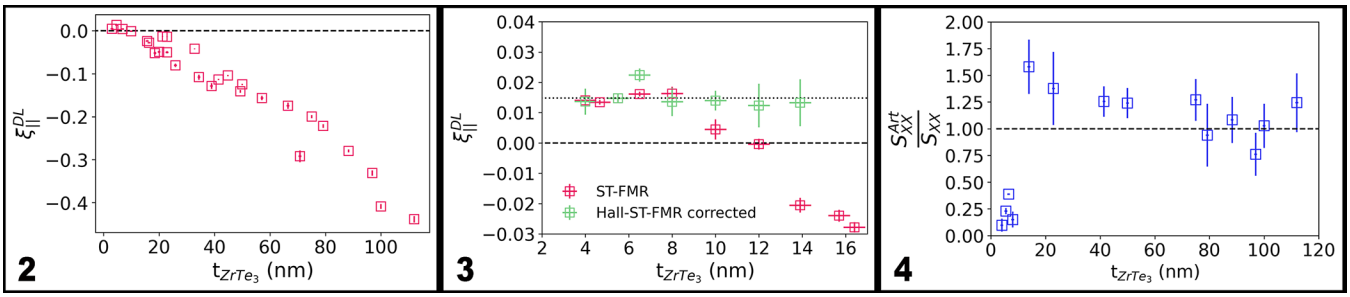

Figure 2, left: Thickness dependence of the apparent in-plane antidamping spin torque efficiency based on the incorrect standard analysis that neglects artifact from spin pumping and resonant heating. Figure 3, middle: Artifact corrected efficiency from Hall-ST-FMR for $t_{ZrTe3} < 15$ nm, showing negligible thickness dependence and absence of a sign change as $t_{ZrTe3} > 10$ nm. Figure 4, right: Ratio between V_{art} and V_S for $t_{ZrTe3} > 15$nm. V_{Art} was on the same order of magnitude as V_S, indicating that the apparent large antidamping torque signal observed for thicker flakes is likely spin-pumping dominated.

Properly accounting for spin pumping artefacts using the Hall-ST-FMR technique, we obtain the artefact corrected efficiency $\xi_{\parallel}^{DL} = 0.015 \pm 0.003$ as shown by the dotted line in Figure 3, largely independent of device thickness for $t_{ZrTe} < 15$ nm. Beyond $ZrTe_3$ thicknesses of 15 nm, the artifact voltages are too large to make an accurate determination of the spin-orbit torque, but it is clear that the apparent thickness dependence of this efficiency in the range $t_{ZrTe} > 15$ nm is due entirely to the effects of the artifact voltages, as shown in Figure 4. The non-conventional torques also remain largely independent of thickness, with values that agree with the conventional STFMR analysis.

Conclusion and Future Steps:

In summary, we have used ST-FMR to investigate the spin-orbit torques generated by exfoliated flakes of the low-symmetry semi-metal $ZrTe_3$ for a wide range of layer thicknesses in $ZrTe_3$/Py(6 nm) devices. We find that the "standard" ST-FMR analysis, which neglects the effects of artifacts due to spin pumping and resonant heating, gives incorrect values of the in-plane anti-damping torque efficiency $\xi_{\parallel}^{DL}$ for $ZrTe_3$ layers thicker than 15 nm. For the thickest layers, this incorrect standard analysis can overestimate the magnitude of $\xi_{\parallel}^{DL}$ by more than an order of magnitude, and it indicates an unphysical strong dependence of the torque efficiency on layer thickness.

ST-FMR measurements in the Hall geometry demonstrate that this strong apparent thickness dependence is due entirely to artifacts from spin pumping and/or resonant heating, not a true dependence of the spin-orbit torque on layer thickness. For $ZrTe_3$, the Hall ST-FMR measurements yield torque efficiencies $\xi_{\parallel}^{DL} = 0.015 \pm 0.003$ for the conventional in-plane antidamping torque and $\xi_{\parallel}^{FL} = 0.003 \pm 0.001$ for the unconventional in-plane field-like torque.

We suggest that ST-FMR measurements in the Hall geometry should be used as a standard technique to allow a clear separation of spin pumping and resonant heating artifacts from true spin-orbit-torque signals.

References:

[1] Saba Karimeddiny, Joseph A. Mittelstaedt, Robert A. Buhrman, and Daniel C. Ralph. Transverse and longitudinal spin-torque ferromagnetic resonance for improved mea.surement of spin-orbit torque. Phys. Rev. Applied, 14:024024, Aug 2020.

[2] Arnab Bose, Sutapa Dutta, Swapnil Bhuktare, Hanuman Singh, and Ashwin A. Tula.purkar. Sensitive measurement of spin-orbit torque driven ferromagnetic resonance detected by planar Hall geometry. Applied Physics Letters, 111(16), 2017.

[3] A. Kumar, S. Akansel, H. Stopfel, M. Fazlali, J. Akerman, R. Brucas, and P. Svedlindh. Spin transfer torque ferromagnetic resonance induced spin pumping in the Fe/Pd bi-layer system. Physical Review B, 95(6):6-12, 2017.

Anisotropic Magnetoresistance in Graphene/ Insulating Ferromagnet van der Waals Heterostructures

CNF Project Number: 598-96

Principal Investigator(s): Daniel C. Ralph

User(s): Bozo Vareskic

Affiliation(s): Laboratory for Atomic and Solid State Physics, Cornell University

Primary Source(s) of Research Funding: Air Force Office of Scientific Research

Contact: dcr14@cornell.edu, bv227@cornell.edu

Primary CNF Tools Used: Veeco Icon AFM, CVC SC4500 even/odd-hour evaporator

Abstract:

Insulating van der Waals magnets are a promising platform for spintronic applications [1]. The insulating nature of these magnets eliminates current shunting observed in spin-torque bilayer devices with metallic magnets which would lead to more efficient spin-torque devices. Furthermore, the atomically clean interfaces of van der Waal heterostructures provide a novel system to study the nature of spin transparency at the interface of two dimensional materials. However, electrical readout of the magnetic state is challenging because insulating magnets do not exhibit anisotropic magnetoresistance (AMR). Previous studies have used tunneling magnetoresistance as a readout mechanism [2,3], but these methods are difficult to incorporate into a bilayer spin-torque device. In order to achieve electrical sensitivity to the magnetic orientation, we fabricate a heterostructure of graphene and insulating ferromagnet chromium tribromide ($CrBr_3$). Low temperature magneto-transport measurements reveal an angular dependence that is consistent with an AMR mechanism, suggesting that the graphene is magnetized by proximity to $CrBr_3$.

Summary of Research:

Flakes of graphene, $CrBr_3$, and hexagonal-boron nitride (h-BN) are mechanically exfoliated on a SiO_2/Si wafer with oxide thickness of 285 nm in an inert glove box environment. Monolayer graphene flakes and few layer $CrBr_3$ are identified by optical contrast. Thickness calibration is performed by a combination of atomic force microscopy (Atomic Force Microscope – Veeco Icon) and Raman spectroscopy. In order to avoid exposure to ambient oxygen and water, $CrBr_3$ flakes were always encapsulated by h-BN prior to removal from the glove box.

The heterostructure is assembled by a dry transfer technique [4] in the glove box. h-BN is initially picked up, followed by $CrBr_3$, and lastly, graphene. Figure 1 shows a schematic of the device. The h-BN and graphene encapsulate the $CrBr_3$ from above and below, respectively. The heterostructure is then dropped onto a set of prepatterned Hall electrodes (Figure 2). Metal was deposited using the CVC SC4500 even/odd-hour evaporator.

DC transport measurements were performed in a liquid helium fridge at 5 K, which is well below the Curie temperature (~34 K) of $CrBr_3$ [5]. An in-plane field of 0.9 T was applied, and the resistance was measured as the applied field angle was swept in the plane. The AMR is defined in the bottom of Figure 3. The angular dependence of the resistance is depicted in Figure 4 and fitted to the equation at the top of Figure 3. R_0, ΔR, and ϕ_0 are treated as free parameters.

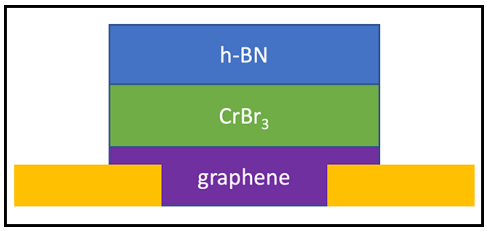

Figure 1: Schematic of monolayer graphene/chromium tribromide ($CrBr_3$) heterostructure. Insulating hexagonal boron nitride (h-BN) and graphene are used for top and bottom encapsulation, respectively, to prevent degradation of air sensitive $CrBr_3$.

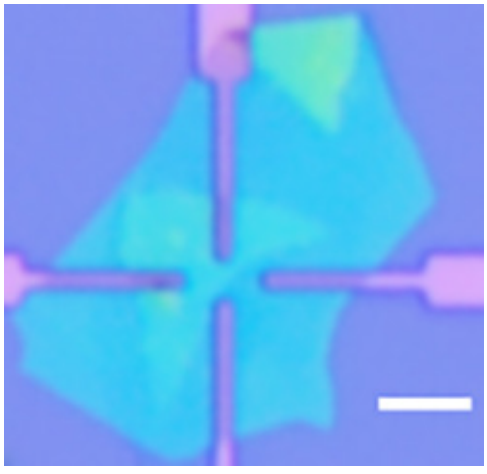

Figure 2: Micrograph of graphene/$CrBr_3$ heterostructure. Scale bar: 5 μm.

$$R = R_0 + \Delta R \cos(2(\phi - \phi_0))$$

$$\text{AMR} = \frac{R(\phi) - R(\phi = \phi_0)}{R(\phi = \phi_0)}$$

Figure 3: Above: fitting equation used to describe the angular dependence of the magnetoresistance subject to an in plane magnetic field. ϕ is the in-plane angle of the applied magnetic field, and $\phi = \phi_0$ corresponds to angle at which the current the current is parallel to the field. Below: definition of the anisotropic magnetoresistance.

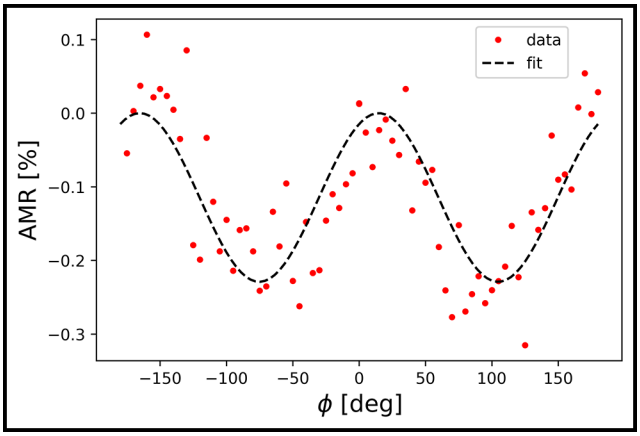

Figure 4: AMR of graphene/$CrBr_3$ heterostructure as a function of in-plane magnetic field angle. An in-plane field of B = 0.9 T was swept while applying a 1 μA current. Measurements were performed at T = 5 K. The fit is described by the top equation of Figure 3.

The periodicity of the AMR is consistent with that of conducting ferromagnetic systems described by the equation at the top of Figure 3. This suggests that the graphene is magnetized by the proximity effect. It is unlikely that the angular dependence of the magnetoresistance is due to spin Hall magnetoresistance since the spin-orbit coupling in graphene is relatively weak and graphene does not exhibit a spin Hall effect. Nonetheless, we can not rule out the possibility that spin-orbit coupling is induced in addition to ferromagnetism in graphene by the proximity effect.

References:

[1] Mak, K. F., Shan, J., and Ralph, D. C.; Probing and controlling magnetic states in 2D layered magnetic materials. Nat. Rev. Phys. 1, 646 (2019).

[2] Klein, D. R., et al. Probing magnetism in 2D van der Waals crystalline insulators via electron tunneling. Science 360, 1218 (2018).

[3] Song, T., et al. Voltage control of a van der Waals spin-filter magnetic tunnel junction. Nano Lett. 19, 915 (2019).

[4] Zomer, P. J., et al. Fast pick up technique for high quality heterostructures of bilayer graphene and hexagonal boron nitride. Appl. Phys. Lett. 105, 013101 (2014).

[5] Zhang, Z., Shang, J., Jiang, C., et al. Direct Photoluminescence Probing of Ferromagnetism in Monolayer Two-Dimensional $CrBr_3$. Nano Lett. 19, 3138 (2019).

Small Devices for Photo-Induced Electrochemical Synthesis

CNF Project Number: 900-00

Principal Investigator(s): Paul L. McEuen[1,2]

User(s): Samantha L. Norris[1], Yanxin Ji[1], Jonas Rein[3], Song Lin[3]

Affiliation(s): 1. Laboratory of Atomic and Solid State Physics, Cornell University, Ithaca NY, USA;
2. Kavli Institute at Cornell for Nanoscale Science, Cornell University, Ithaca NY, USA;
3. Department of Chemistry and Chemical Biology, Cornell University, Ithaca NY, USA

Primary Source(s) of Research Funding: Cornell Center for Materials Research with funding from the NSF MRSEC program (DMR-1719875), Air Force Office of Scientific Research (AFSOR) multidisciplinary research program of the university research initiative Grant FA2386-13-1-4118

Contact: plm23@cornell.edu, sn588@cornell.edu, yj323@cornell.edu

Primary CNF Tools Used: Heidelberg mask writer - DWL2000, ABM contact aligner, Oxford 81/82/100/Cobra etchers, AJA sputter deposition tool, Oxford PECVD, hot press, Unaxis 770 deep Si etcher

Abstract:

We present microscopic (hundred-micron scale) wireless electrochemical synthesizers that allow for high throughput experimentation (HTE) of small (<100 uL) volumes, allowing for more rapid development of electrochemical synthesis methods in the pharmaceutical industry. Current methods of electrochemical HTE for drug synthesis require epoxying macroscopic electrodes to a custom printed circuit board, placing a lower limit on the reaction volume and limiting the ability to scale to 96- or 384- well plates. In contrast, these Small devices for Photo-induced ElectroChemical Synthesis (SPECS) are individually manipulable and optically powered, allowing for more efficient parallelization of the drug synthesis process.

Summary of Research:

SPECS allow for completely wireless electrochemical synthesis. These devices are fabricated using standard photolithographic techniques, and thus can be produced at the wafer scale. The only serial process in SPECS fabrication is their individual manipulation after separation from the substrate, which is easily automated with a commercial pick-and-place tool.

This technology uses microscale silicon photodiodes connected in series with two electrodes to convert incident light to a current and voltage that can be used to induce electrochemical synthesis at the electrodes. The entire device is encapsulated in 1 uL of silicon dioxide except for the electrode surface which remains exposed to the environment. Under an illumination intensity of about 100 nW/μm^2 at 532 nm, a 100 μm diameter device consisting of seven photodiodes can produce about 20 μA and and 4.5V. The current produced by the SPECS increases linearly with incident light intensity and device area, with the voltage increasing linearly with the number of photodiodes in series — this allows the device to be tailored to the desired synthesis process while still allowing for *in situ* tuning.

To create the silicon photodiode devices, we begin by selectively doping the top of the SOI device layer with phosphosilicate glass to create a vertical PN junction. We then electrically isolate the photodiodes by dry etching to the buried oxide layer in the Oxford Cobra inductively coupled plasma (ICP) etcher. We then connect the photodiodes in series to each other and the electrodes, also conformally coating the silicon defining the electrodes in metal at this step. The metal electrodes and interconnects are platinum with a titanium adhesion layer deposited in the AJA sputter deposition tool.

We encapsulate the photodiodes with silicon dioxide with the Oxford plasma enhanced chemical vapor deposition tool, leaving the metal electrodes protruding (Figure 1).

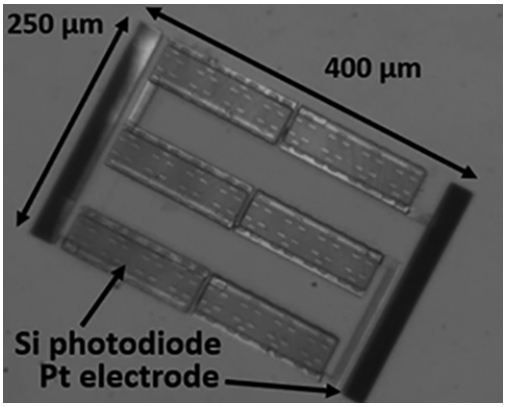

Figure 1: A prototype SPECS device, with six photovoltaic panels and one platinum electrode on each end.

We then sputter and pattern aluminum over the entire device except for the center of the photodiodes. This prevents light from passing through the transparent sections of the device during experiments, which could result in unintended photo-induced synthesis of the reaction mixture.

Due to using planar lithographic techniques to create the SPECS, they are 5 μm thick as fabricated. These thin devices can be released from the substrate by patterning aluminum over them, undercutting the silicon underneath with XeF_2, and then releasing in wet aluminum etchant. After releasing in fluid, the devices are easily pipetted into any container for experimentation (Figure 2). Preliminary results have been achieved with these devices (Figure 3).

To increase rigidity of larger (mm-scale) devices, we transfer them to a transparent substrate. To accomplish this, we bond the wafer with the onboard SPECS to a transparent carrier wafer using a low melting-point thermal plastic polymer and then remove the silicon handle substate via ICP dry etching in the Unaxis 770 Si deep etcher. In the end, we attach the carrier wafer/SPECS stack to a glass substrate and remove the carrier substrate by melting the bonding polymer, followed by dicing to separate the individual devices.

Future work includes electrochemical synthesis using these larger and more rigid SPECS, as well as characterization of their rigidity during sonication, stirring, and other methods of regulating mass transport *in situ*.

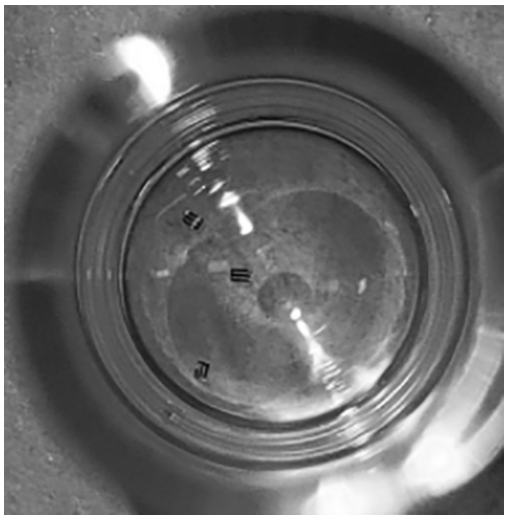

Figure 2: Multiple SPECS after being pipetted into a 5 mm diameter glass vial to be inserted into a 96 well plate.

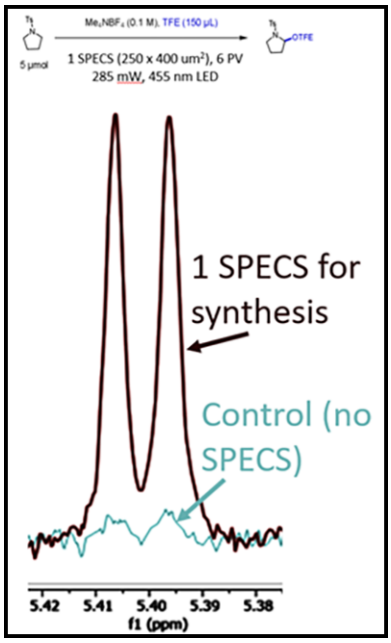

Figure 3: Nuclear magnetic resonance spectroscopy results showing successful Shono oxidation using SPECS, a standard electrochemical synthesis reaction.

Nanofabricated Superconducting Devices for Vortex Dynamics and Qubits

CNF Project Number: 1314-05

Principal Investigator(s): Britton L.T. Plourde

User(s): Brad Cole, Kenneth Dodge, Jaseung Ku, Yebin Liu, Michael Senatore

Affiliation(s): Department of Physics, Syracuse University

Primary Source(s) of Research Funding: Army Research Office

Contact: bplourde@syr.edu, bgcole@syr.edu, krdodgej@syr.edu, jku102@syr.edu, yliu166@syr.edu, masenato@syr.edu

Website: https://bplourde.expressions.syr.edu/

Primary CNF Tools Used: ASML stepper, JEOL 9500, Plasma-Therm 770

Abstract:

We fabricate superconducting microwave devices for studying the dynamics of vortices at low temperatures and for forming novel qubits. Vortices are quantized bundles of magnetic flux that thread many different superconductors over a particular range of applied magnetic field. By using disordered superconducting thin films to form high kinetic inductance wires combined with novel arrays of Josephson junctions, we are able to build structures that can lead to qubits that are protected against decoherence.

Summary of Research:

Superconducting microwave circuits play an important role in quantum information processing. Circuits composed of Josephson junctions and capacitors with superconducting electrodes can serve as qubits, the fundamental element of a quantum computing architecture. Various loss mechanisms limit the ultimate performance of these devices, including trapped magnetic flux vortices. Vortices can be trapped in the superconducting electrodes when background magnetic fields are present and contribute dissipation when driven with microwave currents [1]. Thus, techniques for controlling the trapping of vortices are critical to the development of large-scale quantum information processors with superconducting circuits.

By arranging nanoscale Al-AlOx-Al Josephson tunnel junctions in novel arrays, it is possible to implement new qubit designs that are protected against decoherence [2,3].

We fabricate our microwave resonators from various superconducting films, including aluminum and niobium, deposited onto silicon wafers in vacuum systems at Syracuse University. We define the patterns on the ASML stepper and transfer them into the films with a combination of reactive ion etching and liftoff processing. For defining Josephson junctions, we use the JEOL 9500 along with a dedicated deposition system at Syracuse University. We measure these circuits at temperatures of 100 mK and below in our lab at Syracuse University.

References:

[1] Song, C., Heitmann, T.W., DeFeo, M.P., Yu, K., McDermott, R., Neeley, M., Martinis, John M., Plourde, B.L.T.; "Microwave response of vortices in superconducting thin films of Re and Al"; Physical Review B 79, 174512 (2009).

[2] Doucot, B., Ioffe, L.; "Physical implementation of protected qubits"; Reports on Progress in Physics 75, 072001 (2012).

[3] Dodge, K., Liu, Y., Cole, B., Ku, J., Senatore, M., Shearrow, A., Zhu, S., Abdullah, S., Klots, A., Faoro, L., Ioffe, L., McDermott, R., Plourde, B.; "Protected C-Parity Qubits Part 1: Characterization and Protection"; Bull. Am. Phys. Soc. 2021, http://meetings.aps.org/Meeting/MAR21/Session/X31.3.

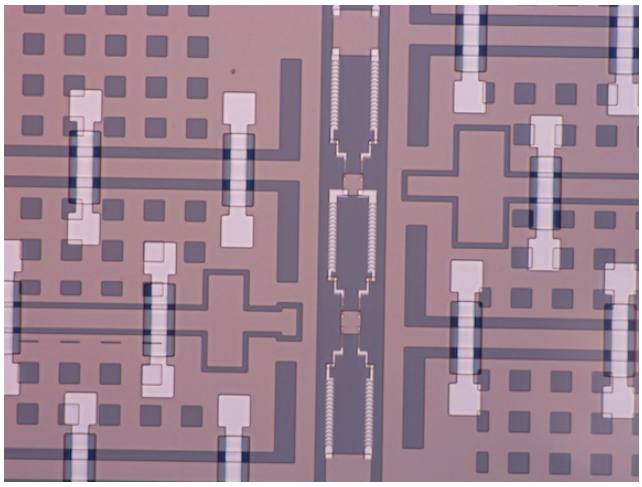

Figure 1: Optical micrograph of plaquette structures formed from arrays of Al-AlOx-Al Josephson junctions for protected qubit design with Nb ground plane and Al/SiOx ground straps.

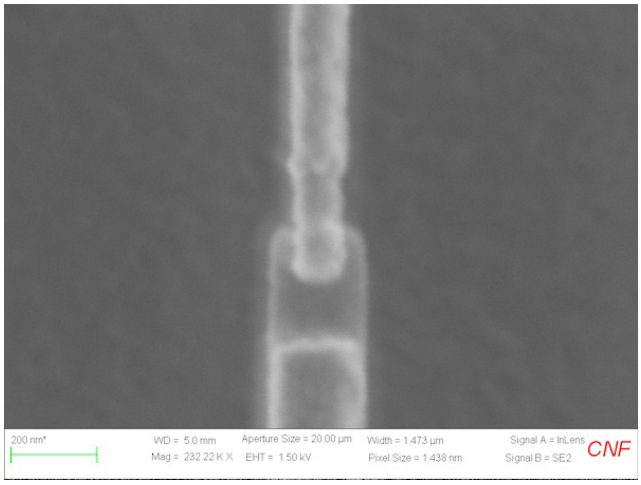

Figure 2: Scanning electron micrograph image of small-area Al-AlOx-Al Josephson junction on protected qubit element.

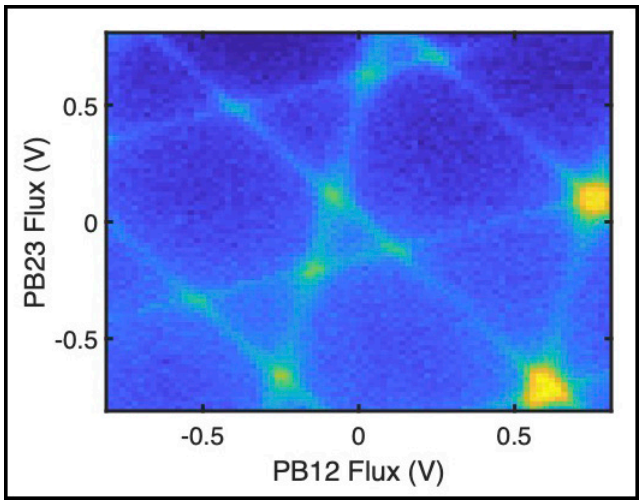

Figure 3: Two-dimensional flux bias voltage modulation of resonant frequency for readout microwave resonator coupled to qubit.

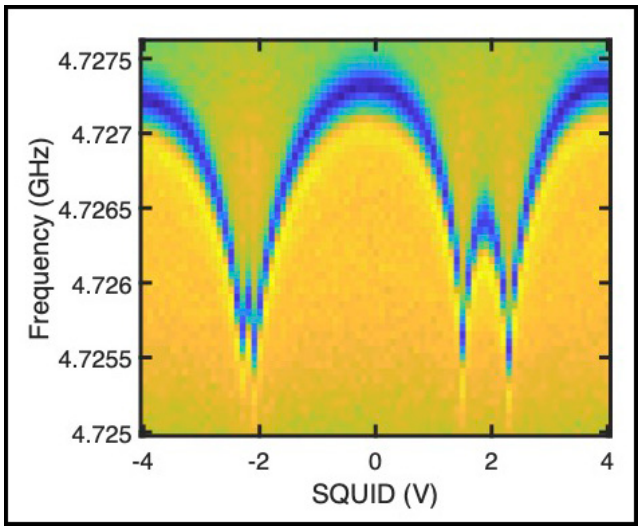

Figure 4: Modulation of qubit transition frequency with flux bias voltage of SQUID tuning loop.

Fabrication of Nanoscale Josephson Junctions for Quantum Coherent Superconducting Circuits

CNF Project Number: 1735-08

Principal Investigator(s): Britton L.T. Plourde

User(s): Andrew Ballard, Brad Cole, Vito Iaia, Indrajeet, Tianna McBroom, Michael Senatore

Affiliation(s): Department of Physics, Syracuse University

Primary Source(s) of Research Funding: Air Force Research Lab, Air Force Office of Scientific Research

Contact: bplourde@syr.edu, alballar@syr.edu, bgcole@syr.edu, vmiaia@syr.edu, indraje@syr.edu, tamcbroo@syr.edu, masenato@syr.edu

Website: https://bplourde.expressions.syr.edu/

Primary CNF Tools Used: ASML stepper, JEOL 9500, Plasma-Therm 770

Abstract:

We fabricate nanoscale superconductor tunnel junctions and other structures for experiments involving quantum coherent circuits. Such circuits have shown great promise in recent years for explorations of quantum mechanics at the scale of circuits on a chip and for forming qubits, the foundational elements of a quantum computer. The quantum state of these superconducting qubits can be manipulated with microwave radiation at low temperatures. We are currently developing superconducting metamaterial structures with novel microwave mode spectra for coupling to superconducting qubits.

Summary of Research:

The unique properties of nanoscale Josephson junctions enable a wide range of novel superconducting circuits for investigations in many diverse areas. In recent years, circuits composed of such junctions have emerged as promising candidates for the element of a quantum computer, due to the low intrinsic dissipation from the superconducting electrodes and the possibility of scaling to many such qubits on a chip [1]. The quantum coherent properties of the circuits are measured at temperatures below 50 mK with manipulation of the qubit state through microwave excitation.

We are developing multimode microwave resonators using combinations of superconducting lumped-circuit elements to engineer metamaterial transmission lines. These structures exhibit novel mode structures characteristic of left-handed materials [2]. We are fabricating such metamaterial transmission lines from Al and Nb films on Si and characterizing these at low temperatures [2]. We are working on experiments to couple these left-handed lines to superconducting qubits for experiments involving the exchange of microwave photons [3,4].

We pattern these circuits at the CNF with nanoscale structures defined with electron-beam lithography on the JEOL 9500 integrated with photolithographically defined large-scale features. The junctions are fabricated using the standard double-angle shadow evaporation technique, in which a resist bilayer of copolymer and PMMA is used to produce a narrow PMMA airbridge suspended above the substrate. Evaporation of aluminum (Al) from two different angles with an oxidation step in between forms a small Al-AlOx-Al tunnel junction from the deposition shadow of the airbridge. We have developed a process for defining these junctions with electron-beam lithography and we perform the aluminum evaporations in a dedicated chamber at Syracuse.

We pattern large-scale features using the ASML stepper, with electron-beam evaporation of Al and sputter-deposition of Nb.

Measurements of these circuits are performed in cryogenic systems at Syracuse University, including dilution refrigerators for achieving temperatures below 30 mK.

References:

[1] Clarke, J. and Wilhelm, F.K.; "Superconducting quantum bits"; Nature, 453, 1031 (2008).

[2] Wang, H., Zhuravel, A., Indrajeet, S., Taketani, B., Hutchings, M., Hao, Y., Rouxinol, F., Wilhelm,F., LaHaye, M.D., Ustinov, A., Plourde, B.; "Mode Structure in Superconducting Metamaterial Transmission Line Resonators"; Physical Review Applied 11, 054062 (2019).

[3] Indrajeet, S., Wang, H., Hutchings, M.D., Taketani, B.G., Wilhelm, F.K., LaHaye, M.D., Plourde, B.L.T.; "Coupling a Superconducting Qubit to a Left-Handed Metamaterial Resonator"; Phy.Review Applied 14, 064033 (2020).

[4] McBroom, T.A., Indrajeet, S., Cole, B.G., Plourde, B.; "Superstrong coupling between a transmon and a metamaterial resonator"; Bull. Am. Phys. Soc. 2021, http://meetings.aps.org/Meeting/MAR21/Session/R30.7.

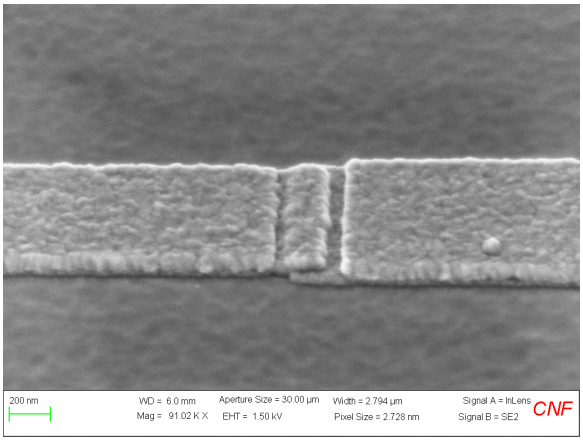

Figure 1: Scanning electron micrograph of Al-AlOx-Al Josephson junction for superconducting qubit.

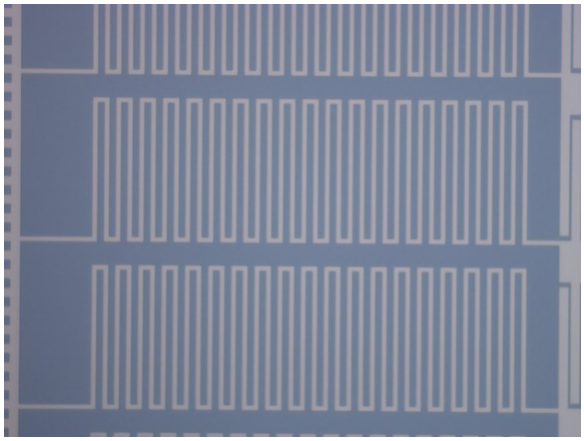

Figure 2: Optical micrograph of Nb meander-line inductor on superconducting metamaterial transmission line resonator.

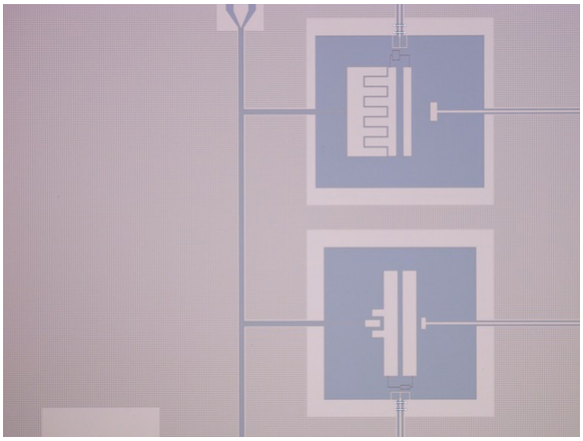

Figure 3: Optical micrograph of superconducting qubits coupled to metamaterial transmission line resonator fabricated from Nb thin film on Si.

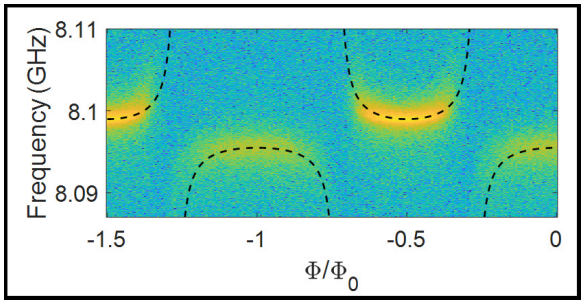

Figure 4: Spectroscopic measurement of microwave transmission through metamaterial transmission-line resonator mode vs. flux modulation of qubit transition frequency.

Nanoscale Magnetization and Current Imaging using Time-Resolved Scanning-Probe Magneto-Thermal Microscopy

CNF Project Number: 2091-11

Principal Investigator(s): Gregory D. Fuchs

User(s): Chi Zhang

Affiliation(s): Applied and Engineering Physics, Cornell University

Primary Source(s) of Research Funding: Air Force Office of Scientific Research (FA9550-14-1-0243, FA9550-18-1-0408), DOE Office of Science, Basic Energy Science (DE-SC0019997)

Contact: gdf9@cornell.edu, cz435@cornell.edu

Primary CNF Tools Used: JEOL 9500, GCA 5x stepper

Abstract:

High resolution, time-resolved magnetic microscopy is crucial for understanding novel magnetic phenomenon such as skyrmions, spin waves, and domain walls. Currently, achieving 10-100 nanometer spatial resolution with 10-100 picosecond temporal resolution is beyond the reach of table-top techniques. We have developed a time-resolved near-field magnetic microscope-based on magneto-thermal interaction, which achieved a spatial resolution on the scale of 100 nm and a temporal resolution below 100 ps. Our results suggest a new approach to nanoscale spatiotemporal magnetic microscopy in an accessible, table-top form to aid in the development of high-speed magnetic devices.

Summary of Research:

Our group has previously developed time-resolved magneto-thermal microscopy for magnetic imaging [1-3]. We apply a pulsed laser to create thermal gradient ∇T. The local magnetization M subjected to ∇T generates an electric field E_{ANE} through the anomalous Nernst effect [Figure 1]. This technique can be used to image both local static and dynamic magnetization, as well as an applied current density [4]. In this work, we extend magneto-thermal microscopy to nanoscale resolution with near-field light. We use a gold-coated cantilever glued on tuning fork as our probe, controlled by atomic force microscopy. We shine a laser on the tip apex, and the near-field enhancement of the electric field at the tip [5-6] heats the sample as a nanoscale heat source [Figure 1]. The heating length scale is comparable to the tip radius, below 100 nm.

We first study a 5 μm × 15 μm CoFeB/Hf/Pt sample fabricated using photolithography with the GCA 5× stepper. We demonstrate magnetic imaging of near-field scanning probe with a multi-domain state. Figure 2(a) shows a far-field image taken using a focused light to confirm the magnetic state. Figures 2(b-d) show topography, far-field and near-field images, acquired simultaneously with the scanning probe. The near-field image resembles the far-field image, but with higher resolution. We note that the smallest feature of the near-field image is ~ 455 nm in this sample, which is below the optical diffraction limit of the set-up. That feature is likely the actual domain wall width rather than being limited by the instrument resolution.

To probe instrument resolution further, we measure in current imaging mode and use a new sample designed with a sharp current density feature. The sample is a thin-film heterostructure composed of 5 nm $Ni_{81}Fe_{19}$/2 nm Ru, then patterned into a 2 μm-diameter disk with two 150 nm necks using JEOL 9500 e-beam lithography. Figure 3 shows topography and near-field current density images taken with the near-field scanning probe. By taking linecuts through two necks, as shown in Figure3(a) inset, we compare signals between focused light far-field and scanning probe near-field microscopy. The scanning near-field image has higher resolution than the far-field image, and by fitting to a model, we demonstrate a spatial resolution on the scale of 100 nm. We note that the resolution here is only an upper bound. We expect a resolution of 50 nm using magneto-thermal microscopy with sharp, high-endurance tips.

We now turn our attention to characterizing the temporal resolution of our instrument. In the measurements, we electrically mix the voltage pulses generated from the sample with reference voltage pulses that are synchronized with the laser but have a controllable delay τ. Figure 4(a) and (b) show the mixed output signal as a function of the delay τ, which can be understood as the temporal convolution signal of the two pulses. The convolved signal widths are roughly 100 ps, similar to the reference pulse width. Therefore, the voltage pulses generated by the near-field thermal excitations must be shorter than 100 ps, demonstrating a time-resolved nano-probe. The picosecond temporal

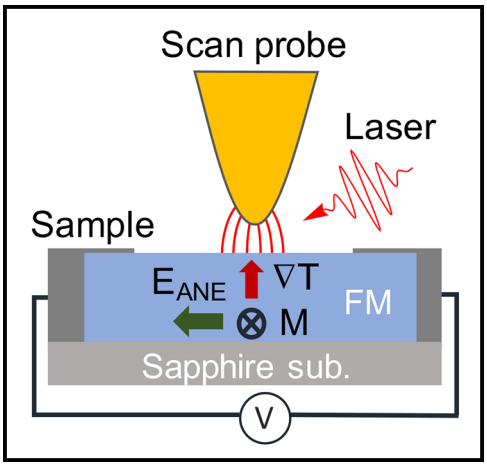

Figure 1: Schematic of scanning near-field magneto-thermal microscopy setup, illustrating laser, sample, scan probe, and near-field interaction.

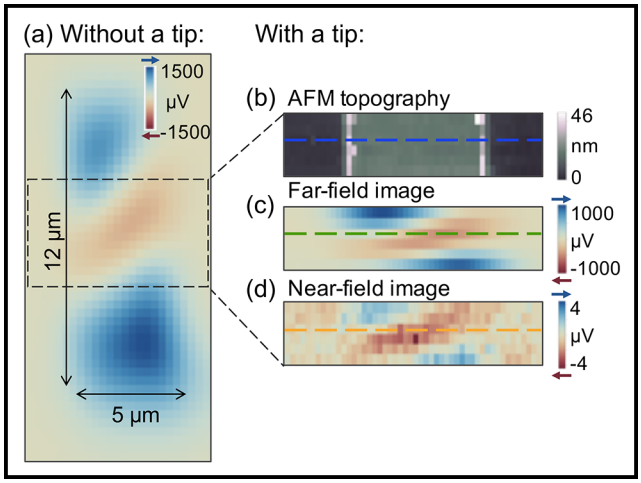

Figure 2: Magnetic multi-domain imaging. (a) Magnetic far-field images of a multi-domain state. With a scanning probe tip, (b) topography, (c) far-field and (d) near-field images acquired simultaneously.

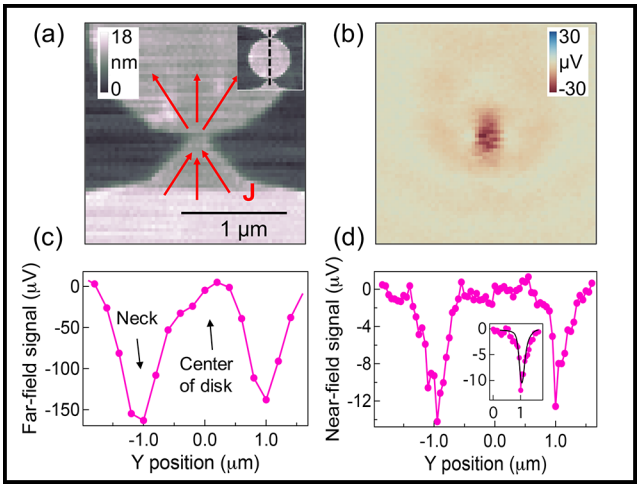

Figure 3: Current imaging and spatial resolution. (a) Topography and (b) current density images. Line cuts of (c) far-field and (d) near-field signals for resolution comparison. (d) The inset shows the simulated fit to the data.

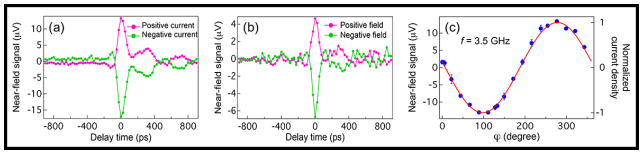

Figure 4: Time-domain measurements of the near-field voltage pulses produced by (a) current density and (b) magnetization as a function of the pulse delay τ. (c) Stroboscopic measurements of microwave current as a function of phase ψ.

resolution enables us to probe a stroboscopic section of the gigahertz frequency cycle. We demonstrate the stroboscopic capability of the scanning probe by measuring a 3.5 GHz microwave current at the nano-constriction. We phase-lock the laser and microwave current such that the thermal pulses constantly probe the current at the same phase ψ. Figure 4(c) shows normalized microwave current density as a function of ψ, showing the phase-sensitive response.

Conclusions and Future Steps:

We have developed a time-resolved scanning near-field magneto-thermal microscopy for magnetic and current imaging. We demonstrated 100 nm scale spatial resolution and picosecond temporal resolution. Next step, we will apply this instrument to study the dynamics of nanoscale spin textures, e.g. magnetic skyrmions.

This work is published in Nano Letters in Ref. [7].

References:

[1] J. M. Bartell, D.H. Ngai, et al., Nat. Commun. 6, 8460 (2015).

[2] J. M. Bartell, et al., Phys. Rev. Appl. 7, 044004 (2017).

[3] I. Gray, et al., Phys. Rev. Mater. 3, 124407 (2019).

[4] F. Guo, et al., Phys. Rev. Appl. 4, 044004 (2015).

[5] J. C. Karsch, et al., APL Photonics 2, 086103 (2017).

[6] L. Meng, et al., Optics Express, 11, 13804, (2015).

[7] C. Zhang, et al., Nano Lett. 21, 4966 (2021).

Strain Tuning of Quantum Emitters in Monolayer Transition Metal Dichalcogenides

CNF Project Number: 2126-12

Principal Investigator(s): Gregory Fuchs

User(s): Jaehong Choi

Affiliation(s): Applied and Engineering Physics, Cornell University

Primary Source(s) of Research Funding: Air Force Office of Scientific Research Multidisciplinary Research Program of the University Research Initiative (AFOSR MURI)

Contact: gdf9@cornell.edu, jc3452@cornell.edu

Primary CNF Tools Used: JEOL 6300, 5X g-line stepper, Oxford COBRA, Oxford 81, DISCO dicing saw, CVC SC4500 odd hour evaporator, Veeco Icon AFM, wire bonder, Heidelberg mask writer - DWL2000

Abstract:

Tensile strain has been known to modulate the band gap of two-dimensional (2D) transition metal dichalcogenides (TMDs), which effectively funnels excitons and activates quantum emitters in a deterministic way. We used an array of cylindrical nanopillars to create quantum emitters and discovered that single photon emitters with high purity are often formed on wrinkles rather than on the pillar apex. We also studied strain-tuned interlayer excitons in heterobilayers of 2D TMDs. We discovered that the strain exerted by nanopillars activates interlayer excitons in WSe_2/WS_2 heterobilayers irrespective of twist angles. We confirmed that the strain profile of the pillar apex is complex and that spectra associated with the pillar apex have multiple emission peaks with higher background. Wrinkles formed around the pillars, on the other hand, often generate spectra with lower background.

Summary of Research:

Monolayer transition metal dichalcogenides (TMDs) have been actively studied for quantum technology and optoelectronics due to their unique properties such as strong excitonic binding, a direct band gap, and spin-valley locking [1]. It has been shown that tensile strain modulates the band structure of 2D TMDs [2-4]. Site-localized tensile strain reduces the local band gap enabling excitons to be funneled into the strain potential before recombination, leading to single photon emission. Nanostructures such as nanopillars [2-3], nanorods [5], and nanobubbles [6] have been used to deterministically activate single photon emitters through this strain confinement. However, the strain induced by these nanostructures often have complex profiles and this typically results in multiple confining sites or large confining potential that hampers the single photon emission.

Our group has strain-tuned monolayer WSe_2 with cylindrical nanopillars and discovered that the wrinkle formed nearby the nanopillar gives rise to single photon emitters with higher purity as with compared to the emitters from the pillar apex (Figure 1) [7].

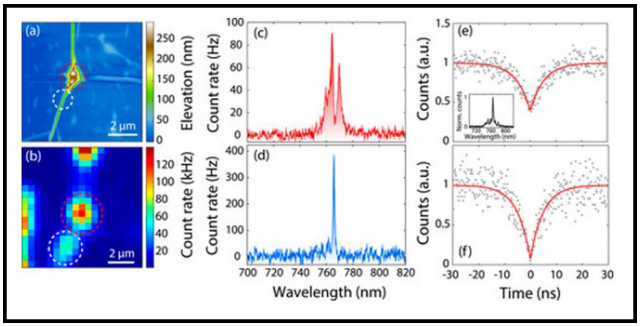

Figure 1: Comparison between pillar emission and wrinkle emission on WSe_2 stacked on nanopillars. (a) Atomic force microscopy image showing a pillar and wrinkles, (b) Photoluminescence map of the pillar (red) and wrinkle (white), (c),(e) spectrum and g2 measurement of emitters from the pillar apex. (d),(f) spectrm and g2 measurement of emitters from the wrinkle [7].

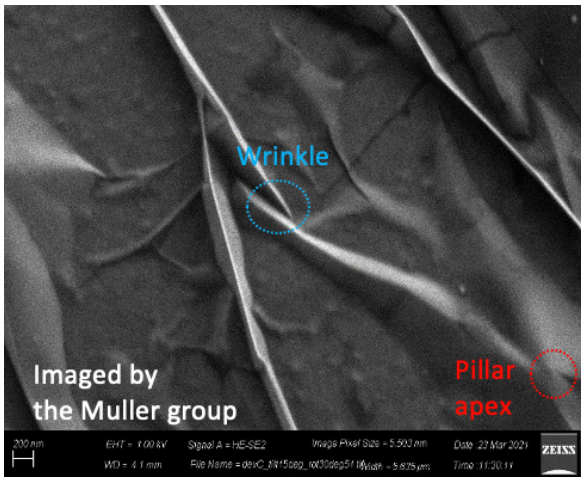

Figure 2: Scanning electron microscopy image of wrinkles formed on h-BN/WSe_2. The sharp folds on the wrinkle (blue) often exhibit sharp emission peaks.

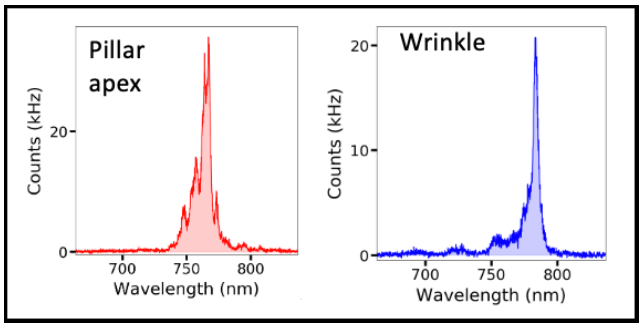

Figure 3: Spectra of interlayer excitons associated with the pillar apex (red) and wrinkle (blue).

The physics behind this finding can be better understood by quantifying the strain profile on the pillar apex and the wrinkle. With high resolution electron microscopy in collaboration with Professor David Muller's group, we found out that wrinkles with a sharp fold gives rise to single photon emitters with high purity (Figure 2). The characteristics of the strain exerted by wrinkles can be further explored by quantifying the strain gradient via electron microscopy, and this is in progress.

We also used nanopillars to activate interlayer excitons in a WSe_2/WS_2 heterobilayer. When two different TMD monolayers are stacked together, the electrons and holes find their energy minima in the composite material. When a bilayer is engineered such that the composite layer forms a type II band alignment, the coulomb-bound electron and hole can be separated into different layers. It has been found that the photoluminescence intensity of interlayer excitons is enhanced at 0° and 60° alignment angles, but significantly suppressed at intermediate angles due to the momentum mismatch [8]. We stacked WSe_2/WS_2 heterobilayer onto nanopillars and studied the strain effect.

We found that strain-tuned interlayer excitons exhibit fairly high photoluminescence intensity at any twist angle, which implies that momentum matching is not necessary when interlayer excitons are confined by the strain potential. We also observed that the spectra associated with wrinkles often exhibit sharper peaks with lower background compared to those associated with pillar apex (Figure 3), which is consistent with our work on monolayer WSe_2 [7].

Conclusions and Future Steps:

Nanopillars create a strain potential that confines excitons. We discovered that the emitters formed on wrinkles produce spectra with low background and sharp emission peaks. Also, strain-confined interlayer excitons exhibit high photoluminescence intensity irrespective of twist angle. Our next step is to quantify the strain profile on the wrinkle via electron microscopy, which will allow us to better understand the physics of wrinkles and design high-quality emitters more deterministically.

References:

[1] Mak, K., Shan, J., Nat. Photon 10, 216-226 (2016).

[2] Palacios-Berraquero, C., et al. Nat Commun 8, 15093 (2017).

[3] Branny, A., et al. Nat Commun 8, 15053 (2017).

[4] Chaves, A., et al. npj 2D Mater Appl 4, 29 (2020).

[5] So, Jae-Pil, et al. Nano Lett 21, 1546-1554 (2021).

[6] Darlington, T.P., et al. Nat Nanotechnol. 15, 854-860 (2020).

[7] Rapahel S. Daveau, et al. APL Photonics 5, 09615 (2020).

[8] Nayak K. Pramoda, et al. ACS Nano 11, 4, 4041-4050 (2017).

Mechanically Driven Electron Spins with a Diamond Thin-Film Bulk Acoustic Resonator

CNF Project Number: 2126-12

Principal Investigator(s): Gregory Fuchs[1]

User(s): Johnathan Kuan[2], Anthony D'Addario[2]

Affiliation(s): 1. Department of Applied and Engineering Physics, Cornell University; 2. Department of Physics, Cornell University

Primary Source(s) of Research Funding: Defense Advanced Research Projects Agency-DARPA DRINQS program (Cooperative Agreement #D18AC00024)

Contact: gdf9@cornell.edu, jk2788@cornell.edu, ajd344@cornell.edu

Website: https://fuchs.research.engineering.cornell.edu/

Primary CNF Tools Used: OEM Endeavor M1, Westbond 7400A ultrasonic wire bonder

Abstract:

Lattice strain has been demonstrated to be an effective method of coherently manipulating electron spins in solid state defect centers such as the diamond nitrogen-vacancy center. In previous experiments, strain is introduced into the diamond lattice through a high overtone bulk acoustic resonator (HBAR). To improve the strain and power efficiency of bulk acoustic resonators for quantum control, we develop and characterize a diamond thin-film bulk acoustic resonator. We measure the electromechanical performance of the device and demonstrate coherent driving of a double quantum transition a nitrogen-vacancy center (NV) of electron spin ensemble.

Summary of Research:

The diamond nitrogen-vacancy (NV) center is a well characterized solid state defect center consisting of a substitutional nitrogen impurity adjacent to a lattice vacancy. The NV center electron spin interacts with many external fields (magnetic, electric, etc.), making it an excellent platform for quantum sensing. In addition to the electron spin, the NV center has a native nitrogen nuclear spin, which is coupled to the electronic spin through a hyperfine interaction. This provides an opportunity to use the nuclear spin for sensing applications, with state preparation and readout facilitated by the electron spin. However, the hyperfine interaction also provides an additional source of decoherence for the nuclear spin, limiting the sensitivity of any potential quantum sensing protocols employing these spins. It has been shown that strong driving of the electron spin can help protect the coherence of the nuclear spin [1]. Previous experiments with high overtone bulk acoustic resonators (HBAR) on diamond have demonstrated electron spin driving with lattice strain for coherent control [2], and continuous dynamical decoupling for protecting electron spin coherence [3].

To achieve strong driving of the electron spin with lattice strain, we fabricate thin-film bulk acoustic resonators (FBAR) on single crystal diamond (Figure 1). The FBAR resonators consist of a 1.5 μm AlN transducer, with a bottom (Al) electrode and a top (Pt) electrode. The transducer is deposited onto a 10 μm thick optical grade diamond, which is created through reactive ion etching. The AlN film is sputtered using the OEM Endeavor M1 tool at CNF. Compared to previous generations of ZnO HBAR on diamond, the AlN diamond FBAR has better power handling, which allows for much stronger acoustic driving of electron spins by simply applying more power. To provide microwave control of the spins, we also fabricate a loop antenna, which surrounds the FBAR.

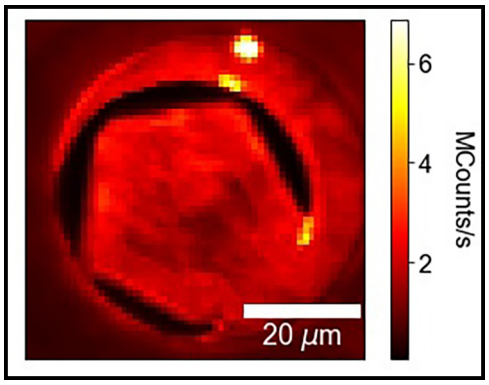

Figure 1: Photoluminescence image of an AlN FBAR on diamond. The FBAR (pentagonal feature) consists of a 1.5 μm AlN film that is sandwiched by an Al bottom electrode and a Ti/Pt top electrode. This stack is on top on a 10 μm diamond membrane.

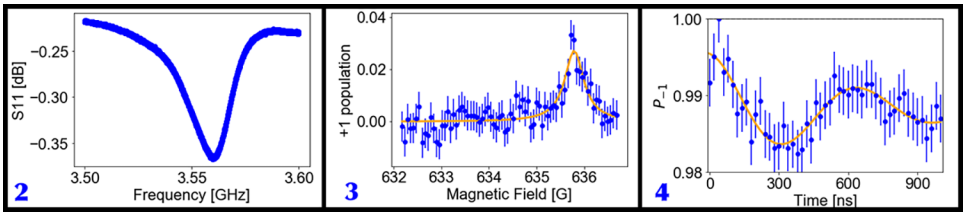

Figure 2, left: S11 measurement of the 3.56 GHz acoustic mode of the AlN FBAR. Figure 3, middle: Spectroscopy of the double quantum transition. The resonator frequency is fixed at 3.56 GHz while the Zeeman splitting between the ms = -1 and ms = +1 states is swept. The peak at approximately 636 G gives the external field necessary to tune the double quantum transition in resonance with the acoustic mode. Figure 4, right: Rabi driving of the double quantum transition with a Rabi field of 1.7 MHz.

We measure the electromechanical resonances of the AlN FBAR by measuring the S11 response with a vector network analyzer. To characterize the device, we focus on an acoustic mode at 3.56 GHz (Figure 1) with a low quality factor (~10). We coherently drive a double quantum transition (ms = -1 to ms = +1) with this mode to measure the lattice strain in the diamond. To ensure that the acoustic mode is resonantly driving the electron spin, we perform spectroscopy where the Zeeman splitting between ms = -1 to ms = +1 is swept [3]. This locates the correct external magnetic field to apply along the NV symmetry axis, which will tune the electron spin transition in resonance with the acoustic mode. Using this field, we drive Rabi oscillations of the electron spin using acoustic pulses and measure the strain in the FBAR through the Rabi frequency [4]. In this device, we drive the electron spin using an electromechanical mode at 3.5 GHz. The measured Rabi field from the oscillations is 1.7 MHz, which is comparable with the hyperfine splitting of the NV center (2.1 MHz).

Conclusions and Future Steps:

We have developed a process for fabricating AlN FBARs on diamond to drive electron spins. To improve the acoustic driving, we aim to improve the quality factor of the resonator. This can be achieved by adjusting the dimensions of the resonator and the diamond substrate. In addition, we are looking at optimizing this process for isotopically pure CVD diamond. Isotopically pure diamond can host NV centers with phase coherence times on the order of 10 μs, making it an excellent substrate for developing a quantum sensor.

References:

[1] M Chen, W. K. C. Sun, K Saha, J. Jaskula, and P. Cappellaro. "Protecting solid-state spins from a strongly coupled environment". New Journal of Physics 20.6 (2018).

[2] E. R. MacQuarrie, T. A. Gosavi, A. M. Moehle, N. R. Jungwirth, S. A. Bhave, and G. D. Fuchs, Coherent control of a nitrogen-vacancy center spin ensemble with a diamond mechanical resonator, Optica 2, 233 (2015).

[3] E. R. MacQuarrie, T. A. Gosavi, S. A. Bhave, and G. D. Fuchs, Continuous dynamical decoupling of a single diamond nitrogen-vacancy center spin with a mechanical resonator, Phys. Rev. B 92, 224419 (2015)

[4] E. R. MacQuarrie, T. A. Gosavi, N. R. Jungwirth, S. A. Bhave, and G. D. Fuchs, Mechanical spin control of nitrogen-vacancy centers in diamond, Phys. Rev. Lett. 111, 227602 (2013).

Fabrication of Nanophotonic Optical Cavity Device from Inverse Design

CNF Project Number: 2126-12

Principal Investigator(s): Gregory D. Fuchs[1]

User(s): Jialun Luo[2]

Affiliation(s): 1. School of Applied and Engineering Physics, 2. Department of Physics; Cornell University

Primary Source(s) of Research Funding: National Science Foundation (ECCS-1839196)

Contact: gdf9@cornell.edu, jl3562@cornell.edu

Website: http://fuchs.research.engineering.cornell.edu

Primary CNF Tools Used: AJA sputter deposition, OEM Endeavor AlN sputtering system, JEOL 9500, JEOL 6300, PT770 etcher, AJA ion mill, P10 profilometer, P-7 profilometer, GCA 5x stepper

Abstract:

On-demand polarized single-photons are essential in realizing many photon-based quantum communication protocols [1]. We developed and fabricated a nanophotonic cavity device from aluminum nitride (AlN) whose structure was calculated from an inverse design method. The structure serves as a platform for enhancing the collection of single photons from isolated defects hosted in hexagonal boron nitride (h-BN). We present an update on our work-in-progress on the fabrication of the device.

Summary of Research:

Hexagonal boron nitride is an interesting 2D material due to bright optically active defects hosted within and to the possibilities of integrating with other 2D materials [2]. Researchers have been able to create isolated defects by methods such as ion implantation with carbon [3]. The defects are stable under room temperature and have zero-phonon line fluorescence at 585 nm [4]. People have been able to create or find isolated these defects. The combination of emission brightness and the capability of isolating them makes h-BN defects promising candidates as single-photon sources. In this project, we aim to fabricate an inverse design nanophotonic cavity structure and characterize its capability of enhancing photon emissions. The cavity structure further enhances the emission of h-BN defects placed on them due to the Purcell effect and modifies the emission angle of these defects so one can more efficiently collect the photons [5].

We fabricated the current generation devices on Si wafers, which allows us to cleave the sample and inspect the cross section. The devices are made from AlN sputtered by the OEM Endeaver M1 AlN sputter system. The structure is patterned with the JEOL 9500 electron beam lithography system and is subsequently etched with a Cl_2 plasma reactive ion etching process in the PT770 etcher.

Figure 1 shows (a) the design target structure and (b) the field profile at resonance at 600 nm. Figure 1c shows the mask pattern prior to AlN etching, indicating a good fidelity of patterning from design structure. However, as seen in Figure 1d, the AlN etching step is problematic due to high aspect ratio (15:1) and results in slanted sidewalls and incomplete etching of the interior of the pattern.

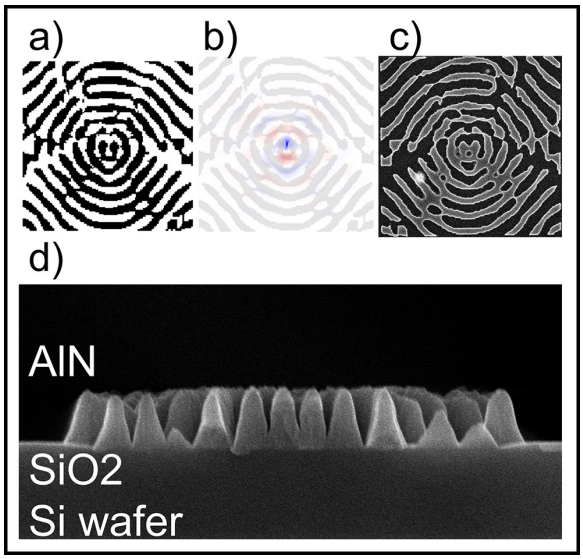

Figure 1: a) The target device structure from inverse design. Black indicates substrate and white air. b) The field mode profile at 600 nm resonance. Note that most of the energy is concentrated at the central region. c) An SEM image of the Cr hard mask before the final AlN etch. d) An SEM image of the cross section of the device.

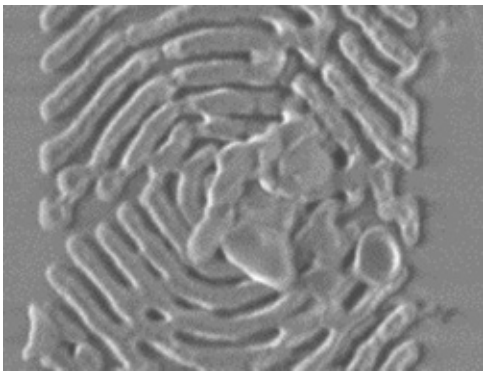

Figure 2: A top-down SEM image of a few h-BN nanoflakes on top of the AlN device.

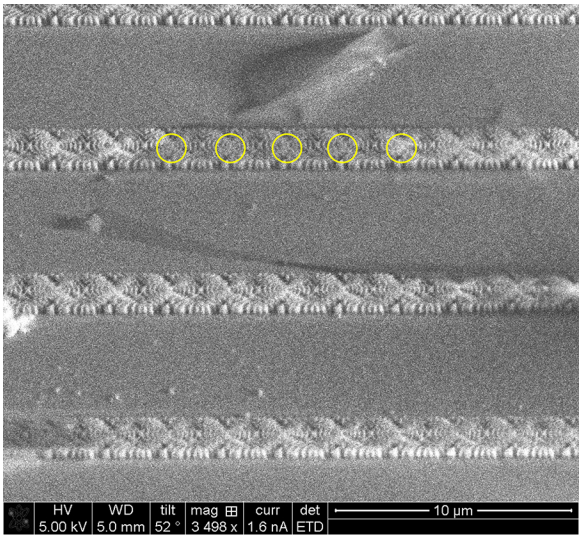

Figure 3: An SEM image of an exfoliated h-BN flake over a few cavity devices. The circles indicate the regions for focused ion beam milling to create defects.

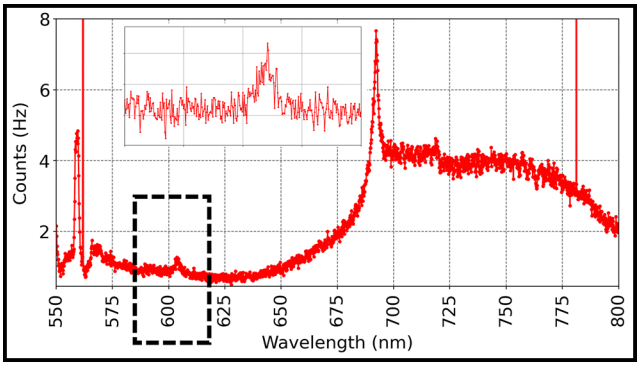

Figure 4: A spectrum taken at the central region of the cavity device. The insert magnifies around the spectral feature around 604 nm.

While we continue to improve the fabrication process, we started testing strategies of placing single emitting h-BN defects on the cavity structure. Figure 2 shows our early attempts of placing h-BN nanoflakes on top of the device through drop-casting sufficiently many of them on a chip containing many of such cavity devices. We also tried placing an exfoliated h-BN flake over the device and creating defects by lightly milling the flake with focused ion beam (Figure 3). Unfortunately, the early attempts did not result in single emitters in the range of the enhancement region. However, we observed an enhancement of the background fluorescence near the device center at 604 nm, which likely comes from the device as shown in Figure 4.

Future Work:

We are exploring ways of creating and positioning single defects in h-BN with better repeatability. We also pursue a different design which optimizes upward photon flux which may achieve a higher photon collection rate.

Acknowledgements:

We would like to thank members of the Rodriguez Group on the discussion on and their designs of the nanophotonic cavity structures.

References:

[1] Bennett, C. H. and Brassard, G. Quantum cryptography: Public key distribution and coin tossing. Theoretical Computer Science 560, 7-11 (2014).

[2] Aharonovich, I., Englund, D., and Toth, M. Solid-state single-photon emitters. Nature Photonics 10, 631-641 (2016).

[3] Mendelson, N., et al. Identifying carbon as the source of visible single-photon emission from hexagonal boron nitride. Nat. Mater. 20, 321-328 (2021).

[4] Jungwirth, N. R. and Fuchs, G. D. Optical Absorption and Emission Mechanisms of Single Defects in Hexagonal Boron Nitride. Phys. Rev. Lett. 119, 057401 (2017).

[5] Molesky, S., et al. Inverse design in nanophotonics. Nature Photonics 12, 659-670 (2018).

Charge-Order-Enhanced Capacitance in Semiconductor Moiré Superlattices

CNF Project Number: 2633-18

Principal Investigator(s): Jie Shan, Kin Fai Mak

User(s): Tingxin Li, Jiacheng Zhu

Affiliation(s): Laboratory of Atomic and Solid State Physics, School of Applied and Engineering Physics; Cornell University

Primary Source(s) of Research Funding: Department of Energy

Contact: jie.shan@cornell.edu, kinfai.mak@cornell.edu, tl684@cornell.edu, jz969@cornell.edu;

Primary CNF Tools Used: Autostep i-line stepper, Hamatech wafer processor develop, Heidelberg mask writer - DWL2000, photolithography spinners, CVC SC4500 odd/even-hour evaporator, DISCO dicing saw

Abstract:

Van der Waals moiré materials have emerged as a highly controllable platform to study the electronic correlation phenomena. In particular, robust correlated insulating states have recently been discovered at both integer and fractional filling factors of the semiconductor moiré systems. In this project, we study the electronic compressibility of $MoSe_2/WS_2$ moiré superlattices by capacitance measurements. Our results reveal the thermodynamic properties and illustrate mechanism for enhanced capacitance in semiconductor moiré superlattices.

Summary of Research:

Quantum capacitance C_Q represents electronic compressibility or thermodynamic density of states of an electronic system that relates to its thermodynamic properties [1]. Quantitative measurement of C_Q can be realized by measuring differential capacitance per unit area C ($C^{-1} = C_g^{-1} + C_Q^{-1}$ with C_g denoting the geometrical capacitance between sample and gate) [2]. Semiconductor moiré superlattices host strongly correlated insulating states [3]. In this project, we demonstrate capacitance measurements on such system, which not only provide thermodynamic quantities but also offer new insight into correlations in van der Waals heterostructures.

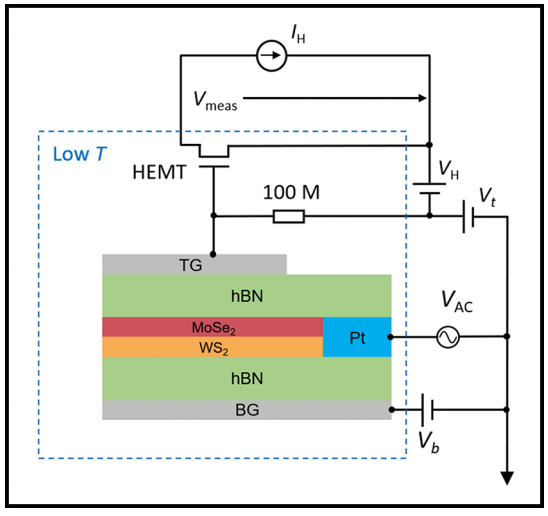

Figure 1: Schematics of a dual-gate device structure and electrical connections for capacitance measurements. TG and BG denote the top and back gate, respectively.

Figure 1 shows the schematics of dual-gated device structures and electrical connections for capacitance measurements. The device is made of an angle-aligned $MoSe_2$ and WS_2 heterobilayer encapsulated by top and bottom graphite gates separated by hexagonal boron nitride (h-BN) dielectrics. Angle-aligned $MoSe_2/WS_2$ heterobilayers form a triangular moiré superlattice with moiré period $a_M \approx 8$ nm due to 4% lattice mismatch between these materials. A commercial high electron mobility transistor (HEMT, model FHX35X) is used as the first-stage amplifier to effectively reduce the parasitic capacitance from cabling [4]. To obtain the top gate capacitance, we apply an AC voltage (10 mV in amplitude) to the moiré superlattice and collected the signal from the top gate through the HEMT.

Figure 2 is an optical image of a typical device. The Pt electrodes are patterned on the Si/SiO_2 substrates by photolithography and metal evaporation. Atomically thin samples of $MoSe_2$, WS_2, h-BN, and graphite are first exfoliated from their bulk crystals onto silicon substrates covered with a 300 nm thermal oxide layer. Selected thin flakes of appropriate thickness and geometry are then picked up one-by-one by a stamp consisting of a thin layer of polycarbonate on polydimethylsiloxane (PDMS). The complete heterostructure is then deposited onto the substrates with pre-patterned Pt electrodes.

Figure 3 shows the measured differential capacitance C in the unit of C_g as a function of top gate voltage measured at 10 K and bottom gate voltage V_b = 5.3 V. We observe a step increase of capacitance around -4 V when the Fermi level enters the conduction band of $MoSe_2$. The capacitance plateaus out above ~ 0 V when the sample is heavily electron doped. We calibrate capacitance using these two limits: $C / C_g = 0$ when the Fermi level lies inside the superlattice band gap (> 1 eV) and the sample is insulating (incompressible); $C / C_g \approx 1$ when the sample is heavily doped and behaves as a good conductor. At intermediate gate voltages, we identify a series of capacitance dips (incompressible states). The most prominent ones appear equally spaced in gate voltage and are assigned integer fillings ν = 1, 2, 3 and 4. The assignment is consistent with the known moiré density and the carrier density n evaluated from the gate voltage and $C_g \approx 2.1 \times 10^{-7}$ Fcm^{-2}. The latter is determined from the permittivity and thickness of the h-BN gate dielectric d ($\varepsilon \approx 3\varepsilon_0$ with ε_0 denoting the vacuum permittivity).

It was independently verified by including a reference capacitor on the measurement chip.

We observe anomalously large capacitance in the compressible regions between the incompressible states. The enhancement is particularly large at small doping densities with C exceeding C_g by ~ 30% for device with $d/a_M \approx 1$. Figure 4 shows devices of different sample-gate separation ($d/a_M \approx 0.6, 0.8, 1.0$ and 1.5). The capacitance enhancement increases with decreasing d/a_M. It is as high as 60% in device with $d/a_M \approx 0.6$ at 10 K.

The experimental results show that the correlation effects are strongly dependent on sample-gate separation in devices with $d/a_M \sim 1$, particularly, for the fractional-filling states since the gate electrodes effectively screen the extended Coulomb interactions. In this regime where electronic interactions dominant and sample gate distance is comparable to electron separations, we need to describe the entire device as one system [5].

In conclusion, our study establishes capacitance as a powerful thermodynamic probe of the correlated states in semiconductor moiré superlattices. It also illustrates the importance of sample-gate coupling and the device-geometry-dependent extended Coulomb interaction at fractional fillings.

References:

[1] Ando, T., Fowler, A. B. and Stern, F. Electronic properties of two-dimensional systems. Rev. Mod. Phys. 54, 437-672 (1982).

[2] Smith, T. P., Goldberg, B. B., Stiles, P. J., and Heiblum, M. Direct measurement of the density of states of a two-dimensional electron gas. Phys. Rev. B. 32, 2696-2699 (1985).

[3] Xu, Y., et al. Correlated insulating states at fractional fillings of moiré superlattices. Nature 587, 214-218 (2020).

[4] Ashoori, R. C., et al. Sigle-Electron Capacitance Spectroscopy of Discrete Quantum Levels. Phys. Rev. Lett. 68, 3088-3091 (1992).

[5] Skinner, B., and Shklovskii, B. I. Anomalously large capacitance of a plane capacitor with a two-dimensional electron gas. Phys. Rev. B 82, 155111 (2010).

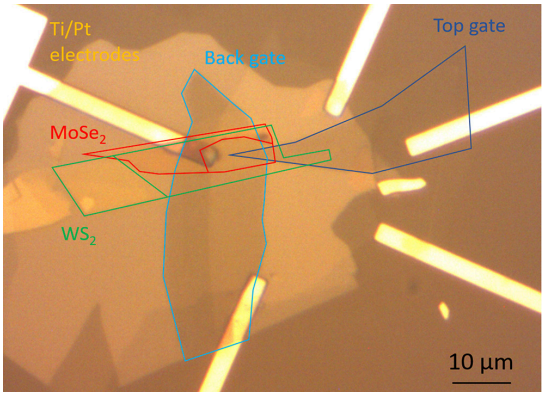

Figure 2: Optical microscope image of a dual-gate device. Colored lines show the boundary of the $MoSe_2$, WS_2, top gate and bottom gate flakes, respectively. Scale bar is 10 μm.

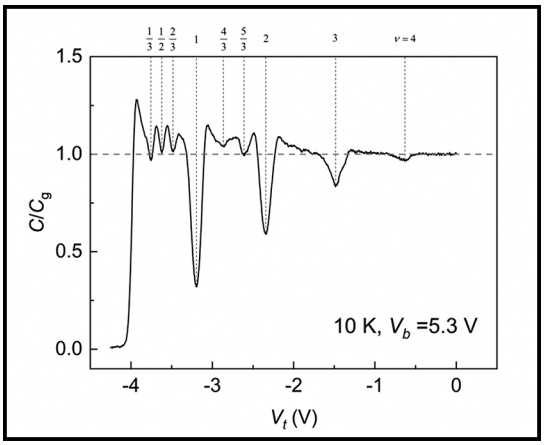

Figure 3: Differential top gate capacitance as a function of top gate voltage at 10 K for Device with $d/a_M \approx 1$. The back gate voltage is fixed at 5.3 V. The filling factors for discernable incompressible states are labeled on the top axis.

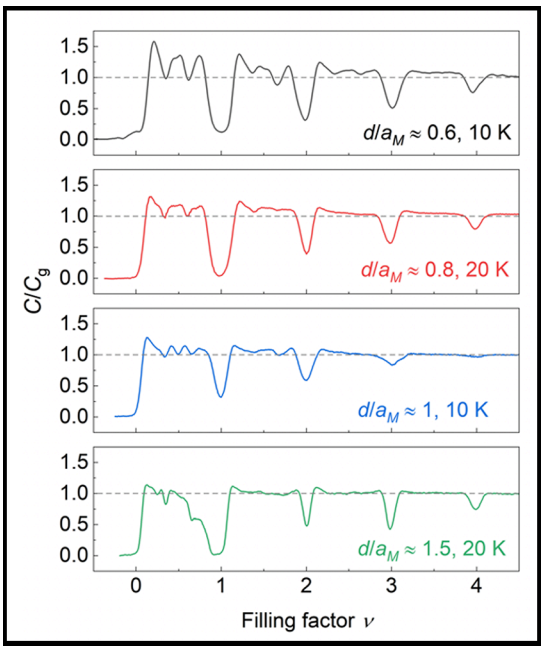

Figure 4: Experimental top gate capacitance as a function of filling factor for devices with $d/a_M \approx 0.6, 0.8, 1.0$ and 1.5 (from top to bottom) at the lowest temperature (10 K or 20 K) allowed by the sample/contact resistance.

Thermal and Electrical Properties of Quasi-1D van der Waals Nanowires

CNF Project Number: 2698-18

Principal Investigator & User: Deyu Li

Affiliation(s): Department of Mechanical Engineering, Vanderbilt University

Primary Source(s) of Research Funding: National Science Foundation

Contact: deyu.li@vanderbilt.edu

Primary CNF Tools Used: Heidelberg mask writer - DWL2000, Autostep i-line stepper, LPCVD nitride - B4, GSI PECVD, AJA sputter deposition, AJA ion mill

Abstract:

Using the microdevices fabricated at CNF, we conducted extensive measurements of thermal transport through quasi-one-dimensional (quasi-1D) van der Waals (vdW) crystal $NbSe_3$ nanowires. Dimensional transition from 3D to 1D was demonstrated when the nanowire diameter scales down below 26 nm. Importantly, we found that one-dimensional (1D) phonons led to superdiffusive transport with the nanowire thermal conductivity becoming divergent with the wire length following a 1/3 power law extending over an unprecedented 42.5 μm. This important result has been published in *Nature Nanotechnology*.

Summary of Research:

Because of the pandemic, no on-site nanofabrication at CNF was conducted during the reporting period. However, using the previously fabricated microdevices, we conducted extensive measurements of thermophysical properties of quasi-1D vdW crystal $NbSe_3$ of different diameters and lengths. The schematic diagram of the measurement scheme, an SEM micrograph of an $NbSe_3$ wire placed on the measurement device, and a TEM micrograph of an ultra-thin nanowire were shown in Figure 1.

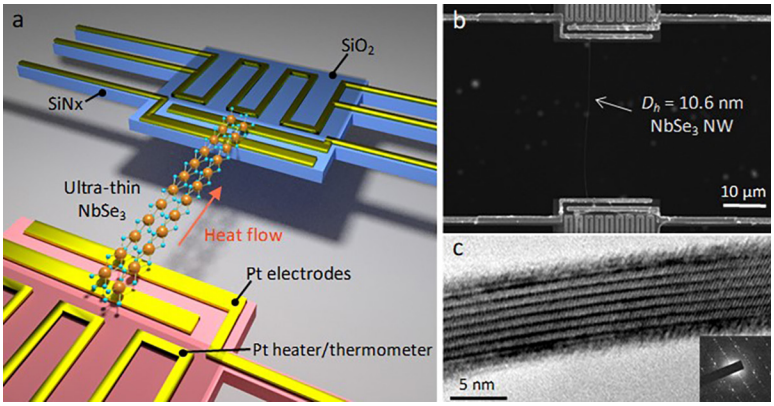

Figure 1: (a) Schematic illustration of the measurement scheme. (b) An SEM micrograph showing a nanowire on the device with a suspended length of 28.2 μm. (c) An HRTEM image of an ultra-thin $NbSe_3$ nanowire showing the crystalline structure.

These measurements have led to a major breakthrough with the first experimental observation of superdiffusive transport of 1D phonons, which has been published in *Nature Nanotechnology* [1].

In 1955, Fermi, Pasta, Ulam, and Tsingou reported their "shocking little discovery" that an excited vibration mode in single atomic chains did not dissipate into heat over a long period of time, which attracted tremendous attention due to its broad implications. A direct consequence of this discovery is that the thermal conductivity of 1D lattices becomes divergent with the chain length, suggesting a type of thermal superconductors of ever-increasing thermal conductivity with the sample length.

The concept remains purely conceptual and is regarded as of academic interest only as single atomic chains of sufficient length remain experimentally unattainable.

Our study shows that the thermal conductivity of ultra-thin $NbSe_3$ nanowires increases with the wire length beyond a record level of 42.5 μm following a 1/3 power law, providing the first experimental evidence for superdiffusive transport.

Figure 2a plots the measured room temperature thermal conductivity (κ) versus the hydraulic diameter (D_h) of the nanowires, with all nanowires of ~ 15 μm long. Interestingly, the data indicate a clear transition at D_h = 26 nm. For thicker wires, κ decreases as D_h reduces due to phonon-boundary scattering; however, as D_h further drops, κ demonstrates an unexpected steep upward trend with ~ 25 fold increase for a 6.8 nm wire.

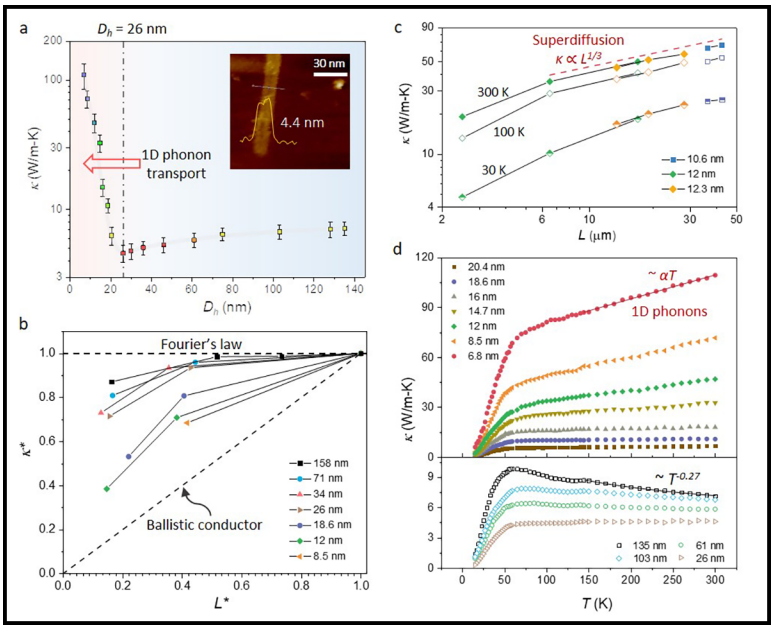

Figure 2: Divergent and superdiffusive transport of 1D phonons. (a) Measured room temperature thermal conductivity (κ) versus the hydraulic diameter (D_h). Inset: AFM scanning profile of the nanowire with D_h = 6.8 nm. (b) Normalized room temperature κ versus the normalized suspended length, which indicates a convergence-divergence transition as D_h decreases. (c) Measured κ versus suspended length at different temperatures. (d) Temperature dependence of κ for different diameter wires.

Next we examine the length dependence of κ, and Figure 2b plots the normalized room temperature thermal conductivity, κ^*, versus the normalized suspended length, L^*, both with respect to the values of the respective longest wires (~ 15 μm), for seven wires of different D_h. Interestingly, for wires with larger D_h, κ first increases with L from ~ 2 to ~ 6 μm, and then converges to a saturated value. However, as D_h reduces to below 26 nm, κ exhibits a much stronger length dependence even for $L > 6\,\mu$m, suggesting a transition from convergence to divergence.

To further explore the length dependence, we measured more samples with much longer suspended length. Figure 2c indicates that for nanowires with D_h in the range of 10 to 12 nm, the length dependence extends beyond 42.5 μm, much larger than the previously reported values for different wires. Interestingly, in the length range of > 6.5 μm, the measured κ follows a trend of $\kappa \propto L^{1/3}$, consistent with the theoretical prediction of superdiffusive phonon transport in 1D lattices.

To further confirm the superdiffusive transport, we also plot the measured κ at 100 K, which again follows the trend of $\kappa \propto L^{1/3}$ in the same length range. This consistent trend over very different temperatures of 100 and 300 K strongly suggests that the length dependence in the range of > 6.5 μm is due to the superdiffusive behavior of 1D phonons, instead of partially ballistic transport.

This intriguing transport is due to excitation of 1D phonons in the ultra-thin nanowires, as shown in Figure 2d with a linear increasing trend for thinner wires in the temperature range of 50-300 K (upper panel) in contrast to the decreasing trend of thicker wire dure to Umklapp scattering (lower panel).

In addition to this important discovery, we have also done other measurements with the microdevices and published two papers [2,3].

References:

[1] L. Yang, Y. Tao, Y. Zhu, M. Akter, K. Wang, Z. Pan, Y. Zhao, Q. Zhang, Y. Xu, R. Chen, T. T. Xu, Y. Chen, Z. Mao, and D. Li, "Observation of Superdiffusive Phonon Transport in Aligned Atomic Chains," Nature Nanotechnology, published online, DOI: 10.1038/s41565-021-00884-6 (2021).

[2] Z. Pan, L. Yang, Y. Tao, Y. Zhu, Y.-Q. Xu, Z. Mao, and D. Li, "Net Negative Contributions of Free Electrons to the Thermal Conductivity of $NbSe_3$ Nanowires," Phys. Chem. Chem. Phys. 22, 21131-21138 (2020).

[3] Y. Zhao, M. L. Fitzgerald, Y. Tao, Z. Pan, G. Sauti, D. Xu, Y.-Q. Xu, and D. Li, "Electrical and Thermal Transport through Silver Nanowires and their Contacts: Effects of Elastic Stiffening," Nano Lett. 20, 7389-7396 (2020).

Superconducting Thin Film Growth, Process Development, Defects Investigation, and Device Fabrication for Radio-Frequency Accelerating Cavities

CNF Project Number: 2779-19

Principal Investigator(s): Matthias Liepe

User(s): Zeming Sun

Affiliation(s): Cornell Laboratory for Accelerator-based Sciences and Education, Cornell University

Primary Source(s) of Research Funding: National Science Foundation under Grant No. PHY-1549132

Contact: mul2@cornell.edu, zs253@cornell.edu

Website: https://physics.cornell.edu/matthias-liepe

Primary CNF Tools Used: Thermal / e-gun evaporation system, Oxford FlexAL atomic layer deposition system, Jelight 144AX UV ozone generator, Arradiance Gemstar-6 atomic layer deposition system, chemical vapor deposition system, Woollam spectroscopic ellipsometer, Zygo optical profilometer, P10 profilometer

Abstract:

Superconducting radio-frequency (SRF) cavities are the essential component for accelerating charged particle beams that have broad applications such as high-energy colliders, high-intensity X-ray sources, high-precision photolithography, and quantum computing. Niobium tin (Nb_3Sn), conventional niobium (Nb) with a processed/designed surface, niobium titanium nitride (NbTiN), and vanadium silicate (V_3Si) are the most promising superconductor candidates for the next-generation SRF cavities. Here, with the capabilities at the Cornell NanoScale Science and Technology Facility (CNF), we mainly focus on SRF thin film growth development, materials characterization together with sample preparation, post-treatment development to improve RF superconducting properties, and SRF device fabrication to fundamentally understand some SRF physics theories.

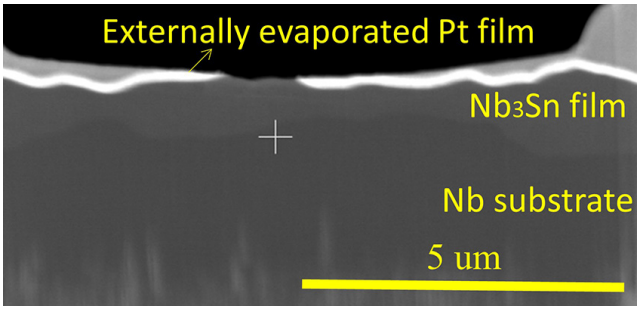

Figure 1: Cross-sectional image of STEM specimens that yield high-resolution atomic imaging.

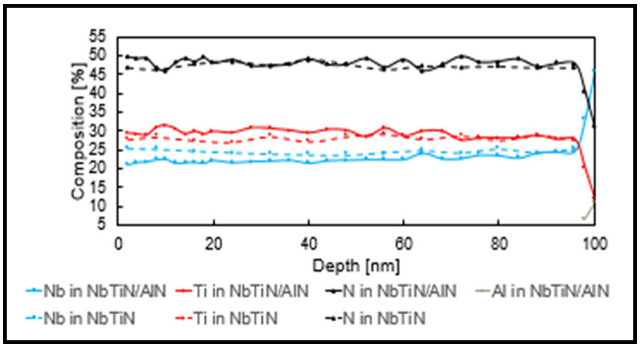

Figure 2: Composition depth profiles of Nb, Ti, N, and Al for atomic-layer-deposited NbTiN/AlN and NbTiN-only films on Nb substrates [5].

Summary of Research:

(1) We demonstrated stoichiometric Nb_3Sn thin films with extremely low surface roughness from electrochemical deposition [1-3]. Reduction of surface roughness and retention of stoichiometry are critical to improving the RF performance of accelerating cavities. We are further investigating the growth mechanism of this Nb_3Sn film using scanning transmission electron microscopy (STEM) through collaborating with Zhaslan Baraissov and Prof. David Muller's research group at Cornell Applied Physics.

High-resolution atomic imaging requires a thin specimen below ~ 10 nm. However, the sample preparation via focused ion beam (FIB) was difficult due to the lack of a proper protection layer for the film surface. We have resolved this issue by depositing an external Pt layer using the e-beam evaporator at CNF (Figure 1), and achieved high-resolution composition and strain mappings [4].

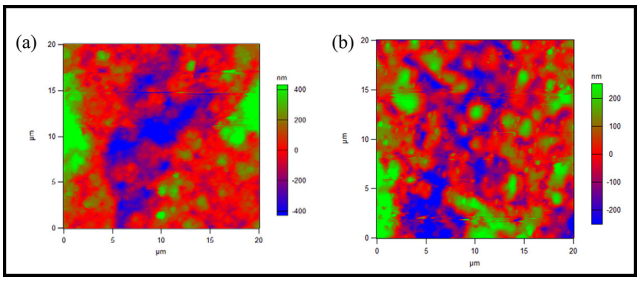

Figure 3: Atomic force microscopy images of Nb_3Sn (a) before and (b) after laser annealing [8].

(2) Alternative deposition approaches such as sputtering, chemical vapor deposition, and atomic layer deposition are being explored to deposit Nb_3Sn, NbTiN, and V_3Si films [2,5-7]. We observed a composition gradient in the atomic-layer-deposited NbTiN films in presence of an hcp-structured aluminum nitride (AlN) layer for the superconductor-insulator-superconductor (SIS) structures (Figure 2) [5]. Moreover, thermal annealing of the sputtered Nb_3Sn and V_3Si films has been systematically investigated on Nb and Cu substrates [6]. In addition, the chemical-vapor-deposition system and process are being developed [7].

(3) Post processes such as ozone treatment, laser annealing, and electropolishing are explored to improve the superconducting film quality. We demonstrated that laser annealing is viable to remove the sharp features on the Nb_3Sn film surface that is coated with a laser absorption layer via an Arradiance Gemstar-6 atomic layer deposition system at CNF (Figure 3) [8]. Also, we successfully electropolished the chemical-vapor-deposited Nb film and reduced the surface roughness by half [9]. Furthermore, we are exploring the Nb surface modification using the Jelight 144AX UV ozone generator at CNF [10].

(4) SRF devices are fabricated using the e-beam evaporator and Oxford FlexAL atomic layer deposition system at CNF, and these devices are being tested to fundamentally understand some SRF theories prior to application of these theories on the large, complex-shaped SRF cavities.

References:

[1] Z. Sun, et al., "Toward stoichiometric and low-surface-roughness Nb_3Sn thin films via direct electrochemical deposition", presented at the International Conference on RF Superconductivity (SRF'21), virtual, June 2021.

[2] Z. Sun, et al., "Study of alternative materials for next generation SRF cavities at Cornell University", presented at the 9th International Workshop on Thin Films and New Ideas for Pushing the Limits of RF Superconductivity, virtual, March 2021.

[3] Z. Sun, et al., "Electrochemical deposition for generating Nb_3Sn films with low surface roughness and stoichiometry", presented at the International Workshop on Nb_3Sn SRF Science, Technology, and Applications (Nb_3SnSRF'20), November 2020.

[4] Z. Baraissov, et al., "Measuring composition variation and lattice strain in Nb_3Sn films", presented at the International Conference on RF Superconductivity (SRF'21), virtual, June 2021.

[5] Z. Sun, et al., "Characterization of atomic-layer-deposited NbTiN and NbTiN/AlN films for SIS multilayer structures", presented at the International Conference on RF Superconductivity (SRF'21), virtual, June 2021.

[6] K. Howard, et al., "Thermal annealing of sputtered Nb_3Sn and V_3Si thin films for superconducting RF cavities", presented at the International Conference on RF Superconductivity (SRF'21), virtual, June 2021.

[7] G. Gaitan, et al., "Development of a system for coating SRF cavities using remote plasma chemical vapor deposition", presented at the International Conference on RF Superconductivity (SRF'21), virtual, June 2021.

[8] Z. Sun, et al., "Surface roughness reduction of Nb_3Sn thin films via laser annealing for superconducting radio-frequency cavities", presented at the International Particle Accelerator Conference (SRF'21), virtual, June 2021.

[9] Z. Sun, et al., "CVD thick Nb film and cavity coating", TESLA Tech. Collaboration workshop, Geneva, Switzerland, Feb, 2020.

[10] Z. Sun, et al., "Surface oxides on Nb and Nb_3Sn surfaces: toward a deeper understanding", presented at the International Conference on RF Superconductivity (SRF'21), virtual, June 2021.

Characterization of Extracellular Vesicles Produced from Glycocalyx-Engineered Cells *in vitro*

CNF Project Number: 2272-14

Principal Investigator(s): Dr. Matthew Paszek

User(s): Erik Chow

Affiliation(s): Department of Biomedical Engineering, Cornell University

Primary Source(s) of Research Funding: National Science Foundation Graduate Research Fellowship

Contact: paszek@cornell.edu, ec829@cornell.edu

Primary CNF Tools Used: Malvern NS300 NanoSight

Abstract:

Extracellular vesicles are key mediators of intercellular communication and are a rising area of biomedical research in disease diagnostics and therapeutics. However, surprisingly little is known about the glycobiology of extracellular vesicles, despite the fact that the cell glycocalyx dictates many of a cell's interactions. Specifically, very little is known about the role of the glycocalyx in EV production and function or whether EVs can be engineered through rational manipulation of the glycocalyx. Here we describe recent efforts to investigate the effects of glycocalyx engineering on the production of extracellular vesicles *in vitro*.

Summary of Research:

Extracellular vesicles (EVs) play a key role in intercellular communication. They have been shown to carry a wide range of cargoes, including DNA, coding and non-coding RNAs, and proteins. Because of the diverse nature of their cargoes, and their innate biocompatibility, EVs have quickly become a prominent focus in numerous areas of biomedical engineering research, including disease pathogenesis, diagnostics, drug delivery, and targeted therapies.

However, there are still many aspects of EV biology which are still poorly understood. One largely unexplored area is the significance of the glycocalyx — a polymer meshwork of proteins, nucleic acids, and glycans, which dictates numerous cellular interactions — on EV biogenesis and function. Specifically, the capacity for the production of rationally designed EVs through engineering of the glycocalyx remains poorly understood. It has been previously shown that engineering the glycocalyx can result in membrane morphologies which are favorable for the formation of certain types of EVs [1]. This report summarizes research from the last year which demonstrates that glycocalyx engineering, specifically be the overexpression of the mucin glycoprotein MUC1, results in an increase in production of EVs with size characteristics consistent with classical exosomes and microvesicles.

To engineer the glycocalyx, MCF10A cells were genetically engineered to overexpress a MUC1.mOxGFP construct on the cell membrane, hereafter referred to as MCF10A-1E7 cells. Expression of MUC1-mOxGFP in MCF10A-1E7s was tied to a tetracycline-inducible promoter, and cells were treated with doxycycline (Dox) for 24 hours at a concentration of either 0.1 ug/mL or 1 ug/mL to induce MUC1-mOxGFP overexpression. MCF10A cells engineered with only the promoter but no MUC1-mOxGFP construct, hereafter referred to as MCF10A-rtTA cells, were used as a negative control. After Dox treatment, the cells were switched to serum-free media and cultured at 37°C, 5% CO_2 for 15 hr to 18 hr. EV-containing media was harvested and EV concentration was measured by nanoparticle tracking analysis (NTA) using the Malvern NS300 NanoSight.

Figure 1 shows that media harvested from MCF10A-1E7 cells contained a higher concentration of EVs of sizes consistent with exosomes (50-150 nm) and microvesicles (100-1000 nm) compared to MCF10A-rtTA cells. Additionally, these data suggest that EV production in MCF10A-1E7 cells increased in a Dox concentration-dependent manner. These findings are further supported by Figure 2, which shows the EV concentrations of each of nine fractions obtained by density gradient ultracentrifugation

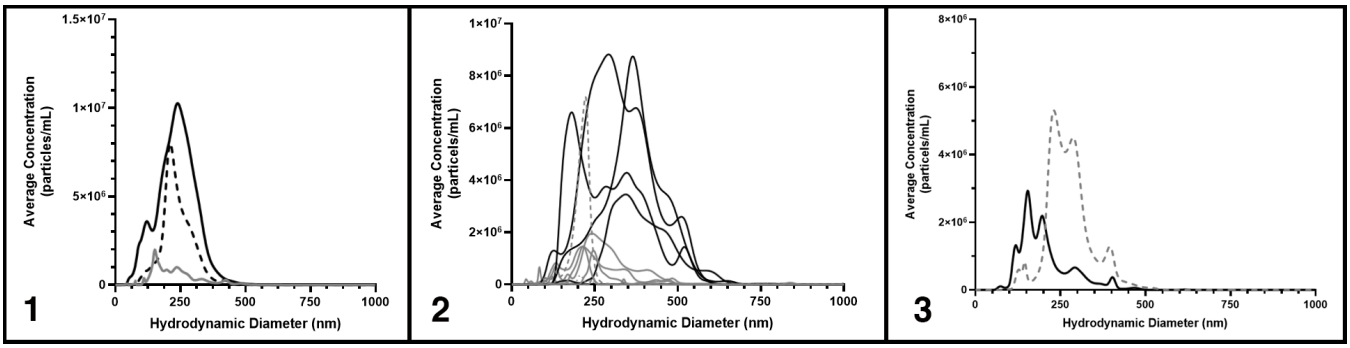

Figure 1. left: EV preparations from glycoengineered MCF10A cells. EV particle concentrations measured by NTA from MCF10A-rtTA cells (solid gray line), MCF10A-1E7 cells induced with 0.1 ug/mL Dox (dashed black line), and MCF10A-1E7 cells induced with 1 ug/mL Dox (solid black line). Curves represent the average reported concentration from five video recordings.

Figure 2, middle: Density gradient centrifugation of EVs from MCF10A-1E7 cells. EV particle concentrations measured by NTA from deionized water (neg. control, gray dotted line); 240 nm NIST nanospheres (pos. control, gray dashed line); density gradient fractions F1, F2, F7, F8, and F9 (solid gray lines); and density gradient fractions F3, F4, F5, and F6 (solid black lines). Curves represent the average reported concentration from five video recordings

Figure 3, right: Triton X-100 Treatment of EVs from MCF10A-1E7 cells. EV particle concentrations measured by NTA from mock-treated sample (neg. control, gray dotted line) or sample treated with Triton X-100 (solid black line). Curves represent the average reported concentration from five video recordings.

of EVs from MCF10A-1E7 cells using a protocol adapted from Jeppesen, et al. [2]. The vast majority of EVs were contained in fractions F3, F4, F5, and F6, which is consistent with previously published data of exosome samples [2]. Deionized water and NIST 240 nm nanospheres were used as negative and positive controls for EVs, respectively.

In order to validate that the particles analyzed by NTA were biological in origin, EVs from MCF10A-1E7 cells were treated with 0.1% Triton X-100 at room temperature for 10 min to solubilize lipid membranes. Mock-treated MCF10A-1E7 EVs were used as a negative control. Figure 3 shows the dramatic reduction in both the EV concentration and the average EV size profile following Triton X-100 treatment, demonstrating that the samples do in fact contain EVs bound by biological lipid membranes.

Conclusions and Future Steps:

Altogether, these data provide the first evidence that EV production can be controlled by engineering the glycocalyx of cells. Further experiments are needed to conclusively prove that the particles detected by NTA contain the classical exosome or microvesicle markers, such as CD63, ALIX, TSG-101, and Annexin A1.

Additionally, future experiments will strive to study the glycobiology of these engineered EVs. More NTA experiments will be conducted at the CNF as part of an effort to reliably segregate exosomes and microvesicles in order to more precisely study the exosome and microvesicle glycocalyx properties.

References:

[1] Shurer, C. R., Kuo, J. C.-H., Roberts, L. D. M., Gandhi, J. G., Colville, M. J., Enoki, T. A., Pan, H., Su, J., Noble, J. M., Hollander, M. J., O'Donnell, J. P., Yin, R., Pedram, K., Möckl, L., Kourkoutis, L. F., Moerner, W. E., Bertozzi, C. R., Feigenson, G. W., Reesink,

H. L., and Paszek, M. J. (2019). Physical Principles of Membrane Shape Regulation by the Glycocalyx. Cell, 177(7), 1757-1770. https://doi.org/10.1016/j.cell.2019.04.017.

[2] Jeppesen, D. K., Fenix, A. M., Franklin, J. L., Higginbotham, J. N., Zhang, Q., Zimmerman, L. J., Liebler, D. C., Ping, J., Liu, Q., Evans, R., Fissell, W. H., Patton, J. G., Rome, L. H., Burnette, D. T., and Coffey, R. J. (2019). Reassessment of Exosome Composition. Cell, 177(2), 428-445. https://doi.org/10.1016/j.cell.2019.02.029.

NanoScale Hole Patterns Etched into Glass for Spectral Sensing

CNF Project Number: 2898-20

Principal Investigator(s): Nadia Pervez

User(s): Tanya Cruz Garza, Marcus Gingerich

Affiliation(s): Chromation, Bronx, NY

Primary Source(s) of Research Funding: VC

Contact: nadia@chromationspec.com, tanya@chromationspec.com

Website: https://www.chromation.com/

Primary CNF Tools Used: ASML 300C DUV, GCA 5x Autostep i-line stepper, Oxford 81 / Oxford 100 etchers

Abstract:

Over the past several years the ASML 300C DUV and GCA 5x Autostep i-line stepper have been used to produce pillar and hole features with diameters ranging from 232 nm to 816 nm on fused silica and silicon wafers as part of an academic account. These wafers have been further processed to include front and backside patterned metals layers in an academic cleanroom in New York City and then sent to our contract manufacturer to process them into spectral sensors. This report details how this process has been exported over to a complete manufacturing process for scale. This manufacturing process is split into parts. The first part consists of contract work at CNF where nanoscale hole features are patterned with the ASML 300C DUV and etched with the Oxford 81 and Oxford 100 etchers on an industrial account created this past year. The wafers are then further processed by a series of contract manufacturers to ultimately produce spectral sensors at scale. The initial results of the process have produced near identical results to the older process with a small decrease in throughput.

Summary of Research:

In previous years, a process for patterning nanophotonic pillar and hole structures was developed at CNF which used the ASML 300C DUV stepper as well as the GCA 5xAutostep i-line stepper. These features were etched into the substrate material using the patterned resist as an etch mask. The ASML 300C DUV stepper process has been used to pattern 4" borosilicate float glass wafers ("borofloat"), 4" fused silica wafers, and 4" silicon wafers. Pillar features like those shown in Figure 1 were fabricated with diameters ranging from 232 nm to 816 nm. Hole features were fabricated with design diameters ranging from 306 nm to 446 nm. Optimal depth of focus (DOF), exposure dose, and etch time were determined for nanophotonic patterns in fused silica by varying these parameters incrementally and examining the resultant features. Photonic crystal geometry was examined in the SEM and photonic crystal performance was assessed optically via extraction of waveguided light.

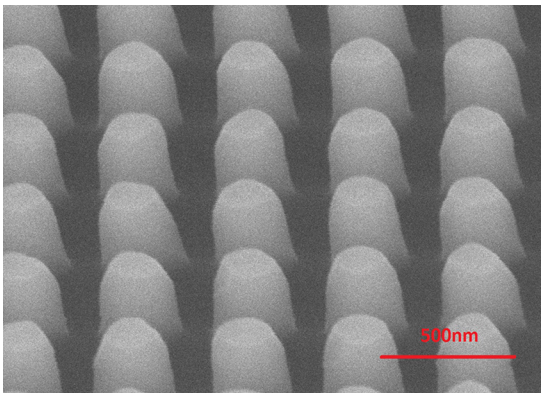

Figure 1: SEM image of photonic crystal pattern, nominally with 270 nm pillar features, fabricated fused silica with process developed with ASML 300C DUV stepper.

For recent applications, nanophotonic patterning is mainly focused on holes versus pillars because pillars are more likely to become damaged in a way that renders them useless for our spectral application during further processing and wafer handling.

In recent years, processing steps have been added to the wafer after nanophotonic crystal pattering to include both front and back side aluminum reflector layers which were developed in an academic cleanroom in New York City. These added layers are combined with single edge angled polishing after die singulation as shown in Figure 2, which is done in Asia. Additional front and backside

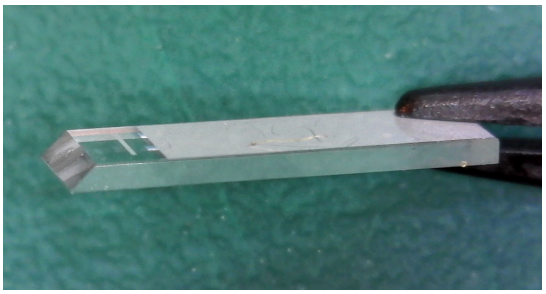

Figure 2: Diced and polished fused silica die with pattered Al reflectors on both sides in addition to the nanophotonic pattern and 45° edge polish.

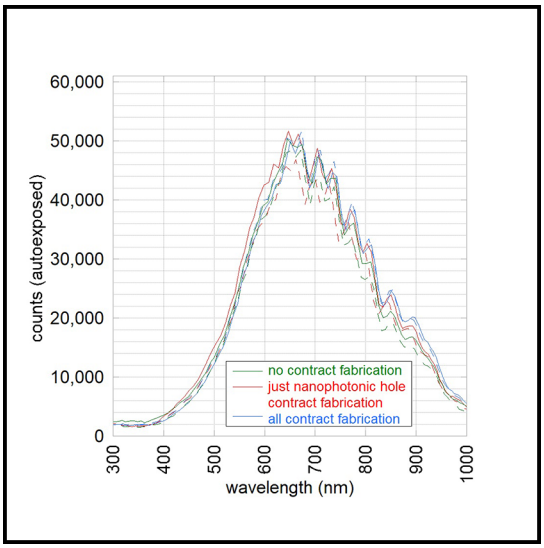

Figure 3: Overlay plot comparing dies with different amounts of contract manufacturing. Data has been normalized to they have the same peak values.

Figure 4: Example of spectrometer batch made with contract manufacturing process that includes fabrication steps at CNF.

patterned black absorber layers were also added to the process in Asia for better light handling. The dies are then built into spectral sensor housing with commercial off-the-shelf linear detectors to make spectrometers.

This last year, the complete process was exported to contract manufacturing, which utilizes the CNF ASML 300C DUV for submicron patterning of the photonic holes that are then etched using the Oxford 81 and Oxford 100 etchers. The nanophotonic patterning that is etched into fused silica wafers at CNF is done by a local CNF user who does contract work. The wafers are then transferred over to a local foundry for front and back side metal patterning. The wafers are then sent to our contract manufacturer in Asia where the additional patterned absorber layers are applied to the front and back side, the wafers are diced, and the die edges are polished at an angle. These dies are then built into spectrometers. Each 4" wafer produces just over 200 dies, allowing in turn which can be built into 200 spectrometers. This process allows for ease of spectrometer scale production into the thousands.

Comparisons were made between wafer dies that had nanophotonic patterns and metal that been made completely without contract manufacturing, dies that had only the nanophotonic patterns made by contract manufacturing, and dies that had both the nanophotonic patterns and metal done by contract manufacturing. Figure 3 shows an overlay of the spectrums produced with all these three different categories of without, partial, and complete contract manufacturing responding to a halogen lamp. The data was taken at differing integration times so that the peak value for each spectrum is normalized to the same value. It was found that the dies made without contract manufacturing had integration times of 0.12-0.14 ms, while the dies with just the nanophotonic pattern made by contract fabrication had integration times of 0.20 ms, and the dies made completely with contract manufacturing had integration times of 0.20-0.22 ms. So there is some small decrease in the brightness of the dies made with contract manufacturing that could be related to small variation in the process. This small variation in brightness is small enough to not be a concerning issue.

The use of the DUV capabilities at CNF has allowed high resolution, robust production of nanophotonic patterns for commercial quantities. Ideally all of Chromation's wafer fabrication would be done at a single foundry, but the DUV lithography capability that CNF has is hard to find elsewhere. Furthermore, the additional layers added to the wafers at our contract manufacturer in Asia was a process specialty designed for our applications that could not be achieved in a conventional cleanroom. A commercial process that includes contract work at CNF is an effective way of producing Chromation's nanophontic spectrometer at scale. Figure 4 shows a batch of spectrometers made with this manufacturing process.

300 mm E-Beam Lithography

CNF Project Number: 2931-21

Principal Investigator & Remote User: Craig McGray

Affiliation: Modern Microsystems, Inc.
Primary Source of Research Funding: Private/Corporate
Contact: craig@modernmicrosystems.com
Website: www.modernmicrosystems.com
Primary CNF Tools Used: JEOL 9500

Abstract:

We require small capacitors on 300 mm oxidized silicon wafers for SEM applications. To fabricate these capacitors, we used the JEOL 9500 system to pattern small (~50nm) features for subsequent metallization and liftoff.

Summary of Research:

Two wafers were coated with a bilayer electron-beam resist and patterned with a 9-die dose array on the JEOL 9500. The wafer was then developed and removed from the CNF for plasma descum, metallization, and liftoff elsewhere.

None of the 50 nm critical features were resolved at any of the attempted nine electron beam doses. An example site of a 50 nm feature is shown in Figure 1. Further, many of the larger features exhibited loss of adhesion, as shown in Figure 2.

Conclusions and Future Steps:

We hypothesize that the bottom layer of electron-beam resist may have been incompletely developed, such that the Cr-Au metallization layer did not adhere well to the underlying oxide. We propose repeating the lithography with a 100 mm oxidized silicon wafer, such that electron microscopy can be performed at the CNF immediately after development to determine if any resist remains in the exposed areas of the wafer.

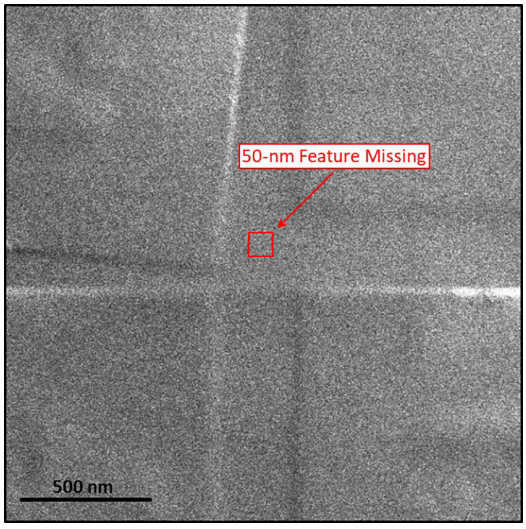

Figure 1: Electron micrograph of the location of a 50 nm critical feature that was not resolved by the electron-beam lithography process.

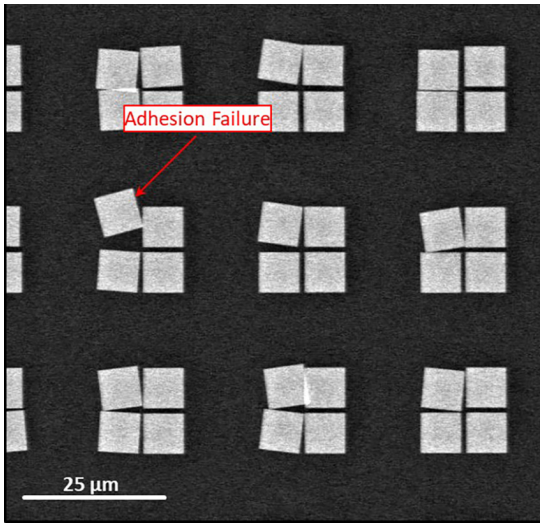

Figure 2: Electron micrograph showing 5 µm features that delaminated from the substrate after liftoff.

Characterization of Additively Manufactured High Aspect Ratio Microchannels via Two-Photon Polymerization

CNF Fellowship

Principal Investigator(s): Christopher Kemper Ober

User(s): Giancarlo D'Orazio

Affiliation(s): Department of Mechanical and Aerospace Engineering, Cornell NanoScale Science and Technology Facility; Cornell University

Primary Source(s) of Research Funding: Cornell NanoScale Science and Technology Facility Fellowship

Contact: c.ober@cornell.edu, gd373@cornell.edu

Website: https://cnf.cornell.edu/

Primary CNF Tools Used: NanoScribe Photonic Professional GT2

Abstract:

Two-photon polymerization and its application to additive manufacturing represents an unprecedented ability to develop nanometer scale 3D and 2D designs. Such microchannels have a variety of research applications, including creating high aspect ratio microchannels for microfluidic devices [1] and making architected gas diffusion layers [2] among a host of other applications. The NanoScribe Photonic Professional GT2 was utilized to develop high aspect ratio microchannels and better characterize the printing and developing process.

Summary of Research:

Two-photon polymerization offers the ability to create structures with delicate features, in the range of hundreds of nanometers. In the case of the NanoScribe Photonic Professional GT2, the manufacturer reported minimum feature size is on the order of 160 nm [3]. Given these capabilities, this 3D printer has a number of applications, among which are the development of microfluidic channels. The printing process itself relies on selectively polymerizing portions of a resin bubble, bonding the print to a substrate, typically glass or silicon. As part of this process, unpolymerized resin remains in the printed object and must be removed during a process called development, wherein a solvent is used to remove this excess resin.

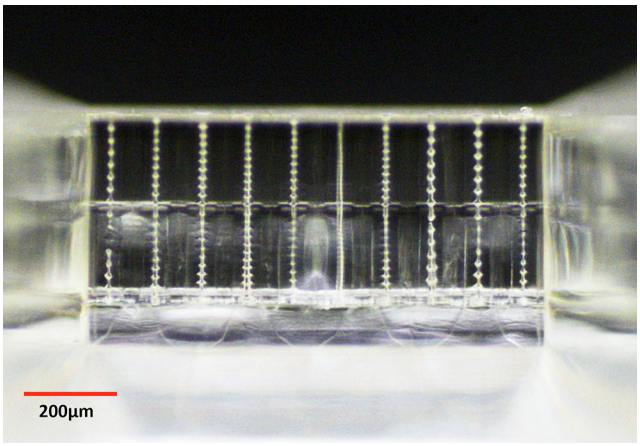

Figure 1: Fully developed microchannels, 400 µm in height, with varying channel diameter.

High aspect ratio microchannels, of up to 100:1 (length: diameter) were printed and sampled for appropriate development. As this is a transport limited process, various methods such as sonication, stirring, and long duration development were attempted. Additionally, the age of the resin and storage method were examined with IP-S resin, a type suited to medium size features (at 200 nm layer height).

In the first case, samples were developed using the suggested 20 minutes of development with propylene glycol methyl ether acetate (PGMEA) to dissolve uncured resin and a subsequent bath of isopropyl alcohol for five minutes to remove the PGMEA. After this, samples were optically characterized using the Nikon Wild light microscope to determine channel development. At this point no samples displayed complete development, requiring modifications to the development procedure. Further, it was determined that the light from the microscope was causing some degree of polymerization of the undeveloped resin. In effect, this prevents further development by clogging channels, meaning it was not possible to optically characterize the samples with unfiltered light.

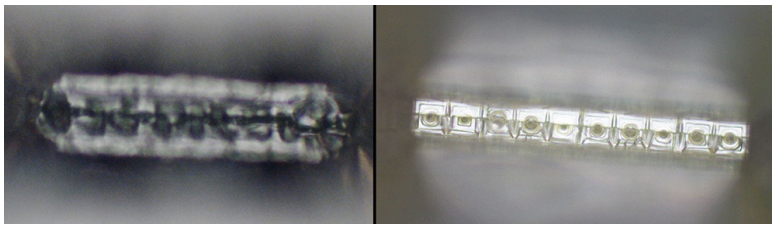

Figure 2: Underside of the microchannels. At left, resin that has been partially cured by a light microscope, inhibiting channel development. At right, fully developed channels from the sample in Figure 1 after 48 hours in PGMEA.

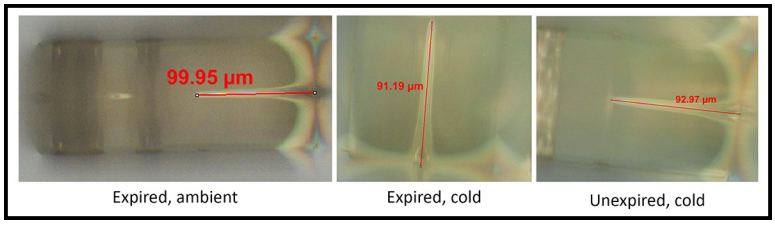

Figure 3: IP-S development performance for the three resin types examined; all showed similar results.

Therefore, it is recommended that for applications where there is not a suitable light source, samples should be tested for an appropriate development cycle with articles not meant for production.

Figure 2 is illustrative of the impact of a light microscope on inhibiting channel development. Partial curing of the resin created a block of material which could not be cleared via extended development (>72 hours) and sonication.

Additionally, the build method, such as creating a totally solid versus shell and scaffold design must be considered for extended development. Long duration development (>24 hours) will produce vacancies in the shell and scaffold designs as the PGMEA develop creates small holes in the shell and dissolves resin within the scaffold. For critical sections, a solid development method must be used, as seen in Figure 1. Here the surrounding structure is shell and scaffold, reducing printing time, while the area surrounding the microchannels is solid.

Another set of tests examined the impact of age and storage conditions of IP-S resin. Resins used in the GT2 printer have short shelf lives and are recommended to be stored cold. Prior to use, the resin should be brought to room temperature. Print quality and development time were explored with expired, cold resin (stored just above 0°C), expired, warm resin (stored at ambient), and unexpired, cold resin (stored in similar conditions to the expired, cold resin). A variety of geometries were printed, demonstrating micron-scale walls, overhangs, and microchannels via the 25X objective lens. All samples were developed for the NanoScribe-recommended 20 minutes in PGMEA and five minutes in isopropanol. Per the previous study, this time was known to be inadequate for complete channel development, however this could be accentuated with the different resins, as there is the possibility that some self-polymerization could occur within the expired materials.

Ultimately the results of testing showed that all resins with the suggested development procedure produced similar results. In fact, in this small sample, the expired, ambient temperature resin exhibited the greatest channel development. This seems to indicate that there is not a significant drawback for using this older resin for short development cycles. Longer development times were not trialed, and these results should not be extrapolated to out beyond short development cycles (<1 hour).

References:

[1] A. C. Lamont, A. T. Alsharhan, and R. D. Sochol, "Geometric Determinants of *In situ* Direct Laser Writing," Sci. Rep., vol. 9, no. 1, p. 394, Jan. 2019, doi: 10.1038/s41598-018-36727-z.

[2] J. Wicks, et al., "3D-Printable Fluoropolymer Gas Diffusion Layers for CO_2 Electroreduction," Adv. Mater., vol. 33, no. 7, p. 2003855, 2021, doi: 10.1002/adma.202003855.

[3] "Photonic Professional GT2: World's highest resolution 3D printer." https://www.nanoscribe.com/en/products/photonic-professional-gt2 (accessed Jul. 16, 2021).

INDEX

Reports by CNF Project Number

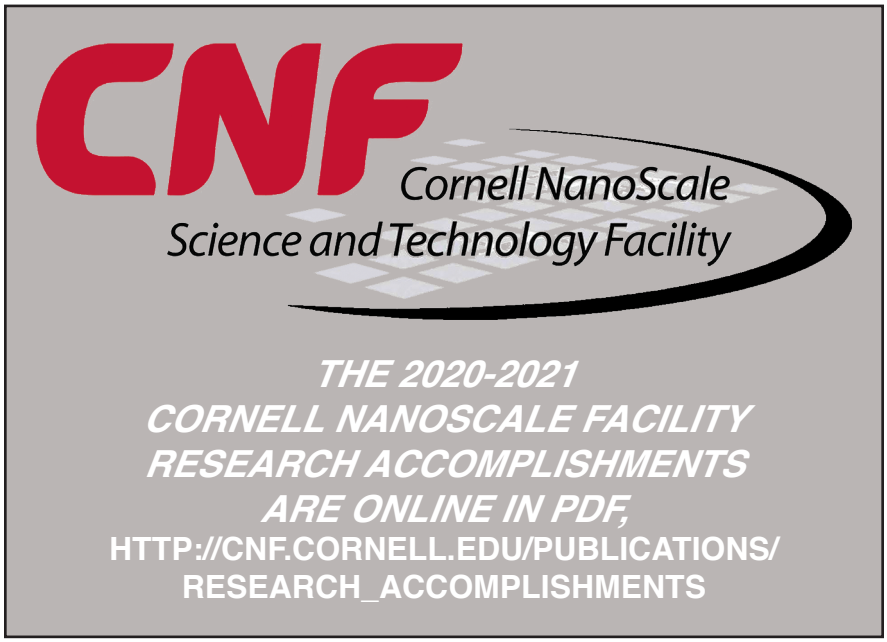

Reports by CNF Principal Investigators & Users

M

N

O

P

R

S

T

V

W

X

Y

Z

CNF maintains social media accounts on Twitter (@CornellCNF), Instagram, Facebook, and LinkedIn. Follow/like us to stay up to date with the latest!

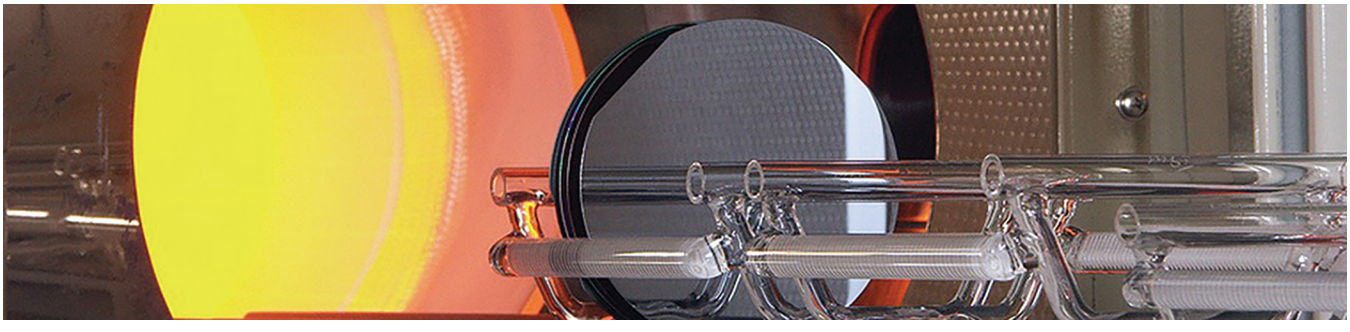

intentionally blank page

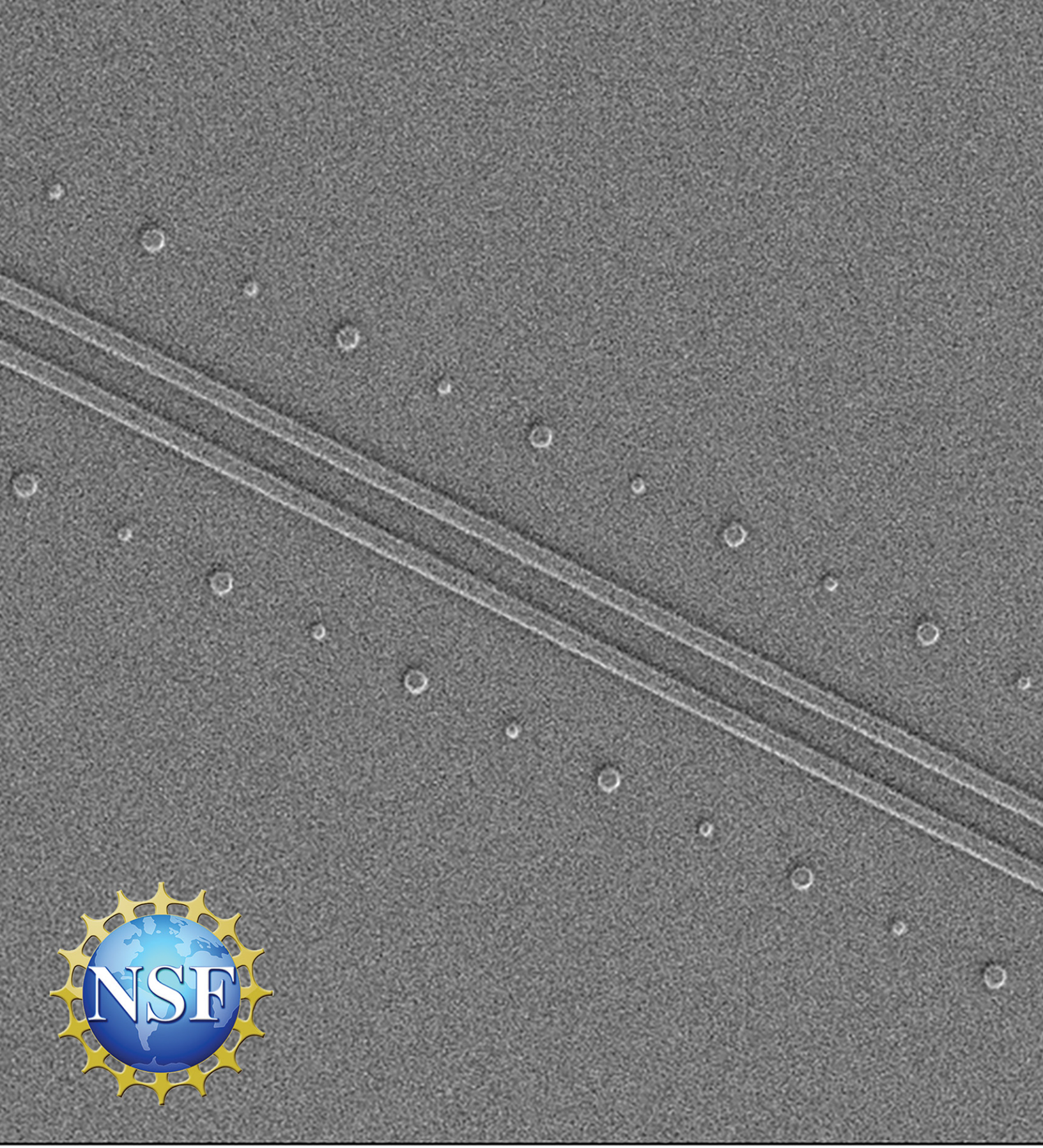

WD = 5.5 mm
Aperture Size = 30.00 µm
Width = 99.48 µ
Mag = 2.56 K X
EHT = 1.50 kV
Pixel Size = 97.